Ricerca di Sistema elettrico

Development of best estimate numerical tools for LFR design and safety analysis

T. Barani, A. Cammi, C. Castagna, L. Cognini, S. Lorenzi, L. Luzzi, A. Magni, D. Pizzocri
N. Abrate, S. Dulla, E. Guadagni, G. F. Nallo, P. Ravetto, L. Savoldi,D. Valerio, R. Zanino
A. Chierici, L. Chirco, R. Da Già, F. Franceschini, V. Giovacchini, S. Manservisi
N. Forgione, B. Gonfiotti, C. Ulissi, M. Eboli
G. Caruso, L. Ferroni, M. Frullini, F. Giannetti, L. Gramiccia, V. Narcisi, A. Subioli
A. Cervone, A. Del Nevo, I. Di Piazza, M. Tarantino

Development of best estimate numerical tools for LFR design and safety analysis

T. Barani, A. Cammi, C. Castagna, L. Cognini, S. Lorenzi, L. Luzzi, A. Magni, D. Pizzocri (POLIMI)
N. Abrate, S. Dulla, E. Guadagni, G. F. Nallo, P. Ravetto, L. Savoldi, D. Valerio, R. Zanino (POLITO)
A. Chierici, L. Chirco, R. Da Vià, F. Franceschini, V. Giovacchini, S. Manservisi (UNIBO)
N. Forgione, B. Gonfiotti, C. Ulissi, M. Eboli (UNIPI)
G. Caruso, L. Ferroni, M. Frullini, F. Giannetti, L. Gramiccia, V. Narcisi, A. Subioli (UNIROMA1)
A. Cervone, A. Del Nevo, I. Di Piazza, M. Tarantino (ENEA)

Settembre 2018

Report Ricerca di Sistema Elettrico

Titolo

Development of best estimate numerical tools for LFR design and safety analysis

Descrittori

Tipologia del documento:	Rapporto Tecnico
Collocazione contrattuale:	Accordo di programma ENEA-MSE su sicurezza nucleare e Reattori di IV generazione
Argomenti trattati:	Reattori Nucleari Veloci, Termoidraulica dei reattori nucleari Sicurezza nucleare, Analisi incidentale

Sommario

Nell'ambito della linea LP2, sono state condotte attività di ricerca al fine di sviluppare, aggiornare e convalidare codici di calcolo e modelli numerici per sostenere la progettazione ed effettuare analisi di sicurezza di un reattore veloce refrigerato a metallo liquido. Nell'ambito del PAR 2016, sono state messe in atto delle azioni al fine di integrare e coordinare tali attività. Si sono, pertanto, definite le aree di simulazione e le interconnessioni rilevanti per la progettazione e sicurezza di reattori Gen-IV. Il presente report rappresenta il proseguimento di tale azione. Ognuna di queste aree di simulazione è coperta da uno o più codici e simula un set di fenomeni multi-fisica e multi-scala rilevanti, e.g. termoidraulica di sistema, di contenimento, di sotto-canale, fluidodinamica tridimensionale, termo-meccanica della barretta di combustibile, del fuel assembly e di componenti, generazione di sezioni d'urto e sviluppo di metodi di aggiustamento delle stesse mediante utilizzo di dati sperimentali, dinamica neutronica tridimensionale, rilascio e trasporto di prodotti di fissione, etc. Tale attività fa parte di un'azione di sviluppo e convalida di una piattaforma di calcolo per sistemi nucleari innovativi, che si dovrà protrarre nel PT2018- 2020 (e successivi).

Relativamente a sviluppo e convalida, riportate nella parte 2 del presente report, sono state effettuate attività relative a:
1. *termo-meccanica della barretta di combustibile – supporto allo sviluppo del codice TRANSURANUS.*
2. *termoidraulica di sistema – supporto alla validazione del codice RELAP5-3D per applicazione ai sistemi a piscina*
3. *accoppiamento codici CFD/SYS-TH e loro validazione a fronte delle campagne sperimentali TALL*
4. *dinamica accoppiata neutronica-termoidraulica tridimensionale - sviluppo e applicazione codice FRENETIC*
5. *modellazione multifisica neutronica – termoidraulica - accoppiamento OpenFoam-Serpent*
6. *termoidraulica multifluid/multiphase e analisi di incidenti severi – supporto allo sviluppo e alla vlidazione del codice SIMMER-III e -IV*

Note: --

Autori: T. Barani, A. Cammi, C. Castagna, L. Cognini, S. Lorenzi, L. Luzzi, A. Magni, D. Pizzocri **(POLIMI)**
N. Abrate, S. Dulla, E. Guadagni, G. F. Nallo, P. Ravetto, L. Savoldi, D. Valerio, R. Zanino **(POLITO)**
A. Chierici, L. Chirco, R. Da Vià, F. Franceschini, V. Giovacchini, S. Manservisi **(UNIBO)**
N. Forgione, B. Gonfiotti, C. Ulissi, M. Eboli **(UNIPI)**
G. Caruso, L. Ferroni, M. Frullini, F. Giannetti, L. Gramiccia, V. Narcisi, A. Subioli **(UNIROMA1)**
A. Cervone, A. Del Nevo, I. Di Piazza, M. Tarantino **(ENEA)**

Copia n.   **In carico a:**

1			NOME			
			FIRMA			
0	**EMISSIONE**	27/11/2018	NOME	A. Del Nevo	M. Utili	M. Tarantino
			FIRMA	*[firma]*	*[firma]*	*[firma]*
REV.	**DESCRIZIONE**	**DATA**		**REDAZIONE**	**CONVALIDA**	**APPROVAZIONE**

(Page intentionally left blank)

LIST OF REVISIONS

Revision	Date	Scope of revision	Page
0	27/11/2018	First issue	213

(Page intentionally left blank)

LIST OF CONTENTS

(Page intentionally left blank)

LIST OF FIGURES

LIST OF TABLES

LIST OF ABBREVIATIONS

AdP	Accordo di Programma
ALFRED	Advanced Lead Fast Reactor European Demonstrator
ATHENA	Advanced Thermal Hydraulic Experiment for Nuclear Application
BE	Best Estimate
BEPU	Best Estimate Plus Uncertainty
BoP	Balance of Plant
BoT	Beginning of Transient
CEA	Commissariat a l'Energie Atomique et aux Energies Alternatives
CFD	Computational Fluid Dynamics
CIRCE	Circolazione Eutettico
CIRTEN	Interuniversity Consortium for Technological Nuclear Research
CHEOPEIII	Chemistry Operation III Facility
CR	Control Rod
DBA	Design Base Accident
DHR	Decay Heat Removal
DHRS	Decay Heat Removal System
DOC	Design-Oriented Code
DSA	Deterministic Safety Analysis
ESFRI	European Strategy Forum on Research Infrastructures
EoT	End of Transient
FA	Fuel Assembly
FALCON	Fostering ALFRED Construction
FPC	Fuel Performace Code
FR	Fast Reactor
GIORDI	Grid to Rod fretting facility
HBS	High Burnup Structure
HELENA	Heavy Liquid Metal Experimental Loop for Advanced Nuclear Applications
HLM	Heavy Liquid Metal
HX or HEX	Heat Exchanger
I&C	Instrumentation and Control
LBE	Lead Bismuth Eutectic
LECOR	Lead Corrosion Loop
LEADER	Lead-cooled Advanced Demonstration Reactor
LIFUS5	Lead-Lithium for Fusion Facility (5)
LFR	Lead Fast Reactor
LM	Liquid Metal
LMR	Liquid Metal Reactor
LWR	Light Water Reactor
MA	Minor Actinide
MABB	Minor Actinides Bearing Blankets
MOX	(U-Pu) Mixed Oxide
NACIE	Natural Circulation Experiment Loop
NPPs	Nuclear Power Plants
O&M	Operation and Maintenance
PAR	Piani Annuali di Realizzazione
PID	Proportional-Integral-Derivative controllers
PLD	Pulsed Laser Deposition
POLIMI	Politecnico di Milano
POLITO	Politecnico di Torino
PP	Primary Pump

PSA	Probabilistic Safety Analysis
RACHELE	Reactions and Advanced chemistry for Lead
RSE	Ricerca Sistema Elettrico
RV	Reactor Vessel
RVACS	Reactor Vessel Air-Cooling System
SA	Safety Analysis
SET-PLAN	Strategic Energy Technology Plan
SG	Steam Generator
SGTR	Steam Generator Tube Rupture
SISO	Single Input Single Output
SYS	System
SYS-TH	System- ThermalHydraulics
TH	Thermal-Hydraulics
TKE	Turbulent Kinetic Energy
TRL	Technological Readiness Level
TSO	Technical Safety Organization
ULOF	Unprotected Loss of Flow
UNIBO	Università di Bologna
UNIPI	Università di Pisa
UNIROMA1	Università di Roma - Sapienza
VOC	Verification-Oriented Code
V&V	Verification & Validation
AdP	Accordo di Programma
ALFRED	Advanced Lead Fast Reactor European Demonstrator
BE	Best Estimate
DSA	Deterministic Safety Analysis
LFR	Lead Fast Reactor
PAR	
PSA	Probabilistic Safety Analysis
RSE	Ricerca Sistema Elettrico
SA	Safety Analysis

FOREWORD

The Lead-cooled Fast Reactor (LFR) technology brings about the possibility of fully complying with all the Generation IV requirements. This capability being more and more acknowledged in international fora, the LFR is gathering a continuously increasing interest, with new industrial actors committing on LFR-related initiatives. In this context, the Italian nuclear community evaluates strategic to continue elevating the competences and capabilities, with the perspective of extending the support to the design and safety analysis of future LFR systems. The most appropriate framework for this advancement is the Accordo di Programma (AdP), within which ENEA and CIRTEN (the consortium gathering all Italian universities engaged in nuclear education, training and research) are already cooperating on the LFR technology since 2006, along with national industry as main stakeholder. Within the AdP, the LFR system chosen as reference for all studies and investigations is ALFRED, the Advanced Lead-cooled Fast Reactor European Demonstrator. As a demonstration reactor, indeed, it was reckoned as the system best fitting with the research and development (R&D) nature of the activities performed in the AdP, being demonstration the step that logically follows R&D in the advancement of the LFR technology by readiness levels. Moreover, ALFRED is envisaged as the key facility of a distributed research infrastructure of pan-European interest, open to scientists and technologists for relevant experiments to be performed on a fully LFR-representative and integral environment, with the long-term perspective of supporting to the safe and sustainable operation of future LFRs, thereby fulfilling the general objectives of the AdP itself.

In the wide spectrum of possible activities to support the further development of the LFR technology, and exploiting the specific expertise acquired by the universities in the past years, within the scope of the 2016 Piano Annuale di Realizzazione (PAR) it was decided to focus the cooperative efforts shared between ENEA and CIRTEN towards the development of an **best estimate computational tools supporting the various stages of design and safety analyses of LFR systems**, so to increase – or help in viewing how to fill the gaps – the modeling capabilities.

(Page intentionally left blank)

1 THERMO-MECHANICS OF THE FUEL PIN – DEVELOPMENT AND ASSESSMENT OF MODELS AND ALGORITHMS DESCRIBING INERT GAS BEHAVIOR FOR USE IN TRANSURANUS

L. Luzzi, D. Pizzocri, T. Barani, L. Cognini, A. Magni

(Page intentionally left blank)

1.1 Background and references

This activity is twofold: first, we present the derivation of two new correlations based on available literature data for helium solubility in oxide nuclear fuel; second, we present a new algorithm for the solution of coupled partial differential equations for inert gas behaviour modelling. Both these contributions are intended for implementation and use in the TRANSURANUS fuel performance code (FPC), for its application to fast reactors.

1.1.1 Helium solubility

The knowledge of helium behaviour in nuclear fuel is of fundamental importance for its safe operation and storage [1.1],[1.2]. This is true irrespectively of the fuel cycle strategy adopted. In fact, both open and closed fuel cycles tend towards operating nuclear fuel to higher burnups (i.e., keeping the fuel in the reactor for a longer time to extract more specific energy from it), thus implying higher accumulation of helium in the fuel rods themselves [1.3]. Moreover, considering open fuel cycles foreseeing the disposal of spent fuel, the helium production rate in the spent nuclear fuel is positively correlated with the burnup at discharge, and the production of helium (by α-decay of minor actinides) progresses during storage of spent fuel [1.4],[1.5]. On the other hand, closed fuel cycles imply the use of fuels with higher concentrations of minor actinides (e.g., minor actinides bearing blankets, MABB), thus being characterized by higher helium production rates during operation [1.4].

Helium is produced in nuclear fuel by ternary fissions, (n,α)-reactions and α-decay [1.6]-[1.8]. After its production, it precipitates into intra- and inter-granular bubbles and can be absorbed/released from/to the nuclear fuel rod free volume [1.9],[1.10]. Helium thus contributes to the fuel swelling (and eventually to the stress in the cladding after mechanical contact is established), to the pressure in the fuel rod free volume, and to the gap conductance (giving feedback to the fuel temperature) [1.11].

Among the several properties governing the behaviour of helium in nuclear fuel, its diffusivity and solubility govern the transport and absorption/release mechanisms [1.12]-[1.14]. Compared to xenon and krypton, helium presents both a higher solubility and a higher diffusivity in oxide nuclear fuel [1.5]-[1.17]. A considerable amount of experiments has been performed with the goal of determining the diffusivity and solubility of helium in nuclear fuel [1.12]-[1.5],[1.18]-[1.27]. In particular, several measurements have been made to determine the helium diffusivity as a function of temperature [1.13]-[1.15],[1.19]-[1.27] and its Henry's constant as function of temperature [1.12]-[1.15],[1.18]-[1.20],[1.28].

In the light of the profound differences in microstructure of the samples, the correlations for He-UO$_2$ Henry's constant derived from rough data fitting must be critically analysed. No correlations are currently implemented in the TRANSURANUS code for this parameter, beside its expected modelling importance.

1.1.2 PolyPole-2 algorithm

The first and basic step of fission gas release (FGR) and gaseous swelling is gas atom transport to the grain boundaries. It follows that modelling of this process is a fundamental component of any fission gas behaviour model in a fuel performance code. Intra-granular fission gas transport occurs by thermal and irradiation-enhanced diffusion of single gas atoms, coupled to trapping in and irradiation-induced resolution from intra-granular bubbles. Diffusion of intra-granular bubbles becomes relevant at high temperatures, above ~1800°C [1.29],[1.30]. Thus, modelling the process of gas transport to the grain boundaries calls for the treatment of different concomitant processes, namely, diffusion coupled with trapping and resolution of gas atoms. Extensive literature deals with the evaluation of the parameters characterizing these mechanisms, both experimental and theoretical work, e.g., [1.29],[1.31]-[1.34]. In this activity, we deal with the numerical problem associated with the computational solution of the equations describing the process. Clearly, this problem has an enormous practical importance for fission gas behaviour calculations in fuel performance

analysis. In fact, the solution of these equations is required in each mesh point of the engineering FPCs. Efficient solutions are thus mandatory to guarantee acceptable overall computational times.

Speight [1.35] proposed a simplified mathematical description of intra-granular fission gas release. He lumped the trapping rate, β (s^{-1}), the re-solution rate, α (s^{-1}), and the diffusion coefficient, D (m^2 s^{-1}) into an effective diffusion coefficient, $D_{eff} = \alpha / (\alpha + \beta) D$, restating the mathematical problem as purely diffusive, i.e., simplifying the system

$$\frac{\partial c_1}{\partial t} = D\nabla^2 c_1 - \beta c_1 + \alpha m + yF$$

$$\frac{\partial m}{\partial t} = +\beta c_1 - \alpha m$$

(1.1)

in which c_1 (at m^{-3}) is the single-atom gas concentration, m (at m^{-3}) is the concentration of gas trapped in intra-granular bubbles, and yF (at fiss$^{-1} \cdot$ fiss m^{-3} s^{-1}) is the production rate of gas atoms, to

$$\frac{\partial c_{tot}}{\partial t} = \frac{\alpha}{\alpha + \beta} D\nabla^2 c_{tot} + yF$$

(1.2)

where c_{tot} (at m^{-3}) is the total gas concentration. Such simplification implies the assumption of equilibrium between trapping and re-solution (quasi-stationary approach). The formulation of Speight is universally adopted for models employed in fuel performance codes, e.g., [1.36]-[1.42]. In addition, the assumption of spherical grain geometry [1.10] is applied. The solution of the diffusion equation for constant conditions is well known. Nevertheless, time-varying conditions are involved in realistic problems. Therefore, the solution for time-varying conditions is the issue of interest for applications to fuel performance analysis, which calls for the development of dedicated numerical algorithms. As briefly stated above, given the very high number of calls of each local model (such as the fission gas behaviour model) in a fuel performance code there is a requirement of low computational cost (in addition to the requirement of suitable accuracy for the numerical solution). Clearly, the numerical solution of the diffusion equation in time-varying conditions may be obtained using a spatial discretization method such as a finite difference scheme. However, the high associated computational effort can make a space-discretization based solution impractical for application in fuel performance codes. Several alternative algorithms, which provide approximate solutions for Eq. 1.2 at high speed of computation and can be used in fuel performance codes, have been developed[1.36]-[1.38],[1.43].

We propose a numerical algorithm for the accurate and fast solution of both Eqs. 1.1, 1.2 in time-varying conditions, which we refer to as PolyPole. We verify the algorithms for Eqs. 1.1 with specifically designed numerical experiments.

As demonstrated in [1.44], the solution of this general system of PDEs (Eqs. 1.1) is of high engineering importance, especially related to modelling fission gas behaviour in the high burnup structure (HBS) during reactivity-initiated accidents (RIA).

1.2 Body of the report concerning the ongoing activities

In Sect. 1.2.1, we provide a complete overview of all the experimental results obtained for helium solubility in oxide nuclear fuel, in terms of Henry's constant. We derive empirical correlations and recommend the most suitable values of the helium Henry's constant. The derivation of empirical correlations is

complemented by an uncertainty analysis. These correlations represent a step forward in the development of a helium behaviour physics-based model in TRANURANUS, with respect to the diffusivity correlations derived as part of the POLIMI activities for the PAR 2016.

In Sect. 1.2.2, we describe an algorithm (PolyPole-2) dedicated to the solution of coupled partial differential equations relevant for inert gas behaviour modelling in fuel performance codes. The here presented algorithm is preliminary verified with a random numerical experiment. This algorithm extends the algorithm for the solution of the effective diffusion equation (PolyPole-1) developed as part of the POLIMI activities for the PAR 2015.

1.2.1 Helium solubility

After the verification of the validity of Henry's law for the He-UO$_2$ system and the classification of the resulting data based on the sample microstructure (not reported here for the sake of brevity, see [1.45]), we derive empirical correlations for Henry's constant of helium in oxide fuel.

As a starting point, we recall Henry's law

$$c_{S,\text{He}} = k_H(T)p \qquad (1.3)$$

where k_H (at m^{-3} MPa^{-1}) is Henry's constant and p (MPa) is the helium pressure. The solubility is thus a function of temperature and pressure. If Henry's law is valid for the He-fuel system[1], Henry's constant is solely a temperature function.

Following [1.45], we collect in Tab. 1-1 an overview of the available experimental data of solubility. Helium solubility in uranium dioxide have been also extensively studied theoretically by [1.46]-[1.49], but this results are not included in the current analysis. Theoretical results are overall in line with experimental ones[1.45].

Assuming the validity of Eq. 1.3, we need to derive a correlation for Henry's constant as a function of temperature. The data presented in Tab. 1-1 are reported in Fig. 1.1, divided based on the microstructure of the sample, i.e., powders and single crystals. As expectable, powders show a generally higher apparent Henry's constant in all the temperature range compared to single crystals, since helium is accumulated in-between different particles. Unfortunately, no data are available for polycrystalline materials (either experimental or lower-length scale simulation results).

Despite the large scatter of the experimental results for the helium solubility in uranium dioxide, the resulting clustering of the data motivated the derivation of two distinct correlations in the form $k_H = A \exp(-B/kT)$. The best estimate correlation for Henry's constant in the powder samples is

$$k_H = 1.8 \cdot 10^{25} \exp(-0.41/kT) \qquad (1.4)$$

and the best estimate correlation for Henry's constant in the single crystal samples is

---

[1] The validity of Henry's law in the system of interest can be verified with solubility data at different pressures and same temperature. The only dataset available with these characteristics is the one by [1.20], reported in Tab. 1-1. At each of three temperatures (1473 K, 1623 K, 1773 K) he performed infusions at three pressures (4.8 MPa, 6.9 MPa, 9.0 MPa) in a UO$_2$ single crystal of 1 μm size. The resulting solubilities show a reasonably linear dependency on pressure at each temperature, corroborating the verification of Henry's law. It is of sure interest to confirm the verification in this temperature-pressure range and to extend it outside of this range and to other fuel crystal sizes/fuel micro-structures. For this purpose, lower-length scale calculations and separate effects can be used in support one of the other.

$$k_H = 4.1 \cdot 10^{24} \exp(-0.65/kT) \tag{1.5}$$

Summarizing the uncertainty analysis concerning the fit of the solubility correlations, it is important to notice that the functional form used is Log k_H = Log A − B/kT Log e. Thus, we have the following confidence intervals at 95% confidence level: Log A (at m^{-3} MPa^{-1}) = 25.25 (23.91, 26.6) for Eq. 1.4, and 24.61 (23.41, 25.82) for Eq. 1.5; B (eV) = 0.41 (0.06, 0.75) for Eq. 1.4, and 0.65 (0.28, 1.01) for Eq. 1.5; the R^2 are respectively 0.83 and 0.83, for Eq. 1.4 and Eq. 1.5. These fitting parameters have been derived applying the LAR (least absolute residuals) method.

Regarding the applicability, the correlation derived fitting the data concerning the powder samples (Eq. 1.4) is usable for the analysis of the helium behaviour in the fuel after the pulverization occurred during accidental temperature transients [1.30],[1.50]. On the other hand, the correlation proposed for Henry's constant in single crystals (Eq. 1.5) is of interest for calculations in meso-scale intra-granular and inter-granular models dealing with single fuel grains.

1.2.2 PolyPole-2 algorithm

In this Section, we present the new numerical algorithm solving Eqs. 1.1 in time-varying conditions, referred to as PolyPole-2 [1.44]. A simplified version of the same algorithm, referred to as PolyPole-1 [1.51], solving Eq. 1.2.

To simplify the notation, it is convenient to re-write Eqs. 1.1 as

$$\frac{\partial}{\partial t} u = (\mathbf{D} + \mathbf{E})u + \mathbf{S} \tag{1.6}$$

in which $u = [c_1\ m]$ and $\mathbf{S} = [yF\ 0]$ are vectors containing the gas concentrations and the fission source term, respectively. The diffusion $\mathbf{D}$ and exchange $\mathbf{E}$ operators are defined as

$$\mathbf{D} = \begin{bmatrix} D\nabla^2 & 0 \\ 0 & 0 \end{bmatrix} \tag{1.7}$$

$$\mathbf{E} = \begin{bmatrix} -\beta & +\alpha \\ +\beta & -\alpha \end{bmatrix} \tag{1.8}$$

The boundary conditions of Eq. 1.6 are $u(r = a, t) = 0$ and $\partial u/\partial r|_{(r\ =\ 0)} = 0$. The initial condition is $u(r, t = 0) = u_0(r) = [c_0(r)\ m_0(r)]$.

Under the quasi-stationary approximation [35], the diffusion-exchange operator $(\mathbf{D} + \mathbf{E})$ is replaced by $D\alpha/(\alpha + \beta)\nabla^2$, $\mathbf{S}$ is replaced by yF and u is replaced by $c_{tot} = c_1 + m$ (i.e., Eq. 1.2).

Here, the objective is to find an approximate solution u^* for the case of time-varying $(\mathbf{D} + \mathbf{E})$ and $\mathbf{S}$. With the *ansatz* that the solution can be approximated as

$$u^*(r,t) \approx \sum_{n=1}^{\infty} z_n^*(t)\psi_n(r) = \sum_{n=1}^{\infty} \mathbf{P}_n z_n(t)\psi_n(r) \tag{1.9}$$

in which $z_n(t)$ and $\psi_n(r)$ are the time coefficients and the spatial modes, respectively, of the solution for constant conditions (exponential in time and cardinal sine in space). The operator $\mathbf{P}_n$ embodies the correction for time-varying conditions and is applied to each mode of the solution. The formulation adopted in this work for this operator is made of two distinct polynomials of second order J

$$
\mathbf{P}_n = \begin{bmatrix} 1 + \sum_{j=1}^{J} p_j dt^j & 0 \\ 0 & 1 + \sum_{j=1}^{J} q_j dt^j \end{bmatrix} \tag{1.10}
$$

This definition of $\mathbf{P}_n$ reduces to a single polynomial correction factor for the PolyPole-1 algorithm [1.51].

The problem of finding an approximate solution for time-varying conditions is basically shifted to the problem of finding the coefficients of the polynomials in $\mathbf{P}_n$. To calculate the coefficients p_j and q_j, $2J$ equations are needed. This set of equations is obtained by sampling the time-varying operators, $\mathbf{D}(t)$, $\mathbf{E}(t)$ and $\mathbf{S}(t)$, at J uniformly distributed instants along the time-step dt. The sets of sampled values, $\mathbf{D}[j]$, $\mathbf{E}[j]$ and $\mathbf{S}[j]$, contain the information on the variation of the operators along the time step and are used to calculate the corrective polynomials as follows.

The time coefficients $z^*(t)$ defined by Eq. 1.9 are assumed to satisfy Eq. 1.6 (here written in vector notation) at the sampling times $t[j]$, $t_i \leq t[j] \leq t_{i+1}$

$$
\left. \frac{\partial (\mathbf{P}_n z_n)}{\partial t} \right|_{t[j]} = \langle \psi_n | \mathbf{D}[j] + \mathbf{E}[j] | \psi_n \rangle (\mathbf{P}_n z_n) + \langle \psi_n | \mathbf{S}[j] \rangle \tag{1.11}
$$

Eq. 1.11 defines a linear system of $2J$ equations for the polynomial coefficients p_j and q_j, and is used to determine the polynomial correction operator $\mathbf{P}_n$. The time coefficients of the analytic solution for constant conditions, z_n, are calculated using averages along the time step of the sampled values $\mathbf{D}[j]$, $\mathbf{E}[j]$ and $\mathbf{S}[j]$.
The PolyPole-2 (and PolyPole-1, identically) solution is then reconstructed as a linear combination of the spatial with the corrected time coefficients, according to Eq. 1.9. The series is approximated by a finite number of terms (M, number of modes). The value of M is determined based on a D'Alembert-like remainder criterion.

The verification of PolyPole-2 is performed via a random numerical experiment [1.44]. The numerical experiment consists of the application of the PolyPole-2 algorithm to the numerical solution of Eqs. 1.6 for many randomly generated histories. The results from the PolyPole-2 algorithm are compared to the reference solution provided by a finite difference (FD) algorithm (developed as part of previous activities. Details of this method can be found in [1.52]). This algorithm can be applied to obtain a reference solution of Eqs. 1.1 and 1.2 (in principle, up to any tolerance) for piecewise-linear operation histories. The considered histories, both for RIA-like and operational transients, are in terms of temperature and fission rate, from which the time-dependent parameters in the diffusion and exchange operators, $\mathbf{D}(t)$ and $\mathbf{E}(t)$, and in the source term, $\mathbf{S}(t)$, are calculated[2].

The figure of merit chosen for this numerical experiment is the fractional intra-granular fission gas release at the end of the considered history, defined as

---

[2] We use the expressions for the diffusion coefficient, D, by Turnbull et al., [1.59], the re-solution rate, α, by White and Tucker[1.39], and the trapping rate, β, by Ham [1.60]. A value of 0.3 is considered for the fission yield, y. For the purpose of this numerical experiment, as long as values and dependencies are realistic, the specific choices are arbitrary.

$$\chi = \frac{\int_0^{t_{end}} yF(t')dt' - c_1(t_{end}) - m(t_{end})}{\int_0^{t_{end}} yF(t')dt'} \qquad (1.12)$$

where t_{end} (s) is the end time of each history considered.

In order to verify the PolyPole-2 algorithm in fast transient conditions, we consider RIA-like conditions. We considered two sets of representative random histories. The first one, which is referred to as *centre*, is designed to represent the intra-granular gas diffusion during an RIA transient in the centre of the pellet. The second one, referred to as *rim*, is designed to be representative of the intra-granular gas behaviour during a RIA transient in the high burnup structure (HBS) at the rim of the pellet (for which a specific formation model has been developed as part of POLIMI activities in previous PARs). These two sets of histories differ in the grain size a, which is assumed as 5.0 μm for the *centre* and as 150 nm for the *rim*, respectively.

We consider an initial gas concentration corresponding to the gas generated during an irradiation up to 50 GWd tU^{-1}. This initial gas concentration is assumed to be stored in the grains in the *centre* (70% as single atoms and 30% as atoms in bubbles) [1.39]. In the *rim*, the initial concentration is set to 10^{26} at m^{-3}, corresponding to the asymptotic gas concentration achieved in the HBS grains [1.53],[1.54]. The RIA-like random histories have the following characteristics (identical for both *centre* and *rim*):

- The peak width, τ_{RIA}, is a random variable, sampled uniformly over 20-60 ms.

- The specific energy, E_{RIA}, is a random variable, sampled uniformly over 400-800 J (gUO$_2$)$^{-1}$.

- The maximum specific power, P_{RIA} (W g^{-1}), is calculated as $P_{RIA} = 62.5\ E_{RIA}/\tau_{RIA}$ [55,56].

- The power pulse shape is calculated according to the Nordheim-Fucks model [55,56].

- The initial temperature, T_0 (K), is calculated as $T_0 = 883\ (5\ 10^{-4}\ E_{RIA} + 0.7772)$ (uniform in the range 863-1039 K) [55].

- The maximum temperature, T_{max} (K) is calculated as $T_{max} = 2564 \quad (5\ 10^{-4}\ E_{RIA} + 0.7772)$ (uniform in the range 2506-3017 K) [55].

- The maximum temperature is reached after $2\tau_{RIA}$, i.e., at the end of the power pulse. The temperature increase in time is calculated as the integral of the power pulse.

- The end time is fixed at 300 ms after the beginning of the RIA-transient.

- The final temperature, T_{end} (K), is calculated as $T_{end} = 1227\ (5\ 10^{-4}\ E_{RIA} + 0.7772)$ (uniform in the range 1200-1444 K) [55].

- Prior to RIA-transient each history has a plateau of 100 hours at T_0, to ensure the establishing of equilibrium between single gas atoms and gas in bubbles.

The results of the RIA-like numerical experiment are presented in Fig. 1.2. Each data point in these figures corresponds to one of the randomly generated operation histories and represents the intra-granular fission gas release (Eq. 1.12) obtained with the PolyPole-2 algorithm versus the reference FD solution. The deviation from the 45° line is a measure of the accuracy of PolyPole-2. Results appear to be distributed between two clusters of data points. The higher intra-granular fission gas release results (5 to 15%, approximately) are the simulations with the smaller grain radius of 0.1 μm. With a small grain radius diffusion to grain boundaries occurs at a higher rate (considering a pure diffusion problem as a first approximation, the diffusion rate is D/a^2), thus leading to higher intra-granular fission gas release compared to behaviour with larger grains.

In Fig. 1.2, we also report the results from the FD solution of Eq. 1.2 for the same input histories. The comparison highlights the effect of the quasi-stationary approximation (implied in Eq. 1.2) for the analysis of fast transients. Results demonstrate that the quasi-stationary approximation is inadequate in describing the fast transients to relatively high temperatures (e.g., RIAs) considered in this study. In particular, the approximation leads to a strong unacceptable under-prediction of the intra-granular fission gas release.

Besides accuracy, speed of computation is an essential feature for an algorithm to be effectively employed in a fuel performance code. The computational time (i.e., the time taken for the analysis of a single operation history) for the PolyPole-2 and FD algorithms are compared in Fig. 1.3. The computational time of PolyPole-2 is approximately two orders of magnitude lower than that of the FD algorithm. Such efficiency of computation, combined with the demonstrated accuracy, makes PolyPole-2 suitable for implementation in TRANSURANUS.

1.3   Role of the activity, general goals and future development

The activity represents an ideal continuation of previous efforts carried out at POLIMI in modelling the impact of inert gas behaviour on the thermo-mechanical performance of oxide nuclear fuels and for the advancement of available numerical tools for the simulation of oxide fuel in LFR conditions [1.57],[1.58]. In this picture, helium solubility (herein treated in terms of its Henry's constant) plays a fundamental role in determining oxide fuel swelling and fuel rod pressurization, thus affecting its thermo-mechanical behaviour under both normal operation and transient conditions. Moreover, since high burnups are attractive from an economical perspective, modelling the formation of the high burnup structure and its peculiar thermo-mechanical behaviour is of the utter relevance to the safe operation of oxide-fuelled rods in LFR systems.

The exposed advancements in the numerical algorithm PolyPole, suited for the efficient solution of the governing equations of inert gas behaviour physics-based models in fuel performance codes, are essential in perspective to improve the numerical capabilities of fuel performance codes. Besides allowing for the treatment of inert gas behaviour models, these advancements pave the way for the treatment of other fundamental meso-scale phenomena (e.g., point defects and thermochemistry).

Future efforts will be devoted to further improvements of the description of helium behaviour. We have now all the instruments (developed among the POLIMI contribution to previous PAR and current PAR 2017) for the definition of a physics-based describing helium behaviour in oxide fuel and for its inclusion in TRANSURANUS. The next steps are going to be the development of the model itself, the implementation of the model in TRANURANUS exploiting the PolyPole algorithms, and the comparison of model results with experimental data. Moreover, the development of a burnup module allowing for accurate, yet fast, prediction of helium production rate is of interest for future activities in different kind of fuels of interest for lead cooled fast reactors (again, in continuity with previous POLIMI activities in PARs).

The overall goal of POLIMI activities within PARs is the set-up and application of an improved LFR-oriented TRANSURANUS version, with focus on the inert gas behaviour physics-based multi-scale modelling approach.

Reference	Sample	He infusion pressure (MPa)	Solubility (at m⁻³)	Temperature (K)
Powders				
Belle (1961)	UO$_2$ powder ($\approx$0.16 μm)	0.1	$2.13 \cdot 10^{22}$	1073
Hasko and Szwarc (1963)	UO$_2$ powder	11	$9.91 \cdot 10^{22}$	1073
Bostrom (as reported by Rufeh, 1964)	UO$_2$ powder ($\approx$0.15 μm)	0.1	$6.59 \cdot 10^{22}$	1073
		0.1	$3.08 \cdot 10^{22}$	1273
Rufeh et al. (1965)	UO$_2$ powder ($\approx$4 μm)	10	$1.81 \cdot 10^{25}$	1473
		5	$4.52 \cdot 10^{24}$	1473
		10	$8.72 \cdot 10^{24}$	1573
Blanpain et al. (2006)	UO$_2$ powder ($\approx$10 μm)	0.2	$1.26 \cdot 10^{23}$	1273
		0.2	$1.14 \cdot 10^{23}$	1473
		0.2	$1.07 \cdot 10^{23}$	1573
Single crystals				
Hasko and Szwarc (1963)	UO$_2$ single crystal	11	$1.65 \cdot 10^{22}$	1073
Sung (1964)	UO$_2$ single crystal ($\approx$1 μm)	4.8	$1.34 \cdot 10^{23}$	1473
		6.9	$2.61 \cdot 10^{23}$	1473
		9.0	$3.35 \cdot 10^{23}$	1473
		4.8	$1.72 \cdot 10^{23}$	1623
		6.9	$3.13 \cdot 10^{23}$	1623
		9.0	$4.05 \cdot 10^{23}$	1623
		4.8	$2.02 \cdot 10^{23}$	1773
		6.9	$4.05 \cdot 10^{23}$	1773
		9.0	$5.83 \cdot 10^{23}$	1773
Blanpain et al. (2006)	UO$_2$ single crystal ($\approx$10 μm)	0.2	$1.07 \cdot 10^{22}$	1573
Maugeri et al. (2009)	UO$_2$ single crystal	100	$1.38 \cdot 10^{23}$	1523
		100	$2.16 \cdot 10^{23}$	1743
Nakajima et al. (2011)	UO$_2$ single crystal ($\approx$18 μm)	90	$1.03 \cdot 10^{25}$	1473
Talip et al. (2014)	UO$_2$ single crystal	98.7	$1.99 \cdot 10^{23}$	1500

Tab. 1-1 – Collection of the helium solubility in oxide fuel [1.45]
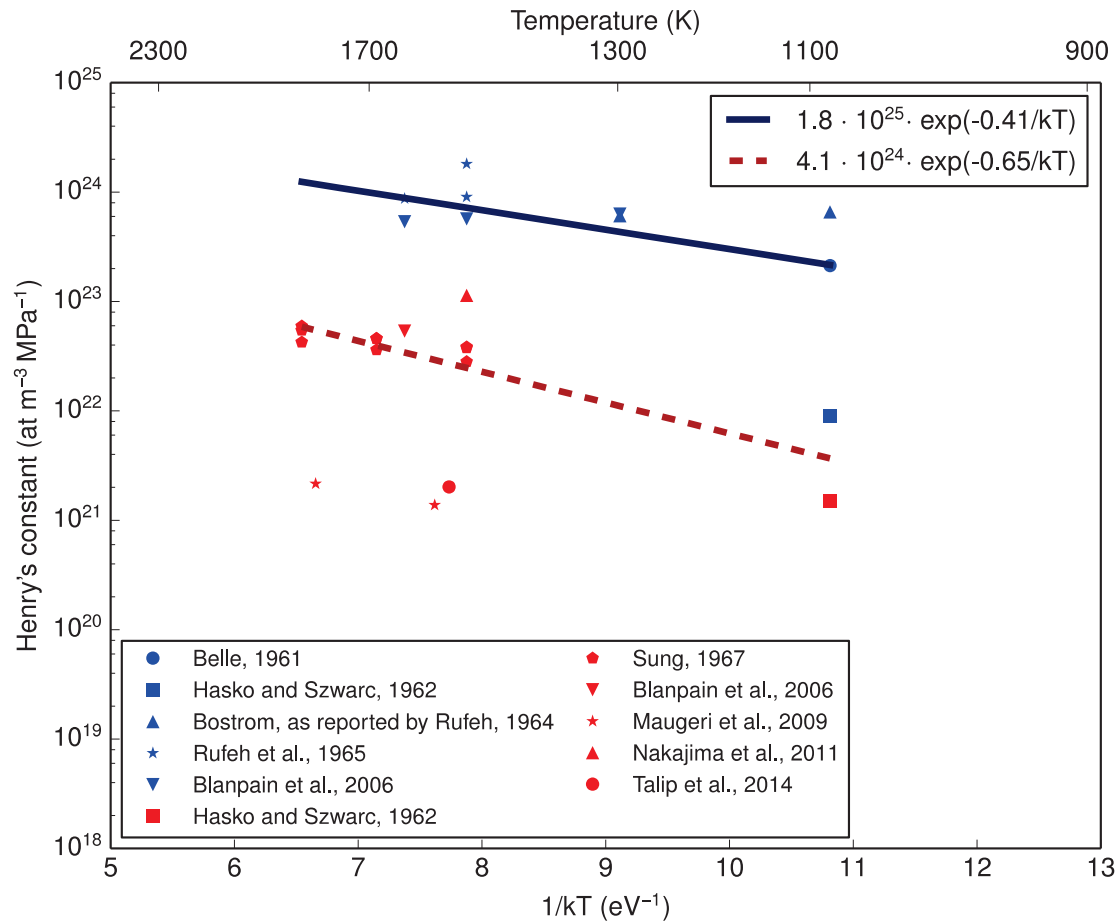
Fig. 1.1 – Plot of the experimental Henry's constant of helium in oxide fuel classified depending on the microstructure of the sample (i.e., blue for the powder samples and red for the single crystal samples). Each cluster is fitted by a distinct correlation (dark red and dark blue) [1.45]

Fig. 1.2 – Comparison between intra-granular fission gas release calculated by the reference algorithm for the general PDE system (non-equilibrium) and the PolyPole-2 results – red points – and the FD results for the quasi-stationary approximation (equilibrium) – black points –. Each data point corresponds to a calculation with randomly generated RIA conditions. The distance from the 45° dashed line is a graphical measure of accuracy [1.44]

Fig. 1.3 – Comparison between the computational times associated with the FD and PolyPole-2 algorithms for the solution of the general PDE system. Each data point corresponds to a calculation with randomly generated RIA conditions [1.44]

1.4 List of References

[1.1] G. Rossiter, Understanding and modelling fuel behaviour under irradiation, in: Nucl. Fuel Cycle Sci. Eng., Woodhead Publishing Limited, 2012: pp. 396–426.

[1.2] D.R. Olander, Fundamental Aspects of Nuclear Reactor Fuel Elements, 1976. doi:10.1016/0022-3115(77)90226-4.

[1.3] V.V. Rondinella, T. Wiss, J. Cobos, H. Hiernaut, Studies on spent fuel alterations during storage and radiolysis effects on corrosion behaviour using alpha-doped UO2, in: 9th Conf. Radioact. Waste Manag. Environ. Remediat., 2003: p. 4593.

[1.4] I. Crossland, Nuclear fuel cycle science and engineering, Woodhead Publishing Limited, 2012.

[1.5] T. Wiss, J.P. Hiernaut, D. Roudil, J.Y. Colle, E. Maugeri, Z. Talip, A. Janssen, V. Rondinella, R.J.M. Konings, H.J. Matzke, W.J. Weber, Evolution of spent nuclear fuel in dry storage conditions for millennia and beyond, J. Nucl. Mater. 451 (2014) 198–206. doi:10.1016/j.jnucmat.2014.03.055.

[1.6] E. Federici, A. Courcelle, P. Blanpain, H. Cognon, Helium production and behavior in nuclear oxide fuels during irradiation in LWR, Proc. Int. LWR Fuel Perform. Meet. San Fr. Calif. (2007) 664–673.

[1.7] P. Botazzoli, Helium Production and Behaviour in LWR Oxide Nuclear Fuels, PhD Thesis, Politec. Di Milano, Italy. (2011).

[1.8] R.C. Ewing, W.J. Weber, F.W. Clinard, Radiation effects in nuclear waste forms for high-level radioactive waste, Prog. Nucl. Energy. 29 (1995) 63–127. doi:10.1016/0149-1970(94)00016-Y.

[1.9] H. Matzke, Gas release mechanisms in UO2 - A critical review, Radiat. Eff. 53 (1980) 219–242.

[1.10] A.H. Booth, A method of calculating fission gas diffusion from UO2 fuel and its application to the X-2-f loop test, At. Energy Canada Ltd. Chalk River Proj. Res. Dev. Rep. AECL-496. (1957) 1–23.

[1.11] J. Piron, J. P.; Pelletier, M.; Pavageau, Fission gas behaviour in water reactor fuels, OECD/NEA. (2000). https://books.google.co.jp/books/about/Fission_gas_behaviour_in_water_reactor_f.html?id=iYdTA AAAMAAJ&pgis=1.

[1.12] E. Maugeri, T. Wiss, J.P. Hiernaut, K. Desai, C. Thiriet, V. V. Rondinella, J.Y. Colle, R.J.M. Konings, Helium solubility and behaviour in uranium dioxide, J. Nucl. Mater. 385 (2009) 461–466. doi:10.1016/j.jnucmat.2008.12.033.

[1.13] K. Nakajima, H. Serizawa, N. Shirasu, Y. Haga, Y. Arai, The solubility and diffusion coefficient of helium in uranium dioxide, J. Nucl. Mater. 419 (2011) 272–280. doi:10.1016/j.jnucmat.2011.08.045.

[1.14] Z. Talip, T. Wiss, V. Di Marcello, A. Janssen, J.Y. Colle, P. Van Uffelen, P. Raison, R.J.M. Konings, Thermal diffusion of helium in 238Pu-doped UO2, J. Nucl. Mater. 445 (2014) 117–127. doi:10.1016/j.jnucmat.2013.10.066.

[1.15] J. Belle, Uranium Dioxide: properties and nuclear applications, Library (Lond). (1961) 569–589.

[1.16] T.H. Rufeh, F; Olander, D R; Pigford, The solubility of helium in uranium dioxide, Nucl. Sci. Eng. (1965).

[1.17] T. Petit, M. Freyss, P. Garcia, P. Martin, M. Ripert, J.P. Crocombette, F. Jollet, Molecular modelling of transmutation fuels and targets, J. Nucl. Mater. 320 (2003) 133–137. doi:10.1016/S0022-3115(03)00179-X.

[1.18] S. Hasko, R. Szwarc, Noble gas solubility and diffusion in UO2, AEC, Div. React. Dev. Washingt. (1963).

[1.19]   F. Rufeh, Solubility of helium in uranium dioxide, M. S. Thesis, Univ. Calif. (1964).

[1.20]   P. Sung, Equilibrium solubility and diffusivity of helium in single-crystal uranium dioxide, PhD Thesis, Univ. Washingt. (1967).

[1.21]   P. Trocellier, D. Gosset, D. Simeone, J.M. Costantini, X. Deschanels, D. Roudil, Y. Serruys, R. Grynszpan, S.E. Saudé, M. Beauvy, Application of nuclear reaction geometry for 3He depth profiling in nuclear ceramics, Nucl. Instruments Methods Phys. Res. Sect. B Beam Interact. with Mater. Atoms. 206 (2003) 1077–1082. doi:10.1016/S0168-583X(03)00914-5.

[1.22]   S. Guilbert, T. Sauvage, P. Garcia, G. Carlot, M.F. Barthe, P. Desgardin, G. Blondiaux, C. Corbel, J.P. Piron, J.M. Gras, He migration in implanted UO2 sintered disks, J. Nucl. Mater. 327 (2004) 88–96. doi:10.1016/j.jnucmat.2004.01.024.

[1.23]   D. Roudil, X. Deschanels, P. Trocellier, C. Jégou, S. Peuget, J.M. Bart, Helium thermal diffusion in a uranium dioxide matrix, J. Nucl. Mater. 325 (2004) 148–158. doi:10.1016/j.jnucmat.2003.11.012.

[1.24]   C. Ronchi, J.P. Hiernaut, Helium diffusion in uranium and plutonium oxides, J. Nucl. Mater. 325 (2004) 1–12. doi:10.1016/j.jnucmat.2003.10.006.

[1.25]   G. Martin, P. Garcia, H. Labrim, T. Sauvage, G. Carlot, P. Desgardin, M.F. Barthe, J.P. Piron, A NRA study of temperature and heavy ion irradiation effects on helium migration in sintered uranium dioxide, J. Nucl. Mater. 357 (2006) 198–205. doi:10.1016/j.jnucmat.2006.06.021.

[1.26]   Y. Pipon, C. Raepsaet, D. Roudil, H. Khodja, The use of NRA to study thermal diffusion of helium in (U, Pu)O2, Nucl. Instruments Methods. 267 (2009) 2250–2254. doi:10.1016/j.nimb.2009.03.025.

[1.27]   P. Garcia, G. Martin, P. Desgardin, G. Carlot, T. Sauvage, C. Sabathier, E. Castellier, H. Khodja, M.F. Barthe, A study of helium mobility in polycrystalline uranium dioxide, J. Nucl. Mater. 430 (2012) 156–165. doi:10.1016/j.jnucmat.2012.06.001.

[1.28]   K. Blanpain, P; Lippens, M.; Schut, H., Federov, A. V., Bakker, The HARLEM Project, Helium solubility in UO2, Work. MMSNF-5, Nice, Fr. (2006).

[1.29]   P. Van Uffelen, R.J.M. Konings, C. Vitanza, J. Tulenko, Analysis of reactor fuel rod behavior, in: D.G. Cacuci (Ed.), Handb. Nucl. Eng., Springer Science + Business Media, LLC, New York, NY, USA, 2010: pp. 1519–1627.

[1.30]   F. Cappia, D. Pizzocri, A. Schubert, P. Van Uffelen, G. Paperini, D. Pellottiero, R. Maci??n-Juan, V. V. Rondinella, Critical assessment of the pore size distribution in the rim region of high burnup UO2 fuels, J. Nucl. Mater. 480 (2016) 138–149.

[1.31]   J. Spino, J. Rest, W. Goll, C.T. Walker, Matrix swelling rate and cavity volume balance of UO2 fuels at high burn-up, J. Nucl. Mater. 346 (2005) 131–144. doi:10.1016/j.jnucmat.2005.06.015.

[1.32]   F. Schmitz, J. Papin, High burnup effects on fuel behaviour under accident conditions: the tests CABRI REP-Na, J. Nucl. Mater. 270 (1999) 55–64.

[1.33]   Y. Guerin, J. Noirot, D. Lespiaux, G. Chaigne, C. Blanpain, Microstructure evolution and in-reactor behvior of MOX fuel, in: ANS Int. Top. Meet. LWR Fuel Performance, Park City, USA, 2000.

[1.34]   T. Nakamura, H. Sasajima, T. Fuketa, K. Ishijima, Fission gas induced cladding deformation on LWR fuel rods under reactivity initiated accident conditions, J. Nucl. Sci. Technol. 33 (1996) 924–935.

[1.35]   M.V. Speight, A Calculation on the Migration of Fission Gas in Material Exhibiting Precipitation and Re-solution of Gas Atoms Under Irradiation, Nucl. Sci. Eng. 37 (1969) 180–185.

[1.36]   K. Forsberg, A. Massih, Diffusion theory of fission gas migration in irradiated nuclear fuel UO2, J. Nucl. Mater. 135 (1985) 140–148.

[1.37] K. Lassmann, H. Benk, Numerical algorithms for intragranular fission gas release, J. Nucl. Mater. 280 (2000) 127–135. doi:10.1016/S0022-3115(00)00044-1.

[1.38] P. Lösönen, Methods for calculating diffusional gas release from spherical grains, Nucl. Eng. Des. 196 (2000) 161–173.

[1.39] R.J. White, M.O. Tucker, A new fission-gas release model, J. Nucl. Mater. 118 (1983) 1–38. doi:10.1016/0022-3115(83)90176-9.

[1.40] T. Kogai, Modelling of fission gas release and gaseous swelling of light water reactor fuels, J. Nucl. Mater. 244 (1997) 131–140. doi:10.1016/S0022-3115(96)00731-3.

[1.41] K. Lassmann, TRANSURANUS: a fuel rod analysis code ready for use, J. Nucl. Mater. 188 (1992) 295–308.

[1.42] R.J. White, The development of grain-face porosity in irradiated oxide fuel, J. Nucl. Mater. 325 (2004) 61–77. doi:10.1016/j.jnucmat.2003.10.008.

[1.43] P. Hermansson, A.R. Massih, An effective method for calculation of diffusive flow in spherical grains, J. Nucl. Mater. 304 (2002) 204–211. doi:10.1016/S0022-3115(02)00873-5.

[1.44] G. Pastore, D. Pizzocri, C. Rabiti, T. Barani, P. Van Uffelen, L. Luzzi, An effective numerical algorithm for intra-granular fission gas release during non-equilibrium trapping and resolution, J. Nucl. Mater. 509 (2018) 687–699.

[1.45] L. Cognini, D. Pizzocri, T. Barani, P. Van Uffelen, A. Schubert, T. Wiss, L. Luzzi, Helium solubility in oxide nuclear fuel:Derivation of new correlations for Henry's constant, Nucl. Eng. Des. 340 (2018) 240–244. doi:10.1016/j.nucengdes.2018.09.024.

[1.46] D.R. Olander, Theory of Helium Dissolution in Uranium Dioxide. II. Helium solubility, J. Chem. Phys. 43 (1965) 785–788. doi:10.1063/1.1696843.

[1.47] E. Yakub, Helium solubility in uranium dioxide from molecular dynamics simulations, J. Nucl. Mater. 414 (2011) 83–87. doi:10.1016/j.jnucmat.2010.12.025.

[1.48] L. Noirot, A method to calculate equilibrium concentrations of gas and defects in the vicinity of an over-pressured bubble in UO2, J. Nucl. Mater. 447 (2014) 166–178. doi:10.1016/j.jnucmat.2014.01.011.

[1.49] E. Yakub, C. Ronchi, D. Staicu, Diffusion of helium in non-stoichiometric uranium dioxide, J. Nucl. Mater. 400 (2010) 189–195. doi:10.1016/j.jnucmat.2010.03.002.

[1.50] A. Bianco, C. Vitanza, M. Seidl, A. Wensauer, W. Faber, R. Macián-Juan, Experimental investigation on the causes for pellet fragmentation under LOCA conditions, J. Nucl. Mater. 465 (2015) 260–267. doi:10.1016/j.jnucmat.2015.05.035.

[1.51] D. Pizzocri, C. Rabiti, L. Luzzi, T. Barani, P. Van Uffelen, G. Pastore, PolyPole-1: An accurate numerical algorithm for intra-granular fission gas release, J. Nucl. Mater. 478 (2016) 333–342.

[1.52] C. Rabiti, Modelling of fast neutron transients in an accelerator driven system, Institut für Kernenergetik und Energiesysteme der Universitat Stuttgart, 2007.

[1.53] S. Bremier, C.T. Walker, Radiation-enhanced diffusion and fission gas release from recrystallised grains in high burn-up UO2 nuclear fuel, Radiat. Eff. Defects Solids. 157 (2002) 311–322. doi:10.1080/10420150213000.

[1.54] D. Pizzocri, F. Cappia, L. Luzzi, G. Pastore, V.V. Rondinella, P. Van Uffelen, A semi-empirical model for the formation and the depletion of the high burnup structure in UO2 fuel, J. Nucl. Mater. 487 (2017) 23–29.

[1.55]   L.O. Jernkvist, SKI2004:34 - Sensitivity study on clad tube failure under reactivity initiated accidents in light water reactors, 2004.

[1.56]   NEA/CSNI/R(2010)1, Nuclear Fuel Behaviour Under Reactivity-initiated Accident (RIA) Conditions, 2010.

[1.57]   L. Luzzi, G. Pastore, P. Botazzoli, Modelli di rilascio dei gas di fissione per combustibili MOX ad elevato burnup, ENEA, Report RDS/2013/022, 2013.

[1.58]   L. Luzzi, T. Barani, E. Bruschi, D. Pizzocri, D. Rozzia, A. Del Nevo, Advancement in FGR modeling for transient analysis of FR fuel, ENEA, ADPFISS-LP2-118, 2016.

[1.59]   J. Turnbull, R. White, C. Wise, The diffusion coefficient for fission gas atoms in uranium dioxide, (1989). http://inis.iaea.org/search/search.aspx?orig_q=RN:21003206.

[1.60]   F.S. Ham, Theory of diffusion-limited precipitation, J. Phys. Chem. Solids. 6 (1958) 335–351.

(Page intentionally left blank)

2 VALIDATION OF RELAP53D BY CIRCE-ICE EXPERIMENTAL TESTS

V. Narcisi, F. Giannetti, G. Caruso, M. Frullini

(Page intentionally left blank)

2.1   Background and references

The Lead-cooled Fast Reactor (LFR) belongs to the six concepts selected by the Generation IV International Forum (GIF) as Generation IV systems (GEN-IV). GEN-IV reactors are developing in order to help meet the word's future energy needs and to minimize the long-term stewardship burden. The goals of the innovative Nuclear Power Plants (NPP) are summarized in four main topics: sustainability, economics, safety & reliability and proliferation resistance & physical protection.

The LFR concept includes the lead and lead-bismuth eutectic alloy (LBE) technologies. Both coolants are chemically inerts and they offer other attractive characteristics in terms of interaction with structural materials and thermodynamic features. LFR systems also well respond to lesson of Fukushima accident allowing natural circulation both in nominal and accident conditions. This feature offers considerable grace time in order to cope with unprotected loss of flow transient and permits to introduce fully passive decay heat removal system (DHR), assuring very high safety features over long periods without need for operator actions, combined with active systems.

Several R&D programs has been promoted in the EU, focused on the development of the LFR systems. In this framework, the validation of the best estimate computer codes is a crucial aspect. The most computational codes are improved to include the capability to simulates the main phenomena occurring in the GEN-IV system reactors. In order to use these analytical tools for the NPP safety assessment, each improvement must be validated against several experimental data which cover every operational scenario of the nuclear system, including accidental sequences. The validation approach is not possible against experimental tests performed on NPP; however, the accidental scenario can be replaced with dedicated facility and the experimental data can be compared with the analytical results.

In this framework, from 2010, "Sapienza" University of Rome (UNIROMA1), in collaboration with ENEA Brasimone Research Center, was involved in the development of innovative LFR technologies (Ref. [2.1], [2.2], [2.3], [2.4] and [2.5]), dealing with several operative aspects. In 2013, UNIROMA1 started to investigate the capability of RELAP5-3D$^{©}$ code (R5-3D) to reproduce the main thermal-hydraulic phenomena in a lead-cooled fast reactor. In Ref. [2.6], a comparison between RELAP5 mod.3.3 and RELAP5-3D highlighted that the correlation implemented in R5-3D for the evaluation of the heat transfer coefficient (HTC) in bundle geometry (the Westinghouse correlation, in Ref. [2.7]), underestimates the HTC in comparison with the actual state of art. In Ref. [2.8], a tool for the generation of new lead and LBE thermophysical properties (according to the NEA recommendation, in Ref. [2.9]) binary files was presented, showing a comparison between the state-of-art data and the RELAP5-3D default properties.

In 2010, in the framework of LEADER project, a new configuration of the steam generator (SG) was proposed for ALFRED (Advanced Lead Fast Reactor European Demonstrator): the super-heated steam double wall bayonet tube type with leakage monitoring. ENEA Brasimone Research Center designed and constructed the HERO (Heavy liquid mEtal pRessurized water cOoled tubes) test section to investigate the capability of a bundle of double wall bayonet tubes 1:1 in length with the ALFRED SG (Ref. [2.10]). In the framework of the H2020 SESAME project (http://sesame-h2020.eu/), a validation benchmark has been proposed, based on the experimental campaign conducted on CIRCE-HERO test facility (Ref. [2.11]). UNIROMA1 has been involved in this experimental campaign, performing the pre-test calculations (Ref. [2.12], [2.13], [2.14] and [2.15]) and carring out the experiment in collaboration with ENEA.

The CIRCE-HERO pre-test calculation has been performed using RELAP5-3D; the nodalization scheme has been developed starting from the thermal-hydraulic model of previous configuration of the facility, called CIRCE-ICE facility. ICE test section was installed into CIRCE facility in order to reproduce a typical primary system of a HLM cooled pool-type reactor; the experimental campaign aimed to investigate mixing convection and thermal stratification phenomena in a HLM pool and to provide experimental data for the

validation of analytical codes. The simulation activities carried out by UNIROMA1 in the previous years, has been highlighted that the nodalization scheme has well reproduced the thermal-hydraulics of the primary flow path in full power conditions and the implementation in RELAP5-3D of the most recent LBE thermophysical properties correlations has allowed a better estimation of the HLM conditions. Concerning the thermal-hydraulic phenomena into the pool, the calculations has highlighted the prospect to reproduce the thermal stratification with RELAP5-3D, but some discrepancy has been noticed comparing the calculated results with the experimental data (Ref. [2.16], [2.17] and [2.18]).

In this activity, the most recent results on the CIRCE-ICE post-test analysis is presented, highlighting the improvements of the model, in simulating both full power conditions and the transition between gas-enhanced (GHC) and natural circulation (NC) conditions, and the capability of RELAP5-3D in predicting thermal stratification inside the pool in both the operative conditions.

2.2 Body of the report concerning the ongoing activities

2.2.1 CIRCE-ICE facility

CIRCE is a multipurpose pool facility designed to host different test sections welded to and hung from bolted vessel heads for the investigation of thermal-hydraulic aspects related to the HLM pool system. The facility consists of a main vessel, earmarked for containing test section and filled with about 70 tons of molten LBE, two auxiliary tanks, dedicated to store LBE during maintenance phases and to transfer liquid metal during loading and drainage phases, and data acquisition system. The main vessel (S100) is characterized by the outer diameter of 1200 mm and the height of 8500 mm. The Fig. 2.1 depicts the isometric view of the facility and the main parameters are summarized in Tab. 2-1.

The experimental campaign is conducted on ICE test section, installed into the main vessel. ICE aims to simulate the primary system of a HLM pool type reactor and the main objectives of the experimental campaign were to investigate thermal stratification and mixing convection phenomena into the pool and to provide experimental data for the validation of analytical codes. These are two of the main topics for the development of LFR system: the thermal stratification could induce thermo-mechanical stress on the structure and the validation of TH (Thermal Hydraulics) codes against the experimental data is a fundamental step in order to justify their use in the design phase for improving safety aspects.

The principal components and the primary main flow path of the test section are depicted in Fig. 2.2 and Fig. 2.3; the inlet section consists of the feeding conduit, which allows the hydraulic connection between the lower plenum of the pool and the fuel pin simulator (FPS). The value of the LBE mass flow rate entering the FPS is measured by a Venturi-nozzle flow meter, installed into the feeding conduit. The fuel pin simulator represents the heat source of the unit. It consists of an electrical pin bundle with a nominal thermal power of 800 kW and an active length of 1000 mm. The bundle is composed of 37 electrically heated pins arranged in a wrapped hexagonal lattice and characterized by a pitch to diameter ratio equal to 1.8 (Fig. 2.4); the relative position between the pin bundle and the external wrapper is fixed by three spacer grids, located along the heat source, and the unit rests to the lower grid, placed at the inlet section of the FPS. Each pin has an outer diameter of 8.2 mm, a thermal power of 25 kW and a heat flux at the pin wall of 1 MW/m2. The hot fluid exits the core and it is introduced into the fitting volume, which allows the connection between the fuel pin simulator and the riser, double wall insulated pipe connecting the fitting volume and the separator. At the inlet section of the riser, a nozzle is installed allowing the injection of argon in order to promote the circulation of the primary coolant. The mixture flows upward and collects inside the separator, where the separation of LBE and Ar occurs (LBE enters the heat exchanger while Ar flows upward into the gas plenum through the free surface). The HX (heat exchanger) is made of 91 bayonet tubes, characterized by an active length of 3462 mm, contained into a cylindrical shell. The relative position between the tubes and the external shell is fixed by only one grid at the outlet section of the HX. Fig. 2.5 shows a sketch of the bayonet element which consists of three concentric tubes. The feed-water flows downward into the inner tube and

then upward into the annular riser between inner and middle tube, where the change of phase take place; the double physical separation is obtained with the second and the third tube and the LBE flows downwards outside the tubes.

The volume between middle and outer tube is filled by pressurized helium to detect any leakage. Exiting the HX, primary coolant flows through the downcomer reaching the lower plenum. The DHR system is located in the upper zone of the pool, as shown in Fig. 2.2. It consists of only one bayonet tube and the decay power is removed by forced circulation of air. The tube is located inside a double wall shell with a thin air insulation gap to thermally decouple the DHR from the external LBE pool. Hot LBE enters the DHR by the upper inlet section, it flows downward decreasing the temperature and it exits the component in the downcomer (Ref. [2.19]).

The test section is equipped with several thermocouples to investigate the thermal behavior of the LBE. The primary coolant temperature inside the FPS is measured by 36 TCs (thermocouples), arranged at 7 different axial levels. Two series of penetration are obtained at the inlet and outlet section of the active zone, as shown in Fig. 2.6. In addition, along the HS active length, four different sections are monitored as depicted in Fig. 2.7, investigating the temperature of the LBE along three characteristic sub-channels and the pin clads. Several TCs are also installed inside the pool in order to investigate mixing convection and thermal stratification phenomena. 119 thermocouples are installed in 17 axial levels and 9 different azimuthal positions, as shown in Fig. 2.8.

2.2.2 Experimental test
The objective of the experimental campaign is to investigate the thermal stratification and the mixing convection phenomena inside the pool of the facility, in both enhanced and natural circulation conditions. The experimental test analyzed is called TEST IV; it aims to reproduce a protected loss of heat sink (PLOHS) plus a loss of flow (LOF) simulating the total loss of primary flow, the loss of the secondary circuit, the consequent scram of the reactor and the activation of the DHR system. To reproduce the accident in CIRCE-ICE facility, the thermal power supplied to the FPS is reduced to the 7% of the nominal power, following a typical decay heat curve for a HLM fast reactor, the argon injection is stopped, simulating the blackout of the primary pumping system, the secondary system is disabled and the DHR system is activated, injected air on the DHR secondary side. The boundary conditions of the TEST IV are summarized in Tab. 2-2.

2.2.3 Thermal-hydraulic model
The nodalization scheme of CIRCE-ICE test facility has been developed using RELAP5-3D© ver. 4.3.4. RELAP5 is a light water reactor transient analysis code developed by the U.S. Nuclear Regulatory Commission (NRC) for use in rulemaking, licensing audit calculations, evaluation of operator guidelines and as a basis for a nuclear plant analyzer. It is a generic code that, in addition to calculating the behavior of a reactor coolant system during a transient, can be used for simulation of a wide variety of hydraulic and thermal transients in both nuclear and non-nuclear systems involving mixtures of steam, water, non-condensable and solute. R5-3D is the last version of the series of RELAP5 code and contains several improvements; two enhancements from the previous versions are the multi-dimensional thermal-hydraulic capability and the addition of new working fluids, including heavy liquid metals (Ref.[2.20]).

The geometrical model consists of two macro-regions, coupled to reproduce the whole test facility: a mono-dimensional model, that simulate the primary main flow path, the HX secondary system and the DHR system (see Fig. 2.9), and a multi-dimensional component, shown in Fig. 2.10, where the internal components are depicted only to display the positioning, to investigate phenomena such as mixing convection and thermal stratification inside the pool.

The 1D scheme reproduces the components described in previous section. The HS is simulated sub-channel by sub-channel using 72 parallel pipes (Fig. 2.11), each composed of 15 control volumes, hydraulically linked with 1536 cross junction to reproduce the mass transfer between the sub-channels. The thermal power supplied by the electrical heated pins is simulated with 5760 heat structure active nodes and other 1728 thermal nodes reproduce the heat dissipation through the hexagonal shroud. In order to simulate the heat transfer between the sub-channels, 3456 heat transfer nodes are introduced, assuming a "fake" material with negligible heat capacity and with LBE thermal conductivity. The FPS nodalization scheme is obtained to compare the LBE temperature in the exact position of the thermo-couples. For the evaluation of the heat transfer coefficient (HTC) on heavy liquid metals, Todreas & Kazimi correlation (Ref. [2.7]) is implemented in R5-3D.

$$Nu = 4.0 + 0.33 \left(\frac{p}{d}\right)^{3.8} \left(\frac{Pe}{100}\right)^{0.86} + 0.16 \left(\frac{p}{d}\right)^{5}$$

Previous calculations on HLM system showed that this correlation underestimates the Nusselt number for pitch-to-diameter ratio greater than 1.2 (Ref. [2.6]). Additionally, R5- 3D does not permit a pitch-to-diameter ratio of 1.8 and the p/d of the pin bundle was set to the maximum allowed value of 1.4. In order to improve the HTC according to Ushakov correlation (more accurate in this case)

$$Nu = 7.55\frac{p}{d} - 20 \left(\frac{p}{d}\right)^{-13} + \frac{3.67}{\left(90\frac{p}{d}\right)^{2}} Pe^{\left(0.56+0.19\frac{p}{d}\right)}$$

and to correct the heat exchange to experimental p/d value, an artificial multiplicative factor of 1.31, evaluated as the ratio between the two correlations in nominal flow conditions, was applied to the HTC. For the non-bundle geometry, the Seban-Shimazaki correlation is used:

$$Nu = 5.0 + 0.025Pe^{0.8}$$

Upstream the FPS, the pressure drop of the Venturi nozzle was simulated by a concentrated pressure loss coefficient K, dependent on the flow conditions, according to the equation:

$$K_{Venturi} = 10.5 \, \text{Re}^{-0.014}$$

The argon injection at the riser inlet section is simulated with boundary conditions: the time-dependent volume sets the gas inlet conditions and the time-dependent junction, connected with the bottom edge of the riser second control volume, adjusts the mass flow rate injection. The pressure of the gas plenum of the facility is regulated by an additional time-dependent volume, that simulates the gas extraction through the gas circuit. The HX primary side is simulated by a single equivalent pipe and one heat structure, which thermally couples the primary and the secondary side. A calibrated fouling factor of 1.02 is evaluated as the ratio between Ushakov and Todreas & Kazimi correlation and it is applied on the LBE side to increase the HTC. The bayonet tubes are modelled using two pipes in order to simulate the descending and ascending side of water/steam tubes and one heat structure to model heat dispersion between the two pipes.

The pressure losses due to grids installed into FPS and heat exchanger are calculated by the Rheme correlation (Ref. [2.21]):

$$\Delta p_{grid} = C_{v} \cdot \varepsilon^{2} \cdot 0.5 \cdot \rho \cdot v^{2}$$

where ρ and v are respectively the density and the velocity of the fluid while ε represents the blockage factor of the grids, calculated as:

$$\varepsilon = \frac{A_{grid}}{A_{flow}}$$

The Cv parameter is a modified drag coefficient and it is calculated as:

$$C_v = MIN\left[3.5 + \frac{73.14}{Re^{0.264}} + \frac{2.79 \cdot 10^{10}}{Re^{2.79}}, \frac{2.6}{\varepsilon^2}\right]$$

The bayonet tube of the DHR system is simulated and it is composed of one pipe for the LBE channel and two pipes to model the descending and ascending air side.

The region number 2 is the 3D component which simulates the volume between the main vessel and the internals. The nodalization scheme is obtained to compare the LBE temperature in the exact position of the thermocouples into the pool, in order to investigate the capability of the code to reproduce thermal stratification and mixing convection phenomena. The model consists of 51 axial levels, 4 radial meshes and 8 azimuthal intervals. The mono-dimensional model and the 3D component is hydraulically coupled with 12 junctions and the heat dispersions through the internals and the main vessel were evaluated with several heat structures.

The dimensions of the whole model are summarized in Tab. 2-3.

2.2.4   Simulation results

The simulation has been carried out using the most accurate LBE thermo-physical properties correlations; recommended by NEA (Ref. [2.9]). Fig. 2.12, Fig. 2.13 and Fig. 2.14 highlight the comparison between the experimental and the simulated boundary conditions, for the heat supplied by the FPS, the FW mass flow rate, the Ar injected inside the riser and the air mass flow rate on the DHR secondary side. The test starts in no-power steady state conditions, where the argon injection, the FW and the air mass flow rate and the FPS are disabled. Fig. 2.15 shows that, at the beginning of the test, the air mass flow rate on the DHR secondary side is near to zero, but the measurement of the air mass flow rate is disabled during the first 25000 s of the test. The control system set the air mass flow to remove about 3 kW; in order to reproduce this boundary condition, in the simulation the air mass flow rate is set to about 25 g/s during the first 25000 s. At 25000 s the transition from enhanced to natural circulation occurs: the FPS thermal power decreases to the decay heat value, the Ar injection system and the FW mass flow rate are disabled and the DHR is fed by air flow rate. In Fig. 2.12 the experimental electrical power of the FPS is compared with the simulated thermal power supplied by the HS. The simulated value has been reduced of 5% of the nominal one to take into account the dissipations which occur in the cables and connectors of the outer circuits, which does not contribute to the thermal power supplied. Fig. 2.13 and Fig. 2.14 show the FW and the Ar mass flow rate, comparing the experimental data and the simulated value. At the beginning of the test and after the transition to natural circulation, the experimental values are respectively close to 0.1 kg/s and 0.35 Nl/s, even if the two system are completely closed; this is due to the signal, which is at digital full scale.

Fig. 2.16 depicts the comparison between the LBE mass flow rate measured by the Venturi flow meter (in red) and calculated by R5-3D (in black). The strong oscillations, during first phase of the experimental test, are due to the volumetric blowers used to inject argon into the riser and, after 13000 seconds, they are dumped by installing a check valve into the gas injection system (Ref. [2.19]). Unless the fluctuations, R5-3D well reproduces the LBE mass flow rate through the main flow path, in both GHC and NC conditions;

after the transition, the code slightly overestimates the mass flow (about 0.5 kg/s). Fig. 2.17 shows the LBE temperature trend at the inlet and the outlet of the FPS active zone. At the inlet section the LBE temperature is uniform and it is well reproduced by R5-3D in both enhanced and natural conditions. At the outlet of the HS, the LBE temperature changes considering different sub-channels, due to the heat dissipation through the hexagonal shell. In order to valuate this effect, Fig. 2.17 shows the temperature measured by the TCs T-FPS-36 (in a central sub-channel) and T-FPS-34 (in a external sub-channel), comparing with the LBE temperature evaluated by the code in the same positions. The Fig. 2.17 shows that the experimental data and the calculated results are in good agreement, highlighting that the code well reproduces the heat dissipation through the FPS external shell. The representation of the LBE temperature evaluated by R5-3D is depicted in Fig. 2.28 in different instants of the test. According to the results of Fig. 2.17, after the transition, the effect of the heat dissipation is decreased and the LBE temperature at the HS outlet is more uniform.

The temperature drop across the HX is compared in Fig. 2.18; the primary inlet and outlet temperature follows a similar trend of the FPS. The HX inlet temperature is lower than the FPS outlet temperature (about 30 K), due to the heat dissipations through the walls of the fitting volume, the riser and the separator, highlighting a good prediction of the heat dissipations by the code. The difference between the experimental data and the calculated value of the temperature at the HX exit depends on the relative positioning between the TCs and the R5-3D control volume, arranged 45 mm upstream. This difference is highlighted both in GHC and NC. After the simulated station blackout, the temperature drop across the HX is due to the heat dissipation through the cylindrical shell, which are well predicted by R5-3D. Fig. 2.19 depicts the comparison of the DHR temperature drop of the LBE. During the first 25000 s, the temperature distribution along the DHR primary side is strongly affected by the thermal stratification of the LBE inside the pool, due to the low air mass flow rate on the secondary side. After the transition, the air start to flow along the DHR and the LBE temperature is well predicted by the code, unless the fluctuations of the measured value at the outlet of the DHR.

One of the main tasks of the activity is the investigation of the capability of RELAP5-3D to reproduce three-dimensional phenomena occurring in large volumes, such as the pool of HLM reactor. CIRCE facility offers useful data for this evaluation. The analysis, presented from Fig. 2.20 to Fig. 2.27, is carried out at three instants of the GHC conditions (at 3300 s, 10000 s and 25000 s) and other three instants of the NC conditions (at 28000 s, 32000 s and 60000 s), showing the evolution of the LBE temperature during the whole test. From Fig. 2.20 to Fig. 2.25 the calculation results are compared with the experimental data, measured by the 119 TCs installed inside the pool (see Fig. 2.8). In the picture (a), the temperature obtained averaging the data acquired by the thermocouples A, B, C, D and E is compared with the temperature calculated in the same position (between the HX and the DHR) by R5-3D; in the same way, the average temperature of the TCs F and G and the temperature measured by TCs I and H are compared with the simulation results in pictures (b), (c) and (d).

The experimental campaign highlighted that phenomena of mixing convection do not occur inside the pool; the LBE temperature assumes the same value at each level. This result is also obtained by R5-3D; for this reason, the analysis is focused on the vertical thermal stratification. The test starts at uniform conditions inside the pool (about 600 K). After the activation of the gas injection system, of FPS and of FW system, the LBE temperature in the upper part of the pool starts to increase, due to the heat dissipations from the primary flow path, and the temperature in the lower part starts to decrease, due to the cold LBE exiting the HX. The qualitative trend of the LBE temperature is the same of the DHR inlet and outlet in the first 25000 seconds. At about 3300 s, the LBE in the upper zone reaches the maximum temperature; the axial distribution of the temperature is shown in Fig. 2.20, which highlights that the code is able to reproduce the increase of temperature due to the heat losses. A slight underestimation of the temperature is highlighted between 3.5 m and 5 m from the bottom of the pool, at the level of the fitting volume. The Fig. 2.26 (a) shows the representation of the temperature obtained by the code inside the main representative section of the 3D model, which includes the FPS and the HX (the DHR is also reported in order to show the outlet level). The

outer shell of the HX, that is not insulated, offers a large heat exchange area, causing a large amount of heat dissipations. This is highlighted in Fig. 2.26 (a), where the main temperature gradient occurs outside the HX and above the temperature is quite uniform.

Then, the temperature inside the pool starts to decrease, following the qualitative trend of the LBE temperature inside the primary flow path; Fig. 2.21 shows the comparison at 10000 s, stressing the capability of the code to reproduce in transient conditions the axial trend of the temperature. Finally, the full power steady state conditions are reached and it is presented in Fig. 2.22 and Fig. 2.26 (b). The axial temperature trend is well reproduced by the code, which is able to simulate the two main T gradient between 5 m and 7 m (HX level) and between 3.5 m and 4 m (fitting volume level).

After the simulated station blackout, the temperature in the upper part of the pool rapidly decreases, due to the reduction of the LBE temperature through the main flow path. Fig. 2.23 shows the comparison at 28000 s; during the experiment, the gradient between 5 m and 7 m, rapidly reduces, obtaining a slightly uniform temperature of about 575 K, and the second gradient moves downward at the DHR outlet level, where the cold LBE exits. The code well reproduces this transition, even if a little gradient is still present in the upper part of the pool. After that, the temperature inside the pool increases, following the same trend of the primary flow path. The code is able to reproduce this evolution, evaluating very well the level where the thermal stratification occurs. Fig. 2.27 summarizes the evolution of the LBE temperature inside the pool, highlighting the disappearance of the gradient in the upper zone and the movement of the second gradient below the DHR. Then the temperature increases, maintaining the same qualitative axial trend.

2.3   Conclusive remarks

The aims of the experimental campaign performed on CIRCE-ICE have been to investigate the main thermal-hydraulic phenomena which characterize the HLM systems and to provide data for the validation of the computational code. The experiment has reproduced a protected loss of heat sink (PLOHS) plus a loss of flow (LOF) simulating the total loss of primary flow, the loss of the secondary circuit, the consequent scram of the reactor and the activation of the DHR system. The goal of the activity has been to investigate the capability of RELAP5-3D to reproduce the transition between gas enhanced circulation to natural circulation and the three-dimensional phenomena inside the large pool.

The thermal-hydraulic model has been developed in order to compare the main parameters in the exact position of the instrumentations. At this purpose, a mono-dimensional nodalization scheme has been developed to reproduce the primary and the secondary main flow path and a detailed three-dimensional component to model the pool.

The comparison between the experimental data and the calculations results has highlighted the capability of R5-3D to reproduce the thermal-hydraulic behavior of the main primary flow path. The code is able to reproduce the LBE circulation in both gas-enhanced and natural conditions; moreover, the LBE thermal-hydraulic properties correlations, implemented in RELAP5-3D as described in Ref. [2.8], well simulate the coolant behavior. The HLM default correlations for the heat exchange, assuming little corrections following the actual state of art, provide good estimation of the thermal power exchanged through the main mono-dimensional components.

One of the main tasks of the activity has been to investigate the capability of RELAP5-3D to reproduce 3D thermal-hydraulic phenomena inside large volumes, such as HLM pools. At this purpose, CIRCE facility, equipped with 119 TCs to obtain the LBE temperature inside the pool, offers useful data. The comparison between experimental data and simulation results highlights that the buoyancy and the mixing convection of the fluid inside the pool is well reproduced. The main phenomenon which occurs inside the pool is the axial thermal stratification, mainly influenced by the heat losses through the wall of the primary flow path. The

code is able to reproduce the heat dissipations and the LBE temperature trend inside the pool. Slight discrepancy has been noticed in the central part of the pool, probably due to a not perfect prediction of the heat dissipations in this level. In fact, the operative range of the heat exchange correlation implemented in RELAP5-3D are not respected in a large volume such as a pool. The fitting volume provides a large heat exchange area in this axial level and an underestimation of the heat transfer coefficient on the pool side provides a slight underestimation of the heat dissipated through its wall. The future activities should be focused on the development and the implementation of correlations for the estimation of the HTC in large HLM volumes.

Parameters	Value
Outside diameter (mm)	1200
Wall thickness (mm)	15
Material	AISI 316L
Max LBE inventory (ton)	90
Temperature range (K)	473 to 773

Tab. 2-1 – CIRCE S100 main parameters

Parameters	GHC	NC
Duration (h)	7	10
Electical power supplied (kW)	720	50
Ar injection (Nl/s)	1.8	0
Feed-water mass flow rate (kg/s)	0.65	0
DHR air injection (kg/s)	~0	0.223

Tab. 2-2 – TEST IV boundary conditions

Parameters	Value
Number of hydrodynamic volumes	1929
Number of hydrodynamic junctions	4856
Number of heat structure mesh points	15353

Tab. 2-3 – CIRCE-ICE nodalization scheme: main parameters
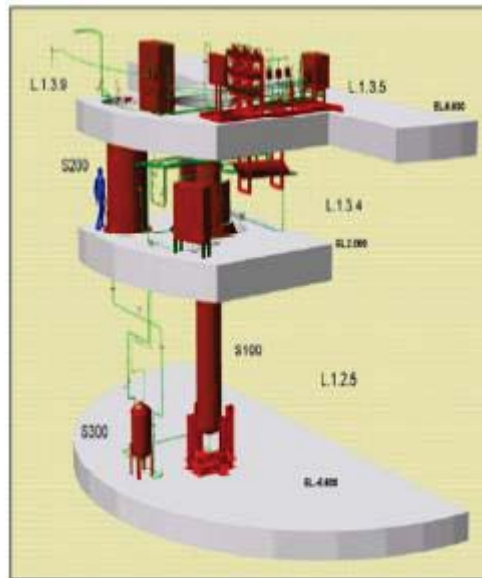
Fig. 2.1 – CIRCE isometric view
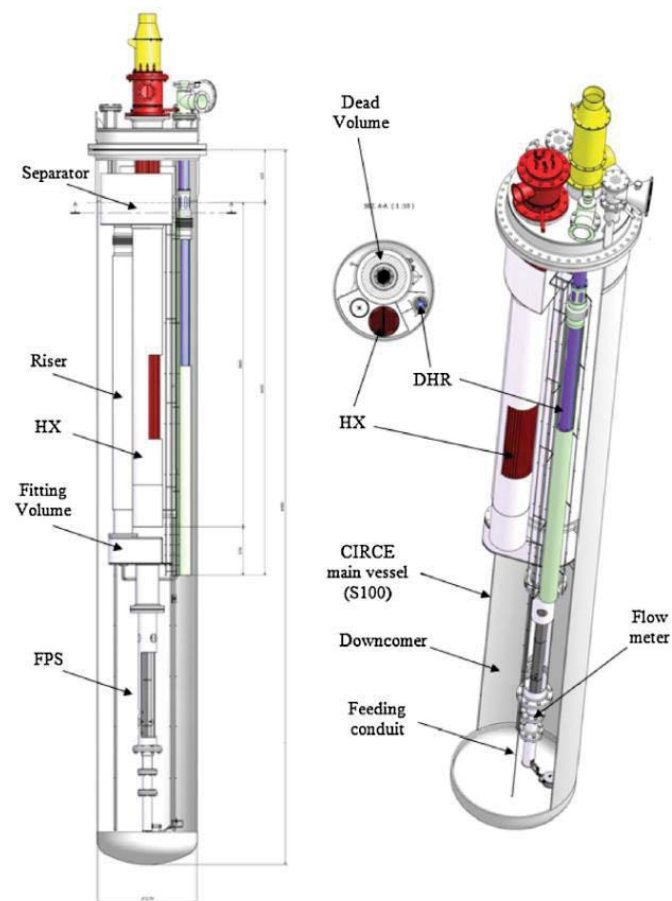
Fig. 2.2 – ICE test section
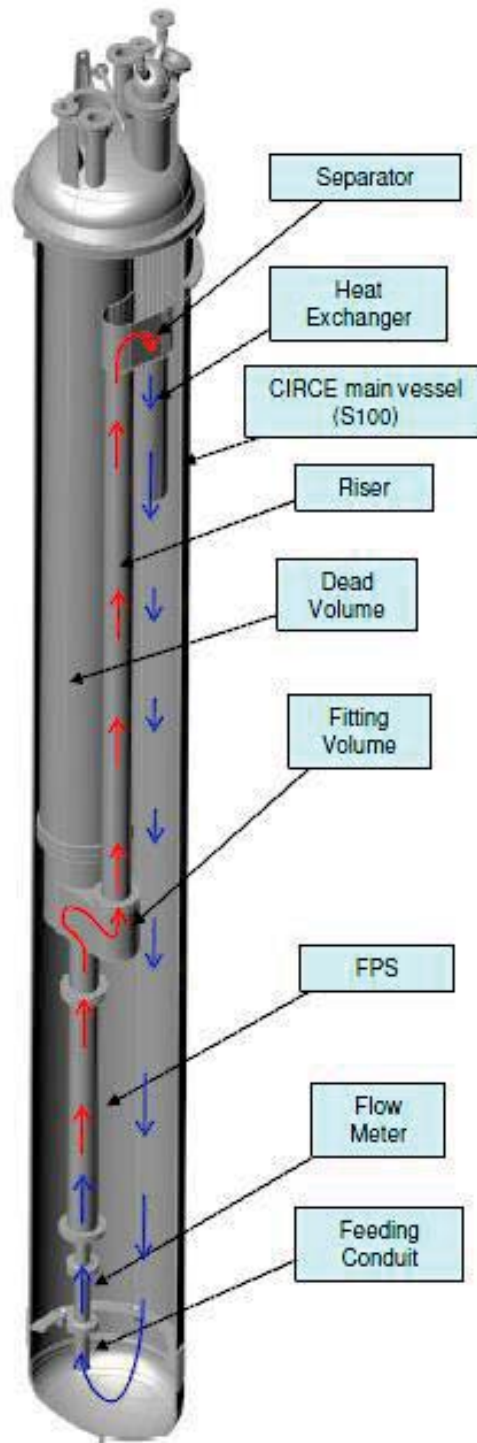
Fig. 2.3 – ICE test section: primary flow path
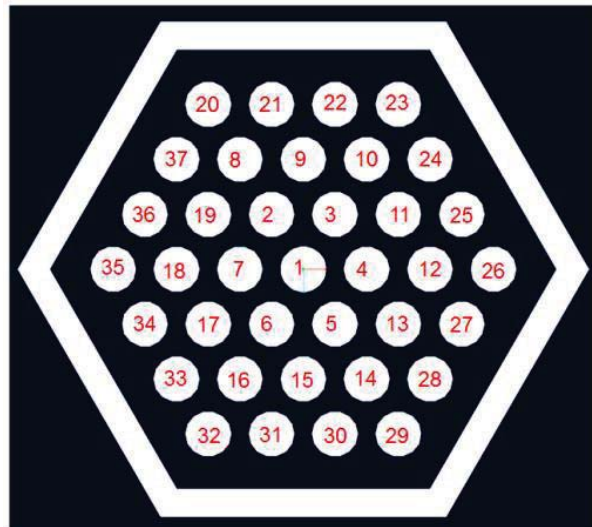
Fig. 2.4 – FPS cross section
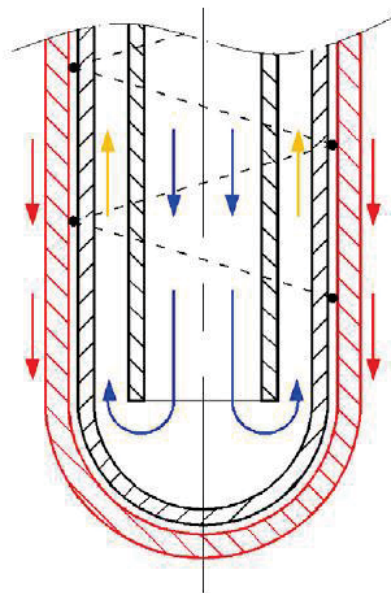
Fig. 2.5 – HX bayonet tube
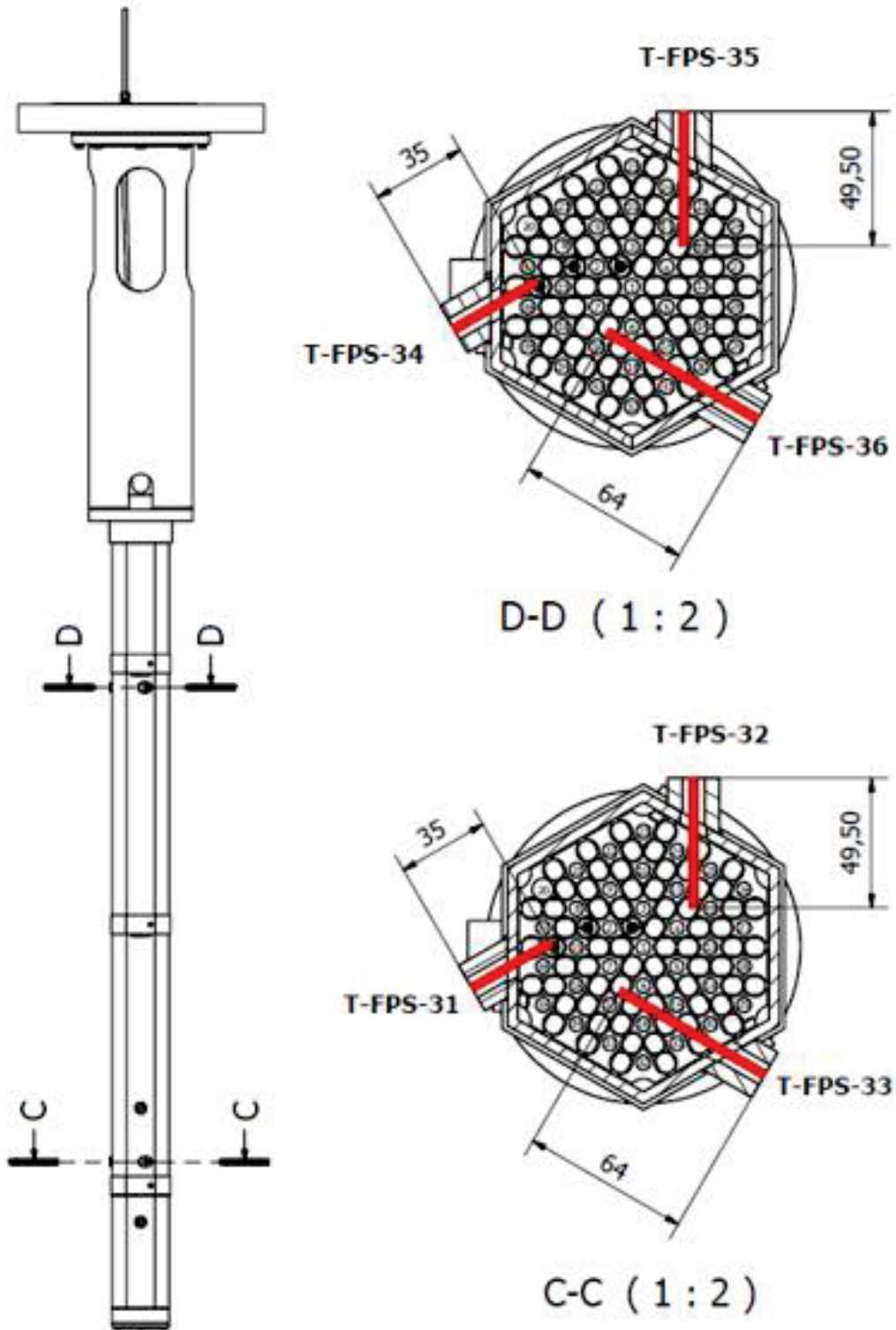
Fig. 2.6 – CIRCE instrumentation: FPS (1)
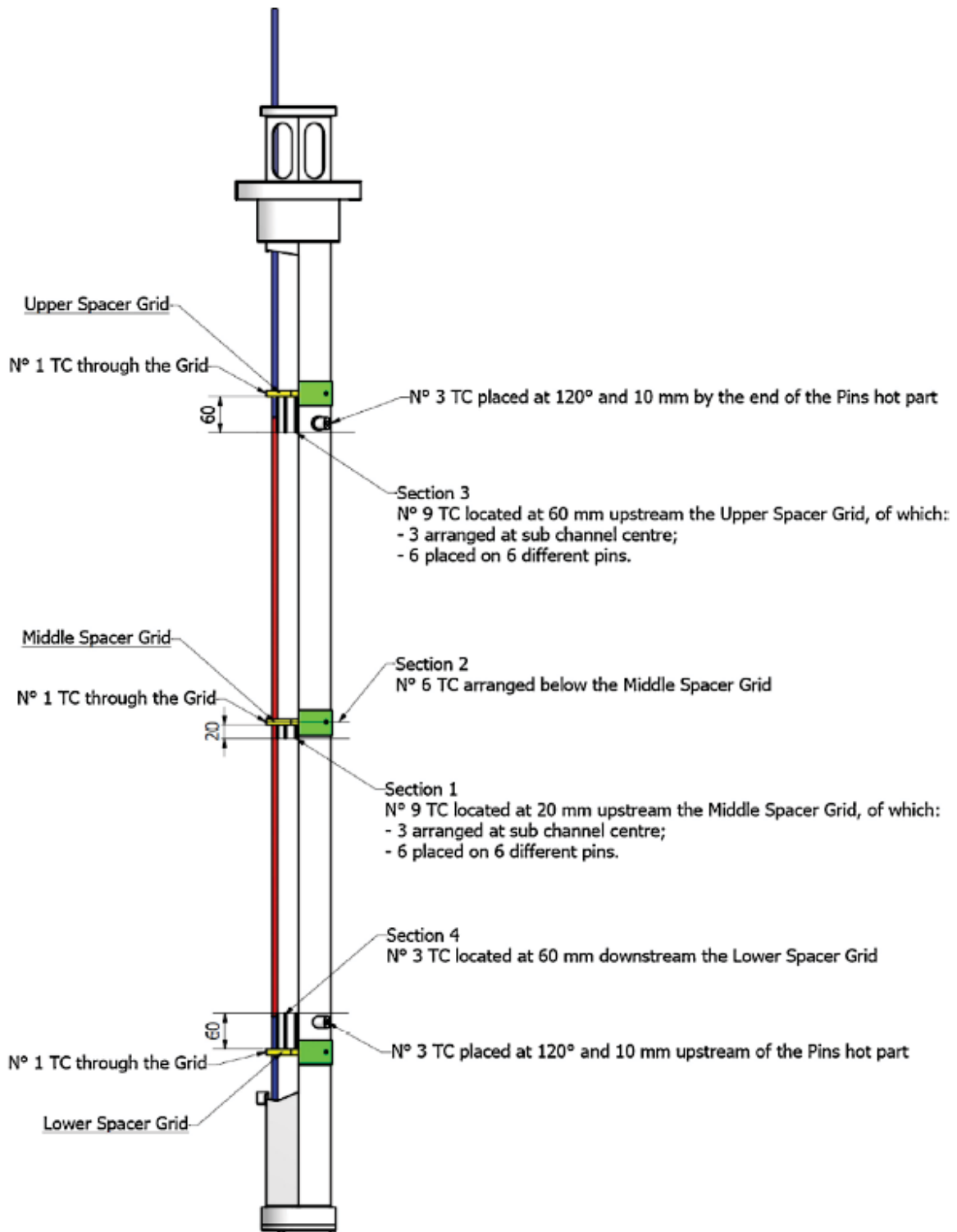
Fig. 2.7 – CIRCE instrumentation: FPS (2)
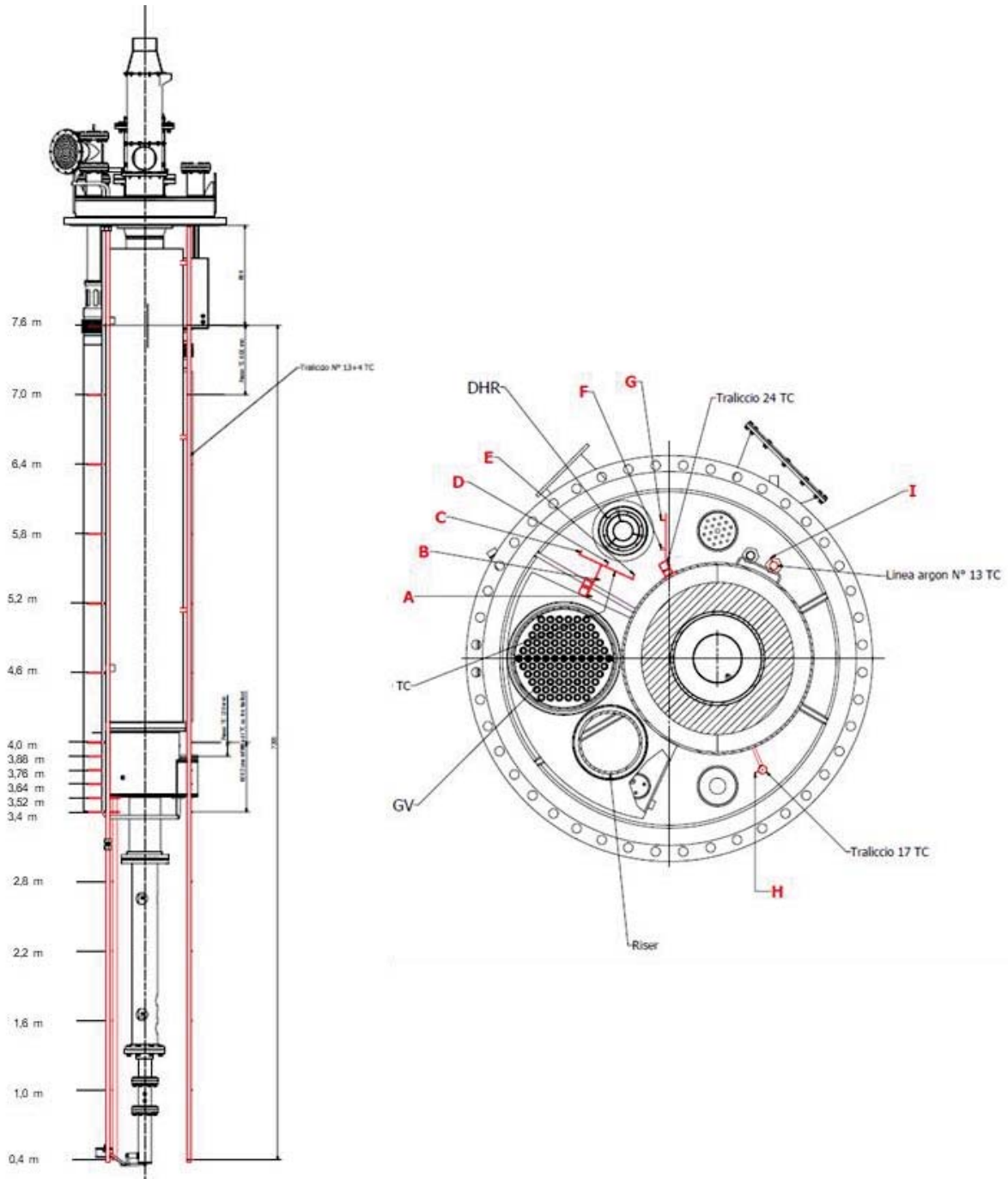
16

Fig. 2.8 – CIRCE instrumentation: pool
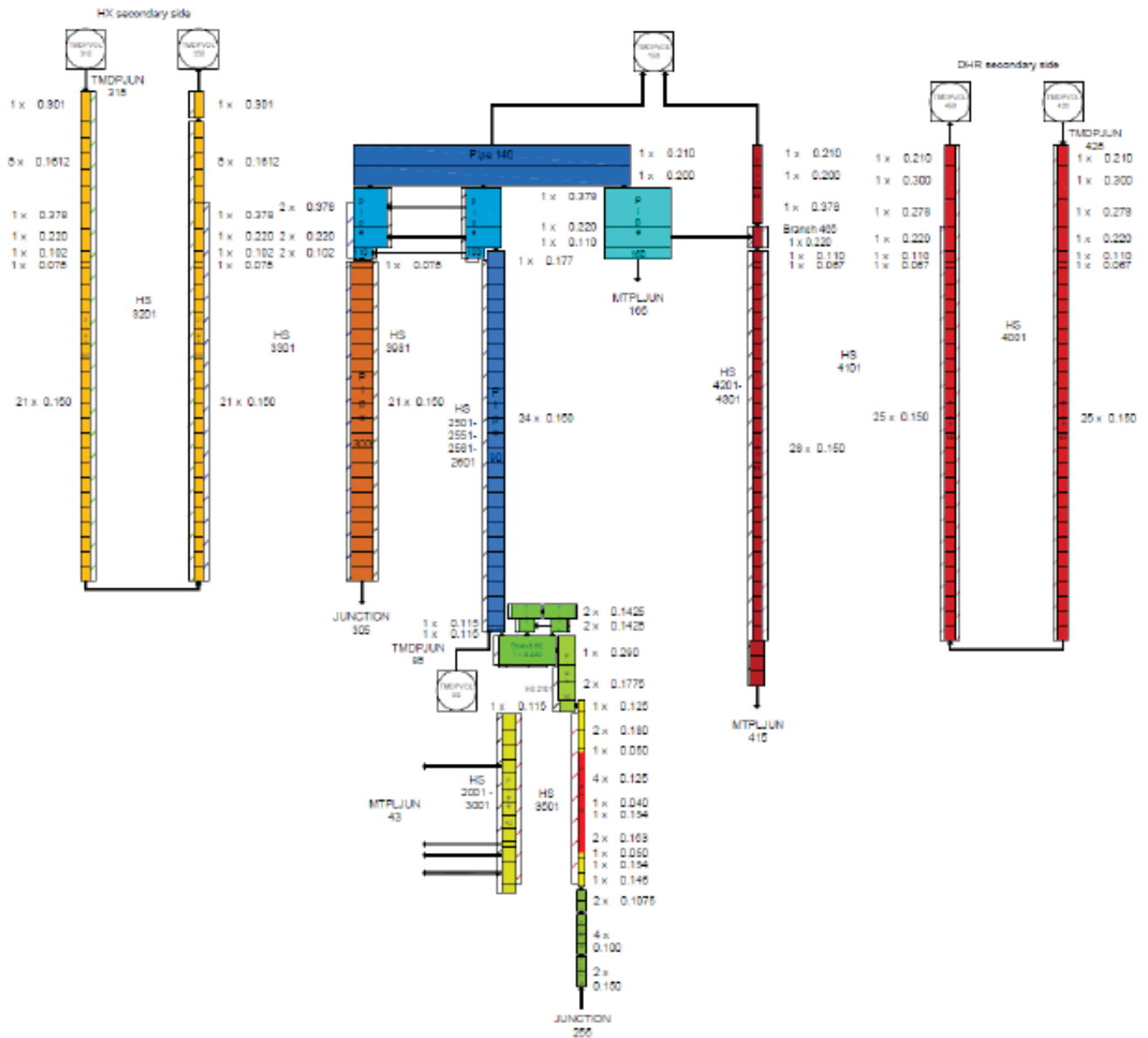
Fig. 2.9 – Nodalizzation scheme: mono-dimensional model

Fig. 2.10 – Nodalizzation scheme: multi-dimensional model

Fig. 2.11 – Nodalizzation scheme: FPS
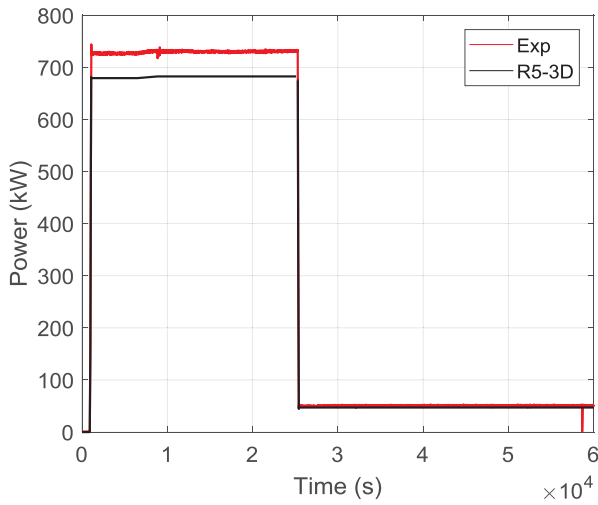
Fig. 2.12 – Power supplied
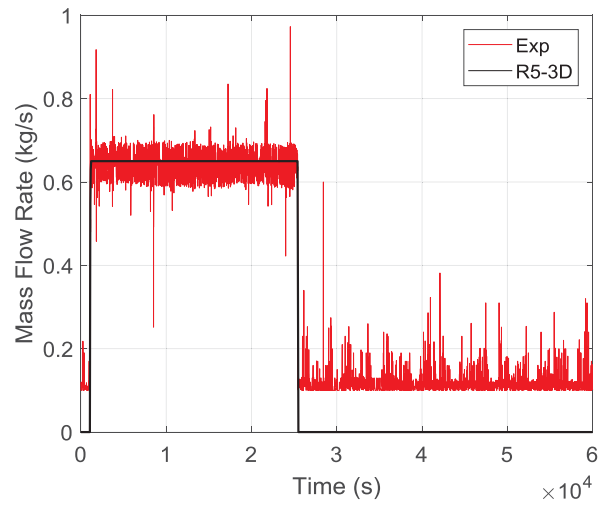
Fig. 2.13 – Feed-water mass flow rate
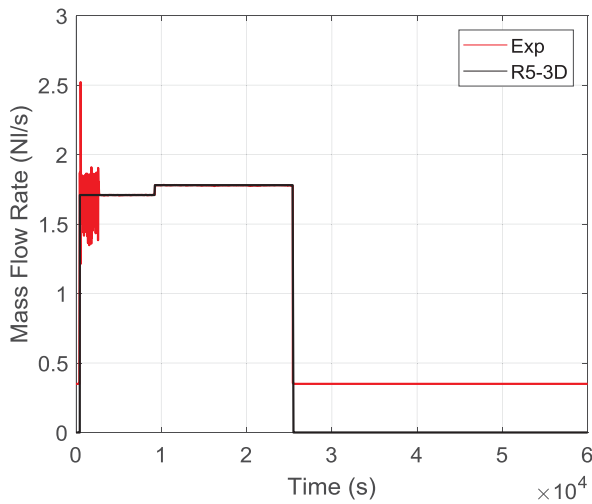
Fig. 2.14 – Argon injection
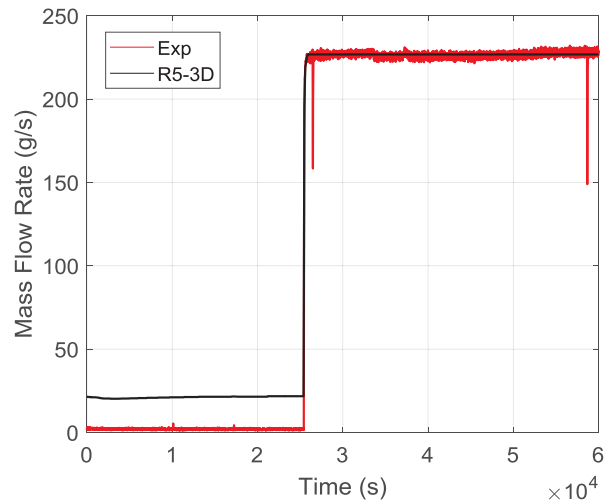
Fig. 2.15 – Air mass flow rate
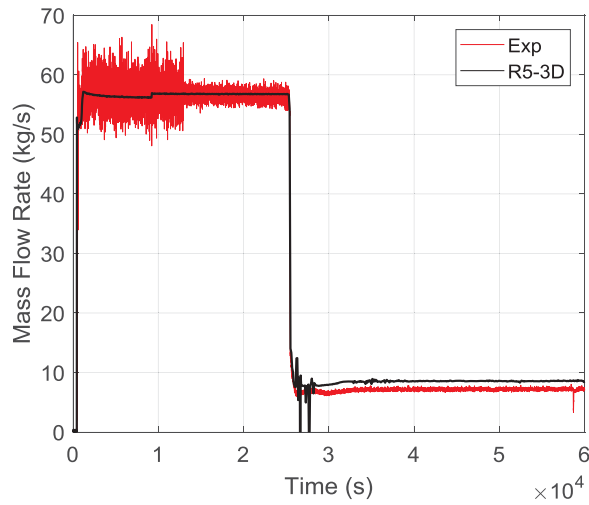
Fig. 2.16 – LBE mass flow rate
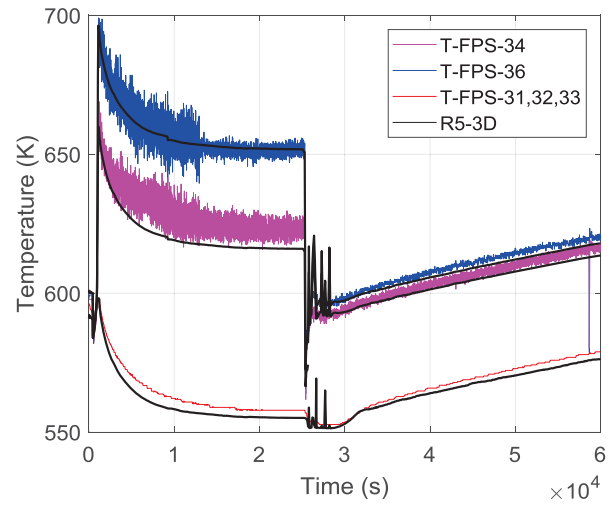
Fig. 2.17 – FPS inlet/outlet temperature
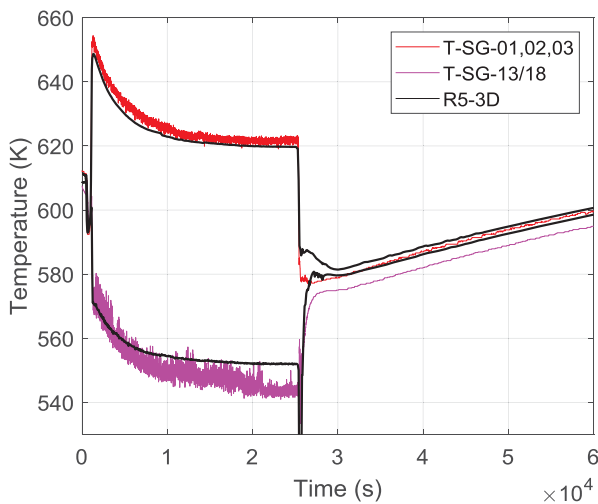
Fig. 2.18 – HX inlet/outlet temperature
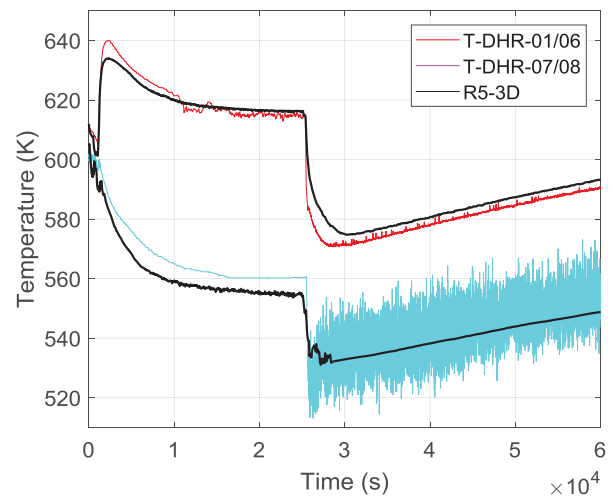
Fig. 2.19 – DHR inlet/outlet temperature
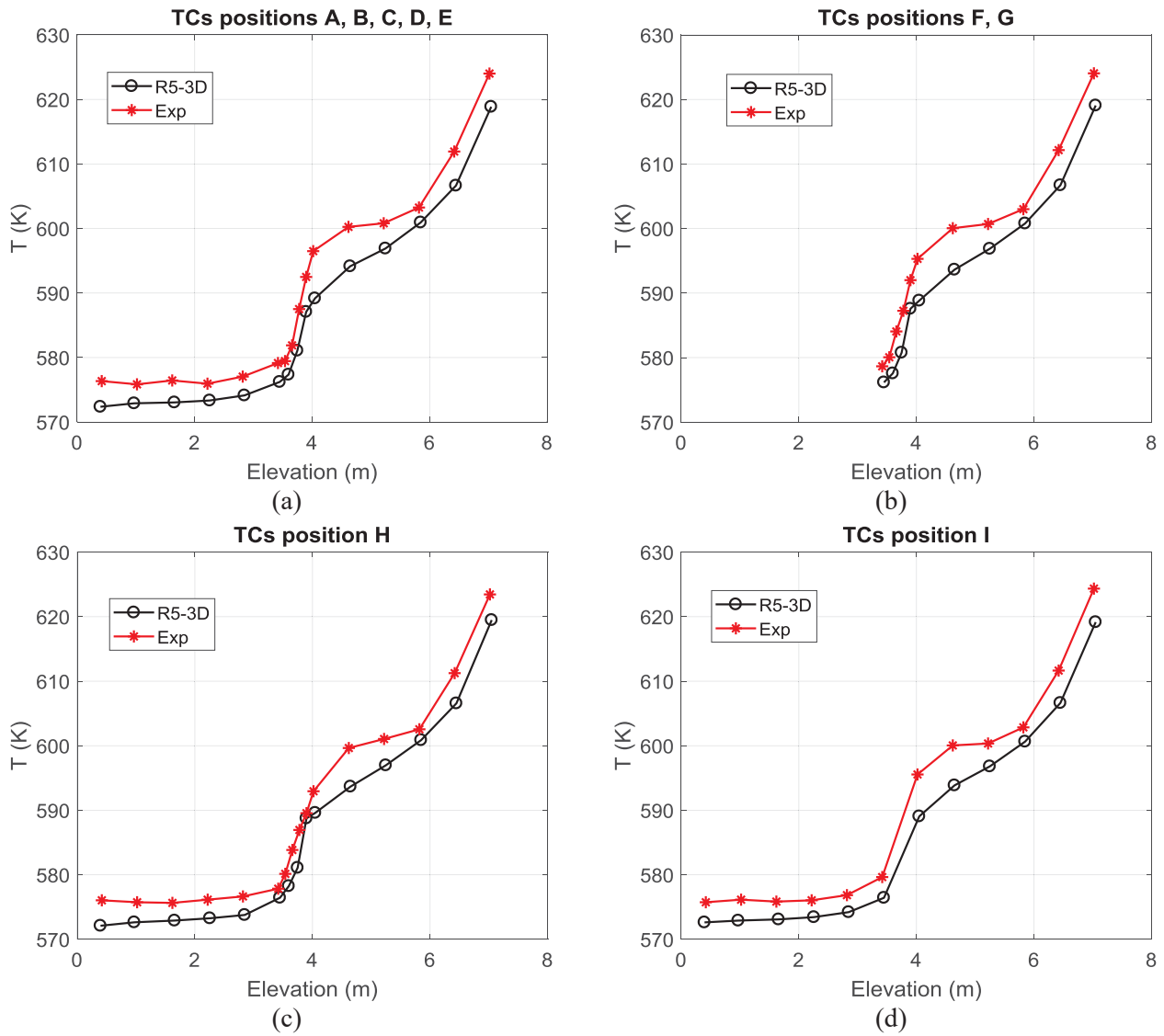
Fig. 2.20 – TS and MC: 3300 s
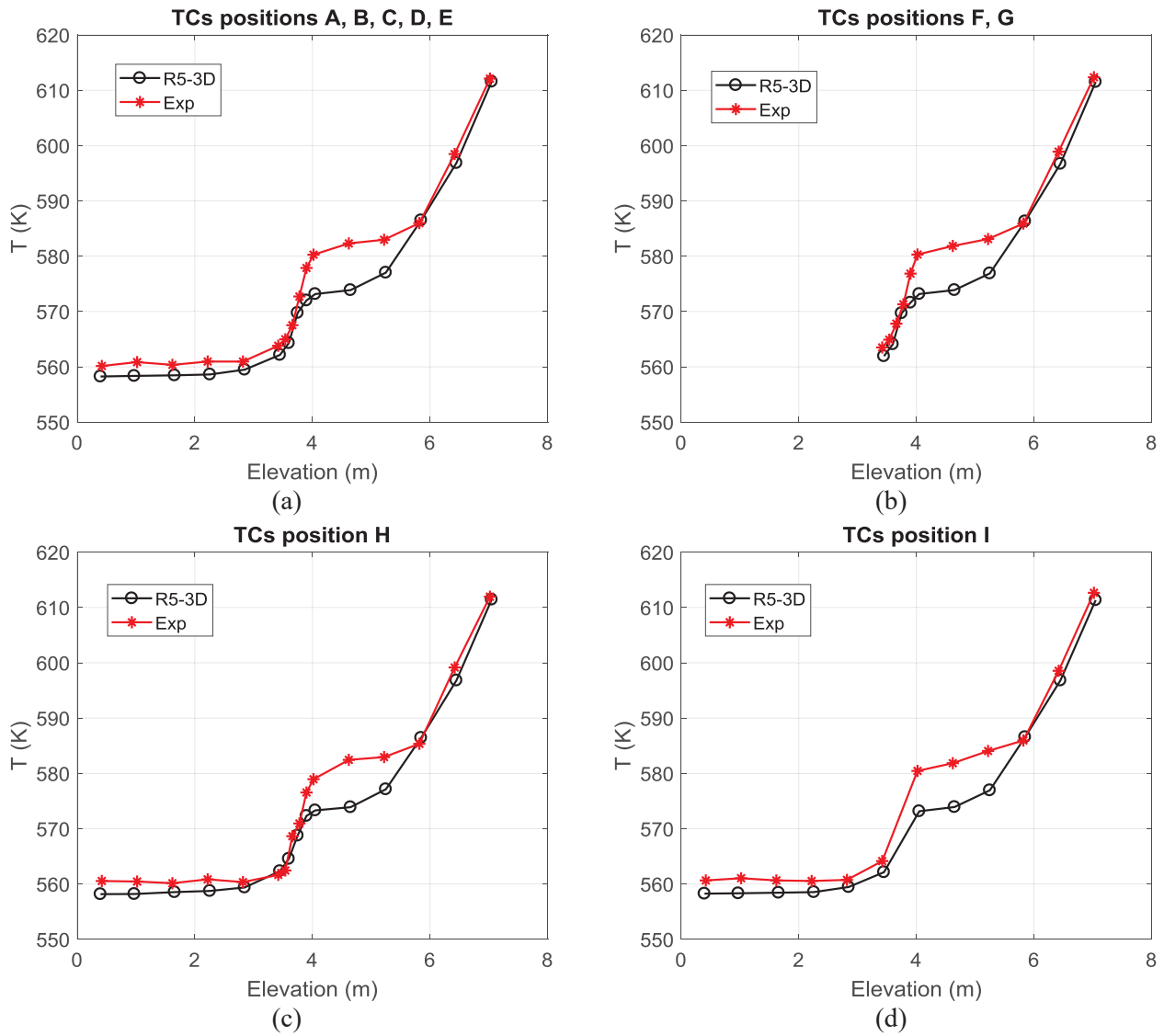
Fig. 2.21 – TS and MC: 10000 s
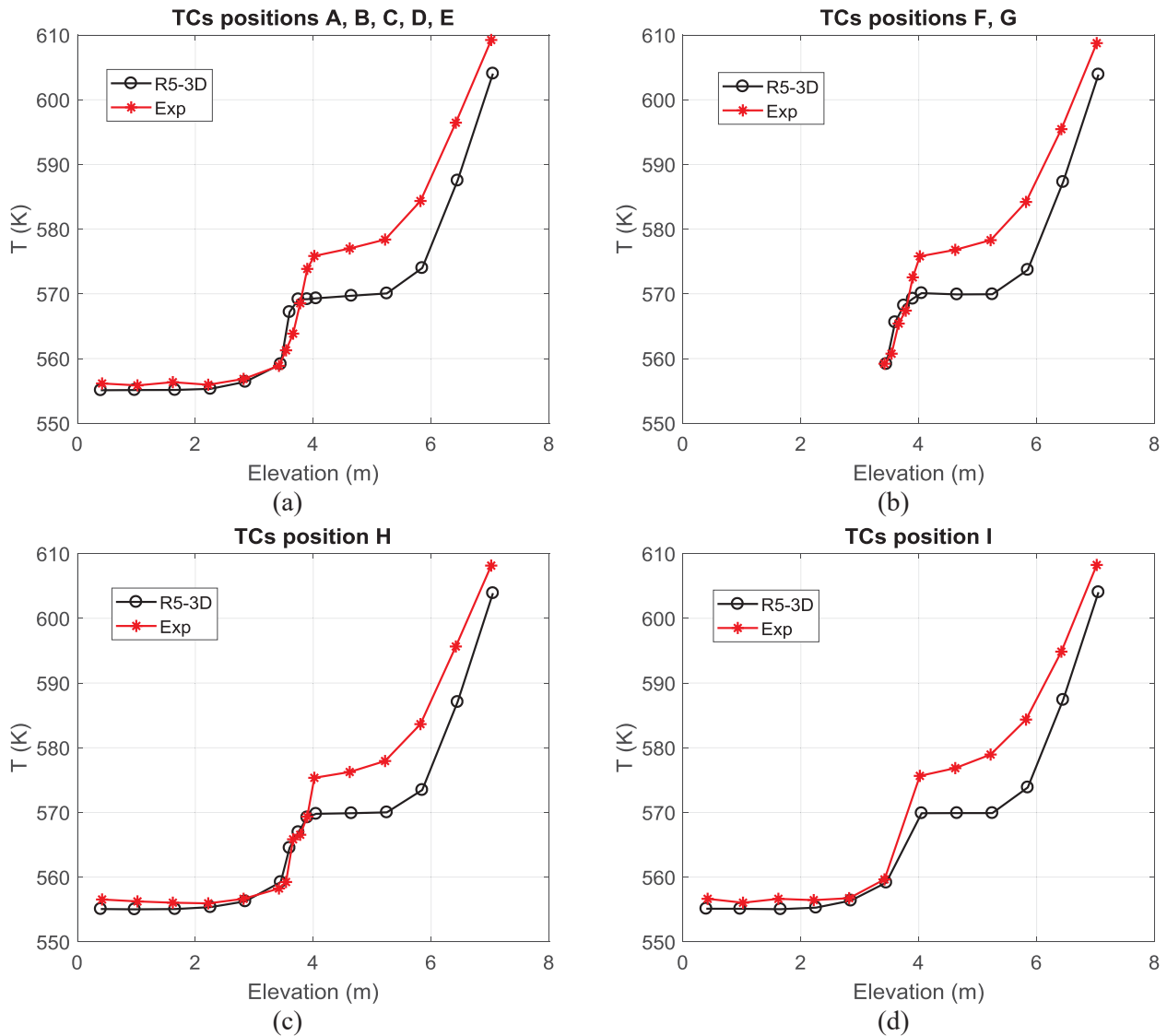
Fig. 2.22 – TS and MC: 25000 s
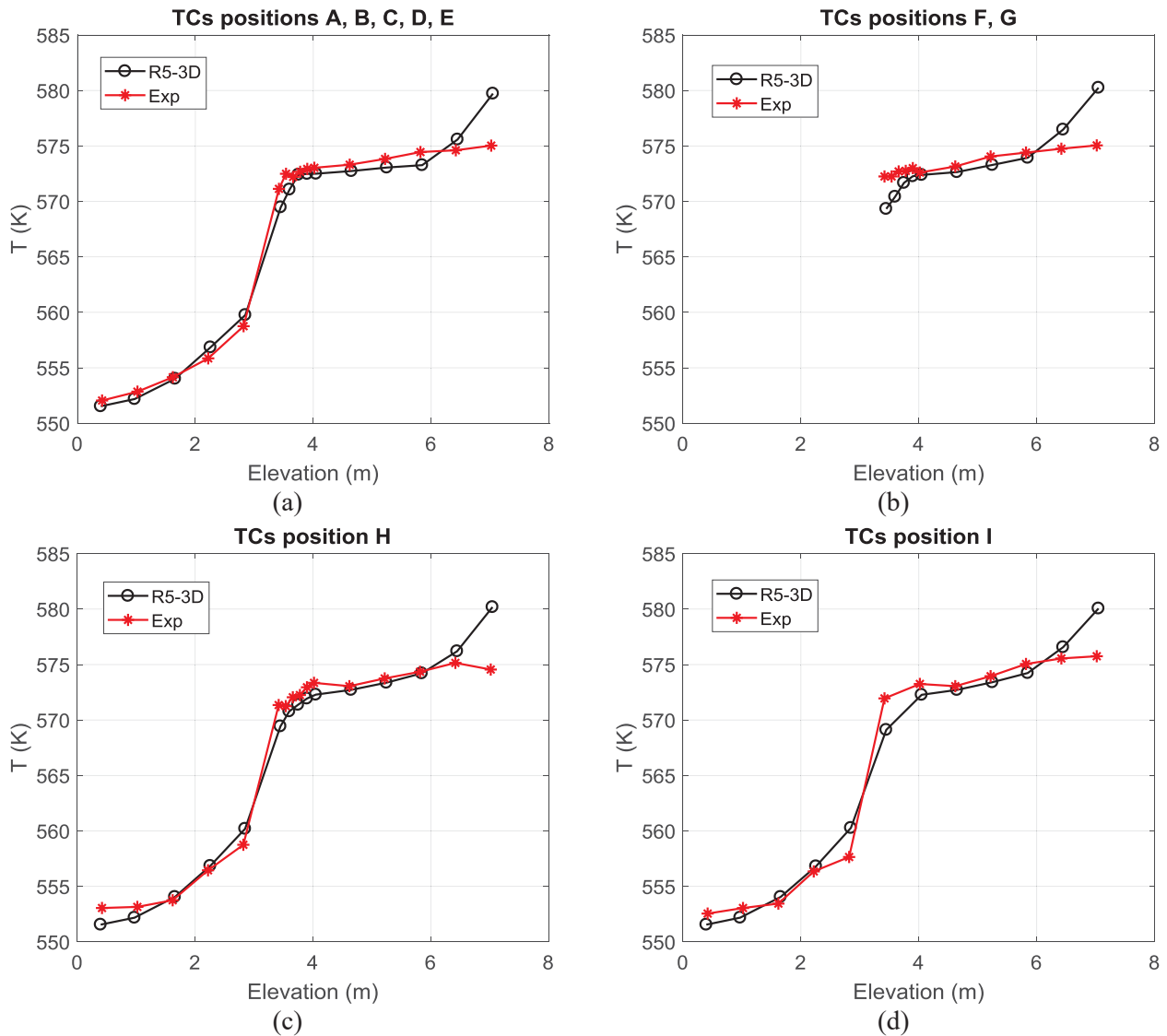
Fig. 2.23 – TS and MC: 28000 s
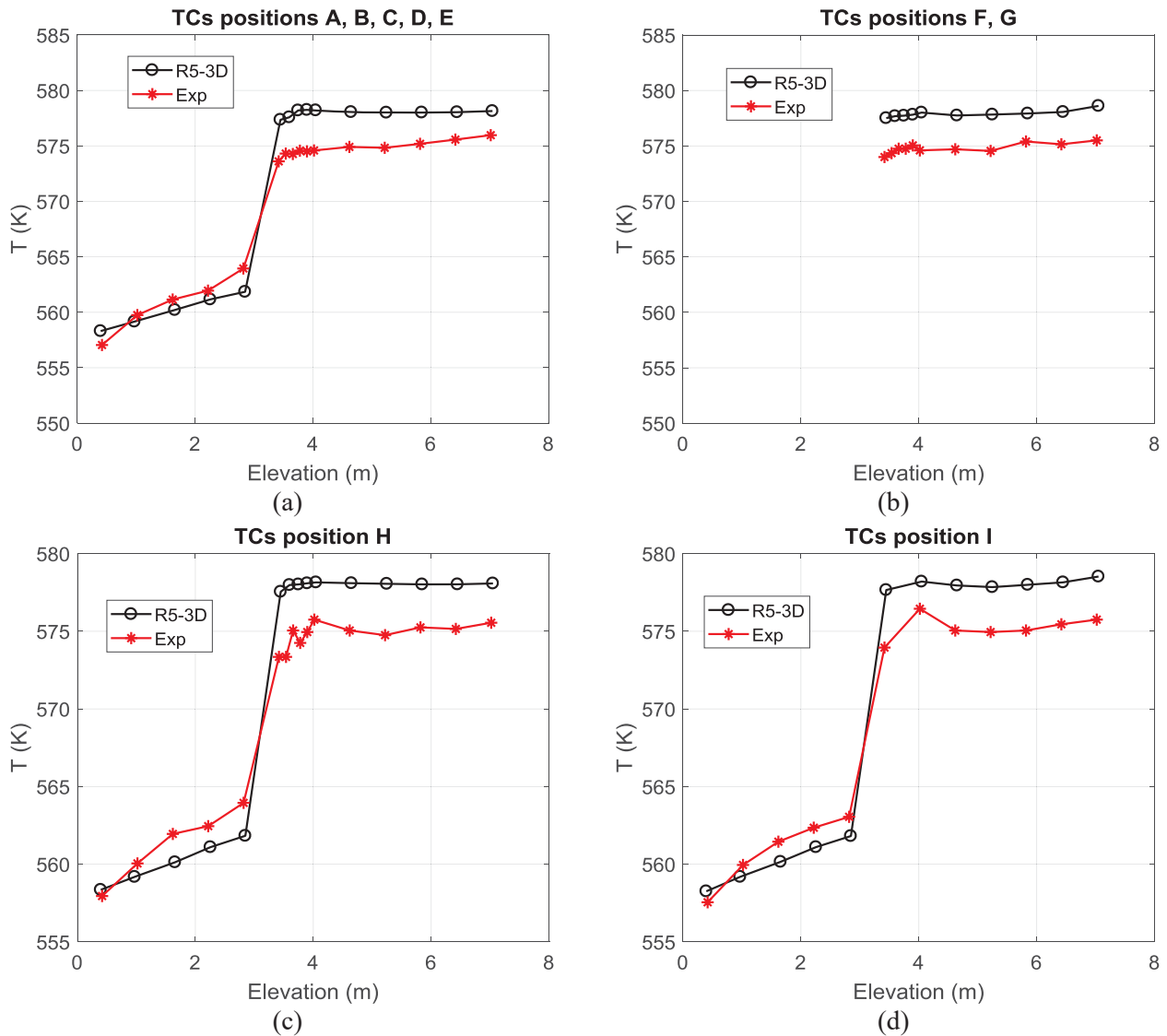
Fig. 2.24 – TS and MC: 32000 s
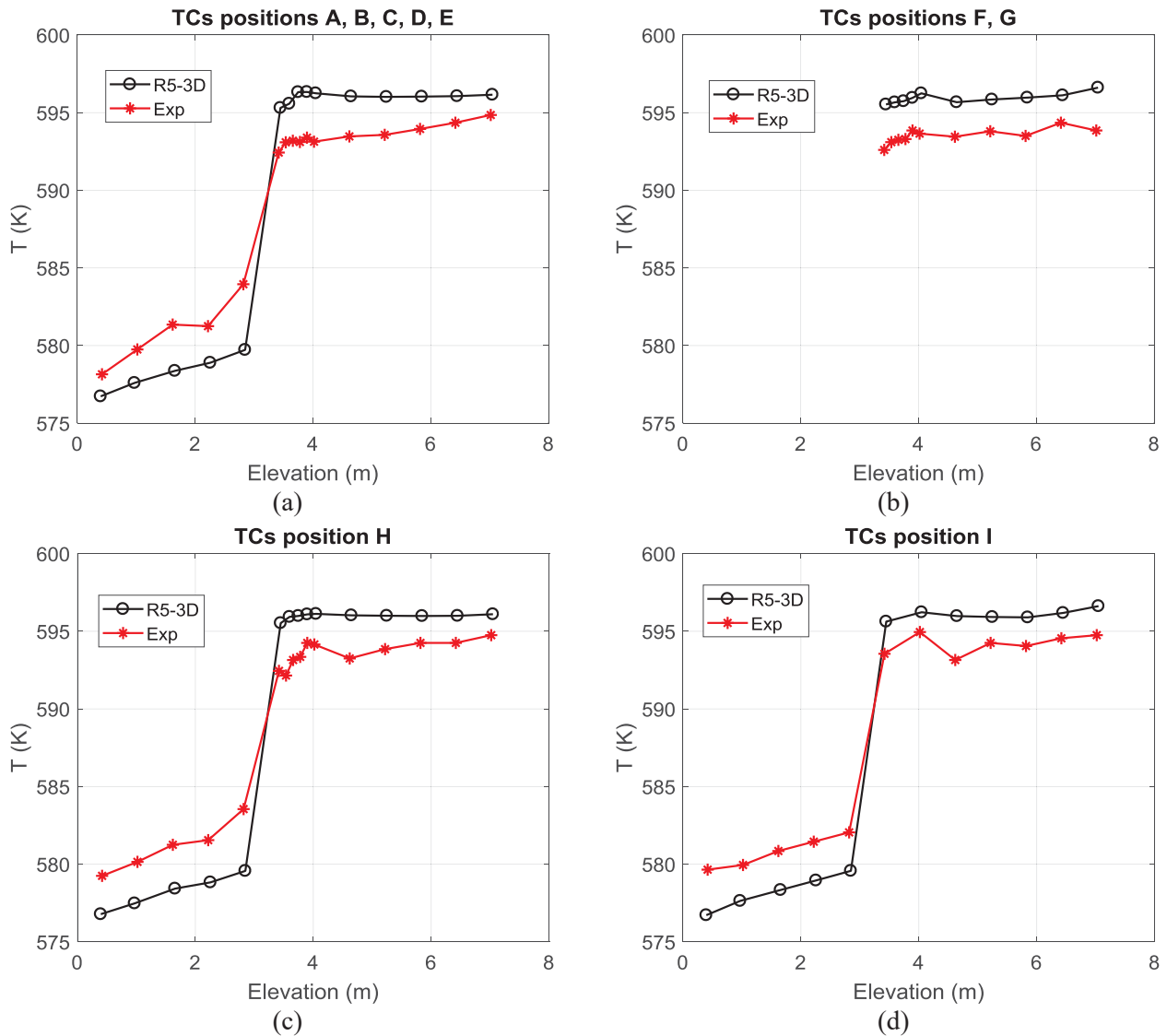
Fig. 2.25 – TS and MC: 60000 s
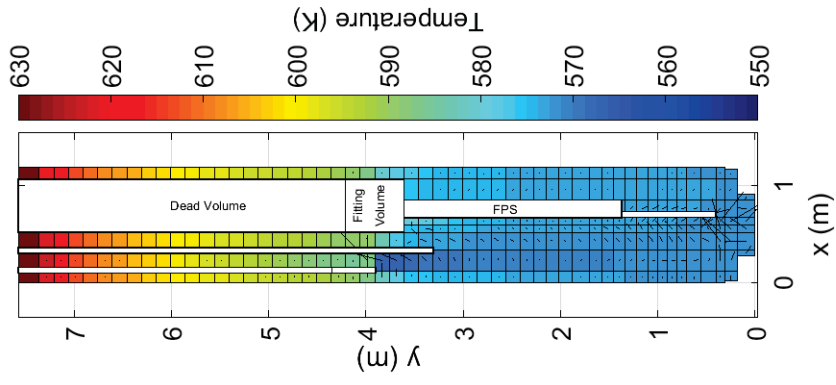
(a) 3300 s
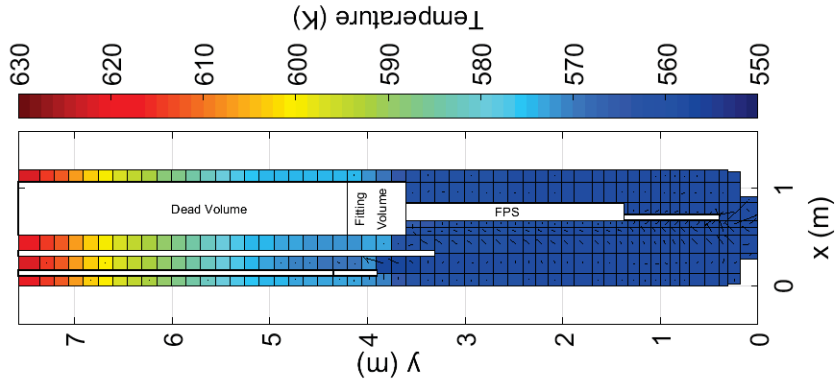
(b) 10000 s
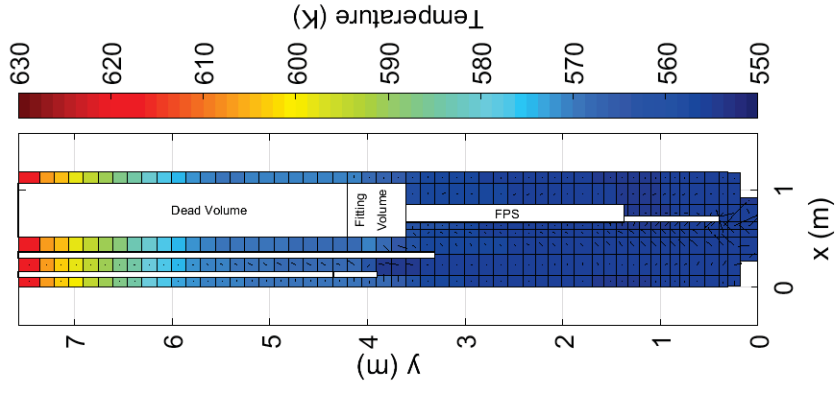
(c) 25000 s

Fig. 2.26 – TS and MC (1)
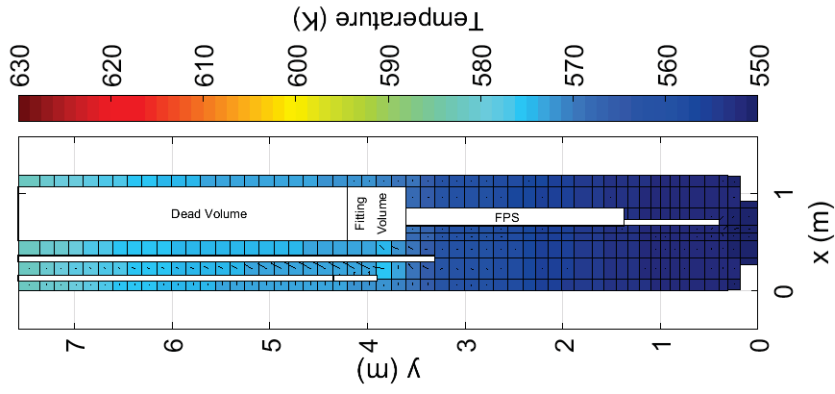
(a) 3300 s
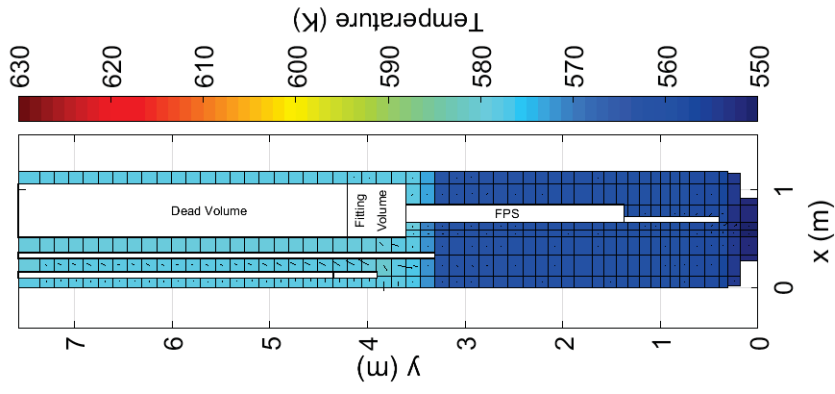
(b) 10000 s
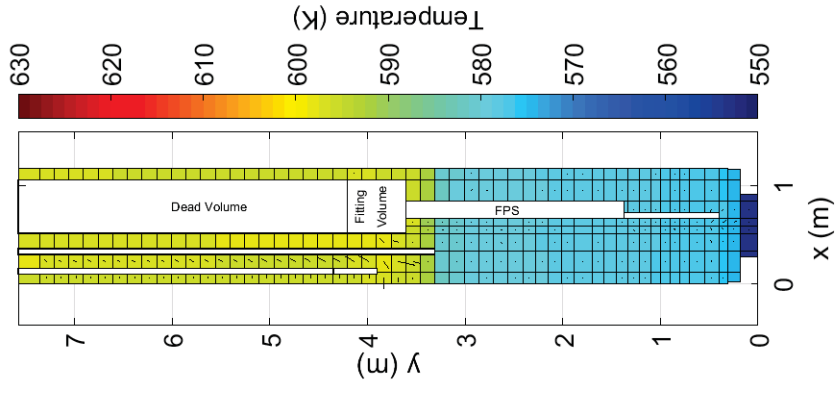
(c) 25000 s

Fig. 2.27 – TS and MC (2)
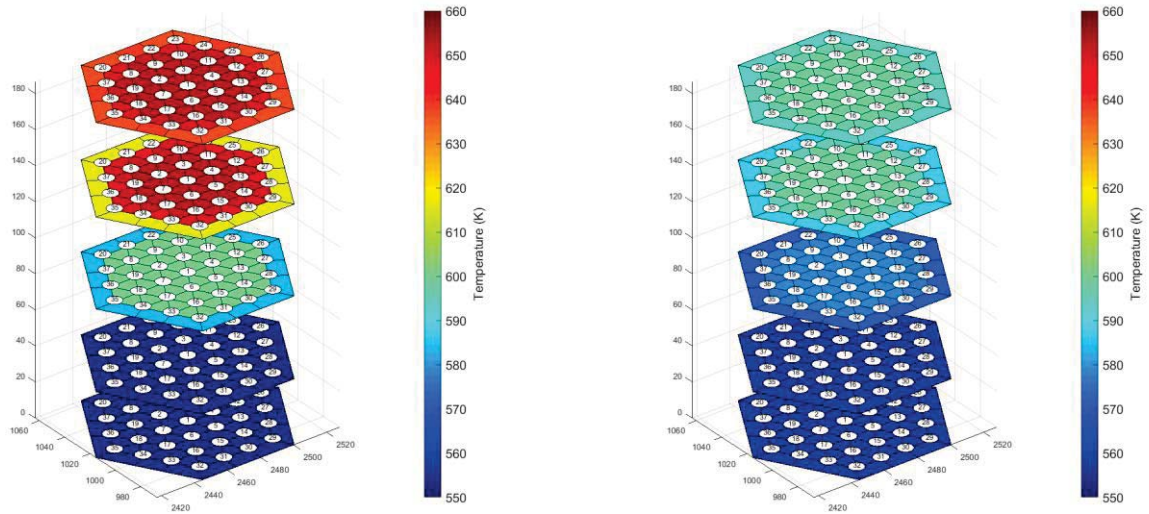
(a) 25000 s

(b) 32000 s
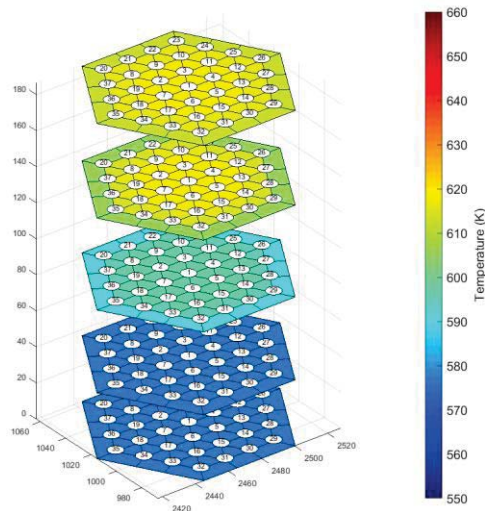
(c) 60000 s

Fig. 2.28 – FPS Temperature

2.4 List of References

[2.1]   L. Gramiccia, D. Vitale Di Maio, F. Giannetti, M. Tarantino, D. Rozzia, A. Toti, Definizione ed implementazione preliminare di un laboratorio per l'investigazione della termofluidodinamica dei

metalli liquidi (Double-wall bayonet tube steam generator for LFR application. Preliminary characterization). Report RdS/2011/50, 2011.

[2.2]   A. Gandini, L. Cretara, F. Giannetti, M. Frullini, V. Peluso, Attività di analisi di sensitività con metodologie GPT applicate a noccioli critici e sottocritici raffreddati a piombo. Report RdS/2012/37, 2012.

[2.3]   L. Ferroni, F. Giannetti, J. Manzano, M. Ciotti, Studi di sostenibilità sui sistemi nucleari refrigerati a piombo. CERSE-UNIRM RL 1190/2013, 2013.

[2.4]   C. Parisi, F. Giannetti, A. Naviglio, G. Caruso, Determinazione dei parametri di sicurezza del core e dell'andamento del burnup di un reattore veloce refrigerato a metallo liquido. ADPFISS-LP2-000, 2013.

[2.5]   A. Cammi, S. Lorenzi, R. Ponciroli, L. Ferroni, F. Giannetti, D. Vitale Di Maio, V. Covicchio, Studi di sostenibilità volti a massimizzare l'utilizzo del combustibile e a minimizzare le scorie nucleari con i sistmi veloci refrigerati a piombo. ADPFISS-LP2-045, 2014.

[2.6]   F. Giannetti, D. Vitale Di Maio, A. Naviglio, G. Caruso, Thermal-hydraulic analysis of an innovative decay heat removal system for lead-cooled fast reactors. Nucl. Eng. Des. 305, 168-178, http://dx.doi.org/10.1016/j.nucengdes.2016.05.005, 2016.

[2.7]   N. E. Todreas, M. S. Kazimi, Nuclear System – Thermal Hydraulic Fundamentals. Taylor $ Francis, ISBN 0-89116-935-0, 1993.

[2.8]   P. Balestra, F. Giannetti, G. Caruso, A. Alfonsi, New RELAP5-3D lead and LBE thermophysical properties implementation for safety analysis of Gen IV reactors. Sci. Technol. Nucl. Install., http://dx.doi.org/10.1155/2016/1687946, 2016.

[2.9]   OECD/NEA Nuclear Science Committee, Handbook on Lead-bismuth Eutectic Alloy AND Lead Properties, Materials Compatibility, Thermal-hydraulics and Technologies. 2015.

[2.10] D. Rozzia, A. Del Nevo, M. Tarantino, V. Narcisi, D. Vitale di Maio, F. Giannetti, G. Caruso, ALFRED-SGBT. Preliminary cheracterization by the HERO test section. ADPFISS-LP2-100, 2015.

[2.11] M. Tarantino, D. Rozzia, A. Del Nevo, F. Giannetti, CIRCE-HERO test setup. Tech. Rep. D4.3, H2020 SESAME project, 2016.

[2.12] V. Narcisi, F. Giannetti, A. Del Nevo, M. Tarantino, G. Caruso, Pre-test analysis of the protected loss of primary pump transient in CIRCE-HERO facility. J. Phys. Conf. Ser. 923 (012005). http://dx.doi.org/10.1088/1742-6596/923/1/012005

[2.13] V. Narcisi, F. Giannetti, A. Del Nevo, M. Tarantino, G. Caruso, Pre-test analysis of accidental transients for ALFRED SGBT mock-up characterization. Nucl. Eng. Des. 333, 181-195, https://doi.org/10.1016/j.nucengdes.2018.04.015, 2018.

[2.14] V. Narcisi, F. Giannetti, G. Caruso, D. Rozzia, A. Del Nevo, M. Tarantino, Installazione della sezione di prova HERO nella facility CIRCE: sviluppo nodalizzazione e progettazione della campagna sperimentale. ADPFISS-LP2-133, 2016.

[2.15] V. Narcisi, P. Lorusso, F. Giannetti, A. Del Nevo, M. Tarantino, Analisi di pre-test della campagna sperimentale CIRCE/HERO con codici di sistema. ADPFISS-LP2-151, 2017.

[2.16] V. Narcisi, F. Giannetti, P. Lorusso, M. Tarantino, A. Del Nevo, G. Caruso, Thermal stratification analysis in CIRCE-ICE pool facility with RELAP5-3D model. Proc. Of Global Symposium on Lead and Lead Alloy Based Nuclear Energy Science – GLANST2017, Seoul, Republic of Korea, September 2016.

[2.17] V. Narcisi, F. Giannetti, M. Tarantino, D. Martelli, G. Caruso, Pool temperature stratification analysis in CIRCE-ICE facility with RELAP5-3D© model and comparison with experimental tests. J. Phys. Conf. Ser. 923 (01 2006), http://dx.doi.org/10. 1088/1742-6596/923/1/012006, 2017.

[2.18] A. Del Nevo, A. Subioli, V. Narcisi, F. Giannetti, Application of RELAP5-3D on Phenix Experimental Test. ADPFISS – LP2 – 144, 2017

[2.19] M. Tarantino, D. Martelli, G. Barone, I. Di Piazza, N. Forgione, Mixed convection and stratification phenomena in a heavy liquid metal pool. Nucl. Eng. Des. 286, 261-277, http://dx.doi.org/10.1016/j.nucengdes.2015.02.012, 2015.

[2.20] INL, The RELAP5-3D© Code Development Team, RELAP5-3D© Code Manual Volume IV: Models and Correlations. INL/MIS-15-36723, Revision 4.3, October 2015

[2.21] M. Schikorr, E. Bubelis, L. Mansani, K. Litfin, Proposal for pressure drop prediction for a fuel bundle with grid spacers using Rehme pressure drop correlations. Nuclear Engineering and Design, 240 1830-42, https://doi.org/10.1016/j.nucengdes.2010.03.039, 2010.

(Page intentionally left blank)

3 APPLICATION OF RELAP5-3D ON PHENIX EXPERIMENTAL TESTS

V. Narcisi, A. Subioli, F. Giannetti, L. Gramiccia, L. Ferroni

(Page intentionally left blank)

3.1   Background and references

The assessment of nuclear power plant (NPP) performances during accidental scenario is the main issue of the safety analysis. Until recent years, most of the safety analyses were successfully performed using thermal-hydraulics system code (SYS-TH), reproducing transient conditions typical of postulated accidents. However, the SYS-TH codes present some limitations when complex feedback exists between core neutronics and thermal-hydraulics, when innovative coolants are used for the core heat removal (for example liquid metals or molten salt) or when multidimensional phenomena are involved in particular configurations of a NPP (Ref. [3.1]).

Sapienza University of Rome collaborates with ENEA Brasimone Research Center in the development of a calculation platform for the fast reactors TH and Neutron Kinetic (NK) from 2012. For the TH part, RELAP5-3D (R5-3D) was selected as reference code and then the validation of R5-3D for liquid metal fast reactor has been started and it is still ongoing. An important aspect is the pool thermal hydraulics and in this framework is inserted this activity.

In absence of the experimental transient data for lead reactors, sodium reactors data are used to preliminary validate the models and the simulation approaches.
Sodium-cooled Fast Reactor (SFR) technology has been established in former fast reactor programs, as the Phénix End-of-Life tests (Ref. [3.2]). Phénix is a SFR operated in France and this experimental campaign has been conducted before the definitive shutdown of the reactor (Ref. [3.3]).

A dissymmetrical configuration test, selected from the End-of-Life series, has been selected as a benchmark transient into H2020 SESAME project (http://sesame-h2020.eu/), in order to demonstrate the capability of the system thermal-hydraulics codes (standalone or in coupling configuration with CFD codes) to predict the three-dimensional pool phenomena. This activity, carried out in synergy with SESAME project, aims to validate the RELAP5-3D$^{©}$ code in simulating pool-type liquid metal cooled fast reactor in accidental scenario, identifying code limitations and source of uncertainties. The activity also tries to improve the understanding of thermal-hydraulic processes and phenomena observed in dissymmetrical test and to develop a reliable approach for the application of thermal-hydraulic system codes in safety analysis of new generation fast reactor systems. Indeed, transients and thermal-hydraulic phenomena relevant for the analysis of liquid metal fast reactors are expected to occur in PHENIX, similarly as larger scale fast reactor systems. This implies that models and correlations that affect the code's calculation of the phenomena of interest can be assessed in a range of thermal-hydraulic parameters representative of candidate designs (Ref. [3.4]).

In this framework, the report provides a full description of two different approaches for the simulation of the three-dimensional phenomena that occur inside the large pools of the reactor: a mono-dimensional model of the pools, obtained adopting three parallel pipes to reproduce the large volumes, and a three-dimensional model, using a 3D component.

3.2   Body of the report concerning the ongoing activities

3.2.1   Phénix reactor

Phénix is a sodium cooled pool-type fast reactor of 563 MWth, with an electric output of approximately 250 MWe, located at the Marcoule nuclear site, near Orange, France. The NPP construction began in November 1968 and the first connection to the French national electricity grid was in December 1973. During the summer of 1976, due to small sodium losses in two intermediate heat exchangers, the plant was temporarily stopped to repair the failures found. The problems of the two IHXs have never been solved but they were closed and, from 1993 to the end of the electricity production in 2009, the reactor has been operated at a reduced power of 350 MWth (140 MWe) (Ref. [3.5], [3.6] and [3.7]).

Fig. 3.1 shows the reactor block, which is a suspended type. The reactor is composed of four vessels, all supported by the upper cover slab. The cover head is attached to a concrete slab by 21 suspension hangers and it is closed off with a flat roof equipped with penetrations necessary for the passage of components and instrumentation. The main vessel ensures the biological protection; it is 10 metres high and 11.8 m in diameter and it contains about 800 tons of primary sodium. Any possible sodium leaks are contained by the double-enveloped vessel, which is welded to the upper part of the main vessel. The roof and the double envelope vessel are both thermally insulated. The external one is the primary containment vessel, an ordinary steel tank which envelopes the internal vessels. The primary containment vessel is welded under the concrete slab and is maintained in a nitrogen atmosphere; its role is to contain radioactive products in the event of a severe accident. The final emergency cooling system is welded onto the outside wall of the third vessel and it aims to maintain the reactor pit concrete at ambient temperature and to ensure the decay heat removal, in the event of a loss of normal cooling systems. Inside the main vessel, the primary vessel separates the sodium coolant in two pools (hot and cold). The primary vessel is composed from a shell which is followed from a conical area that contains twelve channels equipped with sleeves for primary pumps, intermediate heat exchangers and other components. This is followed by a new shell that envelopes the core and is welded to the lateral shielding support (Ref. [3.5], [3.6] and [3.7]).

The primary system is equipped with six intermediate heat exchangers (straight-tube type, see Fig. 3.2 and Fig. 3.3), connected in pairs to the three secondary loops, which are equipped with the mechanical pump, located inside the expansion tank, a buffer tank and the auxiliary systems, which ensure the sodium storage, filling, and purification. Each of them feeds a steam generator that supply the thermal power to the tertiary circuit, based on a Rankine cycle where the operating fluid is the water. The hot primary coolant, contained inside the hot pool, moves through the shell side of the intermediate heat exchangers (IHX) decreasing the temperature and then is collected inside the cold pool. Three primary pumps (Fig. 3.4) drive the sodium from the cold pool to the diagrid, that guarantees the correct distribution of the coolant mass flow rate to each sub-assembly (SA). Another function of the diagrid is to redirect about 10% of the operating flow to the vessel cooling system (VCS), and, together with the strongback and the conical shell, of supporting the above structures. The VCS operation is presented in Fig. 3.5; the cold sodium moves upward inside the zone between the conical shell and the main vessel, refrigerating the latter. Then the sodium is poured in cold pool.

The reactor core consists of an array of hexagonal assemblies, represented in Fig. 3.6. Each assembly is characterized by an overall length of 4.3 m; the fuel is mixed uranium-plutonium oxide (Ref. [3.5] and [3.8]). A central fissile zone, composed by two regions of different enrichment values, is surrounded by annular fertile zones and further out by steel reflectors and lateral neutron shielding rods especially designed to limit the activation of the secondary cooling sodium in the intermediate heat exchangers. The fuel, which is mixed uranium–plutonium oxide, has a Pu enrichment of 18% in the central region (inner core) and an enrichment of 23% in the periphery region (outer core). This difference is designed to "level out" the neutron flux and homogenize heating. The fuel sub-assemblies (SA) contain MOX in the form of 217 pins, which are composed of a stack of pellets, and depleted uranium oxide, which acts as axial blanket, formed by 217 pins in the lower part, and by 37 pins in the upper part; they are all enclosed in a stainless-steel cladding. The spacer wires fix the pins correct positions and they guarantee the flow of sodium and optimize heat exchange. The fuel bundle is located inside a hexagonal stainless-steel wrapper equipped, in the lower part, with a foot that guarantees the positioning of the SA in the diagrid and the inlet for the sodium mass flow rate (see Fig. 3.7).

3.2.2 Dissymmetric test

Before the final shutdown of the PHENIX reactor, an experimental program was set up in order to collect data for code assessment and to address the design of new SFR with respect to fuel, materials, neutronics and thermal hydraulics. The experimental campaign, belonging to the End-of-Life tests, includes:

- The natural convection test, dedicated to the establishment of natural circulation in the primary, secondary and steam generator casing systems;
- The dissymmetrical test characterized by the manual trip of a secondary pump leading to the injection of hot sodium in 1/3 of the cold pool.

During the 2009, two asymmetrical tests were performed, one on each secondary loop (LOOP 1 and LOOP 3). The results of the tests are similar and it proves the repeatability of the test; because of this similarity, only the test on the LOOP 1 are presented in this activity.

The dissymmetrical test supports liquid metal reactor plant design and it demonstrates the effectiveness of the natural circulation cooling characteristics. The test started with nominal steady state conditions, thus at full power and flow. The initiating event was the trip of the secondary coolant pump (on the LOOP 1) in which the speed is reduced from 700 to 100 rpm in about 13 s, producing azimuthal and axial dissymmetry in the cold pool: the lack of the cooling created a hot shock in the cold pool at the outlet of the IHX 1 IHX 3. After 5 seconds from the beginning of the test, the automatic shutdown occurred (the control rods are inserted at velocity of 1.4 mm/s in 45) and the speed of secondary pump on the loop 3 was reduced from 700 to 110 rpm in about 60 s, after the turbine trip signal. At 48 seconds the scram command has been operated and the test stopped after 1800 seconds (Ref. [3.3]). The sequence of the events is summarized in Tab. 3-1.

3.2.3 Phénix model

RELAP5-3D$^{©}$ is the latest in the series of RELAP5 codes, developed at the Idaho National Laboratory (INL). It is a highly generic code that, in addition to calculating the behavior of a reactor coolant system during a transient, can be used for the simulation of a wide variety of hydraulic and thermal transients in both nuclear and non-nuclear systems involving mixtures of vapor, liquid, non-condensable gases, and nonvolatile solute. RELAP5-3D© (R5-3D) has fully integrated, multi-dimensional thermal hydraulic and kinetic modeling capability. This allows the applicability of the code to the full range of postulated reactor accidents. It has implemented all features and models previously available in the ATHENA code (INL): several working fluids (e.g. helium, hydrogen, lead-bismuth, lithium, lithium-lead, molten salts, sodium, sodium-potassium, etc.) and a magneto-hydrodynamic model (Ref. [3.9] and [3.10]).

The nodalization of Phénix NPP is composed of 6940 hydraulic volumes, 11840 hydraulic junctions, 6888 heat structures, and 40170 mesh points in the heat structures. The model consists of:

- A multi-dimensional (MULTID) component, modeling the pools and the core bypass;
- A mono-dimensional model, reproducing the zones where a predominant 1D flow is expected (i.e. hexagonal fuel assemblies; heat exchangers; pump suction and feeding conduit, VCS, and gas plenum).

The MULTID component models the diagrid, the core bypass, the hot pool and the cold pool. It is composed by 35 axial lengths, 6 radial rings and 12 azimuthal sectors. The first three rays are chosen to divide the core in three zones (fuel zone, blanket-reflector zone, and natural circulation zone), and the rays four, five and six are chosen to uniformly divide the cold pool (ray four measures up to the axle of the IHXs and the MCPs, ray five is chosen to have the azimuthal sectors with the same area of ray four, and ray six corresponds to the greater dimension of the primary vessel). The number of azimuthal meshes is chosen on the basis of the geometrical positions of the MCPs and IHXs (see Fig. 3.8) and the axial mesh lengths of the cold and hot pool regions and of the other components (reactor zone, skirt and MCPs pipes, IHX, and VCS) are consistent with the vertical sliced approach (see Fig. 3.9). Each 1D component is placed according with the 3-D geometrical specifications and the relevant elevations are preserved. In order to represent the real quantity of fluid contained in each volume of MULTID component, the porosity factor and the junction factor are used.

The dead zone and the top part of the pool, that includes the layer of argon, have been modelled with two BRANCH components. The level of cold pool (the zone between the primary vessel and the vessel cooling system) and the correspondent layer of argon above it have been modelled with PIPE and BRANCH component. The different SAs (inner fuel, outer fuel, radial blanket, ARA, control rod, ASA, B4C shielding and storage) are modeled with PIPE components composed of 20 meshes, according with the geometrical specification, which have the axial lengths equal or sub-multiple with respect of the meshes of the 3D component. Their connections, below with the diagrid and above with the hot pool, are modelled with several MTPLJUN connected to the correspondent zones of MULTID component. The reactor core is divided into three main parts:

- the assemblies of the inner core and the outer core regions, the first 7 rows, modeled one by one, according to the geometrical specifications;
- the blanket/reflector/storage zone, rows greater than 7, modeled with 36 equivalent PIPE components, with the radial blanket, the ARA and the storage assemblies grouped separately, according to the azimuthal configuration. Each equivalent PIPE represents for the blanket 80/12 of SA, for the ARA 208/12 of SA and for the storage 41/12 of SA;
- the shielding zone where the SAs (i.e. ASA and B4C shielding) are modeled with 24 equivalent PIPE components distributed along the twelve azimuthal meshes. Each equivalent PIPE represents for the ASA 297/12 of SA and for the B4C shielding 765/12 of SA.

Not having been delivered any geometrical details of the subassemblies orifices or form loss coefficients as function of Re to the benchmark participants, fuel assembly orifices (represented with the passage areas and K-loss implemented in the MTPLJUN component) have been set up based on mass flow rate data and overall dynamic pressure drops in the nominal steady state (see Fig. 3.10 and Fig. 3.11). The power generated by each SA is imposed, during the nominal and transient state, with a GENERAL TABLE, where the trend of the power, as function of the time, is indicated. The heat exchange between the inner/outer core fuel assemblies and sodium is modeled with 6 heat structures: three to represent the zones in which the power is generated and three to represent the passive zones. The three active zones consist of the lower axial blanket, the upper axial blanket and the fuel. Their heat structures are modeled with 12 nodes and the first two are made of helium, UO_2, steel 316 and the last of helium, MOX and steel 316, according to the geometrical specifications. The three passive zones consist of SA foot, hexagonal wrapper tube and axial shielding. Their heat structures are modeled with 4 nodes, are made of steel 316 and connect the PIPE representing the SA with the corresponding MULTID zone. While the passive heat structures of the other type of SAs are modeled in the same way, as described above, the active ones differ in shape and materials.

The pumps are simulated with an ascending pipe, which reproduces the annular inlet of the component, connected with the correspondent region of the cold pool, with the PUMP component and with the descending pipe which leads the primary coolant to the diagrid. The nodalization scheme is depicted in Fig. 3.12. The homologous curves of the PUMP components are set-up using PHENIX reference data. The IHXs primary side are modeled separately with PIPE components connected upstream and downstream with the correspondent region of hot pool and cold pool. The IHXs secondary sides are modeled separately with pipe components from an inlet and outlet collectors (dummy) and fed with imposed boundary conditions. Fig. 3.12 shows the representative nodalization scheme of the heat exchangers. Primary and secondary sides of DOTE components are modeled and disabled closing the connections between the IHXs 2 and the hot pool, to prevent the primary mass flow rate passing through. The diagrid is modelled with branch component connected below with the strongback and above with the SAs and the bypass region. The nodalization scheme of the vessel cooling system and the strongback are shown in Fig. 5.12; it consists of the pipe 945, connected upstream with the diagrid, on the top with the gas plenum (972), and downstream with the corresponding regions of cold pool.

The pressure drop in the rod bundle is evaluated using Cheng and Todreas correlation for laminar, turbulence and transition flows, as in Ref. [3.11]. For the evaluation of the heat transfer coefficient (HTC) for liquid metals, RELAP5-3D© uses two different correlations depending on the geometry (non-bundle or bundle) (Ref. [3.9]), for all convective wall heat transfer (turbulent forced, laminar forced, and natural). For non-bundles the Seban-Shimazaki correlation is used:

$$Nu = 5.0 + 0.025Pe^{0.8}$$

where Pe is the Peclet number. When Pe goes to zero, the Nusselt number tends to 5 in order to reproduce the HTC in natural circulation conditions. For the HTC evaluation in bundle geometry, the Westinghouse correlation is integrated in RELAP5-3D$^©$ (Ref. [3.10]) and it is used to calculate the heat transfer coefficient inside the SAs:

$$Nu = 4.0 + 0.33\left(\frac{p}{D}\right)^{3.8}\left(\frac{Pe}{100}\right)^{0.86} + 0.16\left(\frac{p}{D}\right)^{5}$$

where p is the rod pitch and D the rod diameter. The correlation is developed for a range of pitch to diameter ratio from 1.1 to 1.4 and Pe from 10 to 5000. The IHXs are characterized by a p/D equal to 1.43; for this reason, the H. Graber & M. Rieger correlation in Ref. [3.12], not implemented in the current version of R5-3D, is selected to evaluate the HTC in the IHXs primary side:

$$Nu = 0.25 + 6.2\frac{p}{D} + \left(-0.007 + 0.032\frac{p}{D}\right)Pe^{\left(0.8-0.024\frac{p}{D}\right)}$$

developed in 1.2 < p/D < 2.0. In the operational range of temperature, the two correlations have a similar gradient of Nu versus Pe; therefore, a constant HTC multiplication factor (used as in [3.13] for lead) equal to 1.4, calculated as the ratio of H. Graber & M. Rieger and Westinghouse correlations, has been applied in the IHX primary side model.

3.2.4   Results

In order to obtain the initial conditions for the transient test, the operational conditions are analyzed. The Tab. 3-2 summarizes the nominal boundary conditions and the main results obtained after 3000 s of problem time. The screenshot of the coolant temperature profiles in the most representative section is reported in Fig. 3.14. This provide the temperature distributions at the end of steady state calculation. It should be noted that the screenshot includes the temperature of selected SA channels (according with the nodalization approach) belonging to the corresponding section (i.e. azimuthal sector). They are: one selected SA per each rank from 1 to 7, one SA per type (three) for the ranks >7, and one SA per type for the ranks in natural circulation. This last group experiences higher coolant temperatures because they are blind channels, thus not fed by the MCP.

Starting from the steady state conditions, the dissymmetric test is reproduced following the sequence of events shown in Tab. 3-1 (Ref. [3.4]). At the beginning of the test the exchanged power through IHXs is 344.11 MWth (170.132MWth by loop 1 and 173.981 MWth by loop 3). Immediately the secondary mass flow rate of the loop 1 decreases, provoking the quick reduction of the thermal power removed by the IHX-1A and the IHX-1B. Fig. 3.15 compares the thermal power removed by the loop 1 (IHX-1A + IHX-1B) and the loop 3 (IHX-3A + IHX-3B). The delay of the power reduction of the loop 3, due to the delay time of the secondary pump 3 trip, is also highlighted in Fig. 3.16. During the first 30 s of the test, the thermal power removed by the loop 3 increases up to the 83% of the total power; at this time the power removed by the loop 1 reaches and maintains the value of about 20 MW, while the power removed by the loop 3 continues to decrease, reaching the same value of loop 1 at about 70 s. These considerations shown how the exchanged power through IHXs is dissymmetrical at the beginning of the transient.

Fig. 3.17 shows the IHX outlet temperatures. At the bottom edge of the IHX-1A and 1B, the temperature of the primary coolant quickly increases to the peak of 773 K and, after a delay time of about 30 s, also the outlet temperature of the IHX- 3A and 3B reaches the maximum value of 763 K. Hence, being the two hot shocks different for time and value, a dissymmetric distribution of the temperature inside the cold pool is produced, as shown from the temperature distribution in Fig. 3.18.

In the first seconds of the transient, the decrease of the thermal power removed by the loop 1 causes an increase of temperature at the IHX outlet. After 20 s from the beginning of the test, due to the temperature increase (which results in a density decrease), the hot sodium flows up in the cold pool and then cold sodium is sucked by the primary pump 1, as shown by the small peak in Fig. 3.19. With a delay of about 45 s, the same effect, but more accentuated, occurs at the outlet sections of IHX-3A and 3B. After 70 s, the hotter fluid reaches the inlet section of the PP 3 because the upper part of the cold pool is heated during the previous phase. This causes a peak temperature of about 675 K at the pump 3 inlet (see Fig. 3.19). After that, the sodium temperature at the bottom zone of the two zones becomes uniform and the inlet temperature of the pump 3 reaches the same temperature of the pump 1, following the same trend. In the first phase of the transient the inlet temperature of the pump 2 remains always greater than the others, but the difference decreases with the progress of time. The dissymmetric temperature trend causes a different density at the pumps inlet and, consequently, a small mass flow rate variation, as shown in Fig. 3.20.

Fig. 3.21 shows the core inlet temperature measured at the outlet of the primary pumps, in according to the real position of the instrumentation. Following the temperature trends those at the pumps inlet, there is a small azimuthal variation of the temperature, see Fig. 3.22. The core outlet temperature is shown in Fig. 3.23. In order to reproduce the real position in which the temperature is measured, in the figure are plotted the temperatures of the twelve azimuthal meshes, and their average, of the MULTID component at the core outlet. The core power decreases rapidly from 5 to 45 s (before the scram). The primary pumps are not stopped during this test: the primary flow rate is close to the nominal value during the whole transient and therefore, despite an increase of the inlet temperature, the core outlet temperature decreases during the 50 first seconds of the test. After reaching a maximum of 715 K at about 175 s, the outlet temperature decreases throughout the rest of the transient.

The inlet temperature of the IHXs follows the same trend of the core outlet, as shown in Fig. 3.24. The cold shock in the hot pool is seen with a delay by the IHX inlets and it is less severe due to the thermal mixing with the mass of hot sodium over the core. The trend of the coolant temperature of the IHX secondary outlet follows that of the IHX primary inlet (see Fig. 3.25).

3.2.5 Nodalization sensitivity: 1D model

In Phenix, as well as in all pool type reactors, the MULTID component is very useful to reproduce the thermal mixing and stratification phenomena in the hot and cold pool. The scope of this chapter is to investigate the main differences between the results obtained with a multi-dimensional nodalization, previously presented, and those obtained with a one-dimensional nodalization.

The mono-dimensional model consists of 4589 hydraulic volumes, 4984 hydraulic junctions, 6897 heat structures, and 40215 mesh points in the heat structures. The nodalization hereafter presented differs from the multi-dimensional only for the modelling of the pool, the bypass and the diagrid. The hot pool is modelled with 7 components to respect the reactor geometry and to represent the relevant thermohydraulic zones. The annular region, where there are the inlets of the IHXs, is modelled with three PIPE components 312, 314, 315 in Fig. 3.26) having each one 9 axial meshes. The volumes of sodium above the core are modelled with a BRANCH component (306 in Fig. 3.26) modelling the free sodium height at the outlet of the SAs (before the beginning of the control plug), and with 2 PIPES components representing the sodium in the control plug (308 in Fig. 3.26) and that in the free space (310 in Fig. 3.26). Each component is connected

with multiple cross junctions to reproduce the mixing phenomena. The BRANCH 941 represents the upper region of the hot pool, containing the free level of primary coolant. The cold pool follows the same nodalization scheme of the annular region of the hot pool. The diagrid is modelled with BRANCH component (302 in Fig. 3.26) connected below with the strongback and above with the SAs. The bypass zone is modelled with 2 equivalent PIPEs (303 and 305 in Fig. 3.26). These are connected with multiple cross junction to reproduce the natural circulation and with 3722 heat structures to simulate the heat dissipation through the SA hexagonal wrapper tube.

In order to have a comparison between the CPU times, the same time steps are used to run the mono-dimensional blind calculation. The transient required a computational time of 8.24 h, less than 24.36 hours necessary for the multi-dimensional. The main reason is due to the great difference in volumes and junctions number and therefore to the time requested by the code to solve the field equations. The steady state is achieved by running the code for 3000 seconds (problem time). The calculated time trends are comparable to the multi-dimensional results. Minor exceptions are discussed below:

- The small differences at the primary pumps inlet temperature, and so at the outlet temperatures, as shown in Fig. 3.30 and Fig. 3.32, are negligible, being less than 5 K, for comparison purposes between the two nodalizations;
- The different structure of the two nodalizations leads to have a small difference in the pressure drops along the coolant flow path. This is confirmed by the values of the mass flow rate elaborated by the main coolant pumps (Fig. 3.31) with the same rpm;
- Fig. 3.33 shows the core outlet temperature. Having in the mono-dimensional nodalization only one volume at the core outlet, and not 108 volumes like in the multi-dimensional, the temperature measured by the thermocouples cannot be represented with great precision.

During the transient test, the time trends of selected parameters significantly differ (except for the power exchange through the IHX, as shown in Fig. 3.27 and Fig. 3.28) from the multi-dimensional. The parameters that cause the differences are the sodium flow path between the outlet of the IHXs and the inlet of the primary pumps, and the core outlet temperature. In the mono-dimensional nodalization the thermal mixing between the sodium at the IHX outlet and the cold pool is not correctly represented, going the sodium straight up to the pumps inlet. This is confirmed by the lack of the temperature peak on the primary pump 1, in the first seconds of the transient, as shown in Fig. 3.30. Instead the temperature peak at the pump 3 is seen in a different time and with different intensity. The reason is always connected to the sodium movements. This behavior leads to have higher temperature values, in the peaks and in the transient second phase. As consequence these trends influence those of the other parameters (see Fig. 3.29, Fig. 3.32, Fig. 3.33, Fig. 3.34 and Fig. 3.36), which differ from the multi-dimensional in the same points. Fig. 3.31 shows the main coolant pumps mass flow rate. Their lowest values in the transient second phase are caused by the coolant temperature higher values. The nodalization at the core outlet makes uniform the coolant temperature of sodium which then goes up to the IHX inlet. How can be seen in Fig. 3.29, Fig. 3.35 and Fig. 3.36 this, together with the reasons previously explained, leads to have a different trends on the IHX outlet and inlet temperatures.

3.3 Conclusive remarks

The dissymmetric test, carried out on Phenix reactor, offers useful experimental data for the validation of thermal-hydraulic system codes in the asymmetric phenomena prediction in a liquid metal pool reactor.

The mono-dimensional and the three-dimensional models has been developed using RELAP5-3D$^{©}$. The phases of the work are summarized below:

- Realization of a detail 3D model of the Phenix plant and reactor.

- Simulation of the transient: verification of the code performance at steady state level and the analysis of the results.
- Realization of a simplified 1D model of the Phenix plant and reactor.
- Simulation of the transient: comparison with the 3D model focusing the attention on the computational time requested and the differences between the results obtained.

The analysis of the results brings to the following final considerations:

- Steady state conditions are achieved, and they are in good agreement with the benchmark specifications.
- Qualitatively the thermal-hydraulic phenomena and the trends of the parameters are consistent with the expectations.
- The RELAP5-3D© code offers good capability to reproduce the mixing and thermal stratification in pool reactor.
- Sodium fluid properties in RELAP5-3D© are generally in agreement with values from other source data.
- A simplified 1D model allows faster calculations, but it does not allow a detail analysis of the main quantities in the several points of the reactor and the thermal hydraulic phenomena occurring in pool cannot correctly reproduce.

In order to validate RELAP5-3D© system code in simulating sodium fast reactors design, the following activities are planned:

- Comparison of the blind results with the experimental data to do post-test calculations.
- Sensitivity studies to increase the knowledge on relevant aspects of the operation of pool type sodium cooled fast reactors.
- To correctly set up the pressure drops distribution to be able to do studies in natural circulation.
- Starting from the thermal hydraulic model presented, to develop point kinetic model for 3D NK coupling calculation.

Action	Time (s)
Secondary pump trip (on loop1): speed reduced from 700 to 100 rpm in about 13 s	0
Automatic shutdown: insertion of the control rods (1.4 mm/s) in 45 s. Turbine trip. Secondary pump speed reduced (on the other loop) from 700 to 110 rpm in about 60 s	5
Scram	48
End of test	1800

Tab. 3-1 – Dissymmetrical test: sequence of events

Quantity	Unit	R5-3D
Primary circuit balance	MW	340.87
T secondary system IHX inlet	K	593.65
T secondary system IHX outlet	K	786.66
MF IHX-1A secondary system	kg/s	347.13
T Core inlet	K	659.97
T Core outlet	K	792.91
T primary system IHX inlet	K	792.16
T primary system IHX outlet	K	659.73
MF Total PP	kg/s	2211.45
MF Total core	kg/s	1992.45
MF VCS	kg/s	219.00

Tab. 3-2 – Seady state conditions
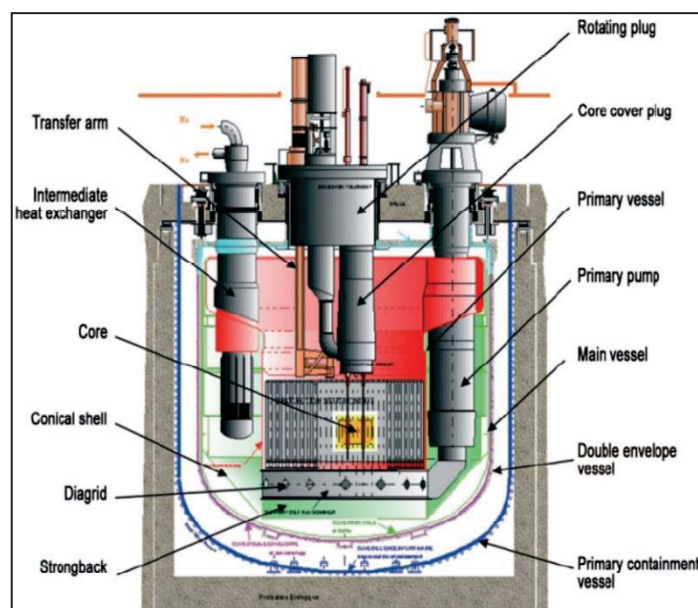
Fig. 3.1 – Reactor block
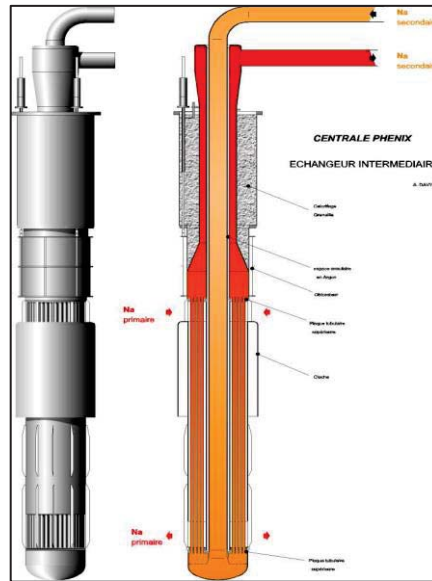
Fig. 3.2 – Intermediate heat exchanger
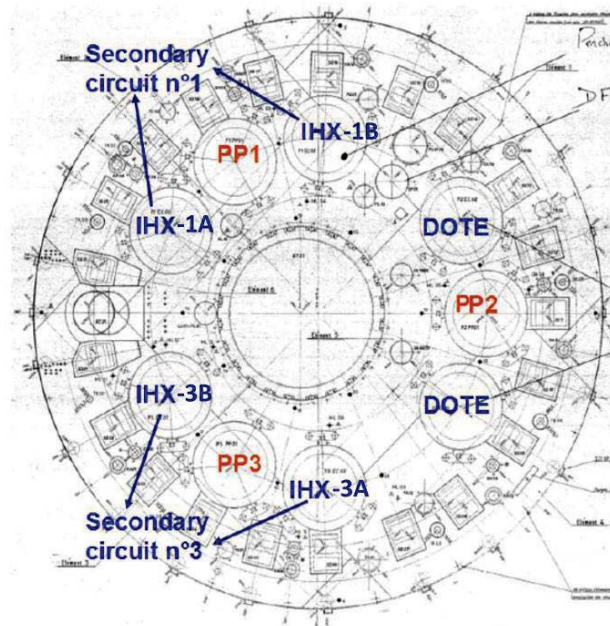
Fig. 3.3 – Reactor top view
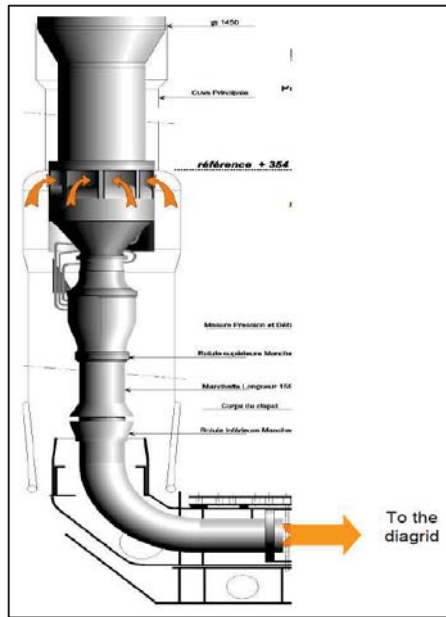
Fig. 3.4 – Primary pump
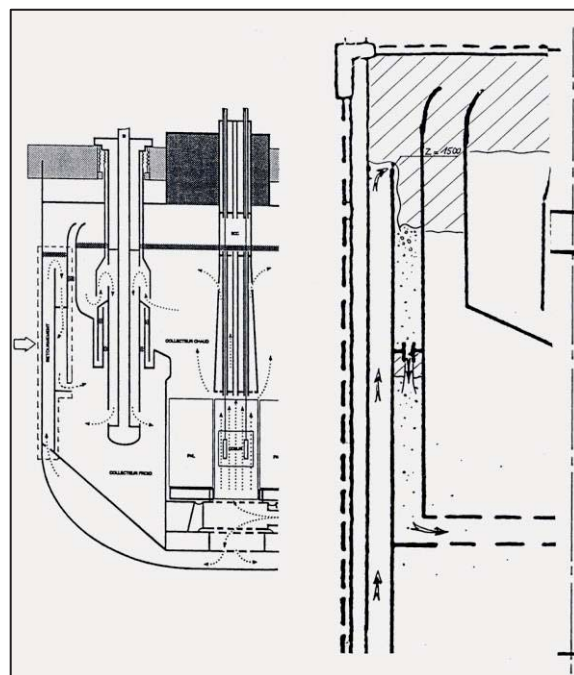
Fig. 3.5 – Vessel cooling system flow path
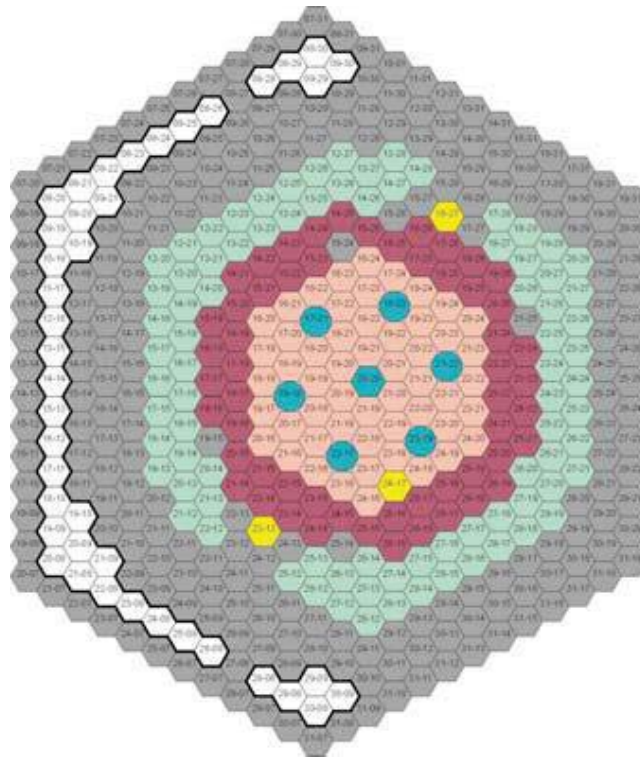
Fig. 3.6 – Reactor core top view
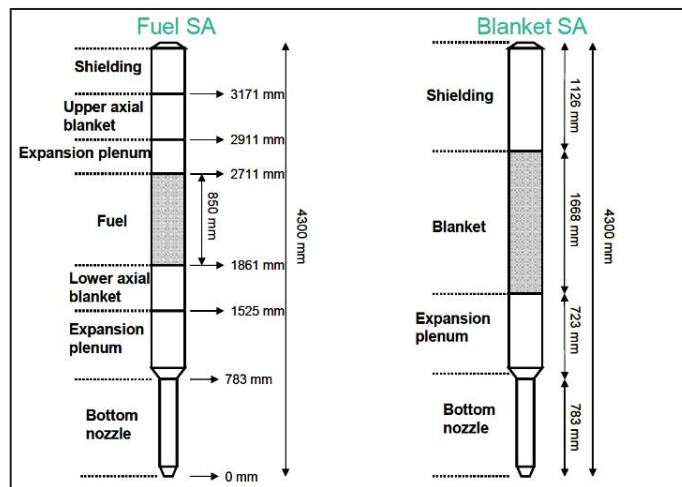
Fig. 3.7 – Fuel and fertile SA axial composition
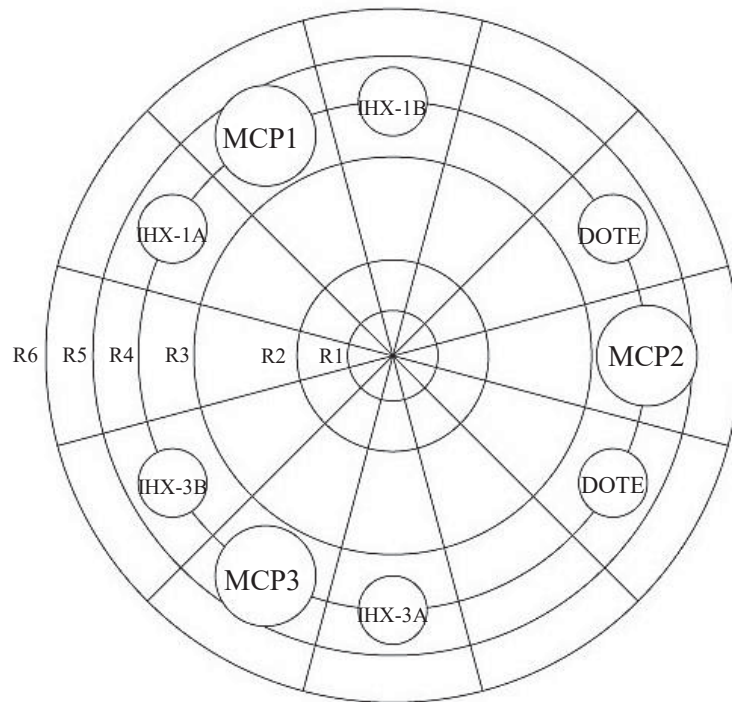
Fig. 3.8 – Overview of radial and azimuthal meshes of MULTID component
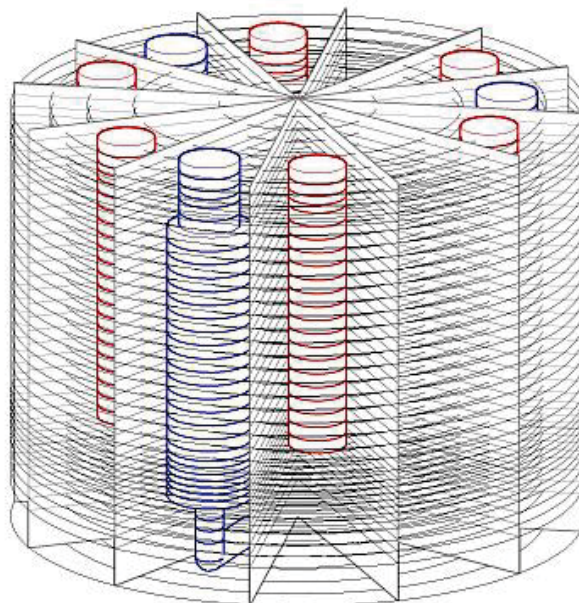
Fig. 3.9 – Scheme of MULTID component for porosity factor
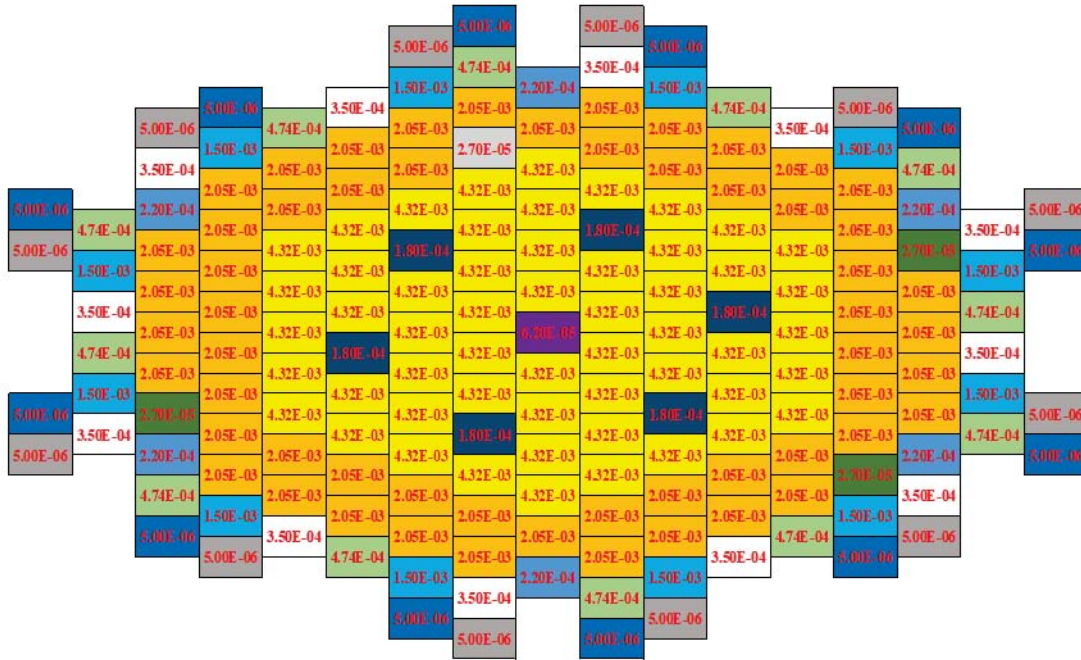
Fig. 3.10 – SAs inlet area (m²)
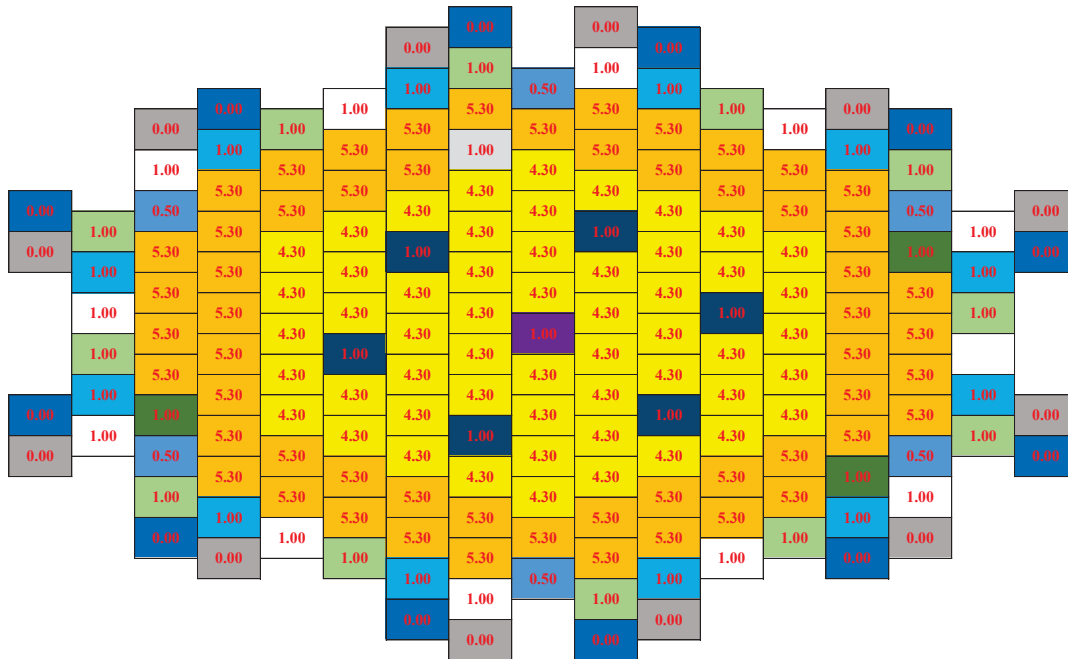
Fig. 3.11 – SAs inlet K loss
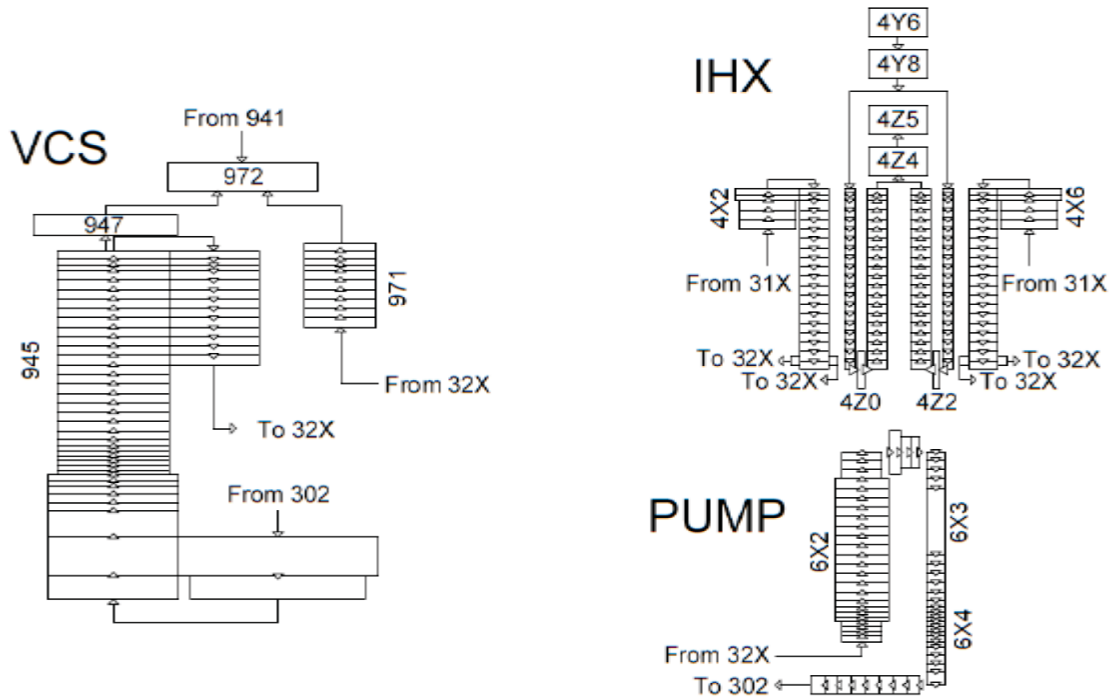
Fig. 3.12 – Pumps, IHXs and VCS nodalization scheme
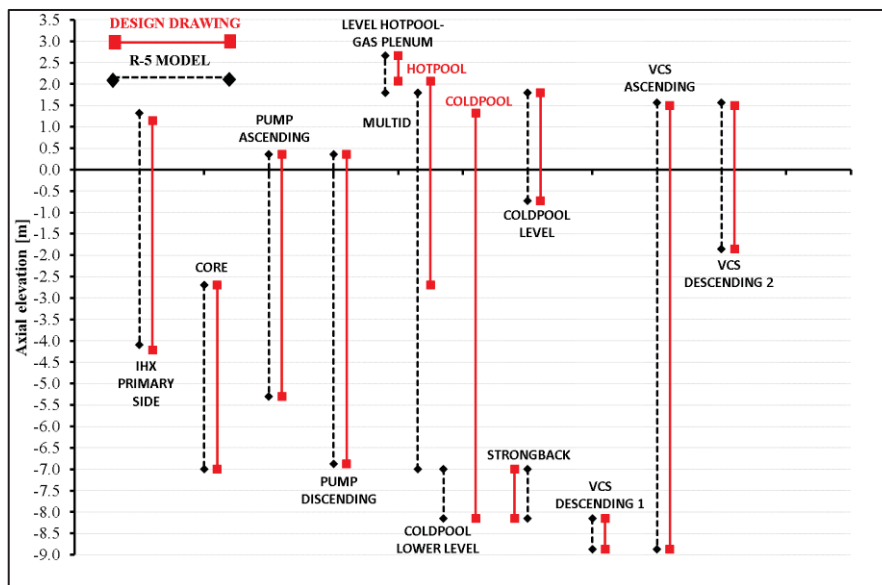
Fig. 3.13 – Comparison of the model and design relevant height
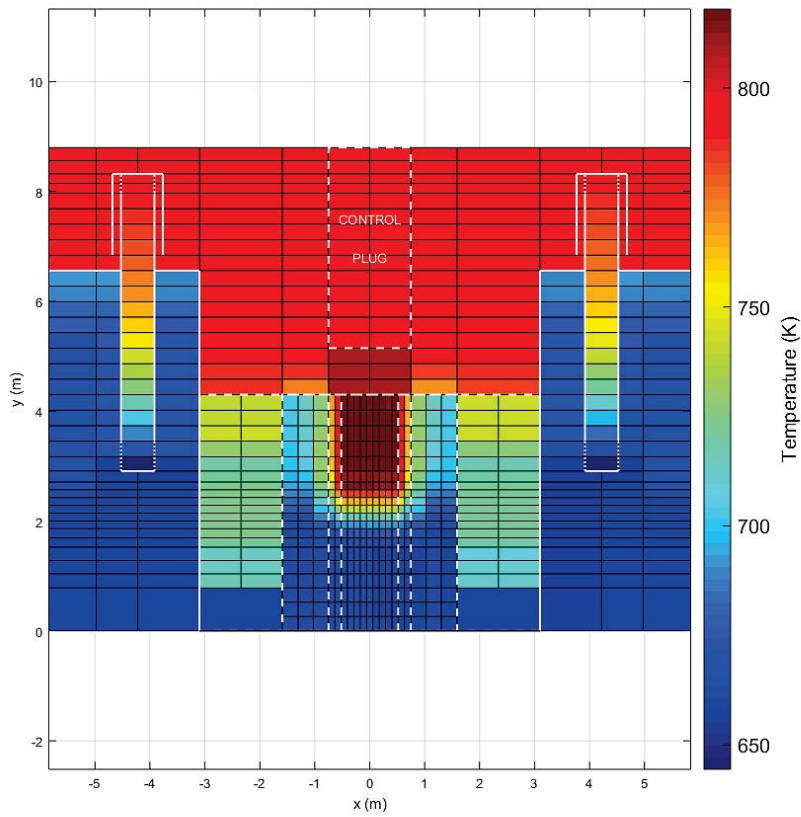
Fig. 3.14 – Steady state conditions
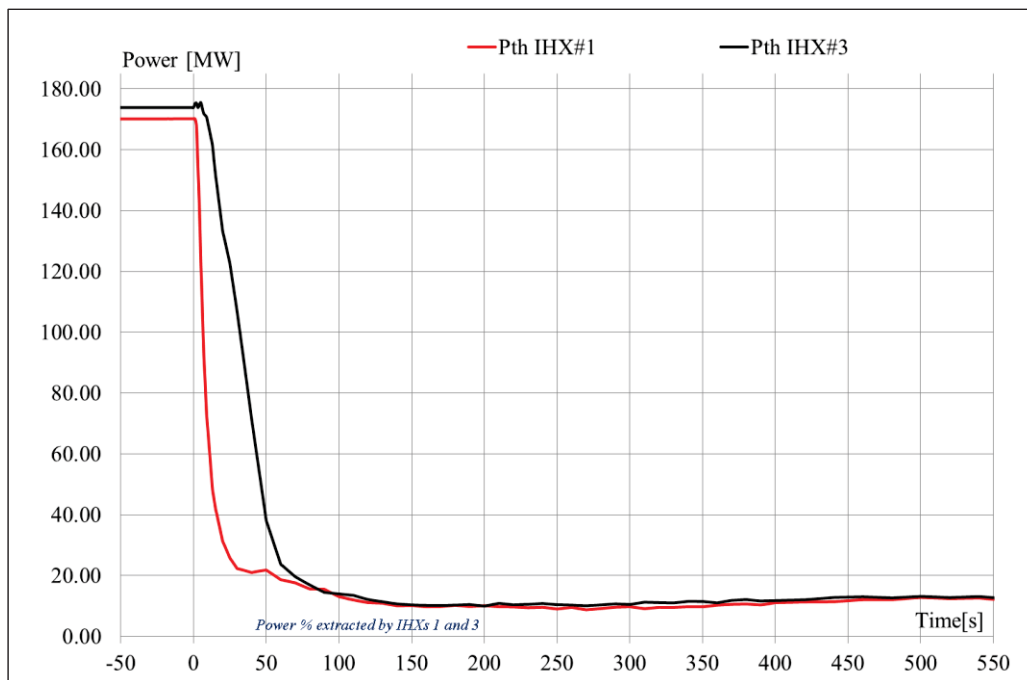
Fig. 3.15 – Power removed by IHXs
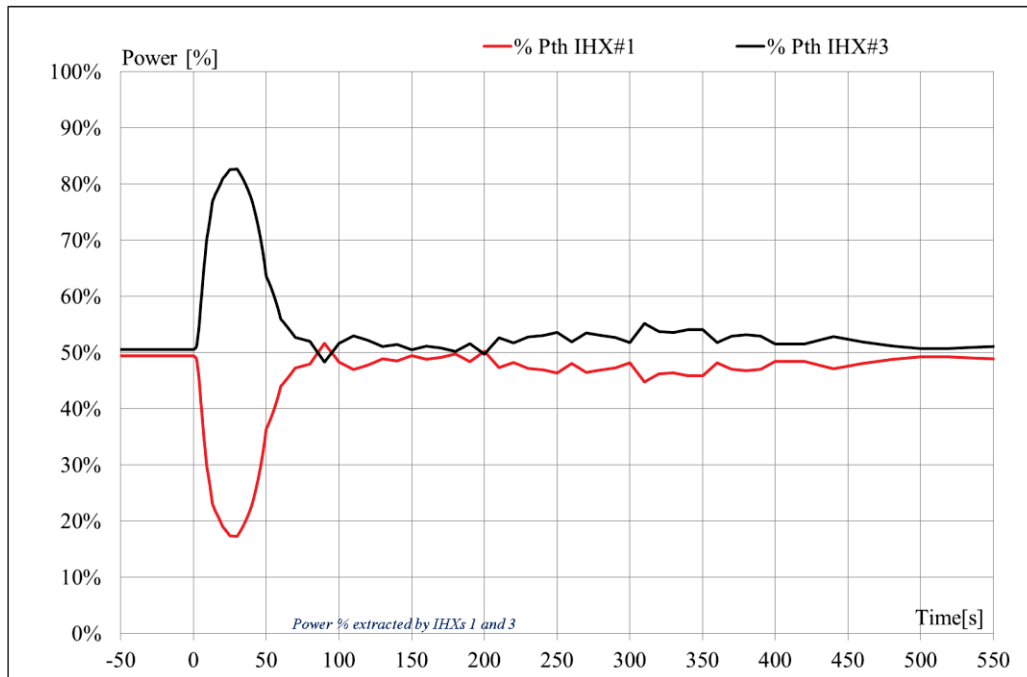
Fig. 3.16 – Power % removed by IHXs
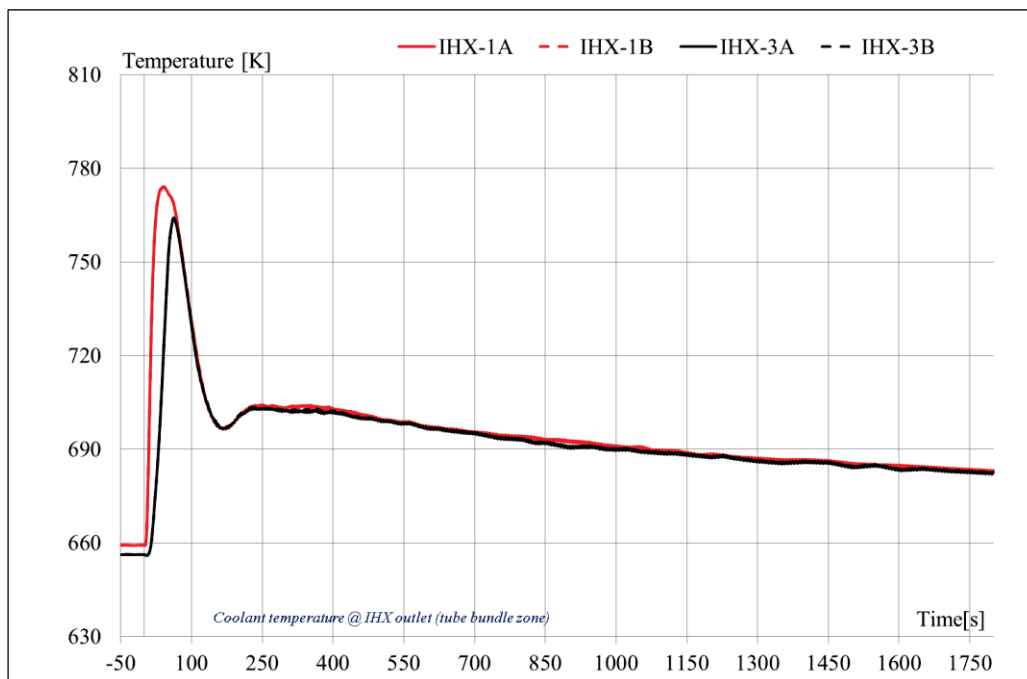
Fig. 3.17 – IHXs outlet coolant temperature
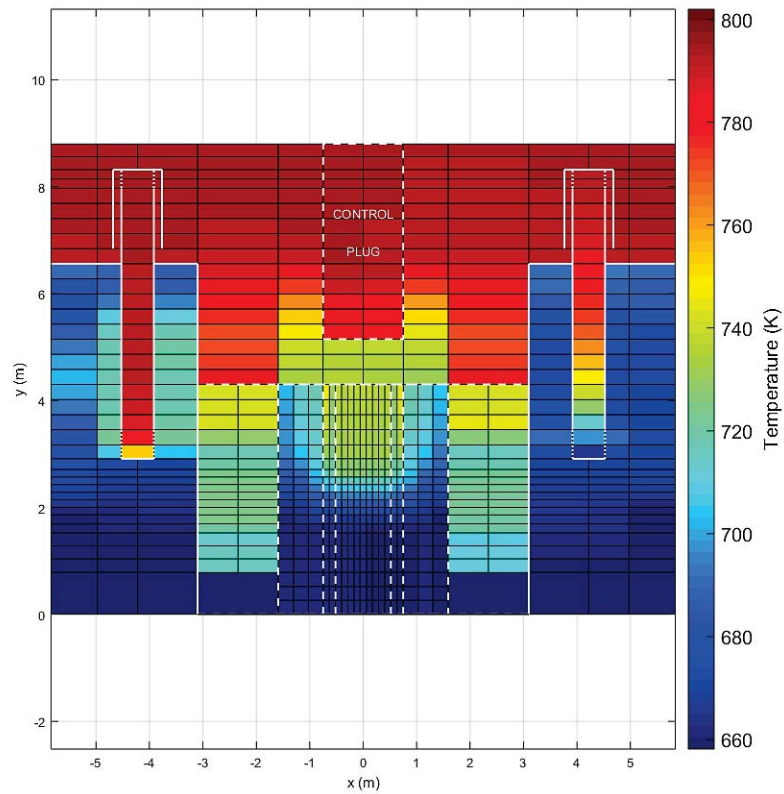
Fig. 3.18 – Transient conditions
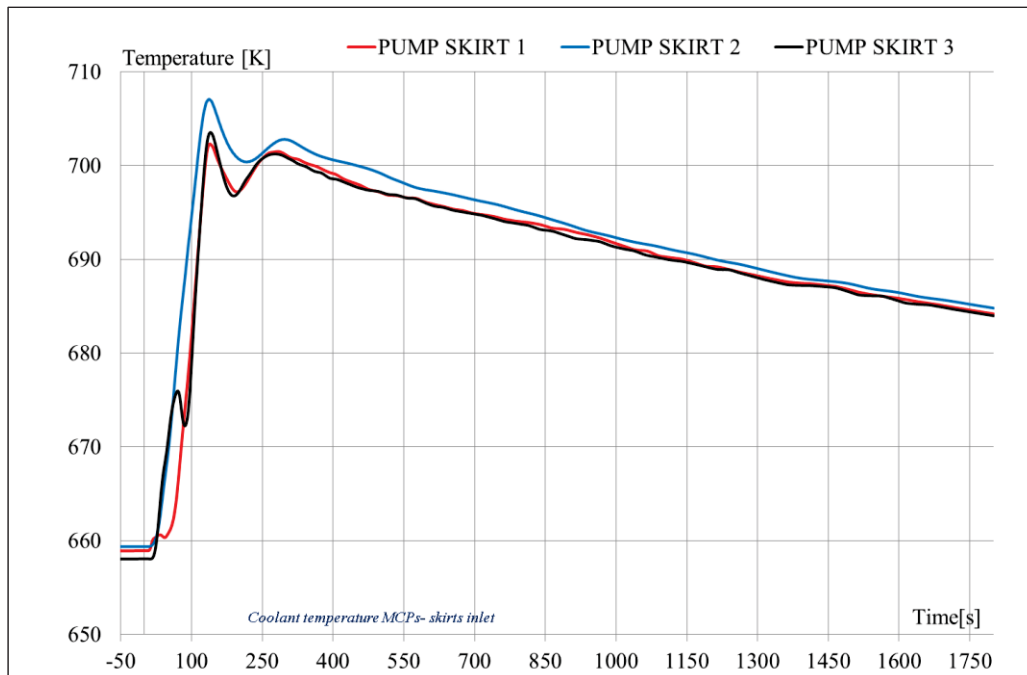
Fig. 3.19 – Primary pumps inlet temperatures
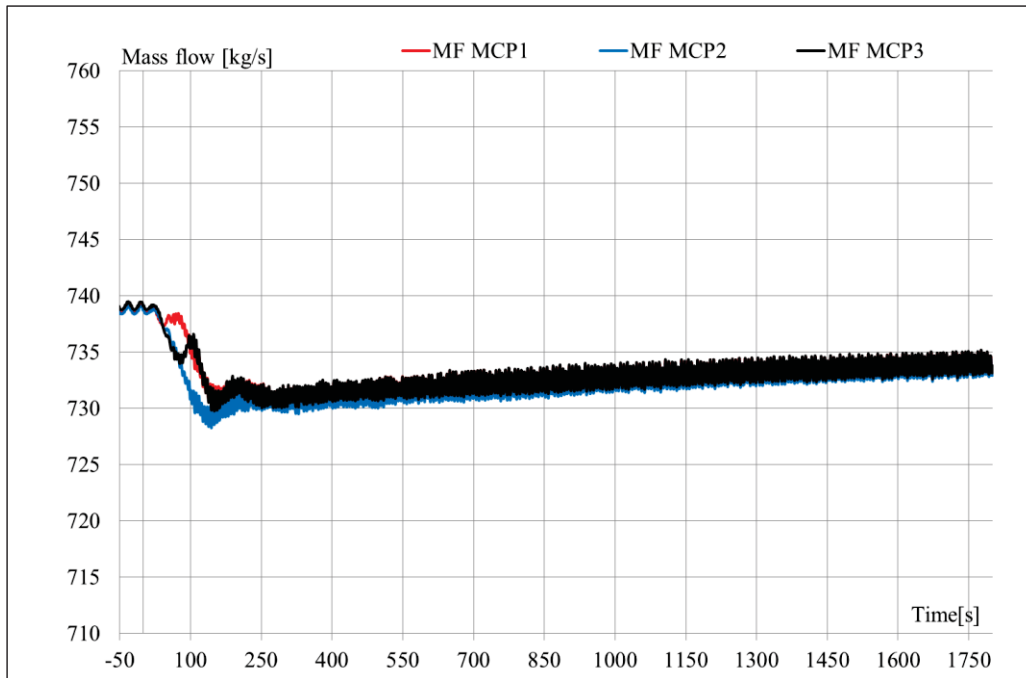
Fig. 3.20 – Primary pumps mass flow rate
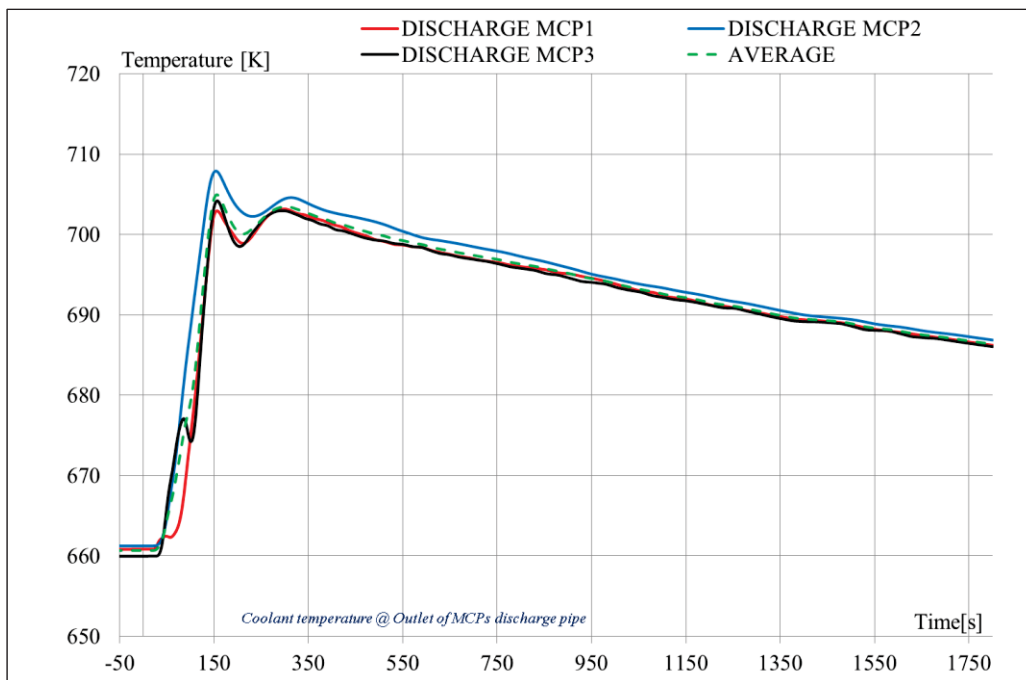
Fig. 3.21 – Core inlet temperature
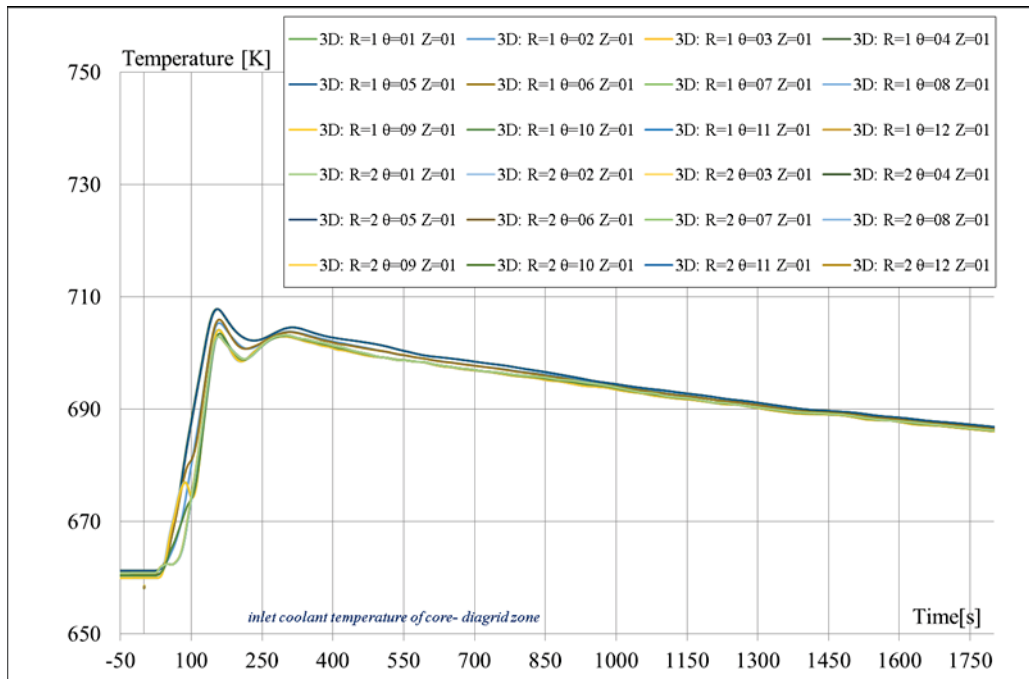
Fig. 3.22 – Core inlet temperature: azimuthal distribution
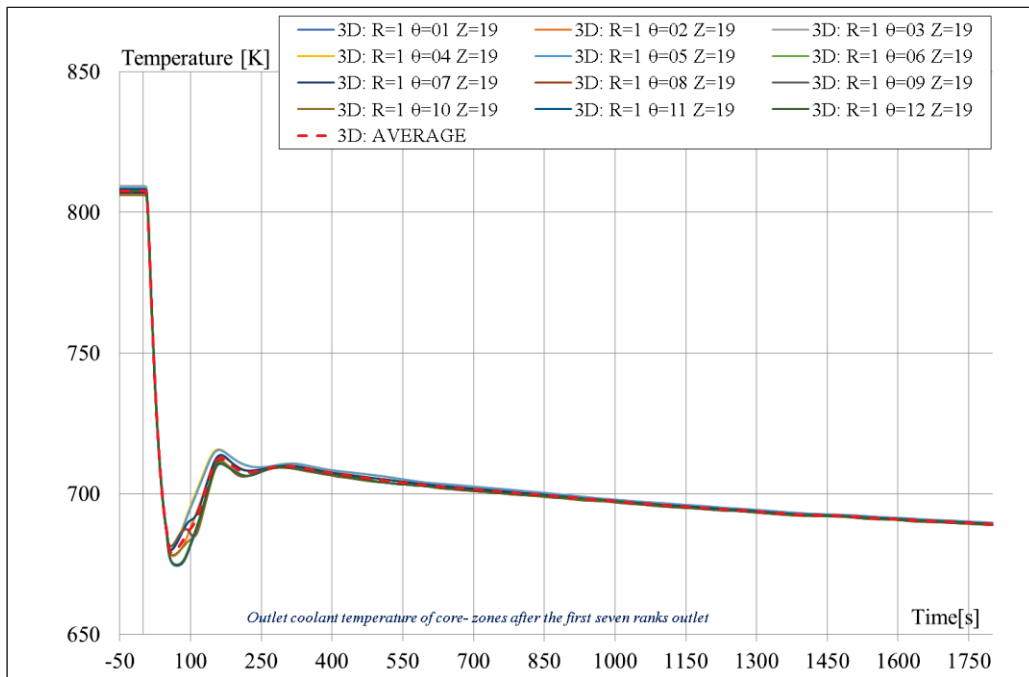
Fig. 3.23 – Core outlet temperature
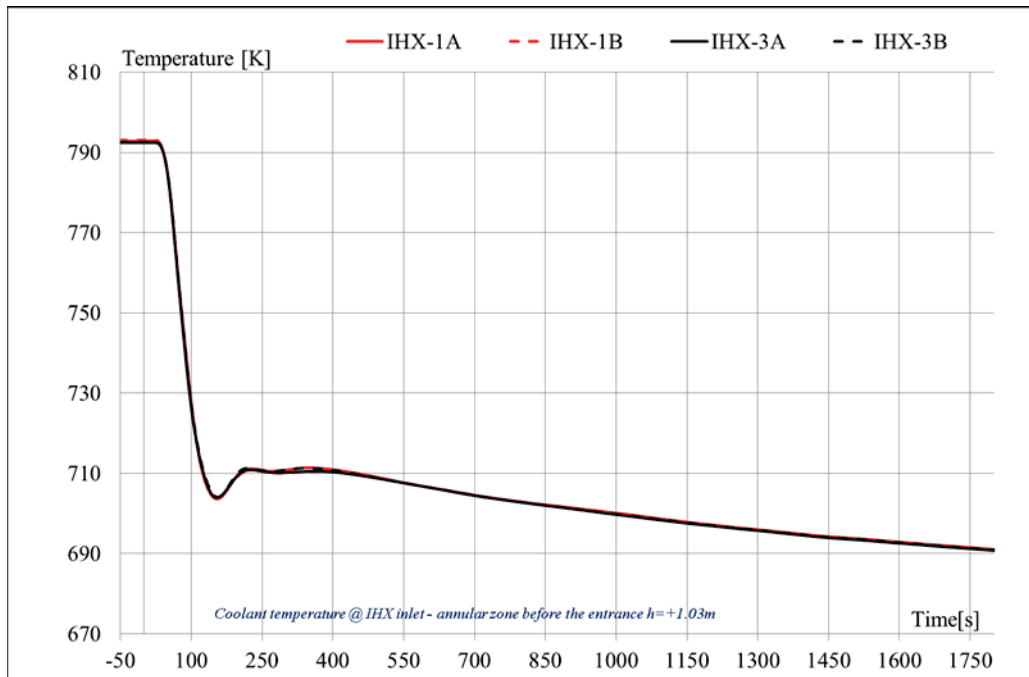
Fig. 3.24 – IHXs primary inlet temperatures
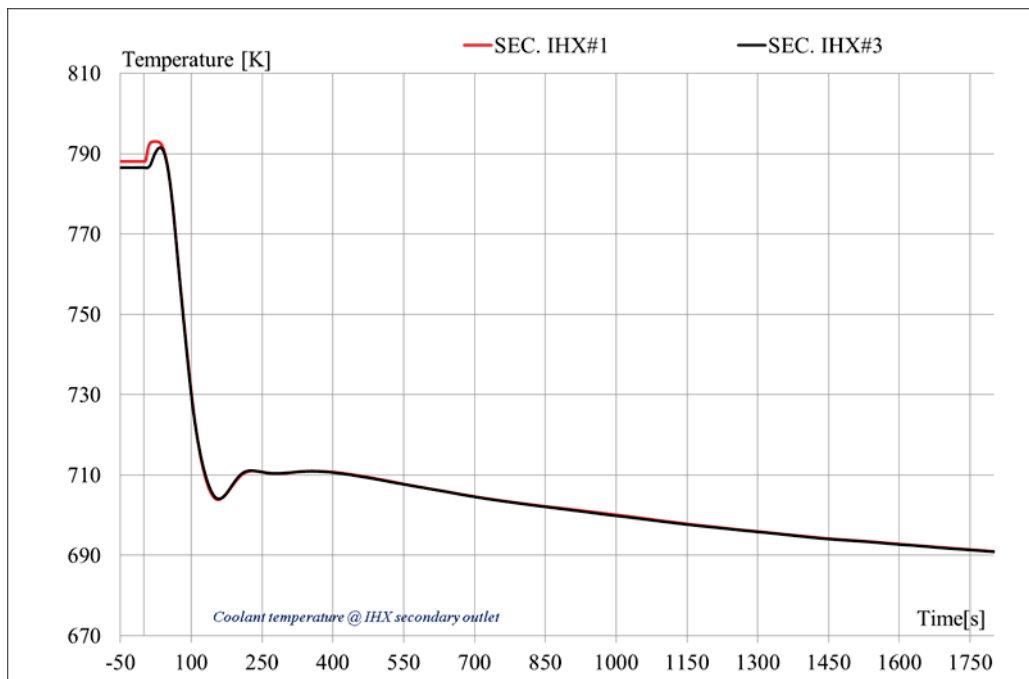
Fig. 3.25 – IHXs secondary outlet temperature
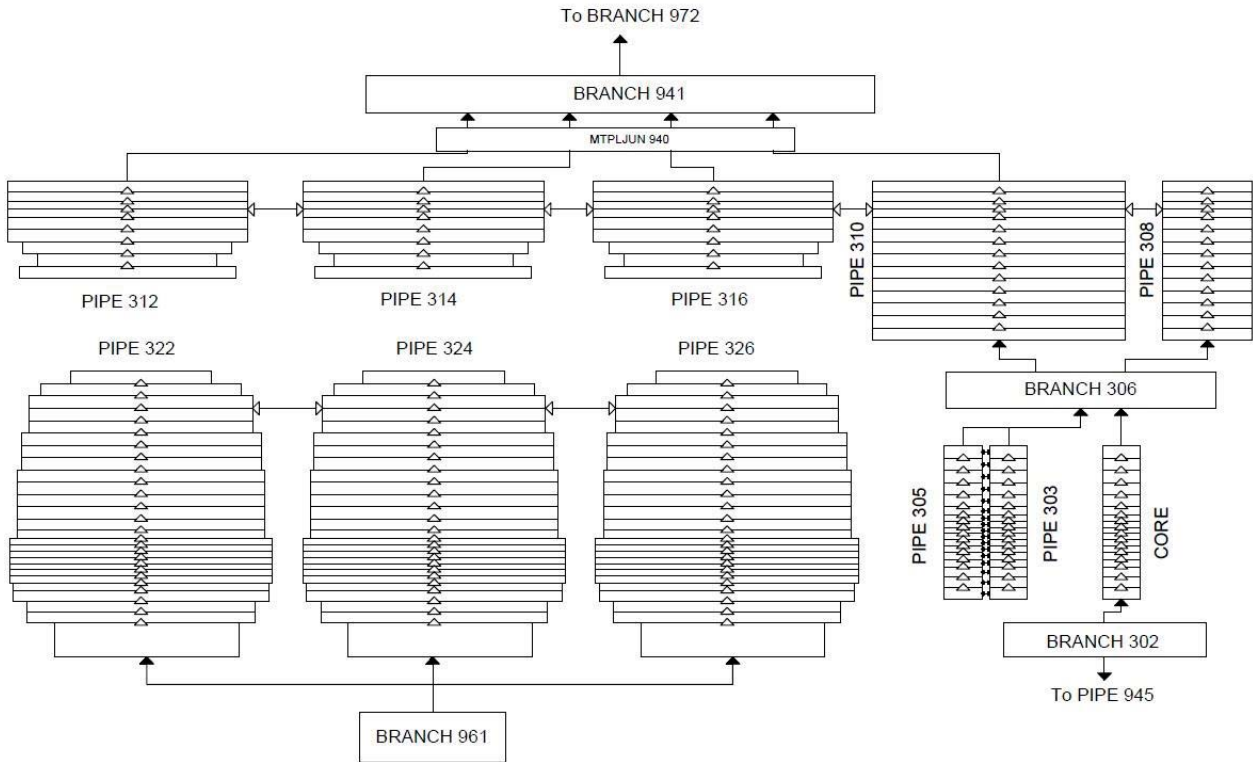
Fig. 3.26 – 1D model: Hot/cold pool, bypass and diagrid nodalization
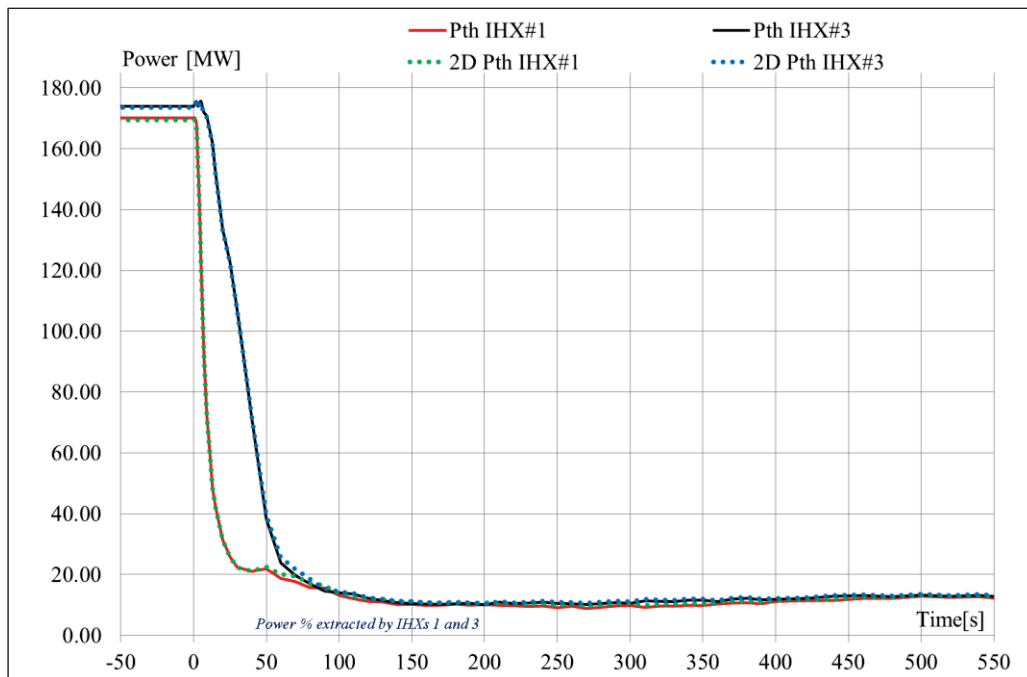
Fig. 3.27 – 1D-3D comparison-Power exchanged through IHX
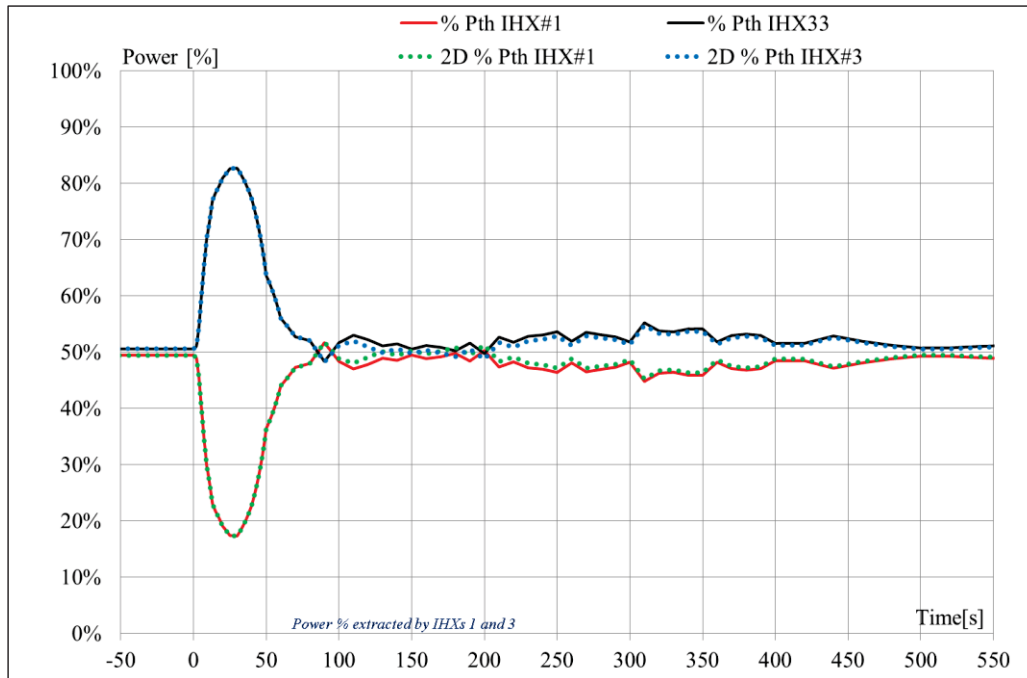
Fig. 3.28 – 1D-3D comparison- Power exchanged through IHX (% of the total)
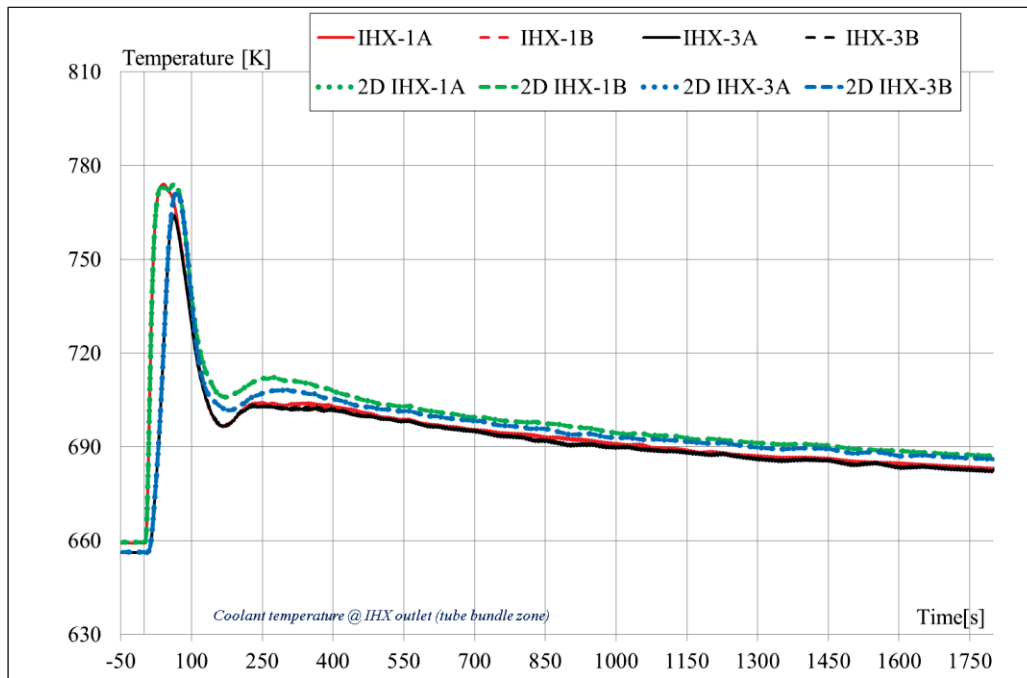
Fig. 3.29 – 1D-3D comparison- IHXs primary outlet temperature
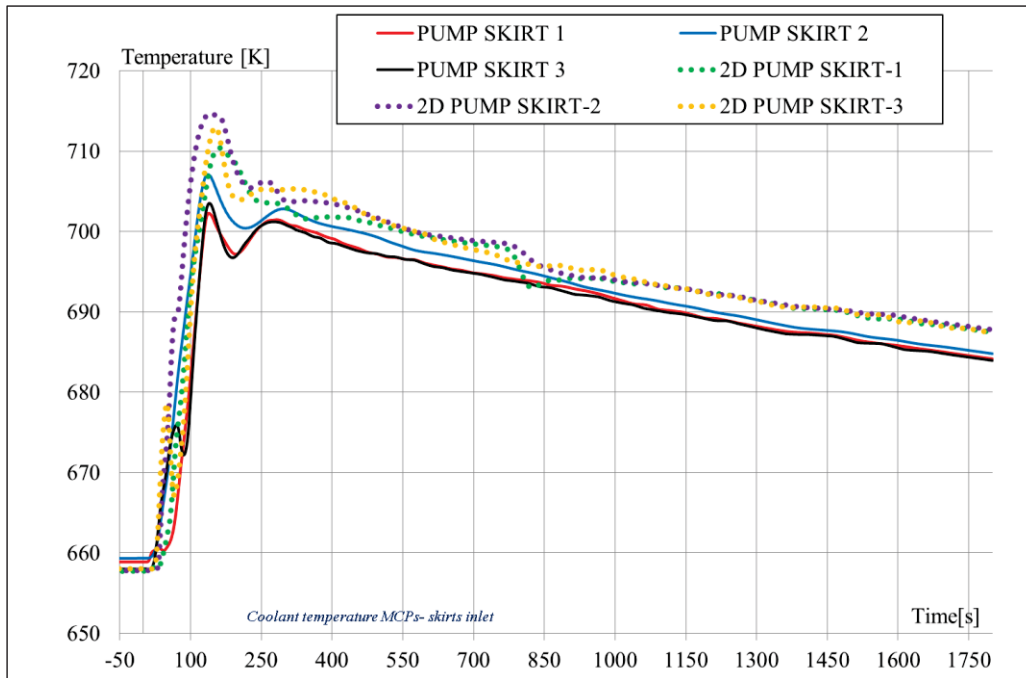
Fig. 3.30 – 1D-3D comparison- Primary pumps inlet temperatures
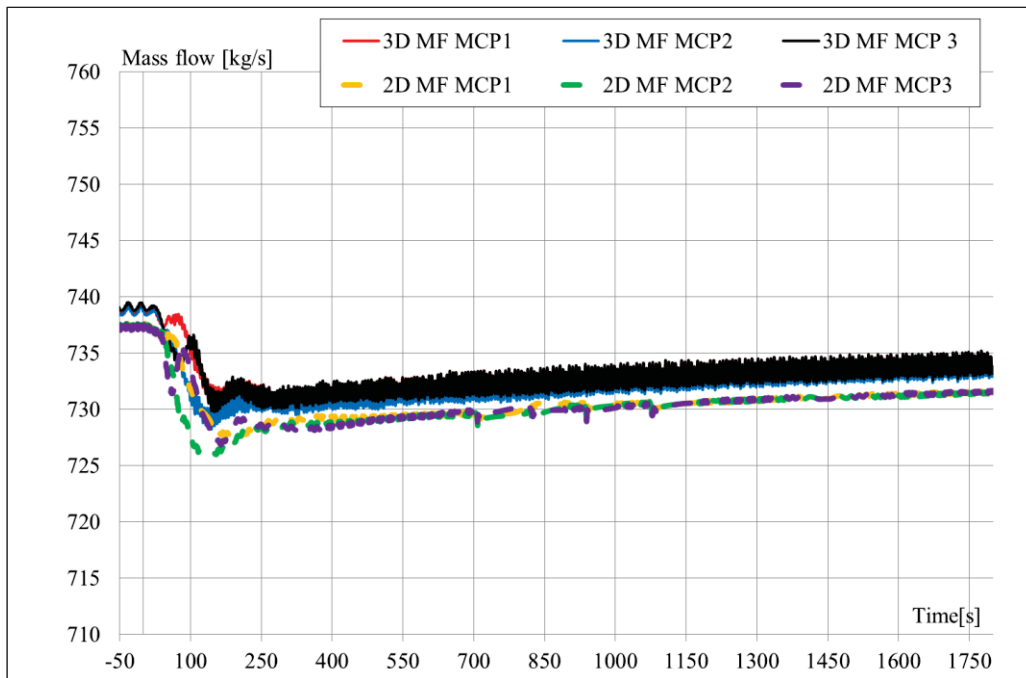
Fig. 3.31 – 1D-3D comparison- Primary pumps mass flow rate
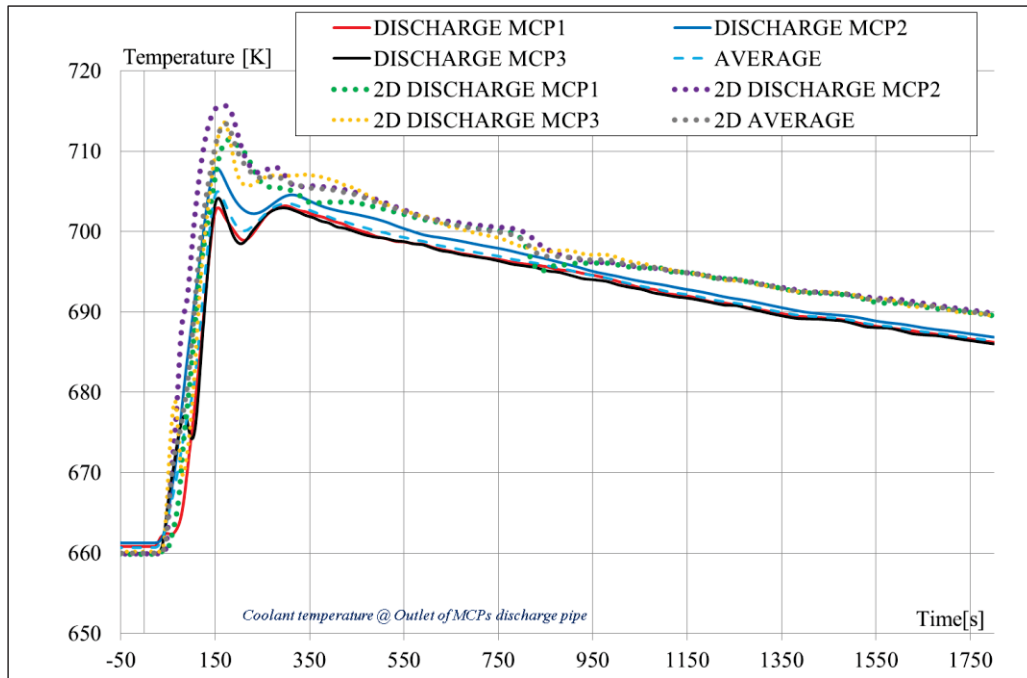
Fig. 3.32 – 1D-3D comparison- Core inlet temperature
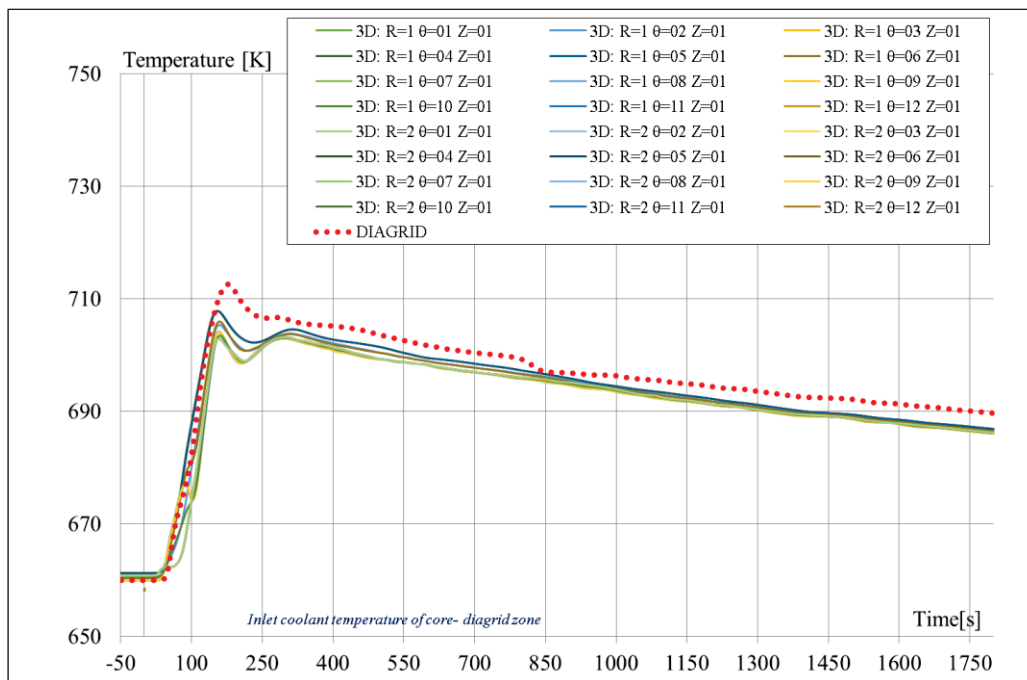
Fig. 3.33 – 1D-3D comparison- Core inlet temperature-diagrid zone
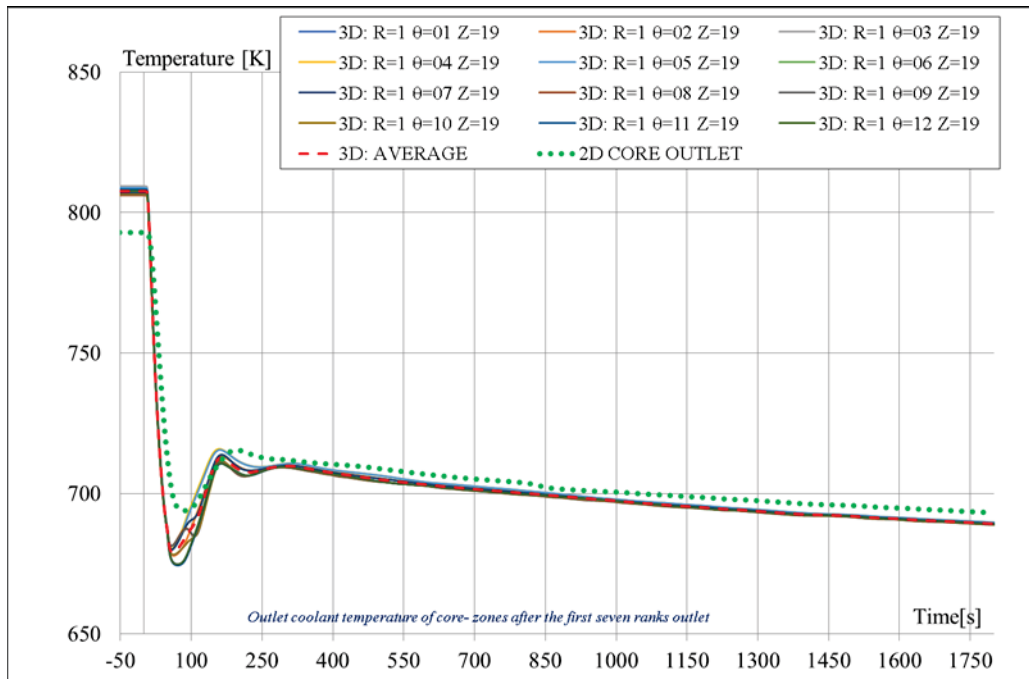
Fig. 3.34 – 1D-3D comparison- Core outlet temperature
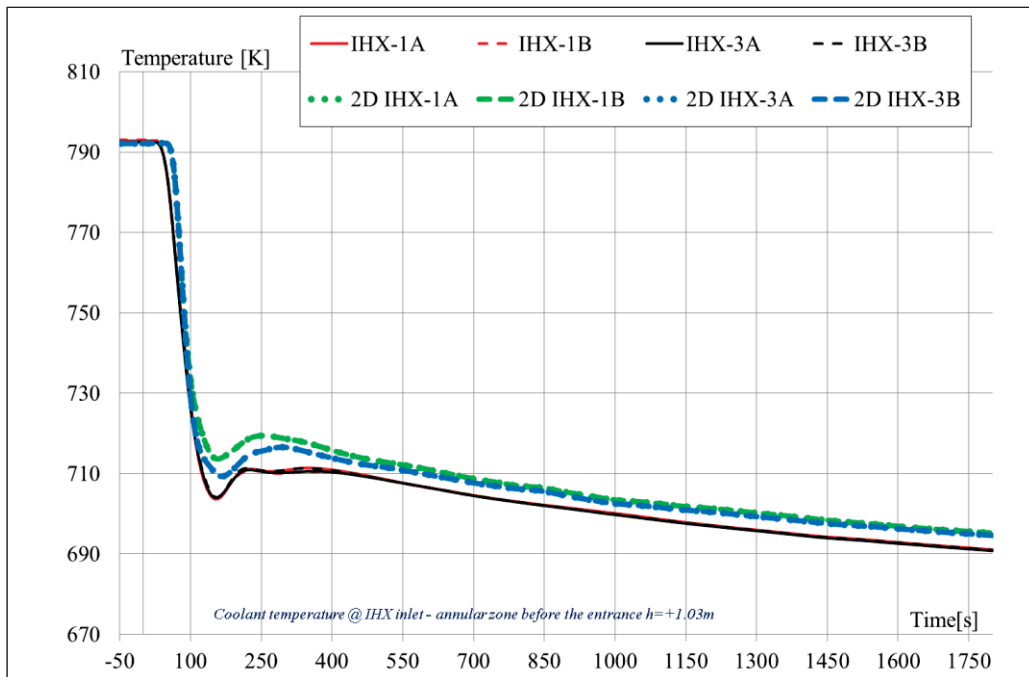
Fig. 3.35 – 1D-3D comparison- IHXs primary inlet temperatures
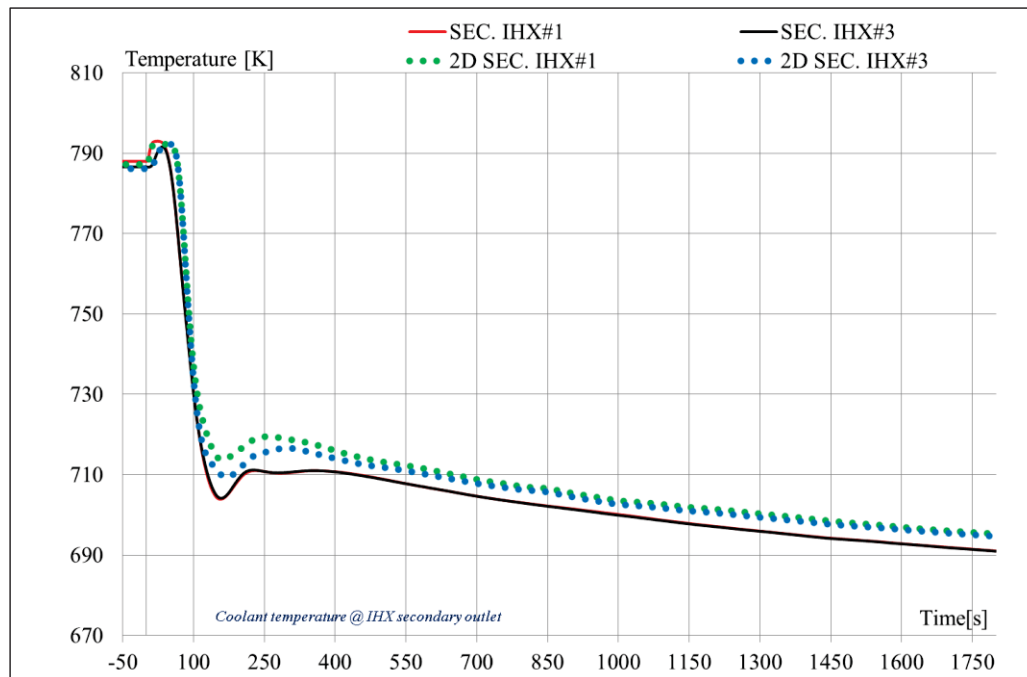
Fig. 3.36 – 1D-3D comparison- IHXs secondary outlet temperature

3.4   List of References

[3.1]   A. Del Nevo, A. Subioli, V. Narcisi, F. Giannetti, *Application of RELAP5-3D on Phenix Experimental Test*. Tech. Rep., ADPFISS – LP2 – 144, 2017.

[3.2]   OECD NUCLEAR ENERGY AGENCY – GIF, *GIF Annual Report 2017*. Tech. Rep., 2017.

[3.3]   B. Grosjean, S. Li, *PHENIX dissymmetric test description*. Tech Rep., 2016.

[3.4]   F. Giannetti, V. Narcisi, A. Subioli, A. Del Nevo, *Phénix transient analysis for the assessment of RELAP5-3D based on dissymmetric test benchmark*. Proc. Of the 26th Int. Conf. on Nucl. Eng. – ICONE26, London, England, July 22-26, 2018. DOI: 10.1115/ICONE26-82419.

[3.5]   J. F. Sauvage, *Phénix 35 years of history: the heart of a reactor*. CEA-EDF, 2004.

[3.6]   IAEA, *Benchmark Analyses on the Control Rod Withdrawal Tests Performed during the PHÉNIX End-of-Life Experiments*. Tech. Rep – TECDOC-1742, 2014.

[3.7]   IAEA, *Benchmark Analyses on the Natural Circulation Test Performed During the Phenix End-of-Life Experiments*. Tech. Rep – TECDOC-1703, 2013.

[3.8]   A. Vasile et al., *The Phénix final tests*. Proc. of Int. Congress on Advances in Nuclear Power Plants – ICAPP 2011, Nice, France, May 2-5, 2011, pp. 11298.

[3.9]   INL, *The RELAP5-3D© Code Development Team, RELAP5-3D© Code Manual Volume II: User's Guide and Input Requirements*. INL/MIS-15-36723, Revision 4.3, October 2015.

[3.10]   INL, *The RELAP5-3D© Code Development Team, RELAP5-3D© Code Manual Volume IV: Models and Correlations*. INL/MIS-15-36723, Revision 4.3, October 2015

[3.11]   A. Del Nevo, E. Martelli, *Validation of a Three-Dimensional Model of EBR-II and Assessment of RELAP5-3D Based on SHRT-17 Test*. Nuc. Tech. Vol. 193, pp 1–14, Jan. 2016. https://doi.org/10.13182/NT14-152

[3.12]   W. Pfrang, D.Struwe, *Assessment of Correlations for Heat Transfer to the Coolant for Heavy Liquid Metal Cooled Core Design*. FZKA 7352, October 2007

[3.13]   Giannetti, F., Vitale Di Maio, D., Naviglio, A., Caruso, G. *Thermal-hydraulic analysis of an innovative decay heat removal system for lead-cooled fast reactors* (2016) Nuclear Engineering and Design, 305, pp. 168-178.

4 VALIDATION OF FEM-LCORE / CATHARE BY TALL 3D EXPERIMENTAL TESTS

A. Chierici, L. Chirco, R. Da Vià, F. Franceschini, V. Giovacchini, A. Cervone, S. Manservisi

(Page intentionally left blank)

4.1   Introductory remarks

In this report we develop the software OpenFoam-FEMLcore-TrioCFD-Cathare platform in the framework of the open-source SALOME platform. The implementation of the OpenFoam software completes the thermohydraulic platform for Lead-cooled Fast Reactor (LFR) of Generation IV with open-source and CEA software. The purpose is to simulate and validate the evolution of different thermo-hydraulic tests with natural circulation flow performed in the experimental TALL-3D facility. We consider the semi-blind test TG03S301(03) by using a defective coupling algorithm with overlapping meshes. In this unprotected loss of flow the system is initially in fully working conditions then the pump is stopped while the supplied power goes on. We use a one-dimensional model of the main circuit described by Cathare code and the three-dimensional test section simulated with OpenFoam and TrioCFD codes. In order to evaluate the behavior of the coupling system we have studied the system by using two-equation turbulence model κ-ω and κ-ε inside Open-Foam and a modified κ-ε model implemented inside TrioCFD.

4.1.1   The OpenFOAM-Salome-FemLCore-Cathare computational platform for LFR

Generation IV reactors, in order to achieve the safety goals and maintain economic competitiveness, employ complex designs with many passive safety systems. The coupling between piping in forced motion and pools in natural circulation leads to the development of complex phenomena. For this reason one needs computationally efficient and sufficiently accurate tools for thermal-hydraulic and safety analysis. One-dimensional System Thermal Hydraulics (STH) codes are not accurate for resolving complex transients with mixing and stratification while Computational Fluid Dynamics (CFD) codes are computationally too expensive for resolving large domains. Development of coupled STH and CFD codes is considered in this work, where a multi-scale and multi-physics platform has been developed with joint effort between ENEA and UNIBO. This platform is capable of 1D-3D multi-scale coupling between open, research and commercial codes. The developed software is used in this report to study the TALL-3D facility. This platform mimics for Lead-cooled Fast Reactors (LFR) an existing numerical platform, the NURESAFE platform, developed by the CEA for coupling different codes in the study of a new design of light water reactors (LWR). The CEA software is not open source but it is based on SALOME platform, which is indeed an open-source software [4.10],[4.8]. The SALOME platform brings several computational and visualization tools. Inside this well-known framework we have used the open-software platform to add new codes and develop coupling interface compatible with open and closed source codes. In this work we have added the capability to operate with the code OpenFoam and use well tested turbulence models [4.11],[4.12].

4.2   Validation of the platform coupling model by TALL-3D facility experimental tests

4.2.1   TALL-3D facility

Overall view of the experimental facility. A general schematic of the experimental TALL-3D facility is reported in Fig. 4.1 on the left with its geometrical dimensions on the right. It consists of a liquid Lead Bismuth Eutectic (LBE) primary loop, an oil-cooled secondary loop, a differential pressure measurement system and a pressurized service loop. Pressurized service loop, preheating system, and data acquisition system (DAS) are not shown in Fig. 4.1. The primary loop operates above LBE melting point $125°C$, in the following ranges of the dimensionless quantities: $Re = \rho v / \mu$ from 0 to 140000, $Pr = C_p \mu / k$ from 0.020 to 0.045, $Pe = RePr = vL/\alpha$ from 0 to 350. The total height of the facility is about $6.5m$. The secondary loop is used to control heat balance in the primary loop and is equipped with automatic temperature control system.

All facility components that come in contact with LBE are made of 316L stainless steel and during actual tests only differential pressure measurement system is continuously heated up. Total electric power is about $80kW$, including Main Heater (MH, $27kW$) and the heater of the test section ($15kW$). The maximum measurable LBE mass flow rate is $5kg/s$ in forced circulation and $0.6kg/s$ in natural circulation in the Heat Exchanger (HX) leg. The maximum LBE temperature is $460°C$ in the hot side and $350°C$ in the cold side.

The secondary loop can operate at temperatures from 50 to 300°C. Maximum temperature difference across the heat exchange is 90°C. The static pressure at the top is 1.3*bar* and at the bottom is 7.8*bar*. The maximum hydrostatic head from the EPM pump is 2*bar*. The maximum values are provided assuming 5*kg/s* mass flow rate and 350°C LBE flow temperature. The minimum value is taken for stagnant flow at 150°C. Dedicated DAS system is implemented for control of the facility and data logging. The DAS system uses Beckhoff hardware and software in conjunction with LabVIEW-based interface and driving logic. The total number of control and data acquisition channels is 589. For details on TALL-3D facility the interested reader can see [4.13]-[4.16].

Primary loop. Thermal hydraulics of the primary loop is the main subject of modeling and data from the primary loop obtained in the experiments is used for calibration and validation of the codes. The primary loop, as shown in Fig. 4.1, consists of the sump tank used to supply LBE into the main loop, three vertical legs and two connecting horizontal sections. The geometrical dimensions are on the right in Fig. 4.1. The distance between the adjacent vertical legs is 0.74*m* and the distance between the horizontal sections is 5.83*m*; the nominal pipe Inner Diameter (ID) is 27.86*mm*. The Main Heater (MH) leg (left) accommodates two components: the pin-type 27*kW* electric heater (in the lower part) and the expansion tank (on the top). The expansion tank has two main purposes: keeping loop pressure during temperature induced deformation of the loop components including LBE volumetric expansion and monitoring the loop LBE level. The Heat Exchanger (HX) leg consists of two parts: the counter-current double-pipe heat exchanger placed at the top and the Electric Permanent Magnet (EPM) pump used for forced circulation of LBE. The heat exchanger is the common component for primary and secondary sides. The 3D leg, placed in the middle of the sketch, connects a pool-type 3D test section to the loop. Depending on flow characteristics, the LBE inside the test section can undergo thermal mixing or stratification. Transition to mixing is the phenomenon that cannot be modeled by a standalone STH code and can only be captured applying CFD tools. Therefore, the test section constitutes the CFD domain of the facility, while the rest of the loop belongs to the STH domain. The boundaries between the domains are defined at the inlet and outlet of the test section. In particular, boundary conditions are taken at two heights in the middle leg: 1211*mm* and 2111*mm*. The data that are continuously monitored for these boundaries include the LBE flow temperature, the differential pressure over the domain and the LBE mass flow rate. Common flow direction in the primary loop is downwards in HX leg, upwards in the MH leg and upwards in the 3D leg. Therefore, the loop section below the heat exchanger up to the 3D test section and the main heater is often referred to as the cold side of the main loop. The part of the loop above the 3D test section and the main heater is called the hot side of the main loop. LBE mass flowmeters as temperature sensitive equipment are located in the cold side. Vertical legs are equipped with ball valves for fine tuning of the hydraulic resistances and to provide possibility to cut off a specific leg. Elevations of the main loop components are provided in Fig. 4.1 on the right. These elevations are used in the nomenclature for instrumentation and equipment. LBE flow temperature around the loop is measured at 23 locations. The list of primary loop inflow TCs is given in Tab. 4-1. Differential pressure can be measured around any of the 12 primary loop sections. During loop operation temperatures up to 500°C, pressures up to 0.7*MPa* and flow rates up to about 5*kg/s* can be achieved in HX leg with corresponding flow velocity of approximately 1.7*m/s*. All parts of the installation that come into direct contact with LBE are manufactured from SS-316L to ensure its corrosion and erosion resistance. Oxygen control system is implemented to monitor chemical potential of the LBE dissolved oxygen. It is required to stay within $1.5 \times 10^{-7} - 1.85 \times 10^{-5} wt$ to stabilize the protective oxide layer on the LBE wetted components. The sensor is with yttrium stabilized zirconia membrane and oxygen saturated Bi reference. The minimal operation temperature is determined by the membrane permeability which becomes active at 360°C, though the recommended temperature interval is 400-450°C. A pre-oxidation procedure was carried out for 48 hours to form such a layer prior to filling of the loop with LBE [4.13]-[4.16].

Secondary loop. The secondary loop, which uses Dowtherm RP heat transfer fluid, is used to balance heat in the primary loop during operation. With reference to Fig. 4.1, the direction of the flow is clockwise, namely the pump supplies the fluid from the oil tank to the main loop heat exchanger, it then passes through

the secondary heat exchanger, and back to the oil tank. The potential heat removal capacity of the secondary loop is 40*kW* but it is limited by the primary heat exchanger to about 10*kW*. A bypass line, normally closed during tests, is used to filter the fluid when necessary [4.13],[4.14].

The oil tank is equipped with a 2*kW* heater, which is used in conjunction with the secondary heat exchanger to control the temperature of the secondary fluid at the outlet of the oil tank. The oil tank is located about 20*cm* above the oil pool where the space is pressurized with inert gas to about 1.5*bar* used as a buffer to maintain the secondary loop pressure. Total volume of the heat transfer fluid circulating in the secondary side is about 35*l*. The actual flow rate depends on the oil pump power and the fluid temperature. It is important to remark that the secondary loop does not have flow measurement equipment and the maximum flow rate is not expected to exceed 50*l/min*. Temperature can be measured at seven locations around the secondary loop in addition to the TCs located inside the primary heat exchanger. The loop is thermally insulated and there are no TCs measuring the temperature of the pipes or thermal insulation [4.15],[4.16].

4.2.2   Thermohydraulics model of the TALL-3D facility.

Thermodynamical coupling and modeling. Thermal hydraulics of the primary-secondary loop and the 3D-test section is the main subject of the numerical test for the 3D-1D coupling and validation of the code interfaces. The series of tests that we consider are the TG03 and in particular TG03S301(03). We have the following tests available on TALL-3D facility [4.15],[4.16]:

- TG03S201 tests. This test is a forced to natural circulation transient with a closed 3D-legand a constant main heater power. In this test it is important to limit 3D effects for standalone STH code validation. By closing the 3D leg and circulating coolant through the main heater and heat exchanger legs we have essentially 1D flow data. STH codes are expected to be able to capture forced to natural circulation transients in loop-type configurations. This test is designed to study reverse flow and address stability as well.

- TG03S202 tests. This test is a natural to forced circulation transient with a closed 3D-leg and a constant main heater power. This test is suitable for standalone STH validation. The main difference with the previous test is that the timescale for this transition is much shorter because of the rapid flow stabilization by the pump. Dynamic effects of natural circulation are expected to be marginal and most important is to be the effect of thermal inertia.

- TG03S301 tests. This test is a forced to natural transient with both main heater and 3D test section heater at constant powers. Loss of flow transients are generally of interest since they can lead to flow oscillations between two parallel flow paths. Complex feedback between 3D phenomena and loop behavior can be expected including limit cycle oscillations (LCO).

- TG03S302 tests. This test is a forced to natural transient with main heater at constant power and 3D test section heater turned on at the time of pump trim. This test is similar to S301 with a difference in timescales. After the initial mass flow rate drop due to pump trip, the initially cold 3D test section pool starts to heat up. Flow inertia in the pool mixes the pool leading to a higher temperature at the bottom of the pool. During this time, the flow rate in the middle leg can become negative. Hotter liquid flowing out of the 3D test section inlet will determine the timing when the flow will accelerate in the 3D leg. This happens when the leg has sufficiently heated up. STH codes should have difficulties in predicting mixing and this type of transients.

- TG03S304 tests. This test is a natural to natural transient with the main heater at constant power and 3D test section heater turned off at the start of the test. In the initial steady state the flow is positive the main heater and 3D test section legs. When the 3D test section heater is turned off, hot LBE stored in the stratified layer will be gradually released from the section. The pool will start to cool down and finally the flow will be reversed. Dynamics of the stratified layer behavior in the pool will determine the timing of the flow reversal and will be challenging to predict for STH codes.

- TG03S305 tests. This test is a forced to natural transient where the main heater at constant power and the 3D pool heater is turned off. This test is similar to S304, with the difference that in the initial

steady state the pool is thermally mixed and the flow distribution between the legs is driven by forced circulation.

- TG03S307 tests. This test is a natural to forced transient where the main heater at constant power and the 3D pool heater is turned off. This is a thermal inertia dominated transient. Initially, the pool and its structures are very hot since the LBE flow rate is small and heater is on. Transient starts by turning on the pump and switching off the 3D heater. This leads to fast mixing of the pool and subsequent cool-down of the initially hot structures.
- TG03S310 tests. This test is a forced to natural transient with main heater at constant power and 3D test section heater turned off. 3D heater is not used in the transient. The effect of the 3D test section is expected to be small. The data can be potentially useful for STH stand-alone validation.
- TG03S312 tests. This test is a forced to natural transient with main heater switched off and 3D test section switched on at the time of the pump trip. This test is similar to S302 with the difference that the main heater is switched off at the start of the test. The flow in the 3D leg is expected to recover from initial stagnation after the pump trip much faster since there is no competition from the main heater leg. In the final steady state the flow in the main heater leg is expected to be negative.

These experiments define a good framework for testing and benchmarking for STH and CFD coupling simulations. In this work we focus on TG03S301 test series.

System Thermal Hydraulics (STH) modeling. The one-dimensional system code computation model is simulated with CATHARE 2.5 code [4.17]-[4.20]. The 1D model is shown in Fig. 4.6 and Fig. 4.7. As shown in Fig. 4.6 the left leg consists of the main heater and it is connected on the top to the main tank and on the bottom to the sump tank. The Main Heater is a rod-like electric heating element. The 1D model of the central vertical leg is shown in Fig. 4.6 in the center. This leg is the key part of the circuit for our test since it contains the 3D test section. It consists of three AXIALS: the ABOVE3D, BELOW3D and 3DPIPE module.

TALL-3D test section is an axial-symmetric cylindrical stainless steel vessel with an inlet at the bottom and an outlet at the top. The upper part of the test section is equipped with two line heaters rolled jointly around the circumference. The heaters enhance the development of thermal stratification in the LBE pool. As one can see in Fig. 4.7 on the right we consider six reference points labeled by S1, S2, S3, S4, S5 and S6. The points S1 and S2 are located along the left vertical leg. The point S1 is in the COR module at the element mesh 3.

We denote such point with COR3 or S1. The point S2 is inside the RESERVE module at the element mesh 4. We denote such point with RESRVE4. The points S3 and S4 are located in the central vertical leg. The point S3 is in the BELOW3D module at the element mesh 25. The point S2 is inside the ABOVE3D module at the element mesh 8. We denote such points with BELOW3D24 and ABOVE3D8, respectively. Finally, the points S5 and S6 are located along the right vertical leg. The point S5 is in the LINUP2 module at the element mesh 14. The point S6 is in the PUMP module at the element mesh 0. In a similar way we denote such points with LINUP14 and PUMP, respectively. The top horizontal part of the LBE circuit, which is not shown, consists of the main expansion tank (labeled with TANK), two AXIALS (LINUP1, LINUP2) and a volume that links this part of the top LBE circuit to the central vertical leg with the three-dimensional test section. The TANK volume and the LINUP2 are connected with the left (with the MH) and right vertical leg (with HX), respectively. The expansion tank is used to monitor the LBE level in the loop and maintain loop pressure during temperature induced deformation along the loop components. The bottom horizontal part of the LBE circuit, which is not shown, consists of two axial modules (LINDOWN, DOWNPUMP) and a volume module (VOLDOWN) which links the bottom to the central vertical leg with the three-dimensional test section. The ICoCo class main functions are defined in Tab. 4-2. The class is constructed with the new Problem_Cathare() constructor which generates the problem ICoCo pointer object. The initialization and the end of the problem is controlled by the initialize() and terminate() function, respectively. The solution of the problem is defined by the initTimeStep(), computeTimeStep() and abortTimeStep(). The initTimeStep()

function sets initial conditions. At each time step the solution is computed with computeTimeStep() and after an analysis test the result can be refused or accepted with the abortTimeStep() command.

The main interface functions of the ICoCo class are defined in Tab. 4-3. The ICoCo allows the data exchange of pressure, temperature and velocity field so that Cathare solution can be extracted or added. The function getValue_cathare("variable","sub-mesh", np, 0) gets the value of the required variable from sub-mesh at point np. The temperature, pressure and mass flow can be therefore known at each point (np) of the one-dimensional mesh. The function setValue_cathare("variable","sub-mesh", np, 0,value) sets that value at variable over the sub-mesh at point np. Both momentum and energy equation have a source term at each mesh that can be modified to force boundary values. DPLEXT and ENTLEXT are the momentum and energy equation source respectively. We use a defective algorithm to impose boundary conditions through these sources.

OpenFOAM TALL-3D test modeling. TALL-3D test section is an axial-symmetric cylindrical stainless steel vessel with an inlet at the bottom and an outlet at the top. The dimensions of the test section and thermal insulation are provided in Fig. 4.8. On the bottom of Fig. 4.9 the OpenFOAM geometry is reported. The Open-Foam code is an open-source software that offers a great variety of models [4.11],[4.12]. This code is now part of the computational platform integrated in the SALOME software. In OpenFOAM code the mesh of an axial-symmetric input geometry should be three-dimensional, one element thick, with angle of 5° and wedge boundary conditions on the axial symmetric surfaces. The mesh used for OpenFOAM is in *unv* format that can be generated from the SALOME mesh generator. The command IdeasUnvToFoam converts the format *unv* to *foam*. The coupling of OpenFoam code is obtained by an interface built on a class, called OFclass, which has been developed over the SALOME platform. The OFclass main functions are defined in Tab. 4-4.

The class is constructed with the OF() constructor which passes the runTime and mesh main OpenFOAM objects. The initialization of the state variable fields velocity, pressure and temperature is defined by the init_field(... ,m) function where the integer number specifies the solver PISO or SIMPLE. The Finite Volume Method needs the function reconstruction which is defined in init_surfaceScalarField(phi_f). The material properties are defined by using init_mat_trsp(...) and init_mat_trsp_var(...). The initialization through the first function defines constant properties only, while the use of the latter one allows modification of the properties as a function of temperature. The introduction of variable properties is needed for particular boundary conditions such as wall functions.

We recall that in OpenFoam the turbulence wall functions are defined through the variables ν_t and α_t. The turbulence model is selected by the function init_turbulence(turb_class). The selection may range from standard two-equation model κ-ω, SST-κ-ω and κ-ε to more sophisticated approximations. The mesh used is defined by setMesh("OFmesh.med","Fmesh.med") where the mesh in MED form for the OpenFOAM and FEMUS code can be used. The mesh for OpenFoam is always a tree-dimensional one while the axial-symmetric mesh for FEMUS is two-dimensional. In this case mesh maps are created between the MED and the original mesh formats. After initialization the exchanging data between them can be performed easily.

The OFclass allows the data exchange so that OpenFoam solution ϕ can be mapped into MEDField $\tilde{\phi}$. The main interface functions of the ICoCo class are defined in Tab. 4-5. The functions GetMedSolution(ϕ," ϕ",np) and SetMedSolution(ϕ," ϕ",np, $\tilde{\phi}$) are used for volumetric source field exchange over the whole domain defined by the mesh. The solution data can be also exchanged only over sub-meshes (geometric groups in *med* or *unv* format) where boundary conditions are defined. It is therefore possible to force or get the boundary condition from another code with GetMedSolution(ϕ," ϕ", np,mesh,"sub-mesh") and SetMedSolution(ϕ," ϕ",np,mesh,"sub-mesh") functions. Boundary conditions are defined by constructing a string wich is converted into an analytic expression by using

get_field_from_exp(on_node, 2, string). The field is returned as a MED field on nodes or over cells. The OpenFoam field ϕ can be integrated with the function get_integral(ϕ,np,"sub-mesh") to pass a scalar single value on the STH codes. The integration can be also performed on patch sub-meshes representing the boundary regions.

FEMLCORE TALL-3D test modeling (CFD). As shown in Fig. 4.10 TALL-3D test section is axisymmetric with an inlet at the bottom and an outlet at the top. The dimensions of the test section and thermal insulation are provided in Fig. 4.8. The mesh format of FemLCore is MED with data in HDF5 storage format. The axial-symmetric mesh can be generated as a two-dimensional one from SALOME platform.

According to the nomenclature the segment AB is the inlet region of the domain, the segment HG is the outlet zone of the domain and finally the segment AH is the symmetry axis of the geometry. The code FemLCore is open-source code developed at UNIBO that is able to solve multi-physics problems [4.4]-[4.6]. The class is constructed with the FEMUS() constructor.

The initialization of the state variable fields velocity, pressure and temperature is defined by the setSystem(...). The Finite Element Method needs interpolation functions which are defined in init_fem(...). The initialization of the mesh is defined by setMesh(). The native mesh is in HDF5 and can be read by a xdmf driver file. The turbulence model is selected by the function InitTurbulence(). Different options are available both for two-equation dynamical and four-equation thermal turbulence models.

TrioCFD TALL-3D test modeling. TrioCFD is a software developed for nuclear plant thermohydraulic simulations from the French CEA and EDF. In TrioCFD the input axial-symmetric geometry should be three-dimensional. The mesh should use the axial-symmetry and only a part of the domain can be simulated, as shown in Fig. 4.11. The mesh used for TrioCFD is in med format which can be generated from the SALOME mesh generator. The coupling of TrioCFD code is obtained by an interface. This class, called ICoCo, has been developed over the SALOME platform. The class is constructed with the openLib() constructor which generates the problem ICoCo pointer objects.

The initialization of the state variable fields velocity, pressure and temperature is defined by the getProblem() function. The initialization and the end of the problem is controlled by the initialize() and terminate() function, respectively. The Finite Volume Method needs the function reconstruction which is defined in init_surfaceScalarField(phi_f). The material properties are defined by using setDataFile(datafile). The solution of the problem is defined by the following three functions: initTimeStep(dt), computeTimeStep(), and abortTimeStep(). The initTimeStep() function sets initial conditions. At each time step the solution is computed with computeTimeStep() and after a brief analysis on convergence the result can be refused or accepted with the abortTimeStep() command. The selection of turbulence model is at the moment very limited to a modified κ-ε two-equation model.

The ICoCo allows the data exchange of pressure, temperature and velocity field so that TrioCFD solution ϕ can be mapped into MEDField $\hat{\phi}$. The function Field<READ> $\hat{\phi}$-name (problemTrio, "ϕ") and Field<WRITE> $\hat{\phi}$-name (problemTrio, "ϕ") are used for volumetric source field exchange over the whole domain defined by the mesh. The solution data can be also exchanged only over sub-meshes where boundary conditions are defined. Boundary conditions can be forced with analytic expressions or by using MED fields. The TrioCFD field temperature can be integrated with the function averageTemperature($\hat{\phi}$, velOutletField) to pass a scalar average temperature single value to an STH code such as CATHARE.

4.2.3 Simulations of the semi-blind test case TG03S301(03)

Combining the simulation of the main circuit with Cathare code and the 3D test section by a CFD code we try to simulate the semi-blind test TG03S301(03). We consider the LBE properties temperature dependent as in Tab. 4-10. The one-dimensional problem is labeled problem C while the CFD with problem OF. In order to set the initial conditions we need to compute an initial state that satisfies the one-dimensional equation.

Initial conditions for STH codes (monodimensional). A solution of this high nonlinear system is computed for the one-dimensional model in its steady state. We start with inlet temperature for the PIPE3D set to $270°C$. The flow rate is set to $4.75kg/s$ with density $\rho = 10448kg/m^3$. The one-dimensional code has a variable time step. We start with dt = 0.01s and allow maximal value of 1s. After 2000s the temperature reaches the steady value reported in Tab. 4-11. Temperature over the outlet (A) and inlet boundary (B) as a function of time is reported in Fig. 4.12.

Initial conditions for CFD codes (three-dimensional). The coupling between the system code and the three-dimensional problem is achieved by a defective algorithm, i.e. a mutual exchange of boundary conditions between the problems. In order to obtain a stable coupling between the two problems both systems must reach the same thermal-dynamical working conditions. For this reason we do not couple the system code and the three dimensional problem from the beginning of the simulation, but we first find the nominal steady state working condition for the one-dimensional system and then we perform several coupled stabilization iterations for the 1D-3D problem. Concerning the boundary conditions for the energy balance equation we impose the temperature evaluated by the system code on the surface inlet, an homogeneous Neumann condition on the outlet and on the walls, except the imposition of thermal heat flux on one side of the cylindrical wall. Concerning boundary conditions for the axial component of the momentum balance equation, we impose the flow rate evaluated by the system code on the inlet surface and a vanishing Neumann condition on the axis. The normal component of the velocity field is set to zero on all the wall boundaries of the domain. The initial condition for the stabilization process is a constant temperature field with $T = 272°C$ and a vanishing velocity in the entire domain.

The temperature evolution and the steady state fields obtained after stabilization are shown in Fig. 4.13. Initial steady state for turbulent flow model case (κ-ω) in Open Foam code and turbulent viscosity ν_t with turbulent thermal diffusivity α_t are shown from the top to the bottom, respectively. We remark that the stabilization process is used as the initial condition for the coupling of the one and three-dimensional problems.

1D-CATHARE stand-alone simulation. We simulate the evolution of an Unprotected Loss of Flow going from forced to natural circulation flow for the test TG03S301(03) with Cathare stand-alone. We consider the system at $t = 0^-$ in fully working conditions. The main initial conditions in forced circulation are obtained as a steady state and they are shown in Table 2.11. At $t = 0^+$ the pump stops working while the power supplied through the rod in MH leg and 3D vessel heater are not switched off. Due to the lack of secondary side mass flow rate measurement, the oil flow rate has been calculated starting from the loss of enthalpy in the primary side, then with a thermal balance in the secondary side. The flow rate evolution in the three legs is presented from Fig. 4.14 to Fig. 4.16. We report the experimental data in the time interval [0,1000s] since we do not have other experimental data on this semi-blind test.

In Fig. 4.14 mass flow rates $\dot{m}$ and temperature T at the points S3-S4 of the central leg are reported as a function of time t. In this Figure one can see the comparison between the Cathare stand-alone simulations and experimental results. The CATHARE results are labeled with C and the experimental results with E. The mass flow results are matched fairly while the temperature results show large discrepancies. On the right of Fig. 4.15 one can see the 3DTEST outlet (top) and 3DTEST inlet (bottom) (bottom) temperature. In Fig. 4.16 mass flow rates m and temperature T at the points S5-S6 of the right leg are reported. In a similar way in Fig. 4.17 the same quantities are reported at the point S1 as a function of time. In Fig. 4.14 the experimental data

for temperatures at the thermocouple points $TC3_{4490}$ (S1) and $TC3_{5615}$ (S2) along the left vertical leg (left), at $TC1_{0346}$ (S5) and $TC1_{1740}$ (S6) on the right vertical leg (right) and at $TC1_{211}$ (S3) and $TC2_{2111}$ (S4) along the central vertical leg (left) are shown. Detailed experimental data are reported in [4.16],[4.15].

Coupling algorithm Cathare-OpenFoam with two-equation κ-ω model. We use a defective coupling algorithm Cathare-OpenFoam with two-equation k-ω model. We use the defective coupling algorithm with overlapping meshes [4.21]. The one-dimensional mesh is defined over all the domain and a three-dimensional mesh is defined only over the three-dimensional test region. We solve at each time step the three-dimensional code (OpenFoam) and the one-dimensional system code (CATHARE) over the overlapping domain. Six reference points are shown on the right of Fig. 4.7. We recall that they are labeled with S1-S2 (COR3-RESERVE4) on the left vertical leg, S3-S4 (BELOW3D28-ABOVE3D1) in the central vertical leg) and S5-S6 (PUMP0-LINUP14) on the right vertical leg. The point S3 (BELOW3D28) is the 1D/3D matching interface for state and turbulent variables at the inlet section of the three-dimensional domain. The point S4 (ABOVE3D1) is the 3D/1D matching interface for the outlet section of the three-dimensional domain. The meshes are generated with GUITHARE for the one-dimensional case and with SALOME modules for the three-dimensional one.

The coupling algorithm for OpenFoam-Cathare coupling can be schematized as follows:

a) Stabilization of the STH Problem to initial experiment setup for velocity, temperature and pressure fields (Cathare);
b) Stabilization of state and turbulent variables in the CFD problem to Cathare setup (OpenFoam);
c) Stabilization leading to matching of the state variables for the 1D and 3D;
d) Set up coupled transient;
e) For each time step:
  e1) Defective correction from 3D near the outlet of the TALL3D component and one step solution for the one-dimensional code for velocity, temperature and pressure fields;
  e2) Boundary conditions from 1D at the inlet section of 3D geometry one step solution for the three-dimensional code for state and turbulent variables;
f) Repeat to end time.

In *step a)* we solve the STH problem for initialization. We define as P1 and P2 the (S3) and (S4) points located in the BELOW3D module and the ABOVE3D module, respectively. The Problem class for the one-dimensional code is set and initialized. The density, which is a function of temperature, is extracted from point1. The pressure from the CATHARE code is extracted at point1 and point2 in order to determine the differential pressure DP. The momentum equation source DPLEXT controls the pressure variable by using the defective mode algorithm applied a control feedback technique, i.e..$DPLEXT = DPLEXT_0 + w\, DP$.

In step b) we solve the CFD problem for initialization. During the mesh generation we create the groups that define the 1D/3D and 3D/1D interfaces. The "inlet" label defines the inlet sub-mesh of the 3D test section while the "outlet" label defines the sub-mesh of the outlet region. For each sub-mesh we use two different representations and the corresponding mapping: the MED and OpenFoam code format. Both the system and CFD codes can read and map the MED format into its own format and vice versa. It is necessary to create one interface function for each state variable. We impose the boundary conditions in velocity and temperature at the inlet from the system code and extract the value at the outlet to impose on the system code. We set the initial condition to OpenFoam and compute the pressure at the inlet and outlet to determine the pressure losses. The mean integral values of the OpenFoam surface variables can be computed directly on the sub-mesh with OpenFoam utility functions. These average values are then passed from OpenFoam code to the STH one-dimensional code at each time step.

In step c), after the initialization of the STH and CDF problems in a segregated way we proceed to the stabilizedcoupling to be used as initial values. For turbulence variables, which are not computed in the STH

code, we use appropriate fully turbulent inlet conditions where the k, ω and and ε variables are compute from the inlet velocity and theoretical intensity constants.

In step d) we set up the solver for solutions.

In *step e)* the STH and CFD problem are solved. The transient loop of Cathare is determined by a pass-fail time step. Logical variables *stop* and *ok* are evaluated to determine the convergence of the nonlinear system. The time step is *0.01s* the same for both the codes. During the transient for each time step, the state values ($\dot{m},T,p$) are solved, where $\dot{m}$ is the fluid flow rate, T the temperature and p the pressure. For one-dimensional system liquid flow rate substitutes the knowledge of the velocity field ($v=\dot{m}/A\rho$). The state ($v; T; p$) is extracted from the one-dimensional simulation at S3 and S4 to determine the source needed for the correction in the mass, momentum and energy equations. The energy and momentum correction is obtained by defective mode algorithm. The sources used to modify momentum and the energy equations are labeled as DPLEXT and ENTLEXT. Analysis of this coupling is reported in a dedicated section later. The OpenFoam time step starts by setting the inlet state with boundary condition from the one-dimensional code. The inlet temperature T_{S3}, obtained by CATHARE, is imposed to interface S3 (inlet) in analytical form. In addition, the liquid flow is imposed from the one-dimensional code to the three-dimensional inlet. After solving the OpenFoam time step the pressure, the temperature and the velocity fields are available. We compute the average pressure at the inlet and at the outlet to compute the pressure losses.

In Fig. 4.17 and Fig. 4.18 mass flow and temperature at reference points for STH Cathare stand alone and CFD OpenFoam are shown. In particular these behaviors at reference points S4 and S4 of the central leg can be seen on the top and bottom of Fig. 4.17, respectively. The Cathare stand-alone results are labeled with C and the Open Foam κ-ω with κω. The application of the three-dimensional correction is clear. With these results is easy to think that the STH code does not give a very accurate results. In Fig. 4.18 Mass flow (right) and temperature (left) at reference point S6 (top) and S5 (below) on the left leg are shown for Cathare stand-alone (C) and coupling Cathare-OpenFoam with κ-ω turbulence model.

The results obtained by using the two-equation κ-ω turbulence model in the OpenFoam code can be seen in Fig. 4.19 and Fig. 4.20. In detail in Fig. 4.19 temperature and streamline profiles over the 3D test component at time t = 0, 4, 20, 80, 180, 580, 1780 and 2780*s* are shown. In Fig. 4.20 turbulent kinetic energy κ over the same interval of time is reported.

Comparison of the Cathare-TrioCFD-OpenFoam coupling results. It is clear that the Cathare stand-alone code results in temperature values at the inlet and outlet are rather higher if compared with experimental results. The STH code should be improved with adding heat losses that probably was not taken into account accurately in the modeling of the experimental setup. In spite of this poor performance of the STH code we try to see if three-dimensional coupling can help in the matching with experimental results. The platform has a various possibilities. It is possible to couple different CFD codes (such as FemLcore, TrioCFD, OpenFoam) and to use different turbulent models. In this paragraph we report two cases: a case with different turbulent models inside OpenFoam and a case where TrioCFD is used as a replace of the OpenFoam model. First we consider the change of the turbulence model of the OpenFoam code. Inside OpenFoam the turbulence model can be set to solve different two-equation models. In particular we use the k- ε model in order to compare with the k-ω previously considered. The turbulence model coupling with the STH code is modeled by assuming fully developed turbulence at the interface point. This allows us to use inlet turbulent boundary conditions. Once an appropriate turbulence intensity and turbulence length scale or eddy viscosity ratio have been estimated the turbulence model variables can be computed from the standard formulas.

The modified turbulent viscosity can be computed as

$$\tilde{\nu} = \sqrt{3/2}\, u I \lambda \,, \tag{1}$$

where u is the mean flow velocity, I is the turbulence intensity and λ is the turbulent length scale. Now the turbulent energy k can be computed as

$$k \;=\; 3(u\,I)^2/2 \,, \tag{2}$$

and the turbulent dissipation rate ε and its ratio ω from the turbulence length scale as

$$\varepsilon = C_\mu\, k^{\,3/2}/l \qquad \omega = C_\mu\, k^{\,1/2}/l \tag{3}$$

where k is the turbulent energy computed in (2). It is important to remark that some CFD commercial and open-source codes, such as OpenFoam, uses a different length-scale definition based on the mixing-length. We therefore may be use

$$\varepsilon = C\mu^{3/4}\, k^{\,3/4}/l \tag{4}$$

where Cμ is 0.09. From the eddy viscosity ratio we have

$$\varepsilon = C_\mu \varrho\, \frac{k^{\,2}}{\mu}\, \mu/\mu_\tau \tag{5}$$

Where $\mu_\tau\,/\,\mu$ is the eddy viscosity ratio. In Fig. 4.21 the flow rate and temperature at the reference points S3 and S4 for k-ω (kw) and k-ε (ke) turbulence models are shown on the top and bottom, respectively. The mass rate flow is similar in these two cases but the inlet and outlet temperature differ in a substantial way. Now if we use TrioCFD we find even different results. In TrioCFD, which is CEA and EDF software used in French nuclear industry only a modified k-ε turbulence model is available and therefore no other choice is allowed [4.22]. In Fig. 4.22 mass flow rate is reported for different models at the inlet point S3 for the test considered in the interval of time [0, 5000*s*]. We report the experimental data, TrioCFD, OpenFoam and Cathare stand-alone results. On the right we compare the mass flow rate of TrioCFD with label TS3, the mass flow rate of OpenFoam with OFS3 and the experimental results with ES3. The result are pretty good with exception of TrioCFD. On the left we compare the same case with OpenFoam with OFS3, Cathare stand alone and the experimental results with ES3. With the exception of Cathare which underestimates slightly the mass flow the other cases are acceptable. On the left of Fig. 4.23 the inlet temperature at the point S3 for OpenFoam (OFS3), TrioCFD (TS3), Cathare stand-alone (CS3) and experimental data (ES3) as a function of time is shown. In a similar way on the left of the outlet temperature at the point S4 is shown for OpenFoam (OFS4), TrioCFD (TS4), Cathare stand-alone (CS4) and experimental data (ES4) as a function of time. Different models give large discrepancies. Cathare stand-alone code gives too high temperature. The best result is given by OpenFoam κ-ω model. However OpenFoam results, as in all the other models, show an increase of the inlet temperature for large times which leads to high values inside the 3Dtest section. Again it seems that the experimental results of the test section have heat losses that are not taken into account.

Evaluation of the defective coupling algorithm on OpenFoam-Salome-Cathare platform. In order to couple the three and one-dimensional codes we use a defective algorithm which imposes boundary conditions over multi-scale interfaces by using feedback control algorithm [4.22]. The points where the boundary conditions are evaluated or imposed are defined in Fig. 4.7 which are labeled S3 and S4. In Fig. 4.24 and Fig. 4.25 one can see performance of the defective coupling algorithm. At the point S3 the liquid flow and temperature values of the one-dimensional code are imposed as inlet boundary conditions for the 3D-CFD code. In Fig. 4.24 one can see mass flow rate (right) and temperature (left) at the point S3 where boundary conditions are imposed on a multi-scale interface from Cathare (1D) to OpenFoam (3D) as a

function of time. In this case the boundary condition m1d and T1d are imposed as uniform Dirichlet boundary value m3d and T31d. Since the meshes are overlapping and no flow may exit from the test section there can be no error in the mass balance equation. In Fig. 4.25 the behavior of temperature and pressure at the point S4 on a multiscale interface from OpenFoam to Cathare as a function of time after the pump shutdown is shown. The temperatures of 1D and 3D simulation at the point S4 are shown in Fig. 4.25 on the left. The energy correction is obtained by computing the enthalpy source EN T LEXT inside the energy equation. We define

$$\text{EN T LEXT} = h_{S4} - \alpha C_p \left(T_{1D} - T_{3D} \right) , \qquad (6)$$

where α is a constant and h_{S4}, T_{S4} are the enthalpy and the temperature at point S4. The T_{3D} is the average temperature at the outlet of the 3D test section which has been computed at each OpenFoam time step. This temperature is imposed on Cathare and the resulting matching is almost perfect at each time step. The momentum correction is obtained by computing DP LEXT as

$$\text{DP LEXT} = \text{DP LEXT}_0 - \beta(\Delta p_{3d} - \Delta p_{1d}) , \qquad (7)$$

where Δp_{3d} and Δp_{1d} are the pressure losses when the gravity contribution is subtracted. The value DP LEXT$_0$ is the old value of DPLEXT which is directly read from the one-dimensional code. The parameter β is set constant. The pressure at the point S4 in the 3D/1D interface is shown in Fig. 4.25 on the right. As one can see almost perfect match is obtained.

4.3   Conclusive remarks

This research activity has the goal of developing a multi-scale and multi-physics computational platform for studying issues of LFR technology based on open-source and commercial software in a strict collaboration between the University of Bologna and ENEA [4.2]-[4.9]. The platform developed during these years is very flexible and include a large number of codes. Many of these codes are used by French CEA and EDF for the developing of nuclear activities. Others are open-source codes and provide computational tools that can be used with no restraints. The platform should be able to couple research, in-house and commercial codes in a such a way that the new and old developments in this field will not be lost.

The LFR technology is very important as a research line in itself but also in many other fields such as in the production of electricity. In the framework of the Generation IV International Forum (GIF), nuclear experts see the fourth generation of nuclear systems as a possible line to respond to the world future energy needs. This could reduce the huge demand for electricity with the corresponding emissions from fossil fuels. Initial development on the LF reactors was focused on pool-type reactors. The main lines were two: one with the Small Secure Transportable Autonomous Reactor (SSTAR) model of $20MWe$ developed in USA and the other with the European Lead-cooled SYstem (ELSY) of $600MWe$ developed in Europe. The SSTAR core is one meter high and $1.2m$ in diameter. The ELSY project was led by Ansaldo Nucleare from Italy and was financed by Euratom. The $600MWe$ design was nearly complete in 2008 and a small-scale demonstration facility was planned. This prototype runs on MOX fuel at $480°C$ with liquid lead pumped to eight steam generators with decay heat removal by convection. However ALFRED reactor design has now superseded old designs.

In previous reports we have developed this platform adding codes that allows the investigation of the thermo-hydraulic issues related to LFR technology. The basic idea is to study multiscale and Multiphysics systems where the main component was a reactor while the primary loop was a simplified circuit [2.3]-[2.5],[2.15],[2.7]. However reactor scale experiments are difficult to manage and the experimental data are not very suitable for CFD simulations. However the verification and validation of this platform are necessary to show the robustness and reliability of these computations. There are many

experimental facilities built to provide experimental data for numerical coupling simulation, but the experimental facility TALL3D seems to provide right amount of data needed for CFD numerical developers. This facility provides a large number of simple but clear tests that can be replicated by coupling a STH code with a CFD code. Experimental temperature profiles inside the three-dimensional region are available and can be compared with CFD profile.

Now in order to show the flexibility of this platform we have studied the TALL3D plant where the one-dimensional component is modeled with Cathare code while the three-dimensional regions with Open-Foam code. The model for TALL-3D has been developed in the previous report and coupling simulations with laminar and turbulent flows have been studied for different configurations. In this report we improve the existing interfaces for CATHARE and develop one for OpenFoam coupling [2.12]. During the analysis of this lead-cooled facility three-dimensional effects cannot be ignored and its features cannot be modeled by simple volumetric balances of energy, momentum and mass. The coupling techniques between system and three-dimensional codes give a good opportunity to explore more complex problems but great difficulties are added from combining multi-dimensional and overlapping meshes together. We have investigated the use of turbulence models that are implemented on OpenFoam in order to improve the three-dimensional coupling. In this work we report the simulation of a semi-blind test, labeled as TG03S301(03). The results are mixed. The one-dimensional system code stand-alone produces temperatures which were shifted to higher values and the corrections of three-dimensional CFD code improve in the right direction. However the results show that a lot of work should be done especially in the modeling of TALL facility both in the STH code and CFD model.

In future works we plan to change the 3D modeling of the test section to include heat losses. The heat losses should take down the heat inside the test section and decrease the outlet temperature. The heat losses on the basement of the 3D section should increase also the natural circulation inside the heated region. We also plan to construct a model which can cope naturally with the flux inversion which is very common in natural convection but it has never taken into account. The flow inversion in the 3D test section leads to a change of boundary conditions when the inlet becomes outlet and vice versa.

	Designation	Thermocouple purpose
1	TC1.0000	TC at the left side of the bottom T-junction
2	TC1.0346	TC at the cold section of the Main heater
3	TC1.1740	TCs at the outlet of the Main Heater
5	TC1.2144	
6	TC1.2641	TCs encompassing the straight pipe section
7	TC1.4990	
8	TC1.5830	TC at the left side of the top T-junction
9	**TC2.1211**	**TCs encompassing the Test Section (above)**
10	**TC2.2111**	**TCs encompassing the Test Section (below)**
11	TC2.2967	TCs positioned above the Test Section outlet with equidistant pitch to trace possible heat waves and temperature profile during flow stagnation
12	TC2.3316	
13	TC2.3670	
14	TC2.4016	
17	TC2.5085	
18	TC3.0000	TC at the left side of the bottom T-junction
19	TC3.0747	TCs encompassing the EPM pump
20	TC3.2665	
21	TC3.4036	TCs encompassing the Heat Exchanger
22	TC3.5830	
23	TC.ET	TC located inside the Expansion Tank
24	TC.ST	TC location inside in the Sump Tank

Tab. 4-1 – Thermocouples and temperature measurement.

name	function
`new Problem_Cathare()`	basic constructor of problem class
`initialize()`	set system problem
`terminate()`	end interface
`presentTime()`	time
`initTimeStep(dt)`	initial time step
`computeTimeStep()`	solve time step
`abortTimeStep()`	abort time step

Tab. 4-2 - STH modeling for TALL3D. Basic functions for the interface ICoCo class over the Salome platform.

Interface name	Description
`getValue_cathare("variable","sub-mesh",np, 0)`	get variable from sub-mesh at point np
`setValue_cathare("variable","sub-mesh",np, 0,value)`	set value at variable over the sub-mesh at point np

Tab. 4-3 - Cathare modeling for TALL-3D. Interface functions for exchange data of the Cathare-Salome platform (ICoCo class).

name	function
OF(runTime,mesh)	basic constructor with OF time and mesh
init_field(...,m)	state variable and solver initialization
init_surfaceScalarField(phi_f)	surfaced field initialization
init_mat_trsp(...)	material property initialization
init_mat_trsp_var(...)	material variable initialization
init_turbulence(turb)	turbulence initialization
init_param()	parameter initialization
setMesh("OFmesh.med","Fmesh.med")	mesh maps OF-MED and OF-FEMUS
setSystem(myproblemP)	set system problem

Tab. 4-4 - OpenFOAM modeling for TALL-3D. Basic functions for interface construction of the OFclass over the SALOME platform for exchange data.

Interface name	Description
GetMedSolution(ϕ," ϕ ",np);	get MEDField $\tilde{\phi}$ from OpenFoam solution ϕ
GetMedSolution(ϕ," ϕ",np,mesh,"sub-mesh")	get MEDField $\tilde{\phi}$ from OpenFoam solution ϕ over sub-mesh
SetMedSolution(ϕ," ϕ ",np, $\tilde{\phi}$)	set MEDField $\tilde{\phi}$ into OpenFoam solution ϕ
SetMedSolution(ϕ," ϕ",np, $\tilde{\phi}$,mesh,"sub-mesh");	set MEDField $\tilde{\phi}$ into OpenFoam solution ϕ over sub-mesh
get_field_from_exp(on_node,2,string)	return a MEDField from string expression on nodes
get_field_from_exp(on_cell,2,string)	return a MEDField from string expression on cells
get_integral(ϕ,np,"sub-mesh")	integration over sub-mesh

Tab. 4-5 - OpenFOAM modeling for TALL-3D. Interface functions of the OpenFOAM-SALOME platform. OpenFOAM solution ϕ mapped into MEDField $\tilde{\phi}$.

Name	function
FEMUS()	basic constructor with OF time and mesh
init_fem (mggeomel,mgfemap)	Fem initialization
setSystem (myproblemP1)	state variable initialization
setMesh()	mesh maps FEMUS-MED
setMeshTurbCase ( )	turbulence initialization
InitTurbulence (model)	set turbulence model
solve_setup (t0,t)	solver setup

Tab. 4-6 - FemLCore modeling for TALL-3D. Basic functions for interface construction of the FEMUS class over the SALOME platform.

Interface name	Description
init_interface (label,Group,2,interface)	interface ϕ - $\tilde{\phi}$ initialization
getUMesh (label)	get sub-mesh in med format
getValuesOnBoundary (label,"NS0", 1, 1)	get boundary values ϕ
setAnalyticSource(label,1,string)	return a MEDField $\tilde{\phi}$ from string expression on nodes
write_Boundary_value(label,"T",1)	write ϕ in x_old the boundary values
setFieldSource (label,1,Interpolated)	write the source
Integrate(field,label,"NS0",1,1,AxiMean)	integrate field

Tab. 4-7 - FemLCore modelling for TALL-3D. Interface functions of the FemLCore-SALOME platform. FemL-Core solution ϕ mapped into MEDField $\tilde{\phi}$.

name	function
Problem * openLib(const char* lib, void* handle)	basic contructor of problem class
initialize()	set system problem
terminate()	end interface
getProblem()	variable initialization
setDataFile(datafile)	data file initialization
presentTime()	time
initTimeStep(dt)	initial time step
computeTimeStep()	solve time step
abortTimeStep()	abort time step

Tab. 4-8 - TrioCFD modelling for TALL-3D. Basic functions for interface ICoCo class over the SALOME platform for exchange data.

Interface name	Description
Field<WRITE> $\hat{\phi}$name(problemTrio, " ϕ ")	put MEDField $\hat{\phi}$ from TrioCFD solution ϕ
Field<READ> $\hat{\phi}$name(problemTrio, " ϕ ")	get MEDField $\hat{\phi}$ from TrioCFD solution ϕ
averageTemperature($\hat{\phi}$, velOutletField)	average temperature
averageVelocity(velOutletField)	average velocity
averagePressure(pOutletTrio)	average pressure

Tab. 4-9 - TrioCFD modelling for TALL-3D. Interface functions of the TrioCFD-SALOME platform (ICoCo class). TrioCFD solution ϕ mapped into MEDField $\hat{\phi}$.

Property	Unit	Correlation	T	error
Molar mass	kg/mol	0.20898		
Melting temperature	K	544.6		
Latent heat	kJ/kg	53.3	-	-
Sat. vapour pressure	Pa	$2.67 \times 10^{10} \exp(-22858/T)$	545-1831	40
Surface tension	N/m	$(420.8 - 0.081\,T) \times 10^{-3}$	545-1400	
Density	g/m^3	$10725 - 1.22\,T$	545-1300	2
Sound velocity	m/s	$1616 + 0.187\,T - 2.2 \times 10^{-4}T^2$	545-1800	5
Bulk modulus	Pa	$(30.22 - 2.8 \times 10^{-3}T - 3.720 \times 10^{-6}\,T^2) \times 10^9$	545-1800	3
Isobaric specific	J/kg· K	$118.2 + 5.934 \times 10^{-3}\,T + 7.183 \times 10^6\,T^{-2}$	545-1300	7
Dynamic viscosity	Pa· s	$4{:}456 \times 10^{-4} \exp(780/T)$	545-1300	5
Electric resistivity	Ω· m	$(98{:}96 + 0.0554 \times T) \times 10^{-8}$	545-1420	0.8
Thermal conductivity	W/mK	$7.34 + 9.5 \times 10^{-3}T$	545-1000	10

Tab. 4-10 - Physical properties used in the modeling of the TALL-3D facility.

	Initial Condition	Unit
T BELOW 3D	272.6	°C
T ABOVE 3D	308.2	°C
MH power	10300	W
LBE mass flowrate	4.75222	kg/s
Oil outlet temperature	126	°C
Oil mass flowrate	1	kg/s

Tab. 4-11 - Initial state condition for the one-dimensional Problem C (cathare). The STH code initial condition satisfies the steady state equation.
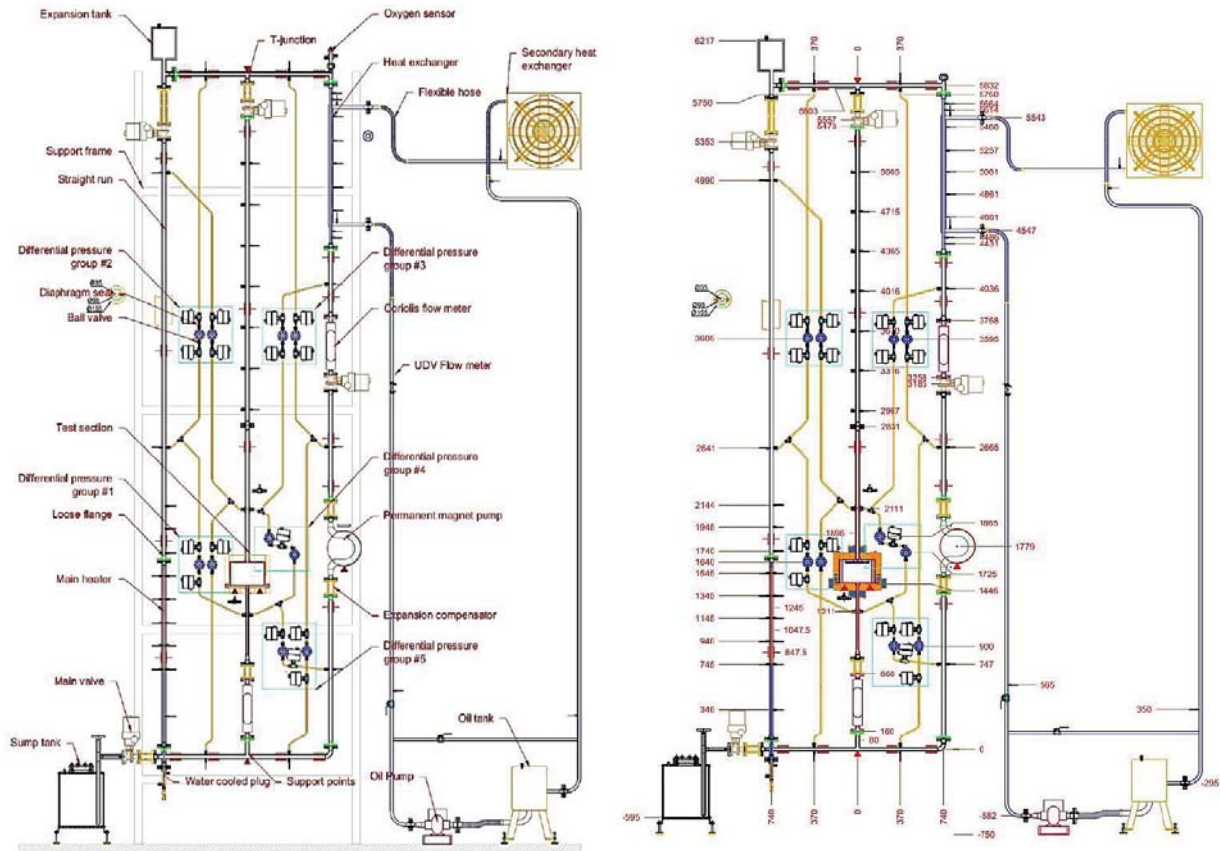
Fig. 4.1 - TALL-3D facility (left) with geometric dimensions (right).
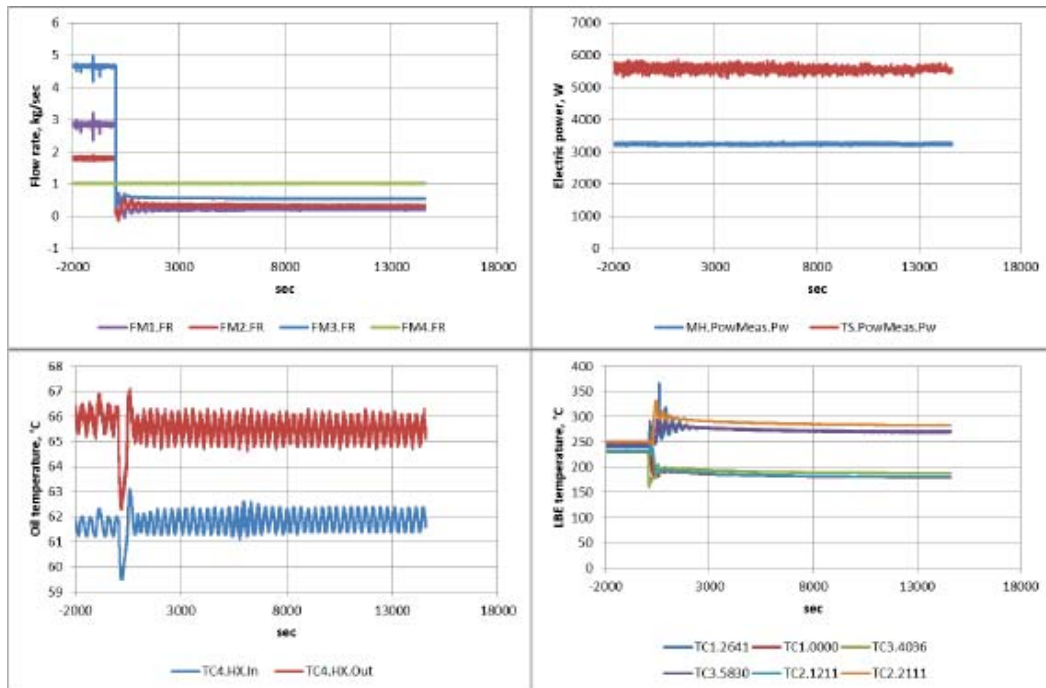
Fig. 4.2 - Experimental data for test series TG03S301.
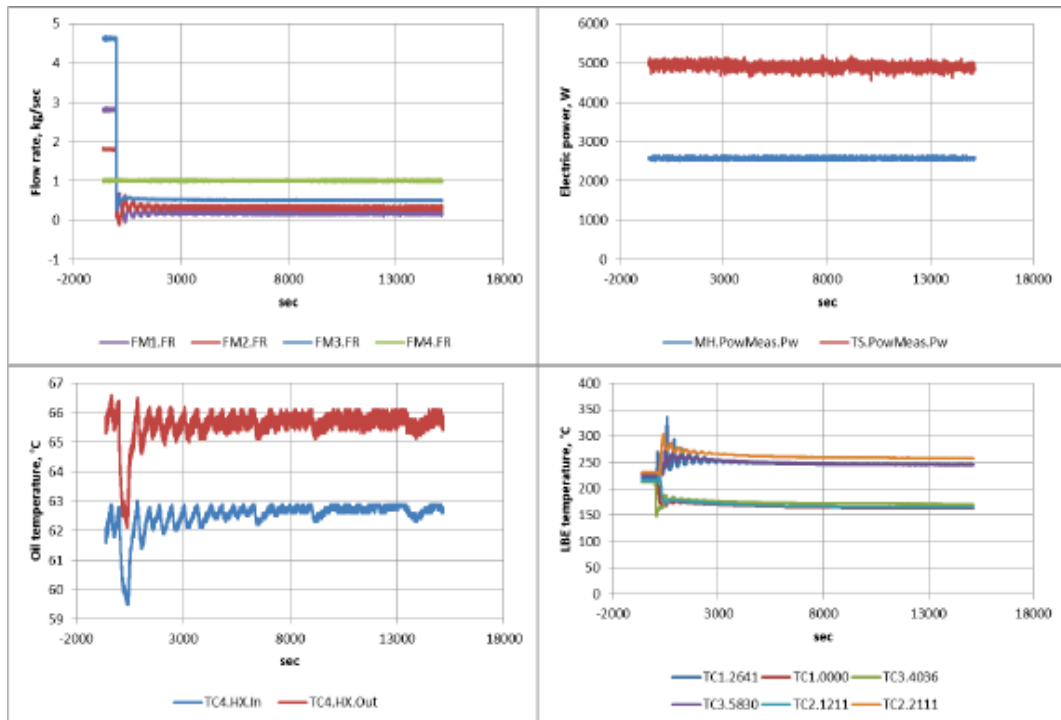
Fig. 4.3 - Experimental data for test series TG03S302.
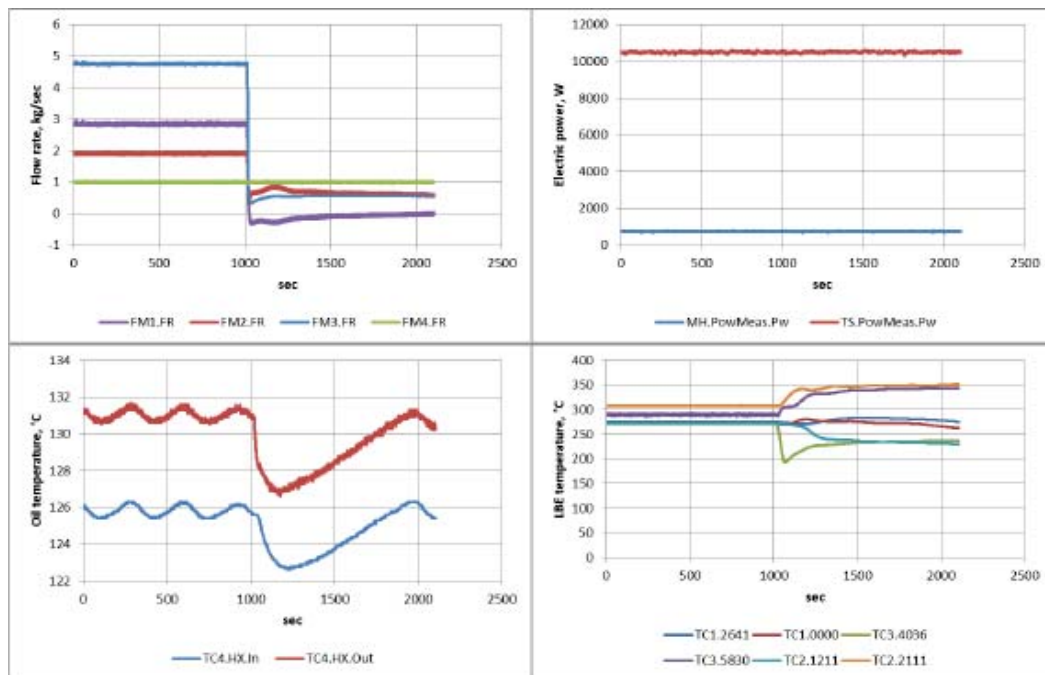
Fig. 4.4 - Experimental data for test series TG03S303.
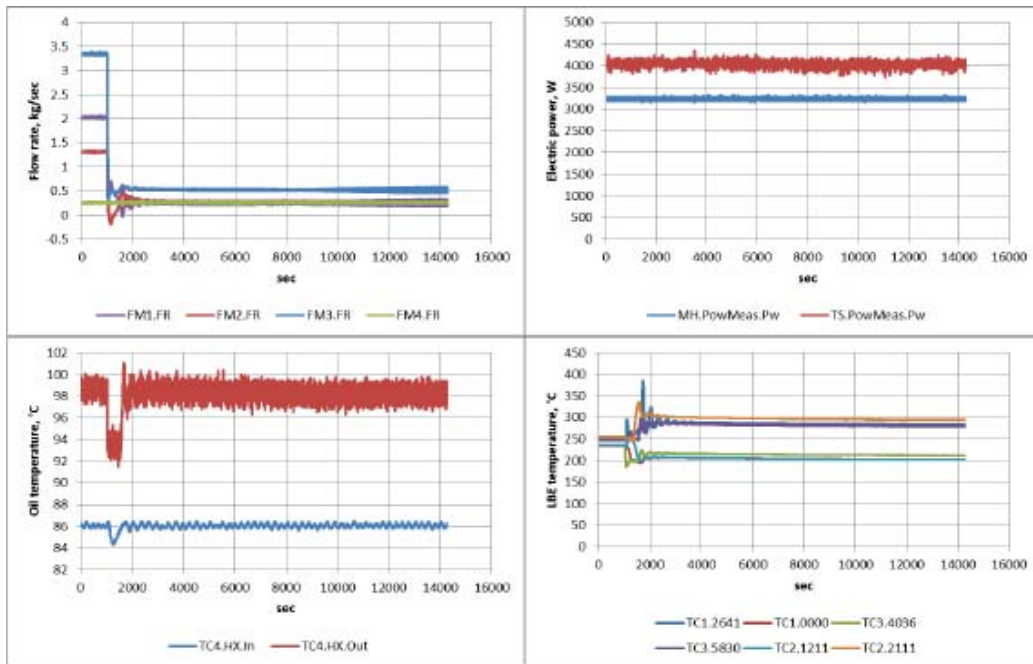
Fig. 4.5 – Experimental data for test series TG03S304.
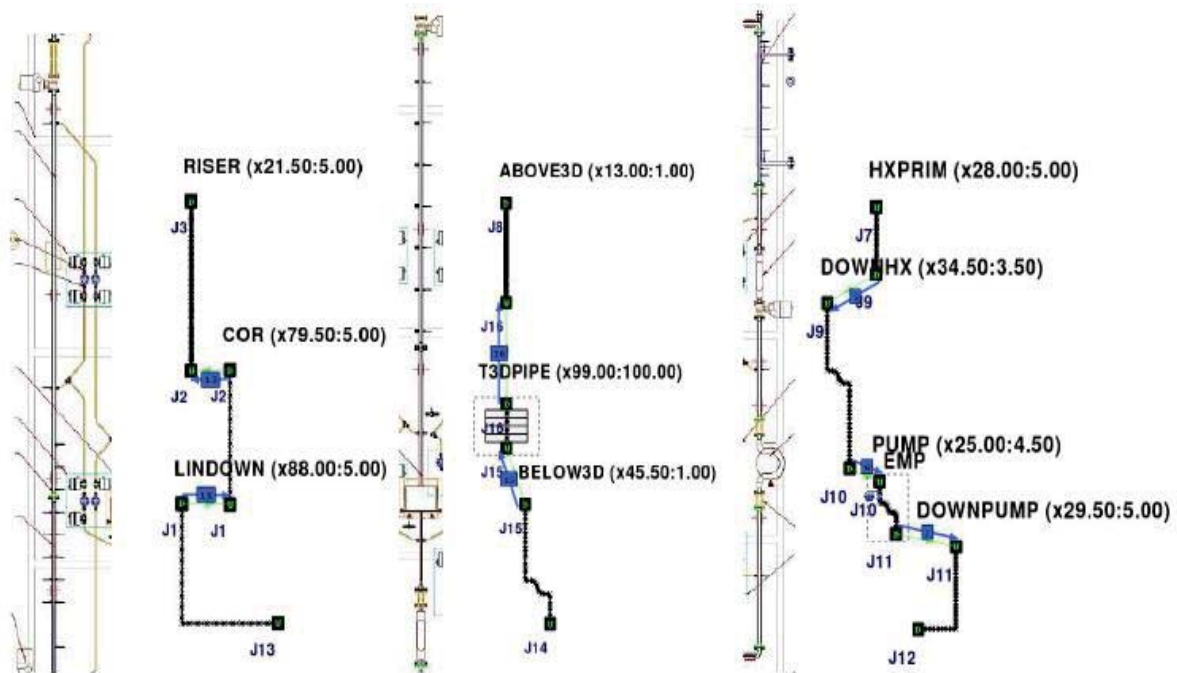
Fig. 4.6 - Left, central and right vertical leg (from left to right) in 1D system model with 3D test section.
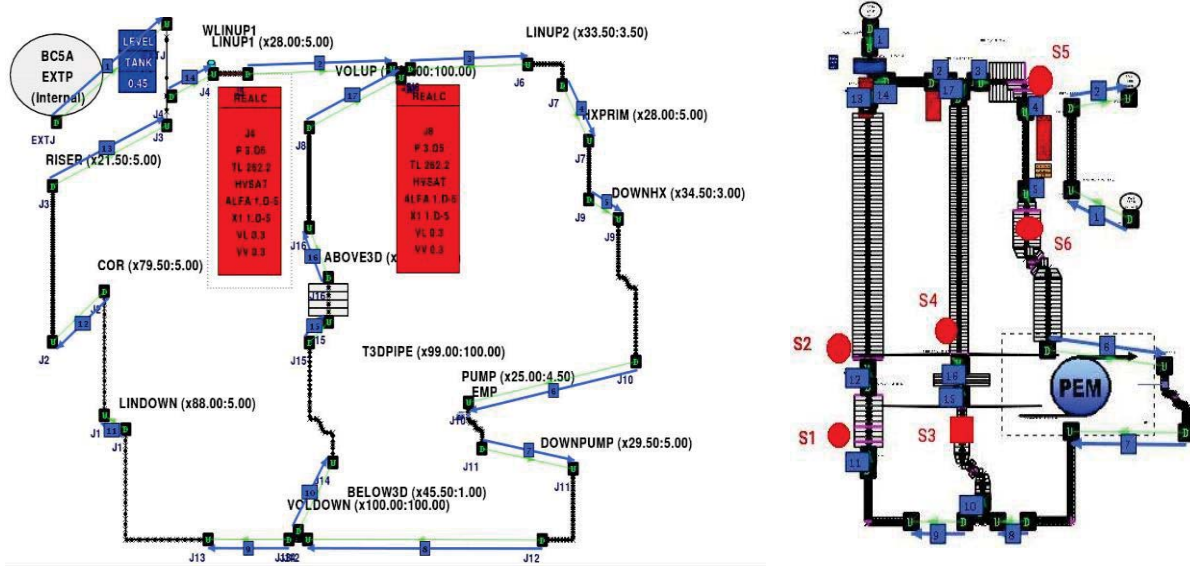
Fig. 4.7 - One-dimensional CATHARE model for the TALL-3D facility (left) and point of interests S1-S2 of the left leg (right), S3-S4 of the central leg and S5-S6 of the right vertical leg.

Fig. 4.8 - Modelling for TALL-3D. Geometry and dimensions.

Fig. 4.9 - OpenFoam modelling for TALL-3D. The three-dimensional test section in Open Foam mesh (format in UNIV or MED).

Fig. 4.10 - FemLCore modeling for TALL-3D. Geometry and dimensions of the three-dimensional test section.
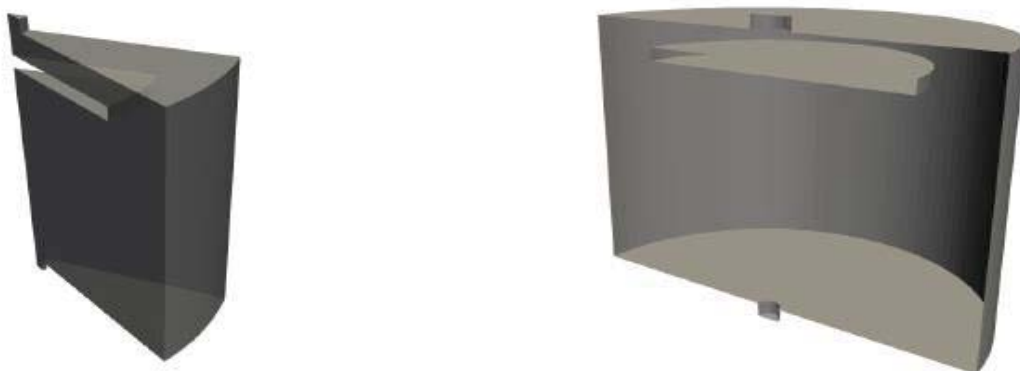
Fig. 4.11 - TrioCFD modelling for TALL-3D. Geometry of the axial-symmetric and three-dimensional test section.
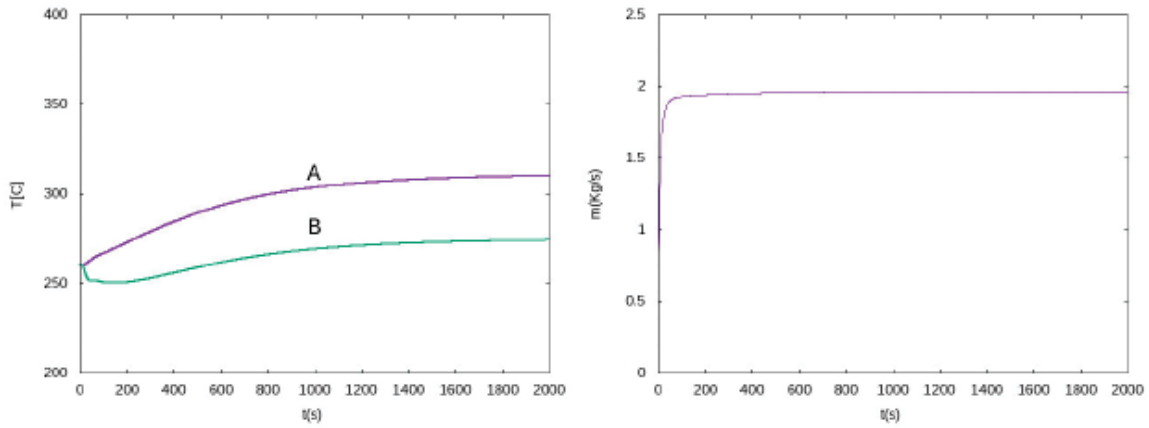
Fig. 4.12 - Temperature over the outlet (A) and inlet boundary (B) as function of time during the stabilization step.

Velocity v

Velocity u

Pressure

Temperature

Turbulent kinetic energy rate ω

Turbulent kinetic energy k

Turbulent viscosity ν_t

Turbulent thermal conductivity α_t
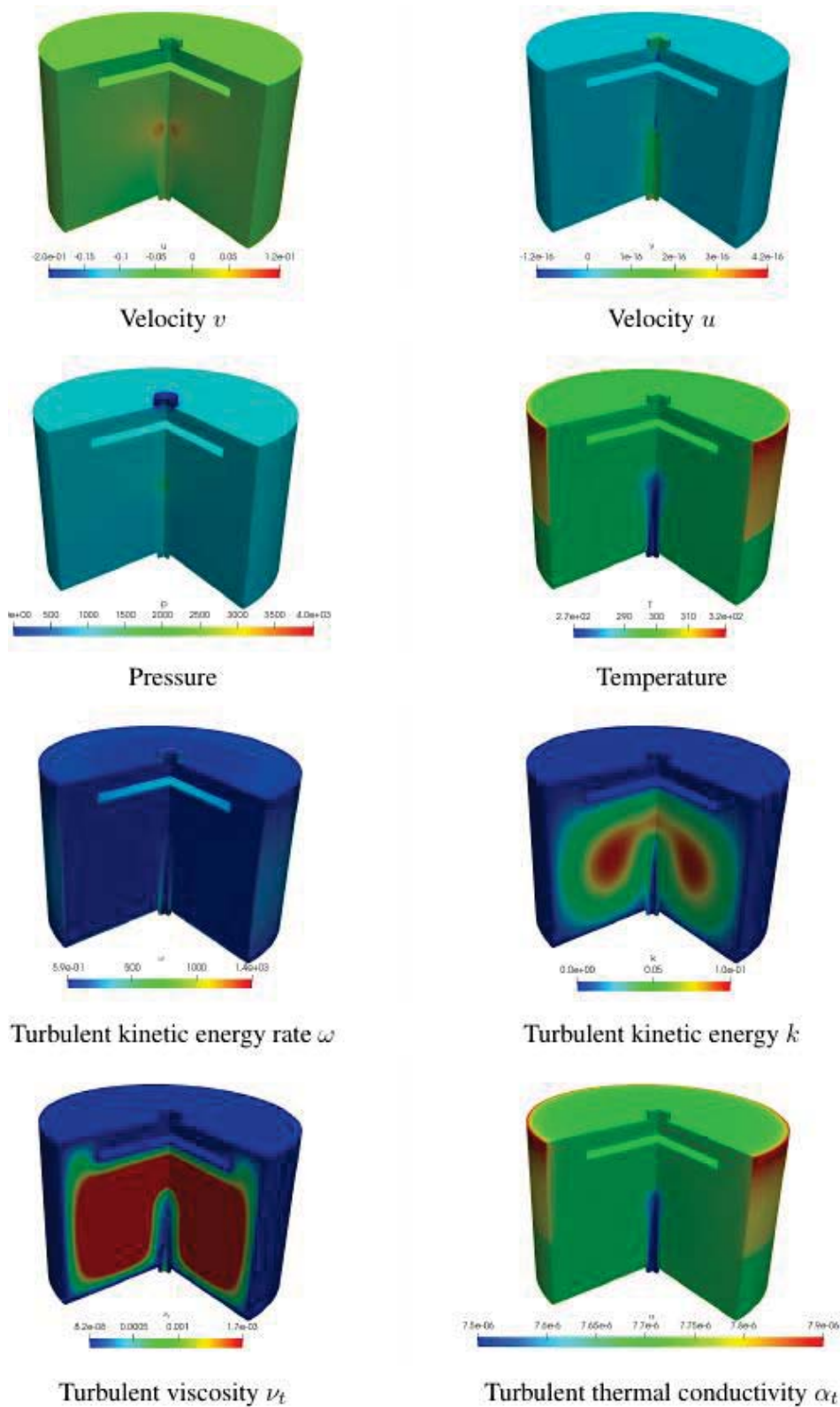
Fig. 4.13 - Initial steady state for turbulent variable for CFD OpenFoam code with the turbulent flow model κ-ω.
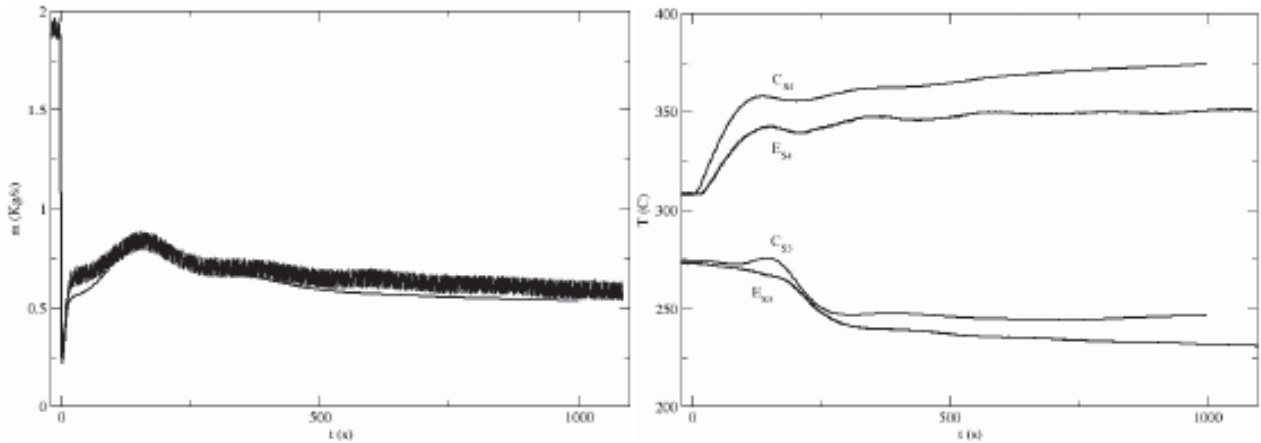
Fig. 4.14 - Cathare stand-alone simulation. Computed mass flow rate ṁ (left) and temperature (right) at the points S3-S4 of the central leg as a function of time t.
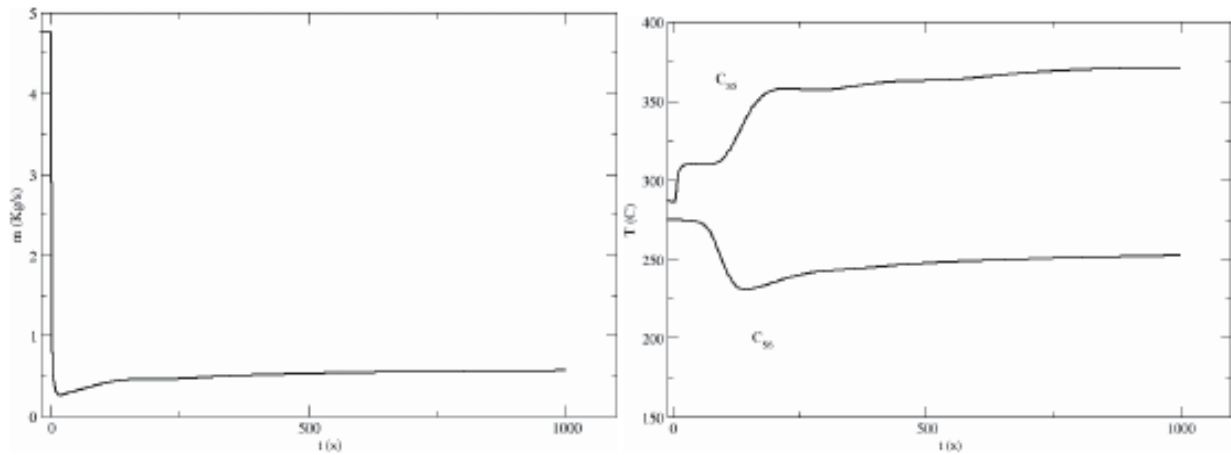
Fig. 4.15 - Cathare stand-alone simulation. Computed mass flow rate ṁ (left) and temperature (right) at the points S5-S6 of the central leg as a function of time t.
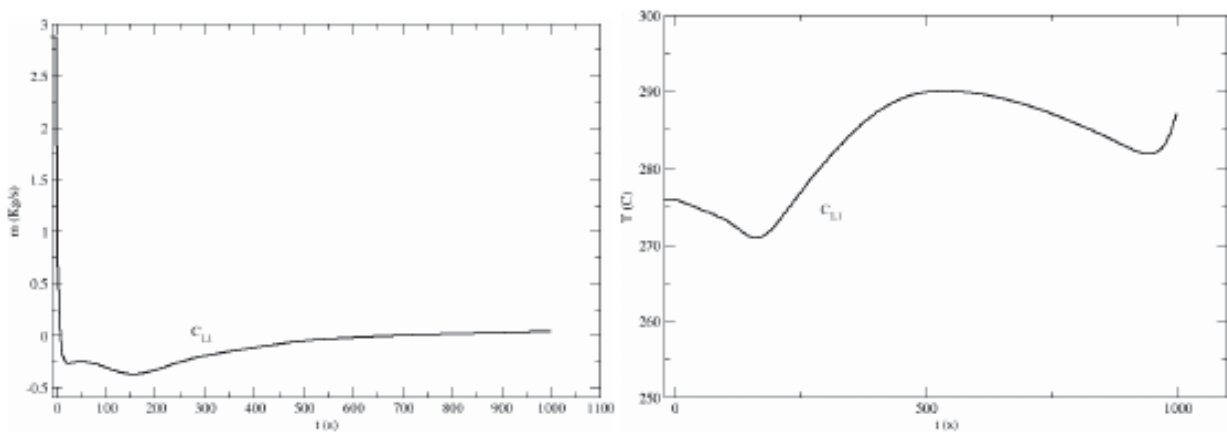
Fig. 4.16 - Cathare stand-alone simulation. Computed mass flow rate ṁ (left) and temperature (right) at the points S1 of the central leg as a function of time t.
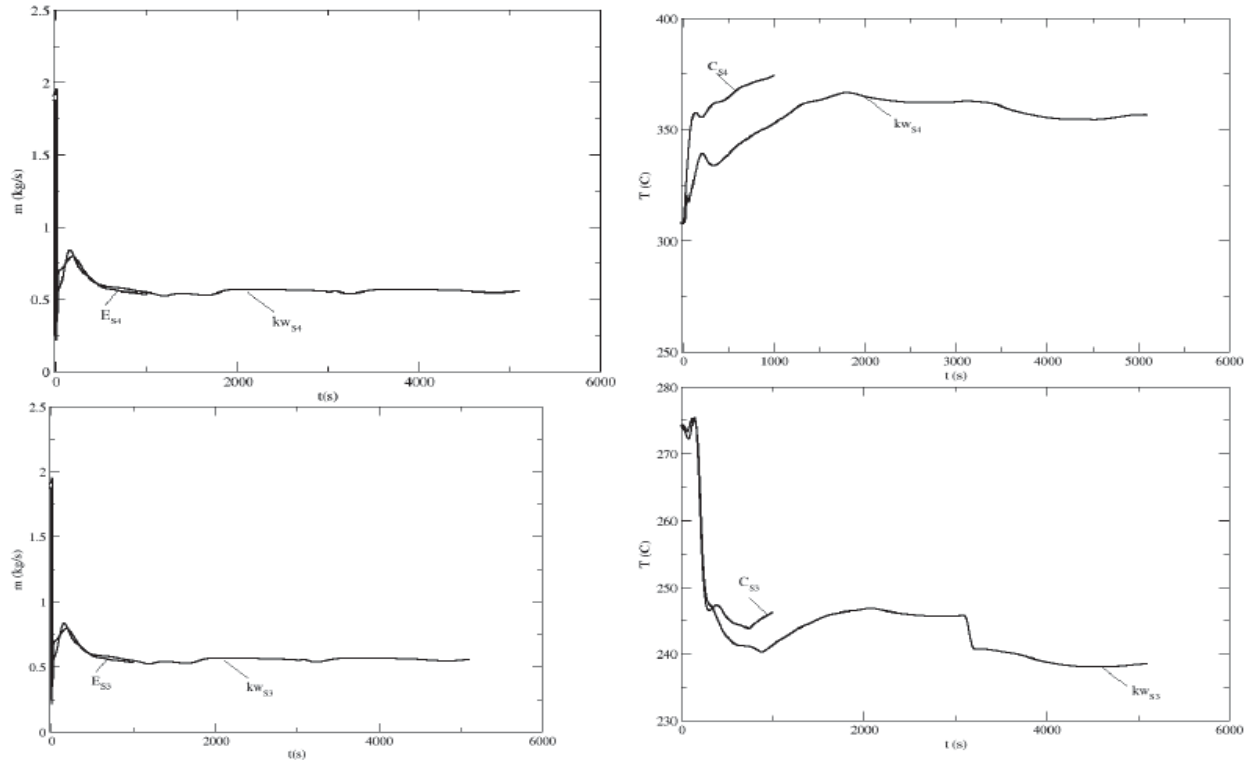
Fig. 4.17 - Mass flow rate (right) and temperature (left) at reference point S4 (top) and S4 (below) of the central leg for Cathare stand-alone (C) and coupling Cathare-OpenFoam with κ-ω turbulence model.
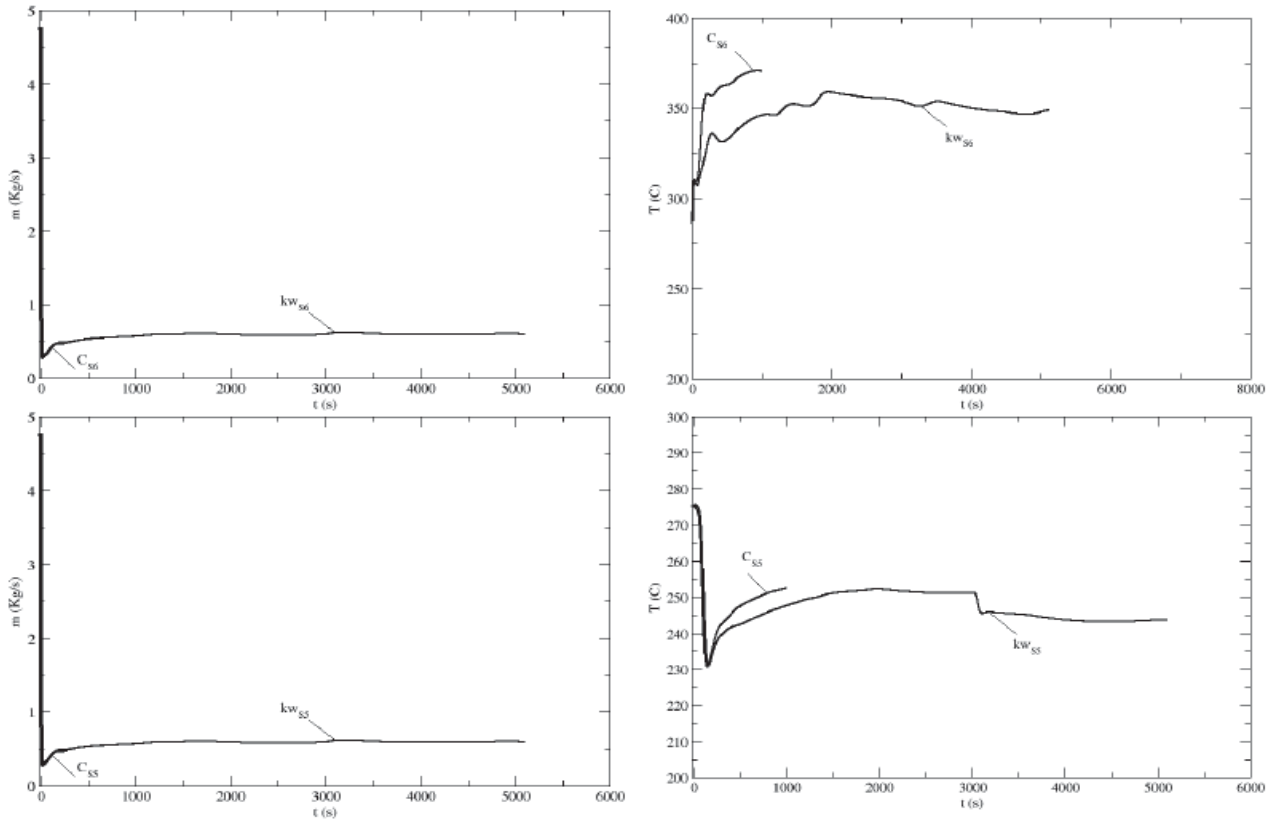
Fig. 4.18 - Mass flow rate (right) and temperature (left) at reference point S6 (top) and S5 (below) on the left leg for Cathare stand alone (C) and coupling Cathare-OpenFoam with κ-ω turbulence model.
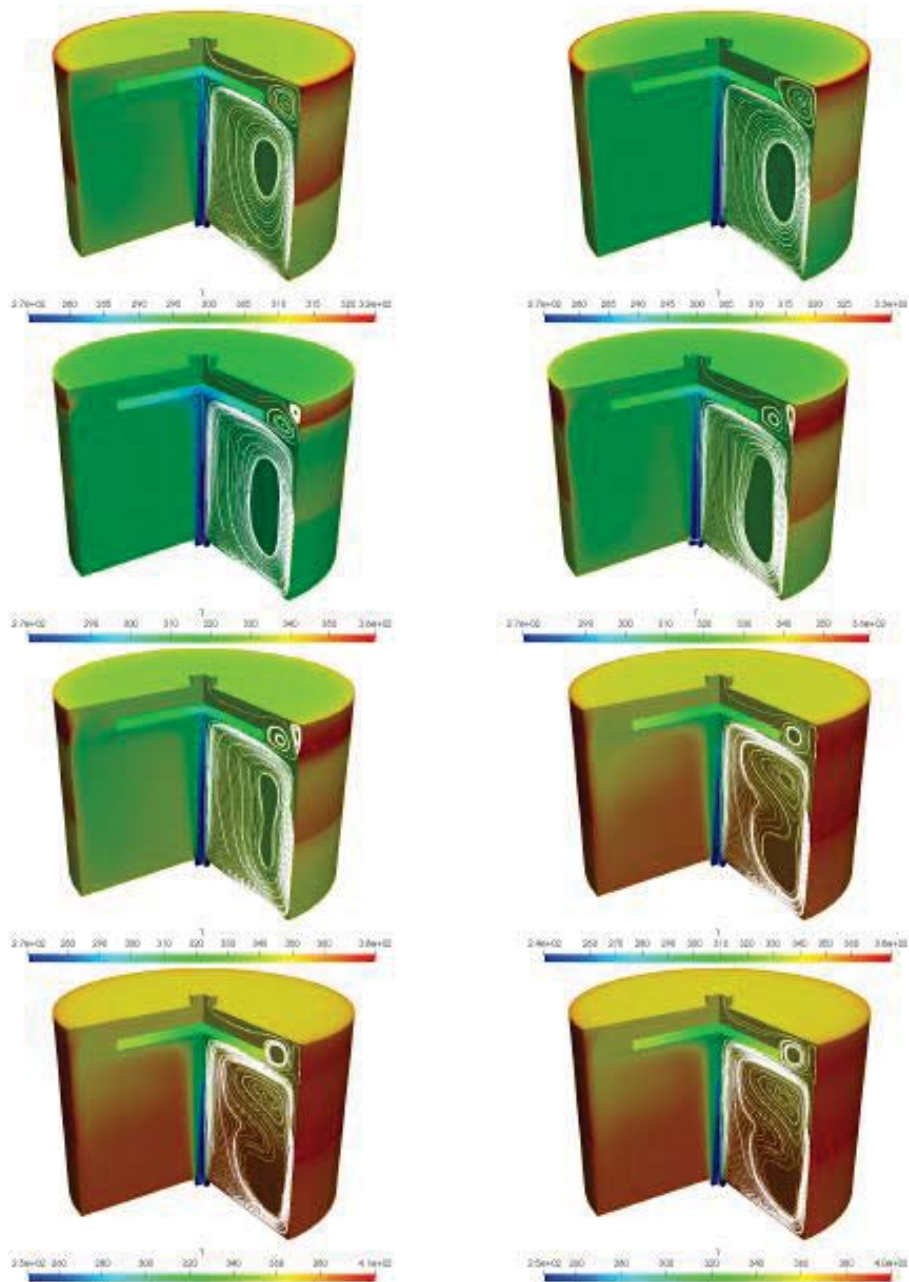
Fig. 4.19 - Temperature and streamline profiles over the 3D test component at time t=0, 4, 20, 80, 180, 580, 1780 and 2780s by using two-equation κ-ω turbulence model in OpenFoam.
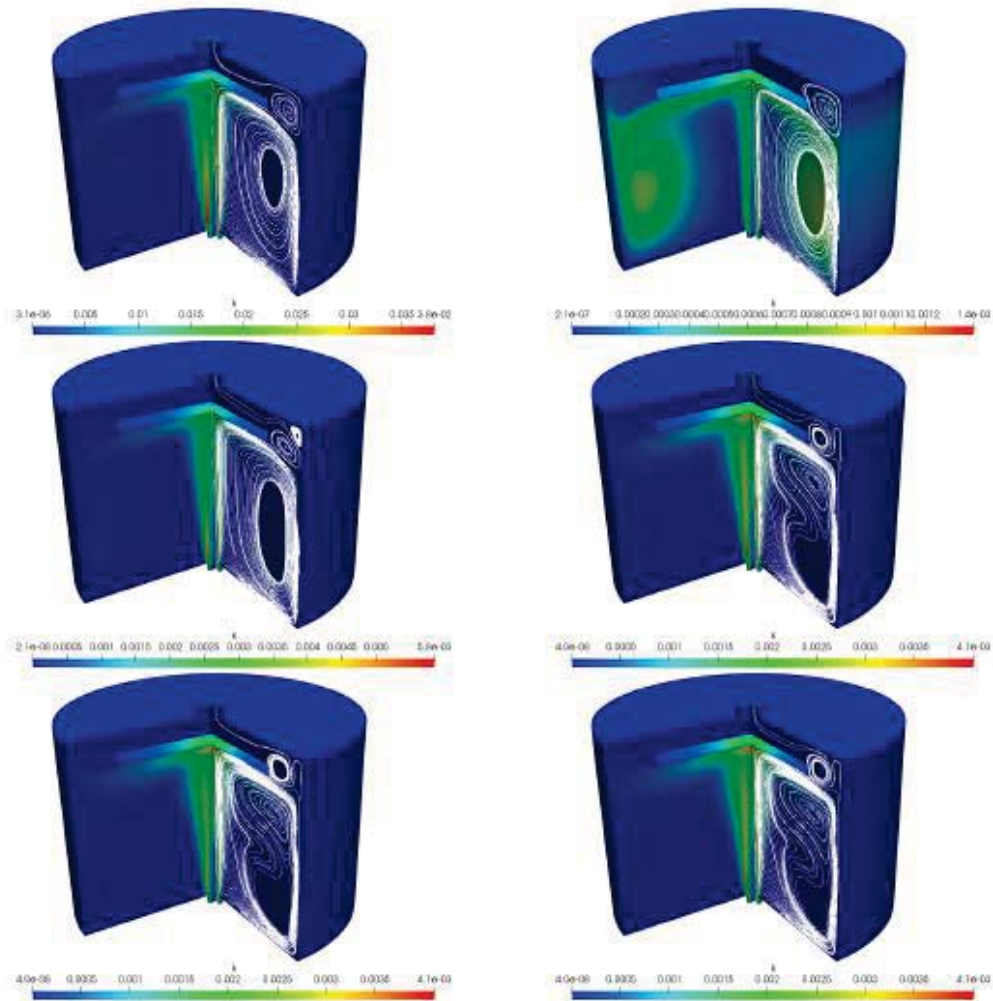
Fig. 4.20 - Turbulent kinetic energy κ and streamline profiles over the three-dimensional test component at t = 0, 4, 20, 80, 180, 580, 1780 and 2780s by using two-equation κ-ω turbulence model in OpenFoam.
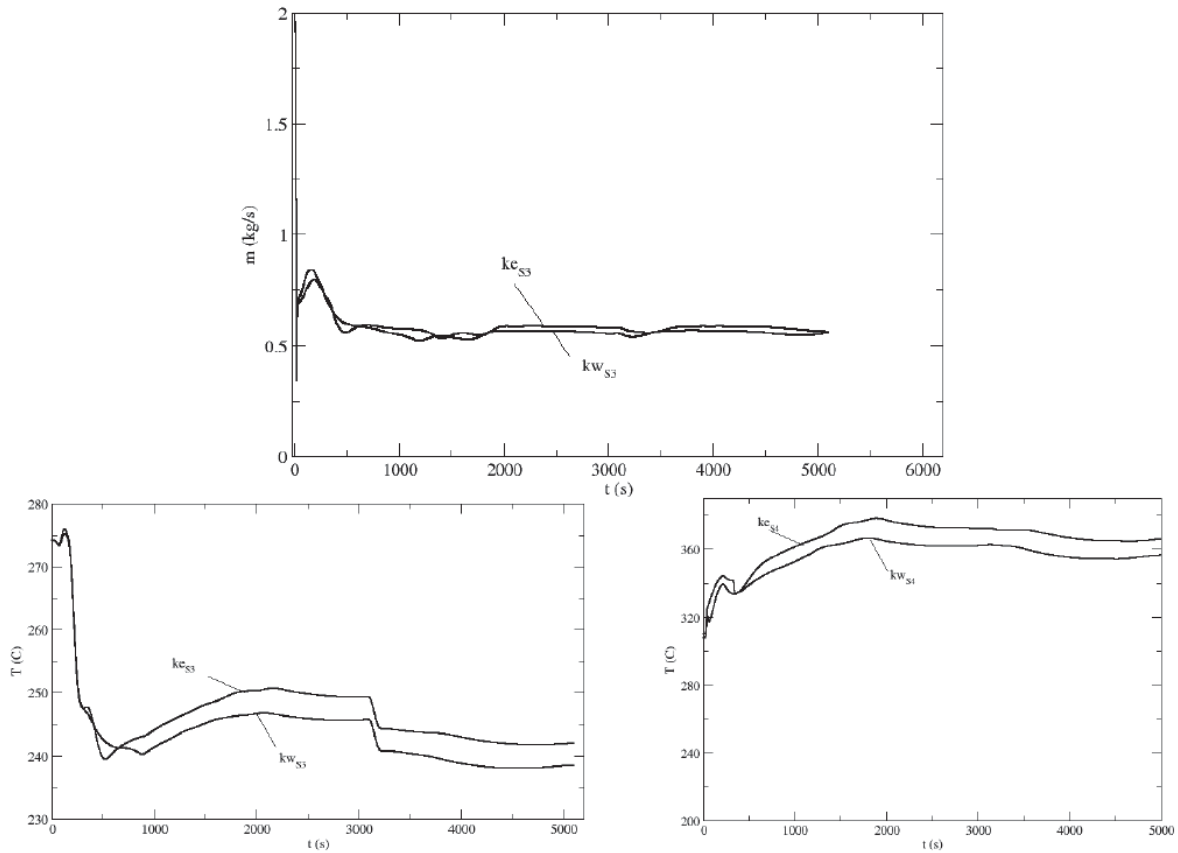
Fig. 4.21 - Mass flow rate (top) and temperature (bottom) at the reference points S3 and S4 for k-ω (kw) and k-ε (ke) turbulence models.
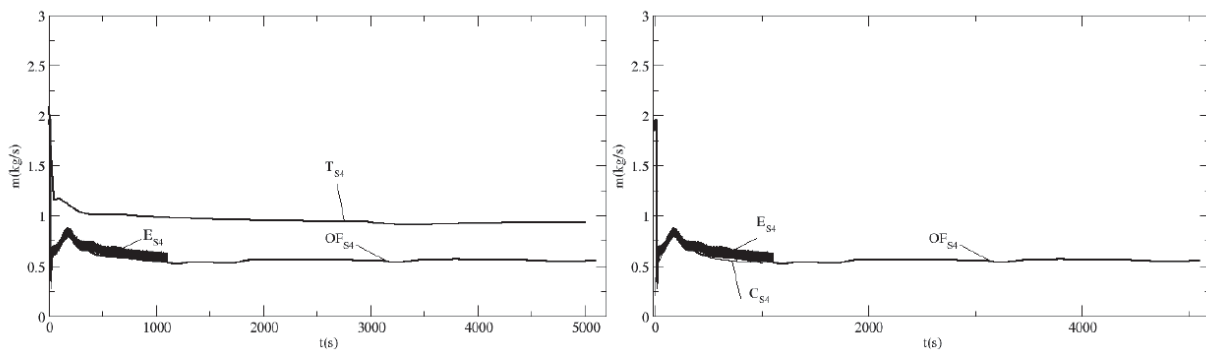
Fig. 4.22 - Mass flow rate for OpenFoam (OFS3), TrioCFD (TS3), Cathare stand-alone (CS3) and experimental data (ES3) as a function of time.
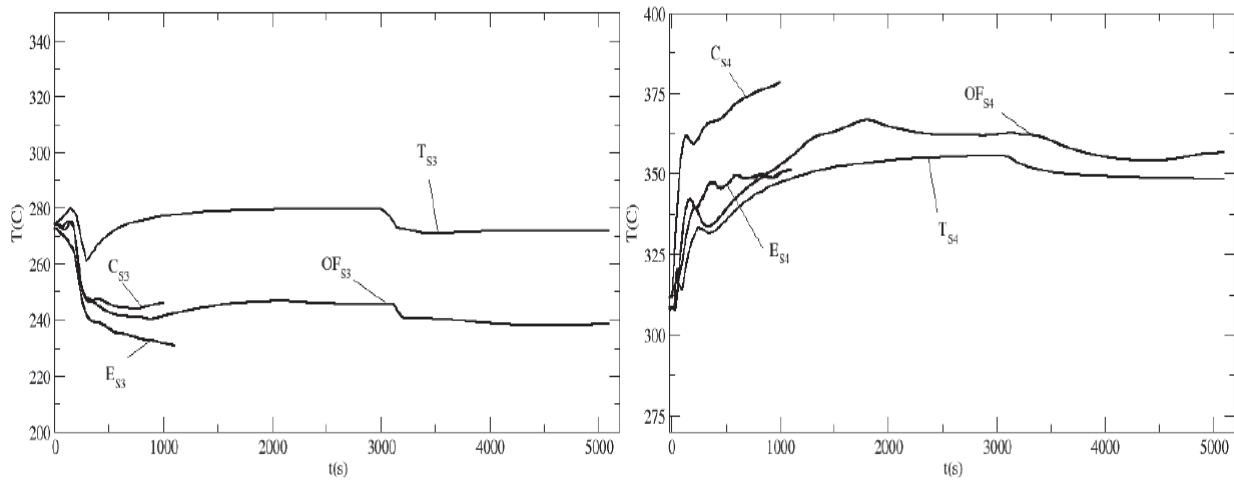
Fig. 4.23 - On the left the inlet temperature for OpenFoam (OFS3), TrioCFD (TS3), Cathare stand-alone (CS3) and experimental data (ES3) as a function of time. On the right the outlet temperature for OpenFoam (OFS4), TrioCFD (TS4), Cathare stand-alone (CS4) and experimental data (ES4).
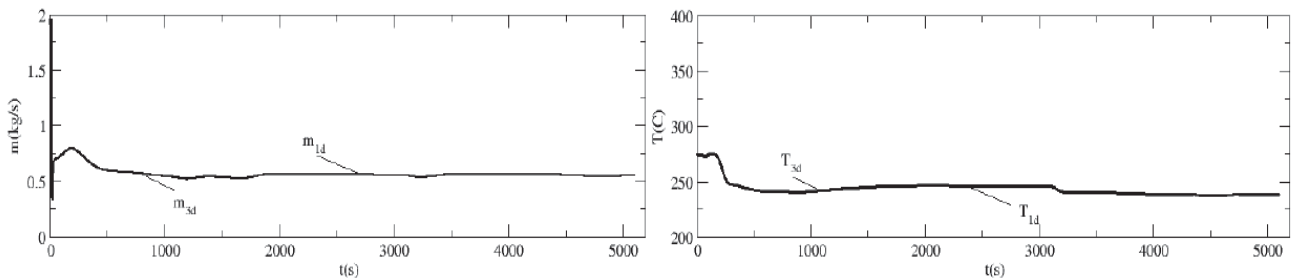
Fig. 4.24 - Mass flow rate for OpenFoam (OFS3), TrioCFD (TS3), Cathare stand-alone (CS3) and experimental data (ES3) as a function of time.
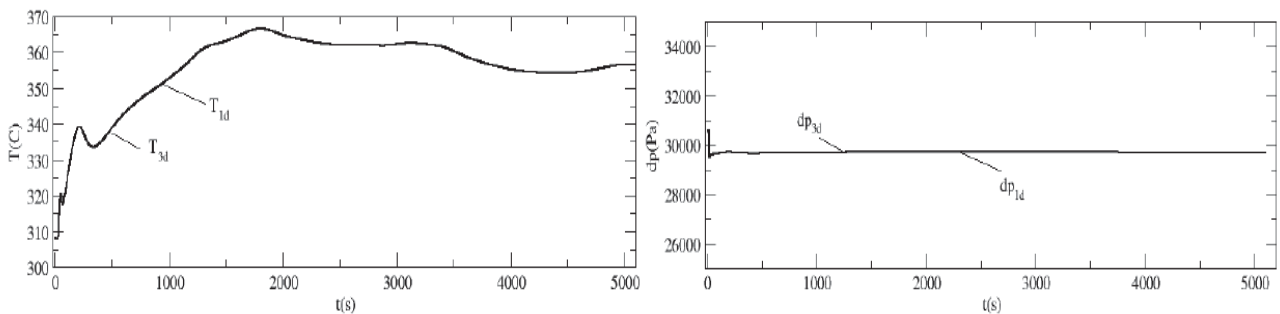
Fig. 4.25 - Temperature (right) and pressure (left) at the point S3 where boundary conditions are imposed on a multi-scale interface from OpenFoam (3D) to Cathare (1D) as a function of time after the pump shutdown.

4.4   List of References

[4.1] F. Cadinu and P. Kudinov, "Development of a "coupling-by-closure" approach between cfd and system thermal-hydraulics codes," vol. Proceedings of the 13th International Topical Meeting on Nuclear Reactor Thermal Hydraulics (NURETH-13), 2009.

[4.2] A. Cervone and S. Manservisi, "A three-dimensional cfd program for the simulation of the thermo-hydraulic behavior of an open core liquid metal reactor," Tech. Rep. lin-thrg 108, 2008.

[4.3] S. Bnà, S. Manservisi, and O. L. Bot, "Simulation of the thermal-hydraulic behavior of liquid metal reactors using a three-dimensional finite element model," tech. rep., 2010.

[4.4] G. Bornia, M. Finelli, S. Manservisi, V. Mikhin, M. Polidori, and K. Voukelatou, "Development and validation of femlcore code for the thermal hydraulics of open cores," tech. rep., 2011.

[4.5] G. Bornia, D. Cerroni, S. Manservisi, M. Polidori, and F. Donato, "Femlcore code: parallelization, turbulence models and code integration," tech. rep., 2012.

[4.6] D. Cerroni, S. Manservisi, and E. Vincenzi, "Developing multiscale transient simulations with femlcore code," tech. rep., 2013.

[4.7] D. Cerroni, R. D. Già, S. Manservisi, F. Menghini, and G. Pozzetti, "Integration of the femlcore code in the salome platform," tech. rep., 2014.

[4.8] A. Attavino, D. Cerroni, A.Cervone, L. Fancellu, and S. Manservisi, "Femlcore-cathare coupling on salome platform," Tech. Rep. RL 1361/CERSE-UNIBO, 2015.

[4.9] R. Da Già, D. Cerroni, A.Cervone, and S. Manservisi, "Validation of the femlcore-cathare coupling model of the tall-3d facility," Tech. Rep. RL 1362/CERSE-UNIBO, 2016.

[4.10] A. Ribes and C. Caremoli, "Salome platform component model for numerical simulation," vol. Computer Software and Applications Conference, 31st Annual International, pp. 553–564, 2007.

[4.11] T. O. Foundation, "Openfoam, user guide, version 6," Tech. Rep. 1, 2018.

[4.12] F. Moukalled, L. Mangani, and M. Darwish, The Finite Volume Method in Computational Fluid Dynamics. An Advanced Introduction with OpenFOAM and Matlab. Springer, 2016.

[4.13] M. Jeltsov, K. Kōōp, D. Grishchenko, A. Karbojian, W. Villanueva, and P. Kudinov, "Development of tall-3d facility design for validation of coupled sth and cfd codes," vol. Proceedings of The 9th International Topical Meeting on Nuclear Thermal-Hydraulics, Operation and Safety (NUTHOS-9), 2012.

[4.14] D. Grishchenko, M. Jeltsov, K. Kōōp, A. Karbojian, W. Villanueva, and P. Kudinov, "Design and commissioning tests of the tall-3d experimental facility for validation of coupled sth and cfd codes," vol. THINS 2014 International Workshop, 2014.

[4.15] D. Grishchenko, M. Jeltsov, K. Kōōp, A. Karbojian, W. Villanueva, and P. Kudinov, "The tall-3d facility design and commissioning tests for validation of coupled sth and cfd codes," Nuclear Engineering and Design, vol. 290, pp. 144–153, 2015.

[4.16] P. KUDINOV, D. Grishchenko, I. Mickus, K. K. Koop, and M. Jeltsov, "Tall-3d setup for first series," Tech. Rep. WP4,D4.5,KTH, 2016.

[4.17] D. Bestion, "The physical closure laws in the cathare code," Nuclear Engineering and Design, vol. 124, pp. 229–245, 1990.

[4.18] F. Barre and M. Bernard, "The cathare code strategy and assessment," Nuclear Engineering and Design, vol. 124, pp. 257–284, 1990.

[4.19]   M. Robert, M. Farvacque, M. Parent, and B. Faydide, "Cathare 2 v2.5: a fully validated cathare version for various applications," tech. rep., 2003.

[4.20]   G. Geffraye, O. Antoni, M. Farvacque, D. Kadri, G. Lavialle, B. Rameau, and A. Ruby, "Cathare 2 v2.5_2: a single version for various applications," Nuclear Engineering and Design, vol. 241, pp. 4456–4463, 2011.

[4.21]   T. P. Grunloh and A. Manera, "A novel domain overlapping strategy for the multiscale coupling of CFD with 1D system codes with applications to transient flows," Annals of Nuclear Energy, vol. 90, pp. 422–32, 2016.

[4.22]   R. Bavière, N. Tauveron, F. Perdu, E. Garré, and S. Li, "A first system/CFD coupled simulation of a complete nuclear reactor transient using CATHARE2 and TRIO-U. Preliminary validation on the Phénix reactor natural circulation test," Nuclear Engineering and Design, vol. 277, pp. 124–37, 2014.

5 THREE-DIMENSIONAL NEUTRONIC-THERMAL-HYDRAULIC DYNAMICS MODELLING: SERPENT-OPENFOAM-FRENETIC COMPARISON AND APPLICATION TO ALFRED DESIGN

N. Abrate, S. Dulla, E. Guadagni, G. F. Nallo, P. Ravetto,
L. Savoldi, D. Valerio, R. Zanino

(Page intentionally left blank)

5.1   Introduction

In the frame of the Italian activities focused on the deployment of LFR technology, Politecnico di Torino (PoliTO) has been developing since few years a code for the multiphysics analysis of liquid-metal cooled cores, named FRENETIC (Fast REactor NEutronics/ThermalhydraulICs) [5.1]. The code aims at the time-dependent simulation of the neutronics (NE) and thermal-hydraulics (TH) of hexagonal fuel assemblies, adopting:

- a multigroup diffusion model for neutrons discretized with a coarse mesh nodal method at the assembly level;
- a 1D+2D advection/diffusion model for the liquid metal flowing within the assembly, assuming no cross-flow among elements.

The models and discretization methods adopted aim at the capability to simulate in a computationally efficient way the core behavior in operational and accidental conditions.

The modules of the FRENETIC code have been validated against other computational tools and against experimental data both in stand-alone configuration (e.g. TH validation against RELAP5 [5.2]) and in coupled calculations, see the EBR-II SHRT-45R test in the frame of a Coordinated Research Project of the International Atomic Energy Agency [5.3].

The above activities have allowed identifying some necessary development activities to be carried out in FRENETIC, such as the inclusion of a module for the simulation of the contribution of photon and decay heat [5.4]. In this perspective, a collaboration has been established with Politecnico di Milano (PoliMI) for the development of a detailed reference model for LFR, based on neutron transport calculated with the Monte Carlo code Serpent [5.5], and a CFD simulation of the fuel assembly (FA) performed with OpenFOAM [5.6], taking profit of the current tools available for the coupling of Serpent with OpenFOAM. The objective of the collaboration was to generate a "reference" solution for the core behavior using this extremely detailed approach and perform a comparison with the results obtained with FRENETIC in the same configuration, in order to assess the accuracy of FRENETIC and identify possible improvements in the core modelling approximations that are part of FRENETIC structure [5.1]. The core design on which the analysis has been focused is the ALFRED design [5.8].

The detail of the Serpent-OpenFOAM modelling are reported in Chapter 6, as part of PoliMI activity on LFR platform. We want to recall here some important aspects of the two simulation approaches, in the perspective of their comparison, highlighting in particular their fundamental differences and the resulting cautions to be taken when comparing results.

Nuclear simulations performed with computational tools such as Serpent and OpenFOAM imply a set of advantages, which could be summarized as the possibility to obtain extremely accurate solution at the fuel pin level, which can be considered as a reference for design evaluation and for benchmarking of other codes. On the other hand, the computational cost associated to this approach is extremely heavy, and with the computational capabilities currently available at the Institutions involved in this activity the only feasible approach has been based on:

- the full-core neutronic simulation with Serpent, providing the power distribution at the pin level;
- the CFD simulation of a single fuel assembly with OpenFOAM, with assumed boundary conditions for both the coolant velocity and heat fluxes, using the power distribution of the Serpent output as heat source.

It is clear from this approach that some aspects of the multiphysics coupling existing in the nuclear core are treated in an approximated way, due to the different domain studied by the two computational tools. In

particular, the power distribution within a fuel assembly is strongly influenced by its localization within the core, as it is clearly visible in Fig. 5.1, where the power map as produced by Serpent is provided, with a zoom on three assemblies in different position within the core.

The position within the core, and resulting power map, has of course a large influence on the boundary conditions to be imposed on the CFD calculation for the single FA, as summarized in Fig. 5.2: while the boundary conditions for velocity, temperature and pressure could be assumed in a reasonable way from the characteristics of the coolant circuit (redistribution plates, lead plenum, …) the boundary heat flux on the 6 sides of the hexagonal assembly is strongly related to its position in the core.

A second aspect to be carefully considered in the analysis of the Serpent-OpenFOAM results is the effect of the temperatures assumed in the Serpent calculation: as a first step, the power map in Serpent has been obtained by setting all materials within the core at room temperature. If the same k_{eff} core calculation is performed at a higher temperature, more representative of the real situation when the system is at power, such power map is spatially distorted, due to temperature feedback, and the multiplication constant itself is modified, as can be seen in Fig. 5.3 and Fig. 5.4.

The simulations at different temperatures allow to assess the role of temperature on the neutronic behavior of the core; however, in real situations the temperature distribution in the core is not homogeneous, therefore the Serpent simulations at constant T provide an approximate picture of the real situation within the core at a certain power level. This limitation has been overcome by a simulation strategy involving the exchange of information between Serpent and FRENETIC, as will be described in the next section.

Last, but not least, the whole Serpent-OpenFOAM approach is simulating the multiphysics core behavior in steady-state conditions, and the possibility to use Monte Carlo codes in the frame of time-dependent simulations is still coveted, but not envisaged on the short-medium terms, for both computational reasons and theoretical aspects related to the stochastic sampling process.

In conclusion, the Serpent-OpenFOAM coupled computational tool is extremely useful to provide reference results in steady-state and allow benchmarking of more approximate models and tools, leaving to such tools the work of simulating the time-dependent full-core behavior, as in the case of FRENETIC.

5.2   Benchmark of FRENETIC against Serpent-OpenFOAM

5.2.1   NE-TH coupling and simulation strategy

The FRENETIC code, as mentioned before, performs the coupled NE-TH simulation of the full-core made of hexagonal FAs. The coupling is achieved by exchanging, at times steps properly defined in accordance to the time scales of the phenomena, information regarding the power distribution (NE information provided to the TH module) and the temperature distribution (TH information provided to the NE module). Such information is homogeneous at the level of the FA on the horizontal plane for different heights, consistently with the coarse mesh neutronic approach, and interpolations are performed if more spatially refined data are required. The temperature feedback on neutronics is evaluated by direct modification of the multi-group cross sections starting from a database at different temperature for both fuel and coolant and performing multidimensional interpolations of the type:

$$\Sigma(T_f, T_c) = \Sigma(T_{f,0}, T_{c,0}) + \frac{\partial \Sigma}{\partial T_f}(T_f - T_{f,0}) + \frac{\partial \Sigma}{\partial T_c}(T_c - T_{c,0}) \tag{5.1}$$

where the derivatives are evaluated as incremental ratios on the existing temperature grid. The cross section values in the database have been generated by Serpent runs at different temperatures (the same kind of runs

used to illustrate previously the hot and cold conditions), adopting a 5-group energy discretization as in [5.9]. The information on the energy cuts adopted at this stage of the work is provided in Tab. 5-1.

As already discussed above, the Serpent-OpenFOAM coupling suffers from the fact that the neutronic calculation is carried out at the full-core level, with the CFD simulation is limited to a single FA. Therefore, the temperature distribution obtained in OpenFOAM is not directly usable to provide the correct input to Serpent for a full-core k_{eff} calculation in the real condition of the core at power. On the other hand, if a FRENETIC run is performed at the full-core level, the temperatures for both fuel and coolant are obtained for each FA at different heights. Therefore, we decided to take profit of this information provided by FRENETIC, implementing a coupling scheme involving all the codes considered in the frame of this work. In summary:

1. Serpent runs at different homogeneous temperatures have been performed (as said above) to generate the multigroup cross sections to be used in FRENETIC;
2. The nuclear data generated have been used in FRENETIC to solve the steady-state problem, providing both the power map and the temperature distribution;
3. The information on the temperature spatial distribution has been introduced into the input Serpent file, thus allowing to have a NE reference simulation with the same temperatures as the FRENETIC run, thus allowing a consistent neutronic benchmarking of FRENETIC;
4. The power distribution as generated by Serpent has been used as input for the CFD OpenFOAM run, using more consistent thermal boundary conditions as provided by FRENETIC;
5. The resulting CFD calculation has been compared to the FRENETIC result, as a benchmark on the single FA performed assuming a fixed internal power source.

These five steps are graphically summarized in Fig. 5.5.

Phase 3 of this process has required a certain amount of additional work and optimization. The FRENETIC run generates the temperature value for each FA at different heights for both the coolant and the fuel. If such information is introduced directly into Serpent, the input file should identify each single mesh used in FRENETIC as a separate universe in Serpent, with its own temperature and composition and the resulting memory requirement would become prohibitive. Therefore, a set of concentric regions has been identified, each characterized by a single temperature value (verifying that the maximum temperature difference between FAs within the same radial region was below 1K). Axially, all the materials composing the regions below the active zone have been assumed to be at 673 K (i.e., the inlet temperature). Similarly, regions above the active zone share the same temperature, which is equal to the average core outlet temperature. The active region of each FA has instead been subdivided into 10 axial segments, each characterized by the corresponding average temperature evaluated by FRENETIC. In this way, a more limited number of regions has been generated, allowing to run a k_{eff} calculation in Serpent with a physically significant temperature distribution. In Fig. 5.6 the radial concentric regions are shown, while Fig. 5.7 shows the axial temperature distribution for both the fuel and the coolant obtained with FRENETIC and then introduced into the Serpent input file.

5.2.2 FRENETIC-Serpent (NE) comparison

In Fig. 5.8 the power distribution along a specific radial direction in the ALFRED core simulated by both FRENETIC and Serpent is provided. The corresponding axial profile is given in Fig. 5.9, where again the Serpent results have been averaged on the same spatial domain of the FRENETIC results, to allow a fair comparison.

The analysis of the radial distribution shows a flatter profile for FRENETIC as compared to Serpent. To understand these discrepancies, it must be noted that in the two models the extension of the radial reflector is

different, in the sense that the dimension of the reflector in Serpent has been reduced as compared to FRENETIC, in order to reduce the computational time. As a consequence, the model in FRENETIC with a larger reflector may produce a more relevant source of neutrons reflected back into the core, with a consequent lesser spatial gradient along the radius. This partial inconsistency has been overcome in the second stage of the work, described in the next section.

The axial profiles instead show around 4% of average underestimation in the linear power for the most loaded assembly, and conversely an overestimation in the peripheral location. These effects are the counterpart of the flatter radial profile observed before, which is to be associated for sure to the reflector role. Moreover, the analysis of the temperature obtained in the calculations show that the original choice of the temperature points for the cross section database (673K and 1073K) might not be optimal for the interpolations to be performed in FRENETIC. These observations have guided the following work for an upgraded ALFRED model to be used in FRENETIC.

5.2.3   FRENETIC- OpenFOAM comparison

In the last phase of the comparison the TH results of FRENETIC have been tested against an OpenFOAM run performed with consistent boundary conditions on the single FA and same imposed internal power source. The comparison of the results in terms of pressure drop and temperatures is given in Fig. 5.10 and Fig. 5.11.

From Fig. 5.10 it can be seen that a good agreement between pressure losses is achieved, even though a discrepancy exists in the first part of the graph. This is associated to the fact that the OpenFOAM domain only includes the active region of the core (from z=1 m to z=1.4 m). Indeed, since periodic boundary conditions have not been employed in the CFD simulation setup, there exists a hydrodynamic entry region where the pressure loss per unit length is larger than the one calculated in FRENETIC, which employs a correlation developed for the fully developed flow region. The temperature profiles on the other side show some discrepancies. In particular, since the power source is fully consistent between the two models, the discrepancy between the coolant temperatures could be associated to an inconsistent implementation of the boundary condition regarding the heat flux, q_{IHX}, in the OpenFOAM simulation. The difference between the average fuel temperature could instead be associated to different implementation of the thermal resistances associated to the gap and the clad. These aspects will be addressed in future work.

5.3   FRENETIC model for ALFRED

The activities performed in the frame of the Serpent-OpenFOAM/FRENETIC comparison have allowed identifying a series of issues, related to the core modelling in Serpent and the generation of information useful for FRENETIC, which have guided a second activity aiming at providing an improved model of ALFRED in FRENETIC. This optimized model can be thus adopted in the future for safety and stability analyses. It can be said that the FRENETIC model described in the previous sections was indeed somewhat simplified, since the focus of that part of the work was to provide a fair comparison between FRENETIC and SERPENT-OpenFOAM rather than a high-fidelity model of the reactor itself. The comparison of results then highlighted the main issues that should be addressed to provide a FRENETIC model consistent with the real configuration and suitable to perform time-dependent simulations. We have then worked on these improvements, both for what regards the geometrical characteristics of the core and for the proper generation of multigroup cross sections. In the following, the details of these additional effort are described, and the resulting improved modelling of ALFRED core is benchmarked against a detailed transport model. Finally, results of a steady-state coupled (NE + TH) calculation are shown.

5.3.1   Serpent-2 model for multi-group nuclear data evaluation

As mentioned above, running the FRENETIC code requires to generate a consistent set of nuclear data [5.3]. In particular, few-group cross sections are needed for each of the materials present in the reactor. For this purpose, the Monte Carlo code Serpent-2 [5.5] is used to collapse the continuous energy data into six groups and to homogenize them over the reactor heterogeneous regions.

The collapsing (in energy) and homogenization (in space) procedure is carried out (similarly to the previously descripted work) by means of a detailed 3D model of the ALFRED reactor, see Fig. 5.12. The core geometry and material composition are consistent with the end of cycle (EOC) configuration (fully withdrawn control rods) provided by [5.8], whereas any missing data was retrieved within the framework of a collaboration with Dr. M. Sarotto from ENEA [5.10]. It is worth mentioning that, during this collaboration, the correct implementation of the ALFRED geometry and material composition in the Serpent model has been assessed by means of a benchmark against a pre-existing ERANOS model.

As far as the statistical convergence of the simulation is concerned, input parameters have been tuned according to convergence studies. In particular, 500 inactive cycles and 1000 active cycles have been employed, with 10^6 particle histories per cycle. These simulation settings guarantee a good fission source convergence, as shown in Fig. 5.13. The adopted indicators were implicit and explicit k_{eff} and Shannon entropy.

After a Serpent simulation has correctly been set up, suitable tallies (both in energy and in space) must be defined to generate the spatially homogenized and energy collapsed cross sections. The procedure is then repeated assuming different temperatures for coolant and fuel to reconstruct the cross section database required by FRENETIC. The issues, and corresponding fix-up, regarding these aspects are here described.

5.3.2 Energy collapsing and spatial homogenization procedures in Serpent-2

Energy collapsing. As far as the energy collapsing is concerned, the calculation of effective cross sections, as well as other nuclear data, is carried out by performing an estimation of the required reaction rate on an energy interval and then dividing it by the flux average on the same interval. This ratio provides an effective cross section in that energy range that (for an infinite medium) exactly preserve the reaction rate. The choice of the boundary of such energy intervals is a delicate task: for the present work we have adopted at first a group subdivision reported in previous studies on LFRs [5.9], while in this second, more refined analysis, an observation of the neutron spectra in the most important regions of the reactor core has been performed. Fig. 5.14 reports such neutron spectra evaluated with the Serpent-2 run at 673 K. In the same figure the original flux subdivisions have been introduced, allowing to highlight a relevant limit of that energy discretization: the fifth group, with upper energy bound at around 10^{-2} MeV, is able to describe the neutron behavior in the fuel regions, but it appears not adequate for the description of the outer regions. In fact, the presence of a larger portion of thermalized neutrons in the reflectors and dummy elements is completely disregarded if a single energy group is assumed down from 10^{-2} MeV.

To fix this issue an additional energy group has been added, considering that six groups are sufficient to approximate the behavior of the energy distribution within the various materials. The resulting energy group boundaries are in Tab. 5-2.

Spatial (radial and axial) homogenization. The energy collapsed cross sections need to be homogenized on spatial regions consistently with the structure of the FRENETIC code (i.e. homogeneous on the hexagonal fuel assembly and axially heterogeneous according to the neutronic coarse meshing). Starting from the core modelling in Serpent as detailed in Fig. 5.12, some regions (specifically the ones far from the fission source) have been merged in a single universe for the cross section tally, in order to achieve a better statistics. In particular, the external lead (in brown in Fig. 5.12), the barrel (in dark grey) and the dummy element region (in light grey), are each considered as a unique radial region. Moreover, the 12 control rods are grouped together as a single detector. The same choice has been made for the 4 safety rods. For the inner fuel,

instead, it has been assumed that cross sections averaged on a subset of FAs (indicated in blue in Fig. 5.12) could be representative of the entire zone. The same strategy has been adopted for the outer fuel region, for which the representative FAs are indicated in red. It should be noticed that fuel assemblies considered for the homogenization are the ones surrounded by the same kind of assemblies. This choice was based on a compromise between a homogenization over the whole inner and outer fuel rings and an assembly-wise homogenization, which would certainly provide a higher but probably unnecessary detail level.

The few-group cross sections evaluated by Serpent have been at first homogenized axially according to the finest achievable discretization, which takes into account all the different regions, as shown in Fig. 5.15. However, the axial discretization employed for the FRENETIC calculation is in general different -and coarser- with respect to the one introduced in the transport simulation. This is due to the requirement of avoiding excessively optically thin regions, which would hinder the convergence of the nodal method employed for the spatial solution of the diffusion problem in FRENETIC. Each of the coarse axial regions defined in the FRENETIC model requires a single spatial value for the multi-group cross sections, which should therefore be mapped to the ones computed by the transport model for the fine subdivisions composing that coarse axial region. This is performed by means of a suitable spatial homogenization procedure, which is carried out in such a way as to preserve the reaction rate for each material.

This leads to the calculation of a new set of cross sections that are averaged on the flux of each material in the "macro-region", i.e. in the coarse axial mesh. Since the flux tallies calculated by Serpent are integrated on the entire volume of each material and collapsed on the energy grid division, there are six values of integrated flux in the volume where the specific material lies, as well as the cross section. The spatial homogenization is then performed according to this formula (for the i-th axial mesh of a given FA):

$$\widetilde{\Sigma_{g,\iota}} = \frac{\int_{V_i} d\boldsymbol{r}\,\overline{\Sigma_g}(\boldsymbol{r})\overline{\phi_g}(\boldsymbol{r})}{\int_{V_i} d\boldsymbol{r}\,\overline{\phi_g}(\boldsymbol{r})} \approx \frac{\sum_{j=1}^{N}\left(\overline{\Sigma_{g,j}}(\boldsymbol{r})\overline{\phi_{g,j}}(\boldsymbol{r})h_{SERP}\right)}{\sum_{i=1}^{N}\left(\overline{\phi_g}(\boldsymbol{r})h_i\right)}$$

where h_i is the axial length of the FRENETIC mesh and h_{SERP} is the length of the j-th Serpent axial region which falls within the i-th axial mesh of FRENETIC. The index j goes from 1 to N, where N is the total number of materials (i.e. Serpent regions) localized in the i-th axial region of the FRENETIC mesh. From the mathematical point of view, the integration should be performed on the correct volume where the homogenization takes place, but since the transport model gives a single value of the group-averaged flux for each material, it was assumed that the integrated flux was simply proportional to the axial length. This means that the flux for the g-th group is averaged as if it was constant over the volume.

5.3.3 Temperature dependence of cross section

A final remark concerns the evaluation of nuclear data at different temperatures. This is associated to the fact that the FRENETIC code evaluates the thermal feedback by interpolating nuclear cross sections between at least two temperatures according to the local temperature of the fuel and coolant. The fuel and coolant temperatures considered for the generation of this cross section library are listed in Tab. 5-3. The table lower triangular layout is due to the fact that the fuel temperature is always greater than the coolant one, at least for the present applications. The temperature of the structural materials is specified in Serpent according to the arithmetic average of the coolant and fuel temperatures.

5.3.4 Steady-state results of the FRENETIC model for the ALFRED reactor

Steady state NE calculation. The nuclear dataset obtained by means of the procedures outlined in the previous sections has been employed to feed the neutronic model of the FRENETIC code. The new dataset is distributed according to the radial "zoning" presented in Fig. 5.16. The axial "macro-regions" indicated in Fig. 5.15, which are each characterized by a single spatial value of the cross section, are then subdivided in a number of sub-nodes which is sufficient to ensure the grid independence of the thermal-hydraulic solution.

The new model developed for ALFRED in the FRENETIC code is at first tested against a reference result in steady-state, represented by the Serpent calculations which were performed for the generation of the cross section dataset.

The benchmark has been performed by imposing the same thermal power of 300 MWth and corresponding boundary conditions for the two calculations (i.e. the transport calculation performed in Serpent and the coarse-mesh diffusion calculation performed in FRENETIC). Since this benchmark is only intended to verify the correct behavior of the NE module, the temperatures of all the materials in the core in FRENETC have been set at 673 K, running the NE module of FRENETIC in standalone mode. It is also worth mentioning that, although a photon transport model is now available in FRENETIC [5.4], it has been turned off for the purpose of guaranteeing a fair comparison between the two simulations. It must be noticed that the core modelled in FRENETIC (Fig. 5.16) includes all elements where lead is flowing, thus excluding the barrel and dummies. This limitation is due to the fact that the TH module is not able to simulate assemblies with stagnant lead nor solid elements such as the barrel. This limitation is however fictitious at this stage, since the code is running in NE standalone, and it will be relaxed at a second stage.

The effective multiplication eigenvalue computed by the two codes is first compared. Serpent calculates 1.08122 ± 3pcm, whereas FRENETIC calculates 1.07673, showing a rather good consistency. The fission power source computed by the two codes has been compared in Fig. 5.17 and Fig. 5.18. The choice of comparing this quantity is physically significant, since the power source represents the exchange variable from the NE module to the TH module in multiphysics simulations. The radial distribution is compared in Fig. 5.17; a qualitative comparison confirms that the FRENETIC code is able to reproduce the radial power distribution: for instance, for the EOC configuration here considered, the maximum value of the power per FA is not located at the core center, but at the beginning of the outer fuel zone, which is more enriched. This peculiar aspect is correctly recovered by FRENETIC as compared to Serpent.

A more systematic comparison is shown in Fig. 5.18. In particular, the plot on the left shows the axial distribution of the computed linear power for the same three FAs selected in Fig. 5.9. The plot on the right shows instead a map of the relative error between the power per FA computed by the two codes. The relative difference rather than its absolute value is here presented, since this choice allows to highlight the fact that FRENETIC overestimates the power per FA at the core center, whereas it underestimates it for the FAs which are located at radially outer positions. This phenomenon is basically of the same kind of the one observed when comparing FRENETIC and Serpent in the first part of the work (see Fig. 5.8), and the reason was identified in the different extension of the domain between the two models, partly explaining the different multiplication constants between the two calculations.

In this case, the possible reasons for this discrepancy are the space homogenization, the energy homogenization and, more importantly, the absence of the barrel and external lead in the FRENETIC model. As a consequence, the FRENETIC model for ALFRED has been improved by introducing the barrel and dummy elements, bearing in mind that this extended computational domain is feasible for NE calculations but suffer the limitation of the TH module.

Improved neutronic model. The radial distribution of the relative error between the power computed by FRENETIC and the result of the transport code has suggested the need to include also the barrel and the lead outside the barrel in the simulated domain. This has been achieved by adding fictitious FAs corresponding to the latter two regions, see Fig. 5.19. In this way, the radial "zoning" of the core has been made fully consistent with the one employed in the Serpent model (Fig. 5.12).

The comparison between the effective multiplication eigenvalue computed by the two codes already outlines the higher fidelity of this improved model to the SERPENT reference. In particular, the value computed by

FRENETIC (k_{eff}=1.08194 as opposed to the previous value of 1.07673) is in very good agreement (around 70 pcm difference) with the 1.08122±3pcm evaluated by Serpent. The results of the NE FRENETIC run for the improved ALFRED model show, as expected, that the relative error on the computed power has been greatly reduced by taking into account the presence of the barrel and of the lead outside the barrel, see Fig. 5.20. The left plot shows a very good agreement for the axial distribution of the linear power along all the three selected FAs. The radial plot of the relative error on the right also shows a significant error reduction. Moreover, the bias previous observed is no longer appearing. This suggests that the remaining source of errors must be attributed to the energy collapse or spatial homogenization procedures carried out to generate the dataset for FRENETIC. To address this issue, further studies are foreseen, which will focus on:

- Improving the choice of the few energy groups, e.g. by means of genetic algorithms [5.10];
- Improving the choice of the tallies to ensure higher fidelity in the description of the radial composition of the core.

Multiphysics FRENETIC calculation. After the successful neutronic benchmark exercise, a steady-state simulation in multiphysics mode, i.e. by taking into account the NE-TH coupling, has been performed. Since, as already mentioned, the FRENETIC TH module is currently not capable of simulating the presence of the barrel, the model without barrel and external lead is chosen for performing coupled simulations.

Results for the variation of the power distribution according to feedback effects are shown in Fig. 5.21, left. Temperature distributions in three representative channels are shown in Fig. 5.21, right. In the latter, the temperature behavior is a clear response to the stepwise axial distribution of the power. For the sake of completeness, Fig. 5.22 shows a radial map of the power per FA (left) and maximum fuel temperature (right) as evaluated in the multiphysics calculation.

5.4   Conclusive remarks

The work performed in this year, partially in collaboration with the colleagues at PoliMI, has allowed to carry forward the development of the FRENETIC code, focusing the effort on the efficient and accurate simulation of the ALFRED core design.

The benchmarking activity with the coupled Serpent-OpenFOAM model has allowed to assess the accuracy of FRENETIC full-core simulation, also highlighting some aspects requiring further R&D work. The following work performed, aiming at improving the ALFRED model in FRENETIC, has produced satisfactory results, with a significant improvement in the prediction accuracy for what regards NE simulations and pointing out the next step to be taken in this perspective.

Based on these results, some of the identified further developments are:

- Extension of the TH in order to allow the simulation of assemblies with stagnating lead in coupled NE-TH mode;
- Improvement of the energy group structure with more advanced methodologies, such as the one in [5.10];
- Improvement of the axial representation of the core, starting from the tally definition in Serpent.

However, we believe that the present state of the FRENETIC code and its associated model for the ALFRED core can provide useful contribution to the analysis of the ALFRED core, performing both steady-state and time-dependent multi-physics simulations of safety relevant scenarios for LFR.

Energy group	Upper Energy [MeV]
1	19.64
2	1.3534
3	$1.8316 \cdot 10^{-1}$
4	$6.7379 \cdot 10^{-2}$
5	$9.1188 \cdot 10^{-4}$

Tab. 5-1 – Upper energy of the 5-group discretization adopted in the generation of cross sections for the Serpent-OpenFOAM/FRENETIC comparison.

Group	Upper E bound [MeV]	Lower E bound [MeV]
1	20	1.353
2	1.353	$1.8316 \cdot 10^{-1}$
3	1.8316e-1	$6.7379 \cdot 10^{-2}$
4	6.7379e-2	$9.1188 \cdot 10^{-3}$
5	9.1188e-3	$2 \cdot 10^{-5}$
6	2e-5	$1 \cdot 10^{-11}$

Tab. 5-2 – Resulting energy group boundaries.

Tcoolant	673	1073	1473
Tfuel			
673	x		
1073	x	x	
1473	x	x	x

Tab. 5-3 – Temperatures values adopted for the Serpent runs used to evaluate the few-group cross sections.
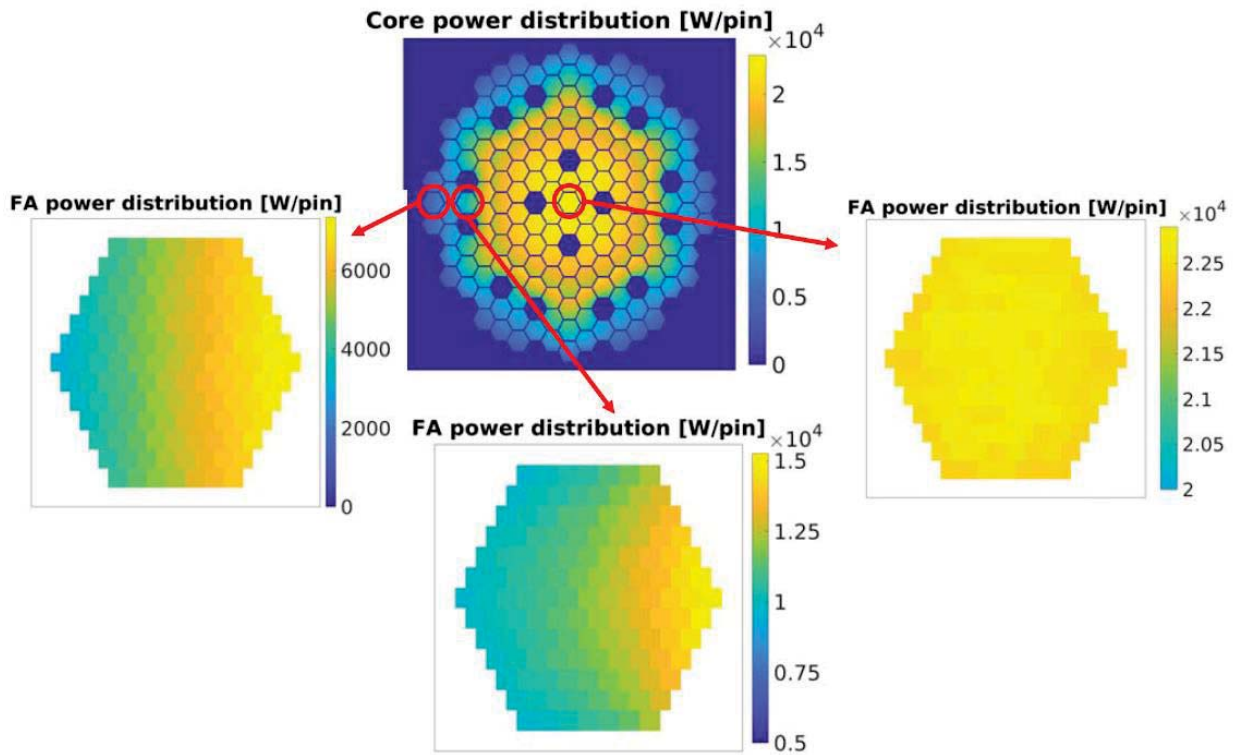
Fig. 5.1 – Power map of the ALFRED core generated by Serpent (top graph) and power distribution within three FA at different position in the core. The different spatial gradients are clearly visible.
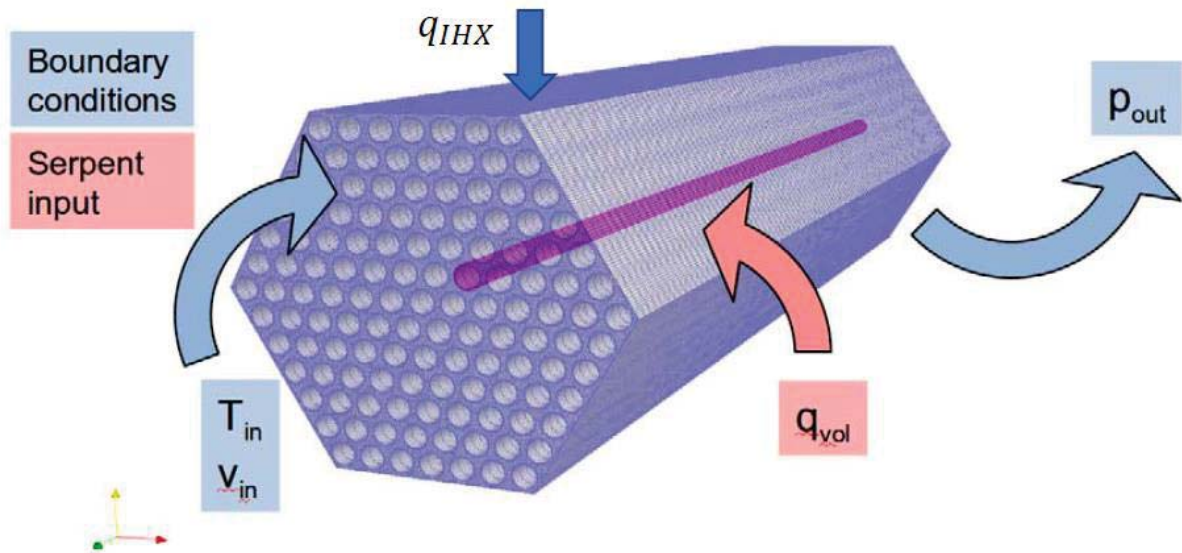
Fig. 5.2 – OpenFOAM CFD model of the single FA of ALFRED: the heat source q_{vol} is retrieved from Serpent, boundary conditions for velocity, temperature and pressure need to be provided, as well as the inter-assembly heat flux q_{IHX}.
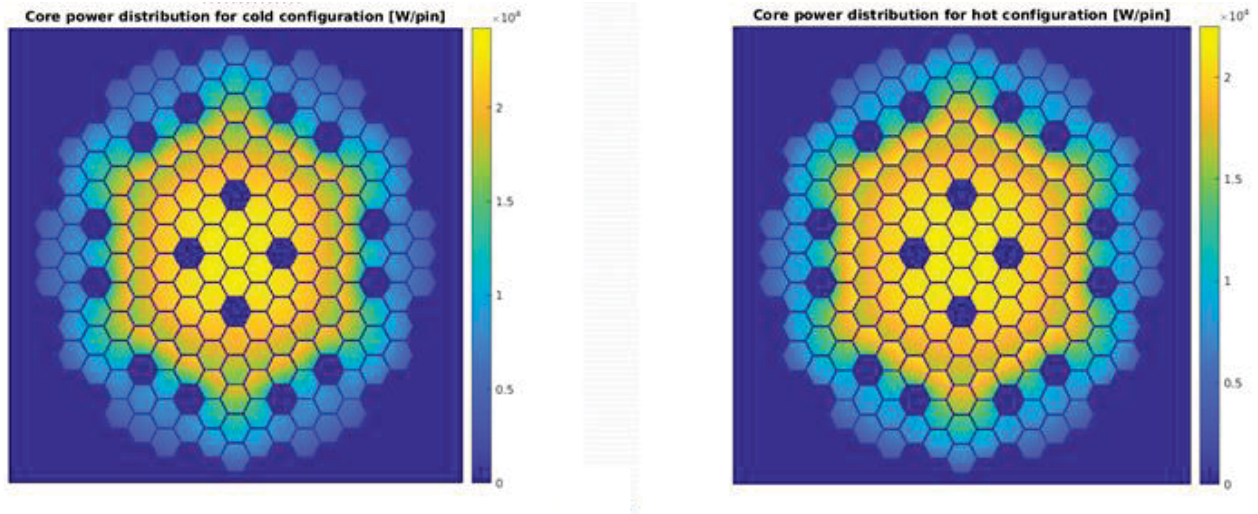
Fig. 5.3 – Serpent radial power map at mid-height in the core at cold condition (T=673K), associated to k_{eff}=1.01027±3pcm (left); Serpent radial power map at hot condition (T=1073K), associated to k_{eff}=1.00772±3pcm (right).
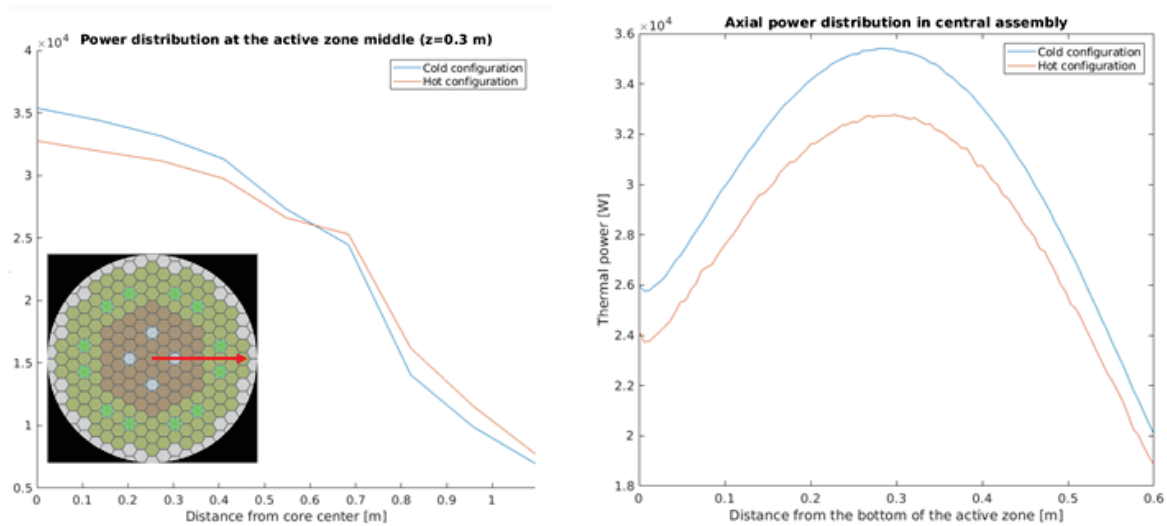
Fig. 5.4 – Comparison of radial (left) and axial (right) power maps calculated with Serpent in cold and hot conditions.
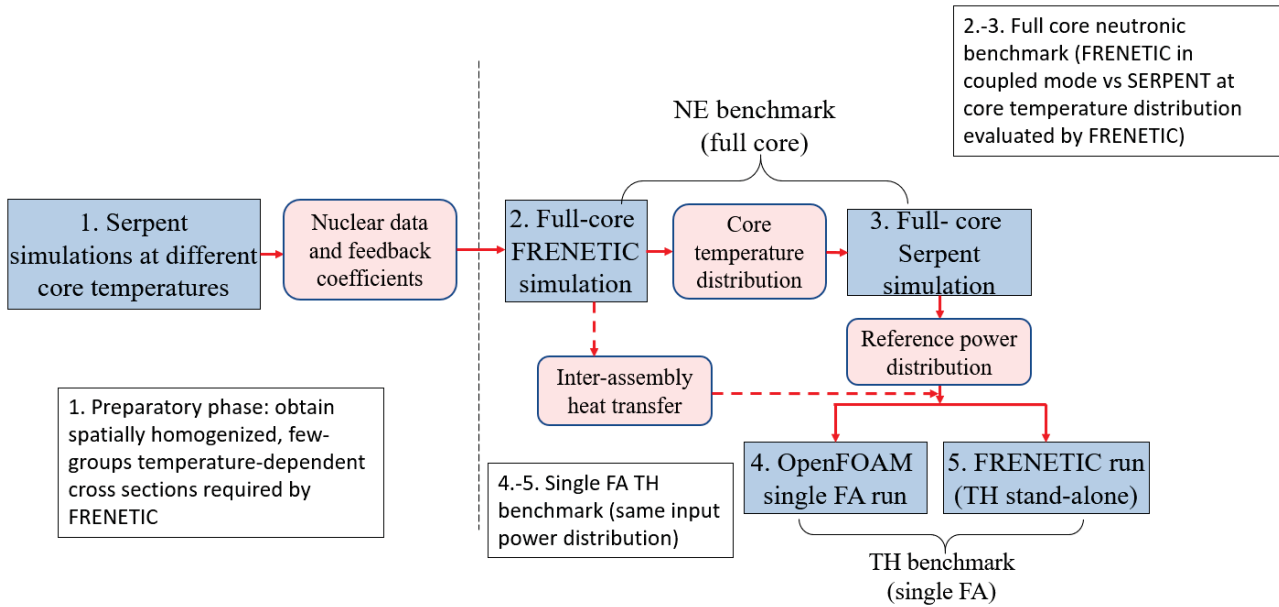
Fig. 5.5 – Coupling scheme and definition of simulation phases.
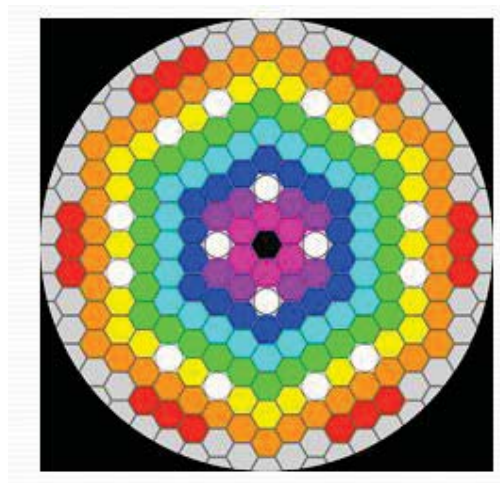
Fig. 5.6 – Identification of the concentric regions at the same temperature (generated by FRENETIC) adopted for the Serpent run.
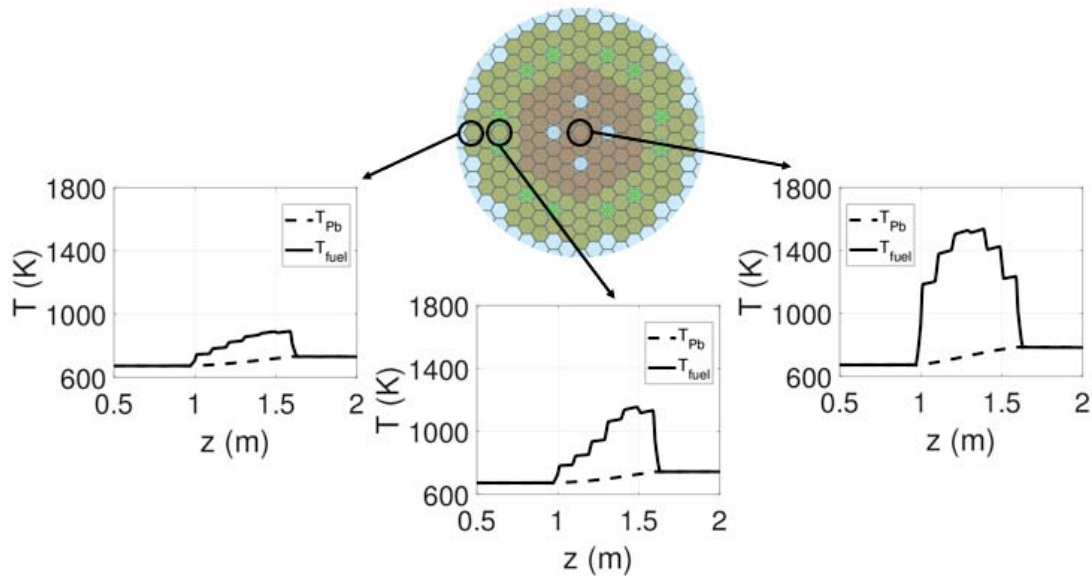
Fig. 5.7 – Axial temperature for fuel and coolant in three different FAs of the ALFRED core calculated with FRENETIC.
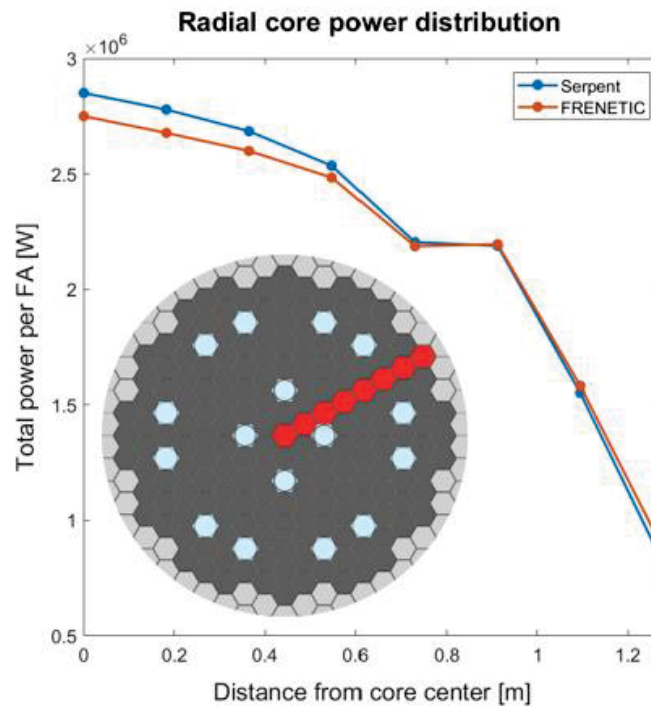
Fig. 5.8 – Radial power distribution for each FA evaluated with FRENETIC (red), as compared with the Serpent results averaged on the same spatial domain (blue). The identification of the radius along which the comparison is performed also provided.
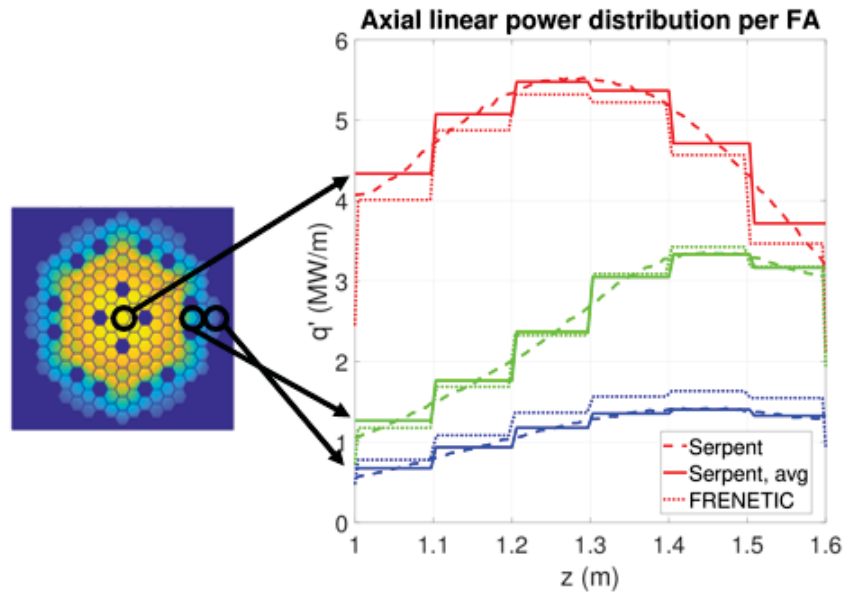
Fig. 5.9 – Axial power distribution for three different FAs evaluated with FRENETIC (dotted), as compared with the Serpent results (dashed), also averaged on the same spatial domain (solid). The localization of the observed FAs is also provided.
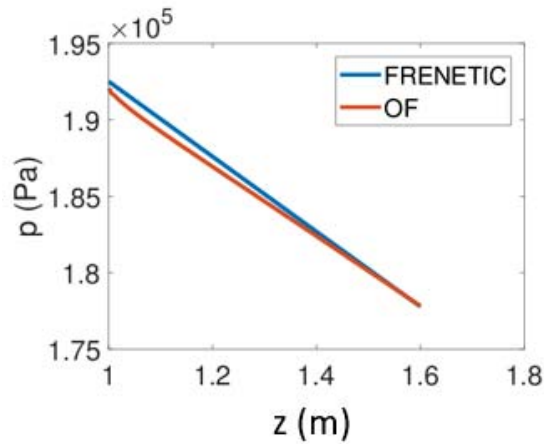
Fig. 5.10 – Pressure drop along the central FA calculated by FRENETIC and OpenFOAM (OF in the legend).
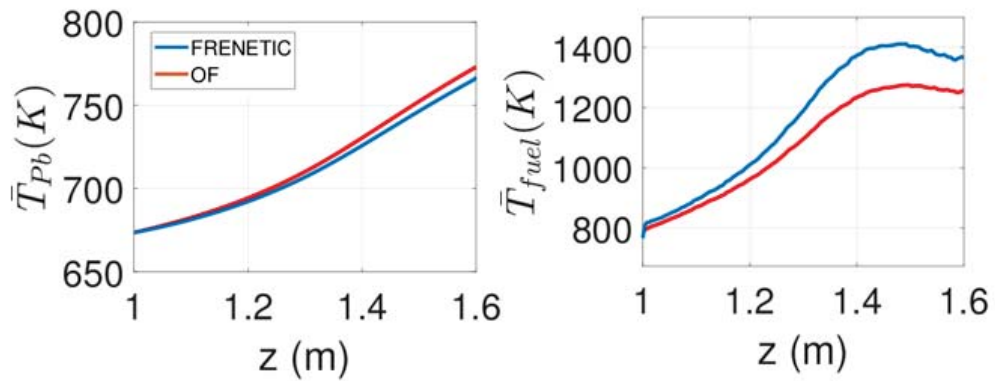
Fig. 5.11 – Axial temperature profile for the coolant (left) and the fuel (right) along the central FA calculated by FRENETIC and OpenFOAM (OF in the legend).
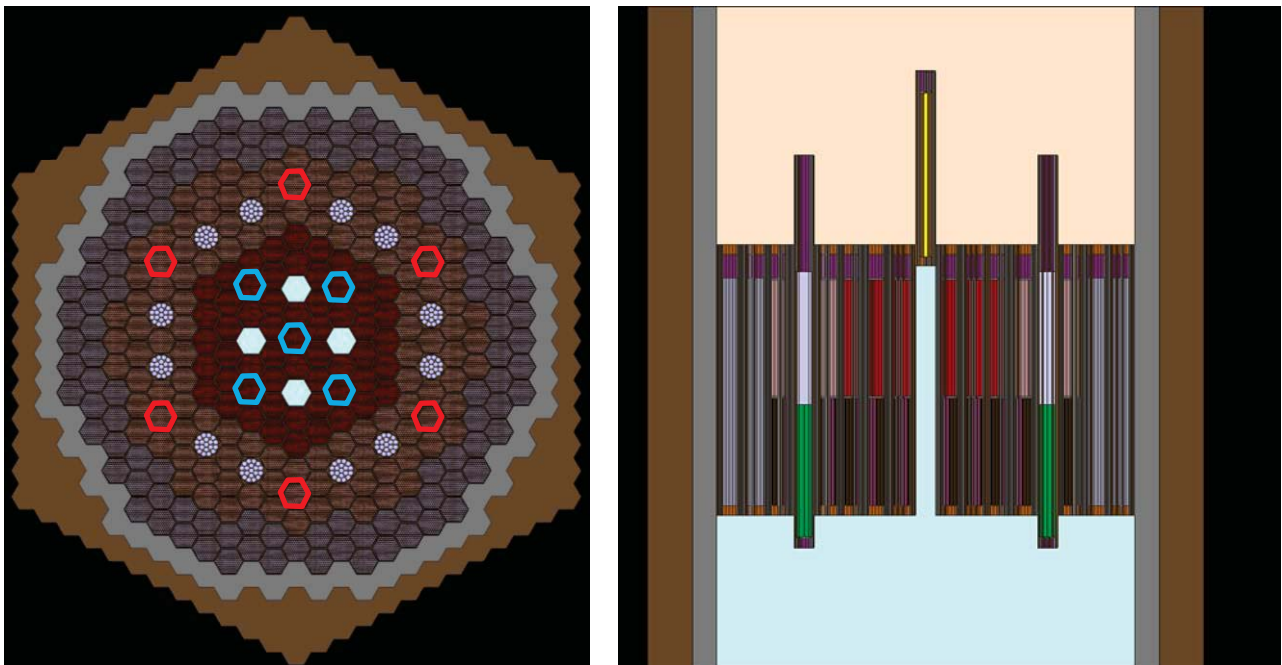
Fig. 5.12 – 1 Radial (left) and axial (right) view of the ALFRED configuration simulated in Serpent.
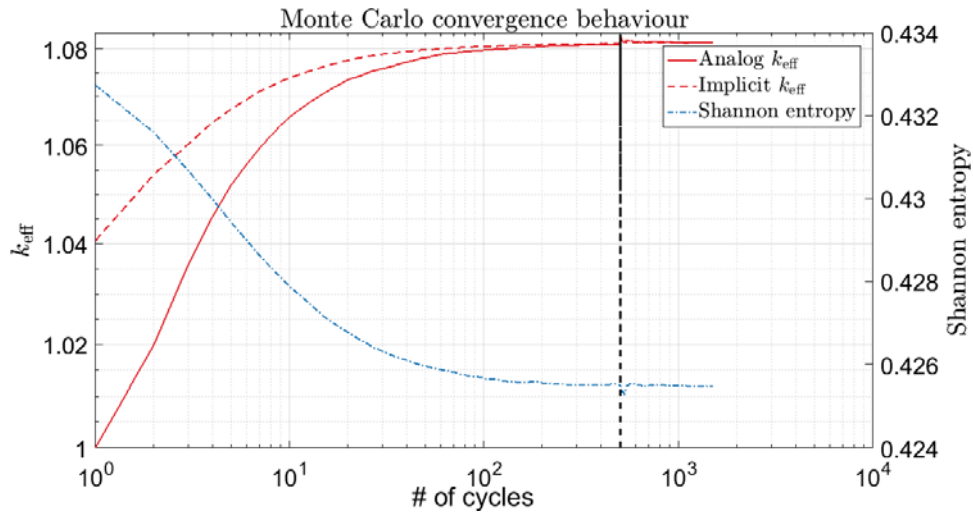
Fig. 5.13 – Monte Carlo Serpent convergence behavior. The vertical black line indicates the boundary between inactive and active cycles.
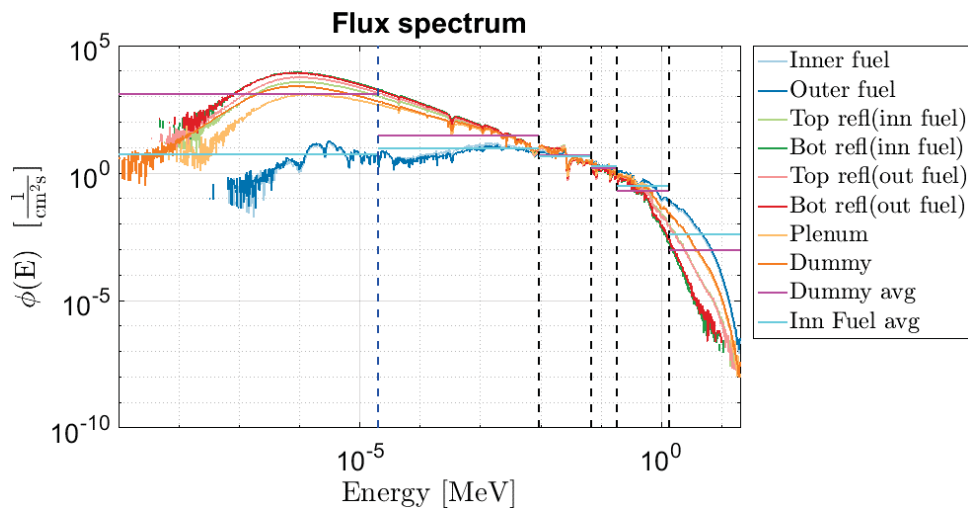
Fig. 5.14 – Neutron flux spectra computed by Serpent for selected regions of the core. Black dashed lines identify the 5-group energy subdivision originally adopted, while the blue dashed line identifies the additional group added to better account for the reflector spectrum.

z (cm)	IF		OF		CR		SR		DD	
340										
	IF_TOP_REF		OF_TOP_REF		CR_TOP_REF		SR_TOP_REF		DR_TOP_REF	
							SR_SPRING			
296							SR_TOP_INS			
							SR_ACT			
264										
					CR_SPRING					
	IF_TOP_PLUG		OF_TOP_PLUG						DR_TOP_PLUG	
212	IF_SPRING		OF_SPRING						DR_SPRING	
							SR_BOT_PLUG			
					CR_DUMM		SR_BOT_REF			
200	IF_TOP_INS		OF_TOP_INS						DR_DUMM	
	INN_FUEL		OF_FUEL							
140										
	IF_BOT_INS		OF_BOT_INS							
140	IF_PLEN		OF_PLEN							
					CR_ACT					
136										
	IF_BOT_PLUG		OF_BOT_PLUG						DR_BOT_PLUG	
68	IF_BOT_REF		OF_BOT_REF						DR_BOT_REF	
					CR_BOT_INS					
					CR_BOT_PLUG					
0					CR_BOT_REF					

Fig. 5.15 – Axial discretization for the FRENETIC model (black lines) on top of fine Serpent axial discretization for each radial region.

IF = Inner Fuel
OF = Outer Fuel
CR = Control Rod
SD = Safety Rod
DD = Dummy element
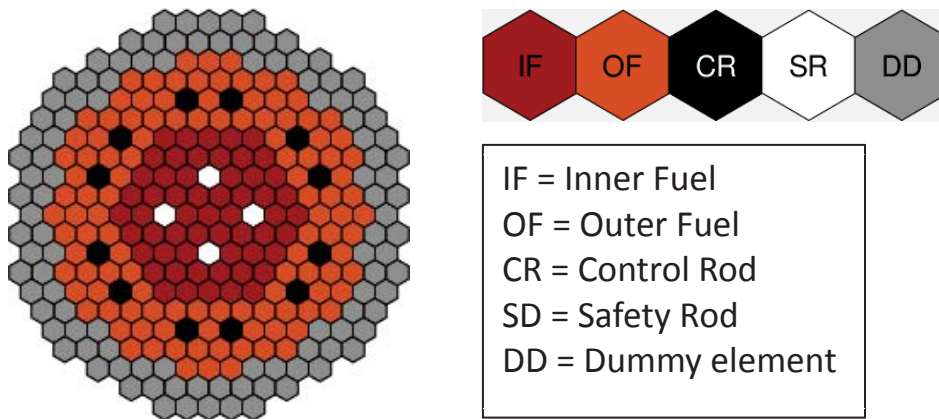
Fig. 5.16 – FRENETIC model of the ALFRED core.
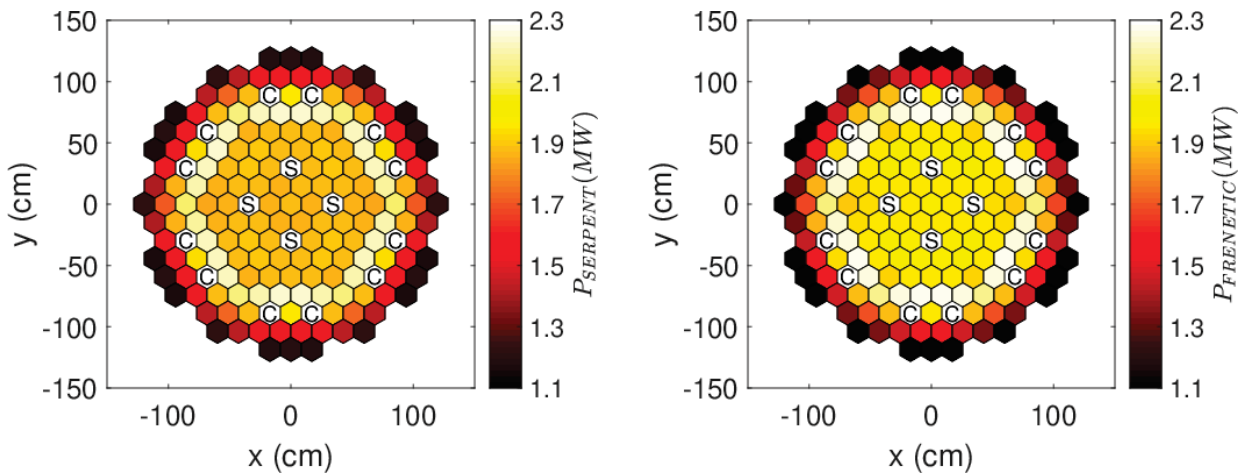
Fig. 5.17 – Radial power map (in MW per FA) computed by Serpent (left) and FRENETIC (right)
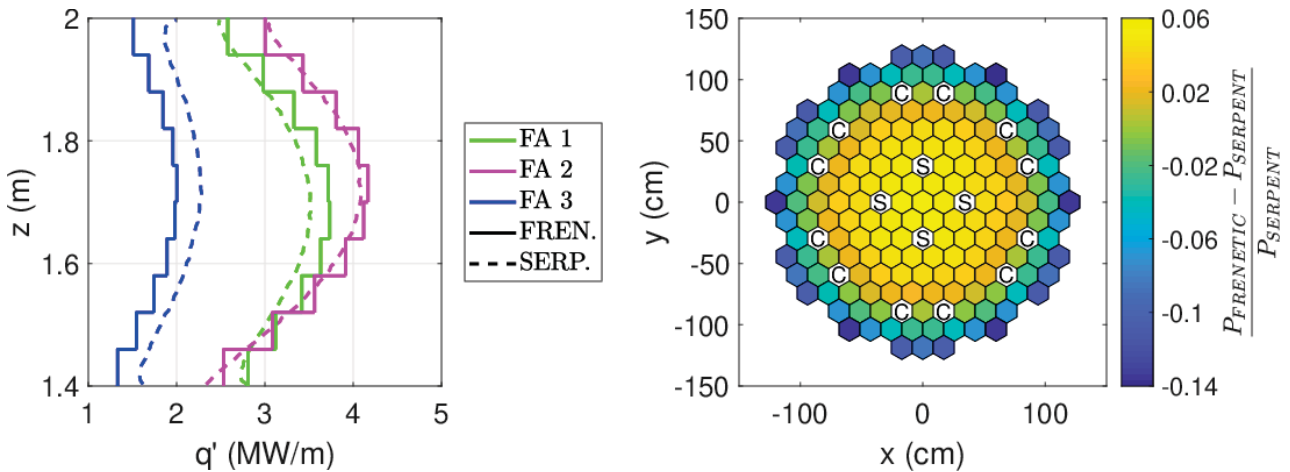
Fig. 5.18 – Comparison between the linear power calculated by Serpent and FRENETIC for three selected FAs (left) and radial map of the relative error between the power per FA evaluated by the two codes (right).

IF = Inner Fuel
OF = Outer Fuel
CR = Control Rod
SD = Safety Rod
DD = Dummy element
BA = Barrel
LL = External Lead
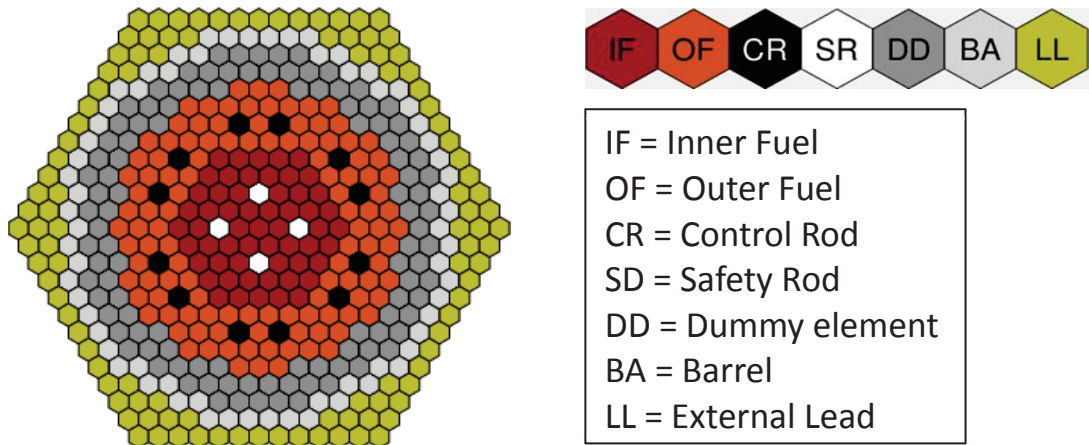
Fig. 5.19 – Radial scheme of the improved FRENETIC model of the ALFRED core.
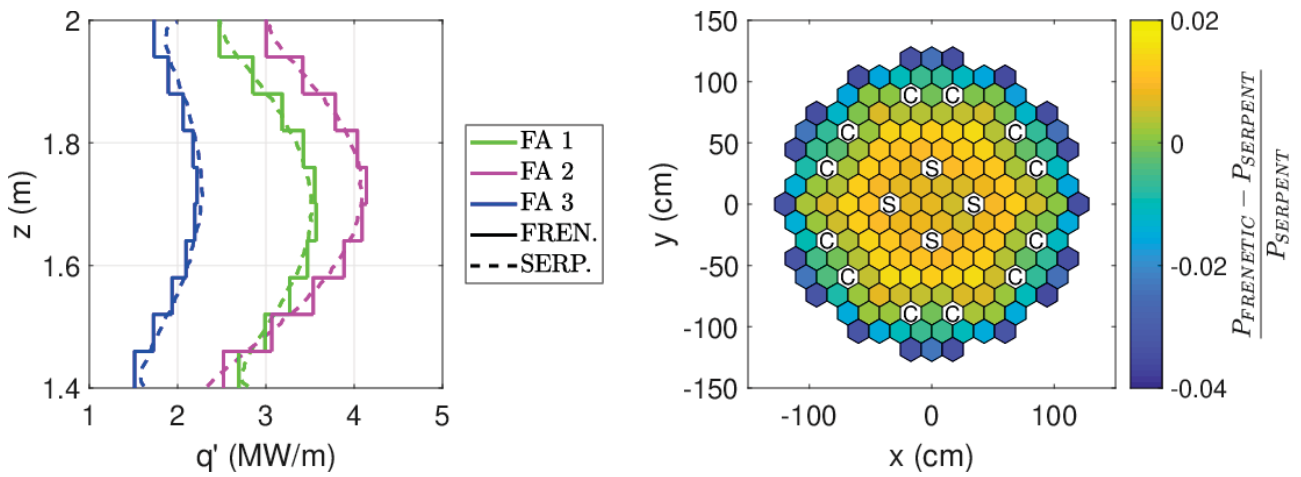
Fig. 5.20 – Comparison between the linear power calculated by Serpent and FRENETIC for three selected FAs (left) and radial map of the relative error between the power per FA evaluated by the two codes (right).
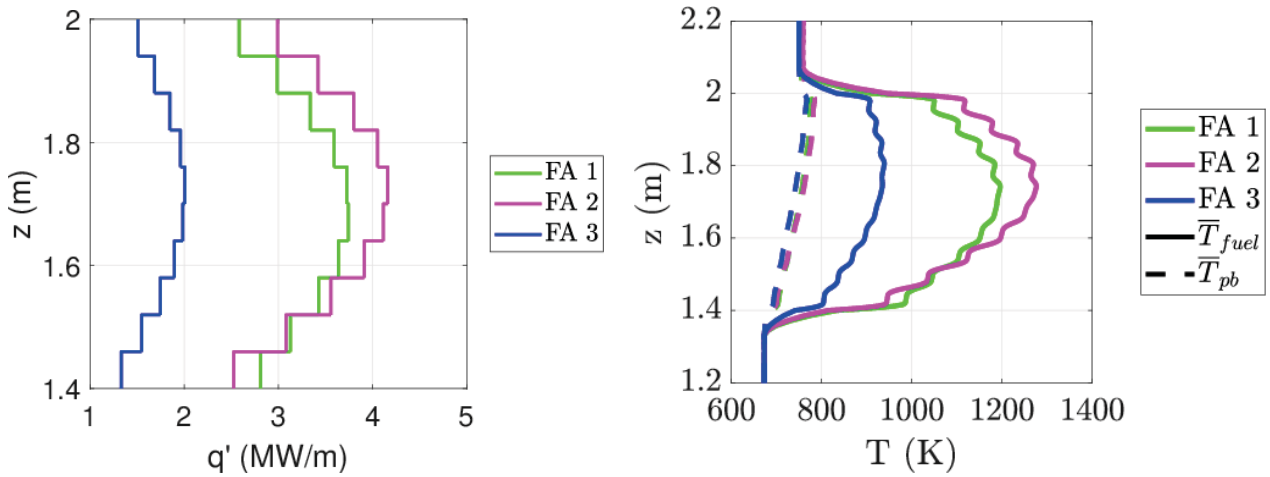
Fig. 5.21 – Linear power calculated by FRENETIC for three selected FAs (left) and axial temperature profiles for fuel and coolant in the same FAs (right)
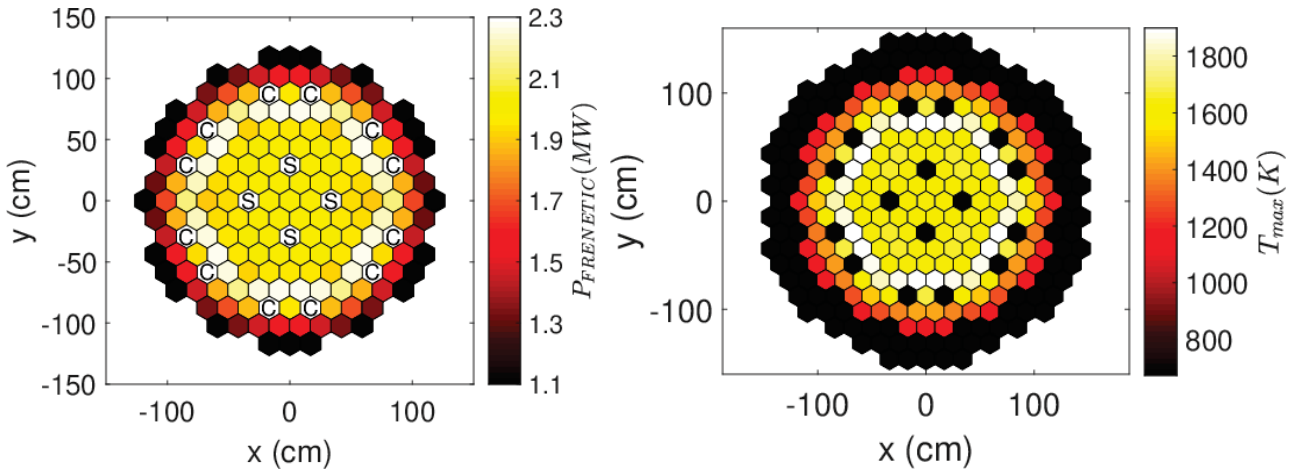
Fig. 5.22 – Radial power (left) and peak fuel temperature (right) distribution computed in the coupled FRENETIC simulations.

List of References

[5.1] R. Bonifetto, S. Dulla, P. Ravetto, L. Savoldi, R. Zanino, *A full-core coupled neutronic/thermal-hydraulic code for the modeling of lead-cooled nuclear fast reactors*, Nuclear Engineering and Design, 261, 85-94, 2013. DOI: 10.1016/j.nucengdes.2013.03.030.

[5.2] R. Zanino, R. Bonifetto, L. Savoldi Richard, A. Del Nevo, *Benchmark and preliminary validation of the thermal-hydraulic module of the FRENETC code against EBR-II data*, proceedings of ATH 2014, Reno, Nevada, June 15-19, 2014.

[5.3] D. Caron, R. Bonifetto, S. Dulla, V. Mascolino, P. Ravetto, L. Savoldi, D. Valerio, R. Zanino, *Full-core coupled neutronic/thermal-hydraulic modelling of the EBR-II SHRT-45R transient*, Internationl Journal of Energy Research, 42(1), 2018. DOI: 10.1002/er.3571.

[5.4] D. Caron, S. Dulla P. Ravetto, L. Savoldi, R. Zanino, *Models and methods for the representation of decay and photon heat in spatial kinetics calculations*, PHYSOR 2016, Sun valley, ID, May 1-5, 2016.

[5.5] J. Leppänen, M. Pusa, T. Viltanen, V. Valtavirta, T. Kaltiaisenaho, *The Serpent Monte Carlo code: Status, development and applications in 2013*, Annals of Nuclear Energy, 82, 142-150, 2013. DOI: 10.1016/j.anucene.2014.08.024.

[5.6] H. G. Weller, G. Tabor, H. Jasak, C. Fureby, *A tensorial approach to computational continuum mechanics using object-oriented techniques*, Computers in Physics, 12, 620-631, 1998, DOI: 10.1063/1.168744.

[5.7] E. Guadagni, R. Bonifetto, A. Cammi, S. Dulla, S. Lorenzi, G. F. Nallo, L. Savoldi, P. Ravetto, R. Zanino, *Numerical benchmark of the FRENETIC multiphysics code*, presented at ICONE conference, London, UK, Jul. 22-26, 2018.

[5.8] G. Grasso, C. Petrovich, D. Mattioli, C. Artioli, P. Sciora, D. Gugiu, G. Bandini, E. Bubelis, K. Mikityuk, *The core design of ALFRED, a demonstrator for the European lead-cooled reactors*, Nuclear Engineering and Design, 278, 287-301, 2014. DOI: 10.1016/j.nucengdes.2014.07.032.

[5.9] V. Fabrizio, S. Dulla, M. Nervo, P. Ravetto, A.G. Bianchini, V. Peluso, *ALFRED Reactor: evaluation of multi-temperature cross section sets by deterministic and stochastic methods*, Report RdS/2013/018.

[5.10] M. Sarotto, private communication, Sept. 2018.

[5.11] M. Massone, F. Gabrielli, A. Rineiski, *A genetic algorithm for multigroup energy structure search*, Annals of Nuclear Energy, 105, 369-387, 2017. DOI: 10.1016/j.anucene.2017.03.022

(Page intentionally left blank)

6 MONTE CARLO – CFD COUPLING FOR LFR MULTIPHYSICS MODELLING

A. Cammi, S. Lorenzi, C. Castagna

(Page intentionally left blank)

6.1 Background and references

The activity is related to the improvement of a multi-physics modelling of Lead-cooled Fast Reactor (LFR). The multi-physics approach allows evaluating a wide set of core parameters (e.g., temperature field, velocity field, and neutron fluxes) [6.1]-[6.3]. This advantage may be valuable for core designing, when verifying the satisfaction of the operational constraints.

In particular, we present a Monte Carlo - CFD coupling aimed at improving the present LFR multiphysics modelling. This way, the neutronics code (SERPENT) is provided with more realistic temperature profiles leading to an improvement in reactivity and power outcomes. On the other hand, the thermal-hydraulics code (OpenFOAM) is provided with more realistic volumetric fission power distribution which leads to an improvement in temperature profile estimation.

Along with the design support, this activity is also aimed at providing assistance to the code verification of the FRENETIC code, in collaboration with Politecnico di Torino.

6.1.1 Monte Carlo - CFD coupling

The LFR technology's severe design limits, along with a relatively low operational experience on heavy liquid metal cooled reactors, require dedicated tools of analysis to study the steady state and the transient behaviour of these GIF-IV systems. The multiphysics interaction between neutronics and thermal hydraulics can be studied with several approaches that are tailored on specific needs from the view point of accuracy and computational time. Diffusion method, deterministic and Monte Carlo approaches are the main options for the neutronics modelling. Subchannel analysis codes and Computational Fluid Dynamics (CFD) codes are the possible options as for the thermal-hydraulics modelling.

Even if coupling with simplified neutronics and thermal-hydraulics approach have been already investigated, only recently, thanks to the increased availability of computational power, the scientific community started to study the multiphysics interaction between neutronics and thermal-hydraulics with high-fidelity modelling options [6.4]-[6.6]. This is the case of the Monte Carlo – CFD coupling which is investigated in this activity. Monte Carlo approach allows accurate results and a flexible implementation, especially with respect to legacy codes in the study of Generation-IV reactors. On the other hand, besides the strong computational burden, coupling neutronics/thermal-hydraulics techniques can can present instability behavior [6.8], especially when stochastic neutron transport approaches are employed due to the impossibility to adopt the common techniques used for the solution of non-linear problems (see Fig. 6.1).

The tools used for the coupling are OpenFOAM and Serpent. OpenFOAM is an open source library for numerical simulation in continuum mechanics using Finite Volume Method. The toolkit is very flexible thanks to the object-oriented programming, allowing users to customize, extend and implement complex physical model [6.9],[6.10]. OpenFOAM grants the parallelization of the developed solvers thanks to dedicated routines based on geometrical domain decomposition. Serpent is a three dimensional continuous energy Monte Carlo (MC) neutron transport code, developed by the VTT Technical Research Centre in Finland [6.11]. Its application is focused on lattice physics application ranging from the generation of homogenized few-group constants for reactor simulation code to fuel cycle analysis. The choice of these two codes is motived by the strong compatibility of OpenFOAM with Serpent. The output of the finite volume being the "average" values of the fields in the cells of the domain, it is very suitable for passing temperatures and density fields to a Monte Carlo code for neutron transport. Moreover, Serpent was developed with a direct interface with OpenFOAM, that can be employed during transport and burnup calculations. This strong compatibility was the ultimate reason to choose this software and methods combination.

6.2 Body of the report concerning the ongoing activities

The activity focuses on the development of a Monte Carlo – CFD coupling for the ALFRED reactor. In the first section of this paragraph, the two techniques considered for the coupling are presented. In the second and third section, we briefly present the model adopted for the neutronics (full core SERPENT of ALFRED) and for the thermal-hydraulics (FA model of ALFRED with OpenFOAM). In the fourth section, the results of the coupling for a one-sixth FA are presented.

6.2.1 Monte Carlo – CFD coupling techniques

Neutron transport is strongly influenced by temperature and density distributions in all materials. This influence lies in the macroscopic cross sections:

$$\Sigma_{reactivity} = N(T) \cdot \sigma_{reactivity}(T) \tag{6.1}$$

This dependency of the neutronics on thermal hydraulic variables can be written in symbolic form as:

$$\phi = \mathcal{N}(\Theta) \tag{6.2}$$

where here, only for the sake of simplicity, all thermal hydraulic variables of interest, i.e. temperatures and densities, have been collapsed into Θ, and operator $\mathcal{N}$ associates the solution of the neutron transport problem ϕ to its input thermal hydraulic variables Θ.

The thermal hydraulics dependency on neutronics is much more evident since the volumetric power generation q is proportional to the fission reaction rate through the fission energy release. Therefore, a change in neutron flux and/or spectrum modifies the volumetric power distribution. Being the effective neutronic feedback on the thermal hydraulics, the power distribution was chosen as the main field for this analysis, and therefore the neutronics problem can be symbolically rewritten as:

$$q = \mathcal{N}(\Theta) \tag{6.3}$$

This dependency of temperature on the volumetric power distribution can be written in symbolic form as:

$$\Theta = \mathcal{T}(q) \tag{6.4}$$

where the operator $\mathcal{T}$ associates the solution of the thermal hydraulic problem to the input volumetric power distribution q.
Having explored all the main feedbacks, a symbolic representation of the coupled system can be built. Starting from the neutron transport problem in equation 2.3 and substituting equation 2.4, follows:

$$q = \mathcal{N}\big(\mathcal{T}(q)\big) \tag{6.5}$$

This means that the neutron flux distribution that solves the coupled problem is the fixed point of the coupled system. Most coupled calculations, currently, use a fixed-point iteration algorithm. The stability of such algorithm is case dependent and is left to the user to determine an appropriate under-relaxation factor for each individual case—the exception is an adaptive method based on stochastic approximation [6.12] which is stable for every coupled case and is optimized in terms of calculation time if the thermal hydraulics is solved in a simple and computationally inexpensive way. Pounders [6.13] suggests to use a simple estimate of the spectral radius of a fixed-point iteration in order to estimate a near-optimal under-relaxation factor for coupled neutronic and thermal-hydraulic calculations.

The fixed-point coupling method

Since the neutron flux distribution that solves the coupled problem is the fixed point of the coupled problem, the fixed-point method can be used to solve it. The fixed-point method is a computational method used to solve the generic problem

$$x = G(x) \tag{6.6}$$

and consists in iterating the following:

$$x_{n+1} = G(x_n) \tag{6.7}$$

starting from a chosen starting condition x_0. The fixed-point method is a general numerical method and can be applied to any problem in which the solution is the fixed point of a certain function. The stability of this algorithm entirely depends on the Jacobian matrix associated to the fixed-point problem

$$J_{i,j} = \frac{\partial G_i}{\partial x_j} \tag{6.8}$$

and it can be shown that this algorithm is stable if [6.13]

$$\varrho(J) < 1 \tag{6.9}$$

where $\varrho(J)$ is the spectral radius of the jacobian matrix associated to the fixed-point problem, i.e.,

$$\varrho(J) = max\{|\lambda_1|, \dots, |\lambda_N|\} \tag{6.10}$$

and λ_k are the eigenvalues of the Jacobian matrix. The fixed-point method is therefore conditionally stable, and in cases in which the method is unstable the problem can be solved by introducing an under-relaxation step, i.e. by substituting the already defined iteration with the following:

$$x_{n+1} = \alpha G(x_n) + (1 - \alpha)x_n \qquad 0 \le \alpha \le 1 \tag{6.11}$$

The α parameter is called under-relaxation factor and the effect of the underrelaxation is dampening the variation of the unknown x in the iteration. The new iteration can be written as:

$$x_{n+1} = G_\alpha(x_n), \qquad G_\alpha(x) = \alpha G(x) + (1 - \alpha)Ix \qquad 0 \le \alpha \le 1 \tag{6.12}$$

The stability of the under-relaxed fixed-point method depends on the eigenvalues of the new Jacobian matrix

$$J_{i,j} = \alpha \frac{\partial G_i}{\partial x_j} + (1 - \alpha)\delta_{i,j} \tag{6.13}$$

which depend in turn on the under-relaxation factor. It can be proved that not all under-relaxation factors are suitable for the stabilization of the method for a considered case but each case has its maximum under-relaxation factor that stabilizes the problem. An under-relaxation factor equal to 1 obviously corresponds to a standard non-relaxed fixed-point method. The under-relaxation factor can be a constant set by the user or it

can change from one iteration to the next, like in the *stochastic approximation* algorithm, described in the next section.

In the specific case of the coupling between neutronics and thermal hydraulics, the fixed-point method was implemented in the following loop:

1. Start from chosen temperature and density fields T_o, ρ_0
2. Solve the neutron transport problem $\tilde{q}_{n+1} = \mathcal{N}(T_n, \rho_n)$
3. If this is not the first coupled iteration, perform an under-relaxation step $q_{n+1} = \alpha\tilde{q}_{n+1} + (1 - \alpha)q_n$; if this is the first iteration instead take $q_1 = \tilde{q}_1$
4. Solve the heat transfer problem $\{T_{n+1}, \rho_{n+1}\} = \mathcal{T}(q_{n+1})$
5. Check the convergence, calculating the relative variation Δ_{n+1} of the power distribution

$$\Delta_{n+1} = \frac{\int |q_{n+1} - q_n| dV}{\int |q_n| dV} \qquad (6.14)$$

If convergence is reached end loop. Otherwise, loop back to point (2).

This can be more easily visualized with the flow chart in Fig. 6.2.

The stochastic approximation algorithm

Numerical stability is a critical aspect of coupled neutronics and thermal hydraulics calculations handled with the fixed-point method, being it conditionally stable. Therefore under-relaxation is necessary in order to ensure the convergence of the volumetric power distribution in unstable cases it but up to this point no a priori information is available on a suitable under-relaxation factor. This means that the user has full responsibility on the stabilization of a coupled case if no other analysis has been previously conducted. A solution to this problem can be found in the stochastic approximation algorithm [6.12].

The stochastic approximation algorithm is a fixed-point coupling method in which the under-relaxation factor and the number of neutron histories are changed at each iteration following an optimization criterion and in particular the underrelaxation factor follows a rule such that any case is effectively stabilized and the simulation time is minimized. This method was conceived in a framework in which the thermal hydraulics are solved with one-dimensional codes for subchannel analysis, which are computationally cheap, and the neutron transport with Monte Carlo codes, which instead have a high computational cost for high precision calculations. Therefore, in order to minimize the calculation time, the number of neutron histories must be minimized.

The optimization is carried on by having the under-relaxation factor equal to the relative computational cost of the iteration

$$\alpha_n = \frac{s_n}{\sum_{i=1}^n s_i} \qquad (6.15)$$

where s_n is the number of neutron histories at iteration n, and proportional to the statistical error involved in Monte Carlo calculations

$$\epsilon \sim \frac{1}{\sqrt{s}} \qquad (6.16)$$

This second requirement gives

$$\alpha_n \propto \frac{1}{\sqrt{\sum_{i=1}^{n} s_i}} \tag{6.17}$$

and both requirements combined generate two rules that determine at each coupled iteration the number of neutron histories and the under-relaxation factor that have to be used:

$$\begin{cases} \alpha_n = \dfrac{s_n}{\sum_{i=1}^{n} s_i} \\[2mm] s_n = \dfrac{s_1 + \sqrt{s_1^2 + 4 s_1 \sum_{i=1}^{n} s_i}}{2} \end{cases} \tag{6.18}$$

From this rules, it follows that the first iteration has always $\alpha = 1$ and

$$\lim_{n \to \infty} \alpha_n = 0 \tag{6.19}$$

The stochastic approximation method was implemented as well in this work and in particular the number of neutron histories was modified at each iteration by changing the number of active cycles in the neutron transport simulation. This implementation can be easily visualized in Fig. 6.3.

In detail, the structure of the algorithm is as follows:

1. Start from chosen temperature and density fields T_o, ρ_0
2. If this is the first coupled iteration, input the number of active cycles for the first iteration s_1 and have $\alpha_1 = 0$. Otherwise, calculate the new values of s_{n+1}, α_{n+1}
3. Solve the neutron transport problem $\tilde{q}_{n+1} = \mathcal{N}(T_n, \rho_n)$
4. If this is not the first coupled iteration, perform an under-relaxation step $q_{n+1} = \alpha_{n+1}\tilde{q}_{n+1} + (1 - \alpha_{n+1})q_n$; if this is the first iteration instead take $q_1 = \tilde{q}_1$
5. Solve the heat transfer problem $\{T_{n+1}, \rho_{n+1}\} = \mathcal{T}(q_{n+1})$
6. Check the convergence, calculating the relative variation Δ_{n+1} of the power distribution

$$\Delta_{n+1} = \frac{\int |q_{n+1} - q_n| dV}{\int |q_n| dV} \tag{6.20}$$

If convergence is reached end loop. Otherwise, loop back to point (2).

6.2.2 Full core SERPENT model of the ALFRED reactor

A detailed model of ALFRED is set up with a heterogeneous description of the reactor. The SERPENT model represents the 171 FAs, 110 dummy elements, 12 CRs and 4 SRs, the inner vessel and the surrounding lead (Fig. 6.4a). The zones above and below the active zone are also modelled (Fig. 6.4b) in order to take into account the CRs and SRs position as well as the contribution of these zones to the reactivity effect (i.e., in particular for the lead density). For the isotopic composition of the input materials concerning ALFRED (fuel, cladding, coolant, control rods), the reader may refer to [6.14]. Fig. 6.5 illustrates the power peaking

factor (ppf) distribution inside one-fourth of reactor core for the first Beginning of Cycle (BOC). The maximum ppf is 1.28, which is related to the most powerful fuel assembly with the power of 2.25MW.

A first verification of this model has been performed comparing some relevant core parameters (see Tab. 6-1) with the results obtained with the deterministic transport code ERANOS and the Monte Carlo code MCNPX during the LEADER project [6.14]. An additional comparison has been also carried out considering the main reactivity feedback (see Tab. 6-2). The results can be considered satisfactory as first verification of the model.

6.2.3 CFD model for the FA of ALFRED

The conjugate heat transfer multi region model available in the OpenFOAM has been used for the modelling of the thermal-hydraulics allowing the study of both the fuel and the coolant. The solver *chtMultiRegionFoam* implements the mass, momentum and energy equations for the fluid and of the heat diffusion equation for the solid. In this analysis, the solver uses the SIMPLE (Semi-Implicit Method of Pressure-Linked Equations) algorithm for finding the steady-state configuration.

The model of fluid flow is based on Reynolds-Averaged Navier-Stokes (RANS) equations for mass and momentum conservations plus the energy equation.

$$\begin{cases} \rho(\boldsymbol{u} \cdot \nabla)\boldsymbol{u} - \nabla \cdot \left[-p\boldsymbol{I} + (\mu + \mu_t)(\nabla \boldsymbol{u} + (\nabla \boldsymbol{u})^T) - \frac{2}{3}\rho k \boldsymbol{I} \right] = 0 \\ \nabla \cdot \rho\boldsymbol{u} = 0 \\ \rho C_p \boldsymbol{u} \cdot \nabla T - \nabla \cdot \left[C_p \left(\frac{\mu}{Pr} + \frac{\mu_t}{Pr_t} \right) \nabla T \right] = 0 \end{cases} \tag{6.21}$$

Due to the high Reynolds number characterizing the flow in the ALFRED reactor, a turbulence model is applied in the RANS framework. In particular, k-ε model is used as a turbulence model [6.15] where k is the turbulence kinetic energy and ε is the turbulence dissipation rate calculated based on the following equations.

$$\begin{cases} \nabla \cdot (\rho \boldsymbol{u} k) - \nabla \cdot (\rho D_k \nabla k) = G_k - \frac{2}{3}\rho(\nabla \cdot \boldsymbol{u})k - \rho\varepsilon + S_k \\ \nabla \cdot (\rho \boldsymbol{u}\varepsilon) - \nabla \cdot (\rho D_\varepsilon \nabla \varepsilon) = \frac{C_1 G_\varepsilon \varepsilon}{k} - \left(\frac{2}{3}C_1 - C_{3,RDT} \right)\rho(\nabla \cdot \boldsymbol{u})\varepsilon - C_2\rho\frac{\varepsilon^2}{k} + S_\varepsilon \\ \mu_t = \rho C_\mu \frac{k^2}{\varepsilon} \end{cases} \tag{6.22}$$

These two equations implemented in OpenFOAM are different from the original k- ε model. The second term on the right hand side incorporates the Rapid Distortion Theory (RDT) contribution, buoyancy contribution are not included, and the coefficient C_3 is not the same as $C_{3,RDT}$ [6.10]. Tab. 6-3 shows the default model coefficients applied in OpenFOAM model.

The model for the solid region, i.e., the fuel, implements the heat equation

$$\nabla \cdot \left[\frac{k_f}{\rho_f C_{p,f}} \nabla T \right] = q \tag{6.23}$$

The cladding and gap region are not modelled to not compromise the quality of the mesh. In order to take into account their effect in terms of temperature distribution, two thermal resistances are considered in the interface between the fuel and the coolant. In particular, a thermal resistance for the cladding (length of 0.6 mm) and the helium gap (length of 0.15 mm) are added, with thermal conductivity of 15 W m^{-1} K^{-1} and 1.125 W m^{-1} K^{-1} respectively.

As for the boundary conditions, the coolant inlet temperature and velocity are kept constant (400 °C and 1.4 m/s, respectively), as well as outlet pressure. Since the single CFD model is not capable of evaluating the heat flux, the latter is taken from a constant value that will be provided by the SERPENT code in the coupling mode.

The correlations adopted for density and thermal conductivity of the coolant and the fuel are reported in Tab. 6-4.

The geometry of one-sixth of the FA used in the coupling with SERPENT is shown in Fig. 6.6a. The mesh is composed by 860310 cells for the coolant and by 615679 cells for the fuel (Fig. 6.6b). A sensitivity analysis has been carried out to ensure that the temperature distribution does not change with further refinement of the mesh.

6.2.4 SERPENT – OpenFOAM coupling for one-sixth of FA

Both the fixed-point and the stochastic approximation algorithms have been implemented for the Monte Carlo – CFD coupling. Some modifications have been taken in the OpenFOAM solver, in particular:

1. the volumetric power distribution is included in the energy equation for solid materials, reading it from a separate OpenFOAM input file;

2. the relative integral variation of the volumetric power distributions from the previous iteration to the current one is calculated, in order to perform a convergence check with the wrapper code at each coupled iteration;

3. the relative density in fluid materials with respect to a reference density is calculated. This feature was used in order to feed the density field to Serpent 2.

The coupling is carried out by a bash script in the Linux environment. The wrapper code manages the process and is capable to restart the calculation from a determined iteration. A configuration file, read by the bash script at each iteration, reports the settings of the simulation.

The Serpent – OpenFOAM coupling for the ALFRED reactor is tested on a one-sixth of FA [6.18]. Thanks to the relative low reactivity feedbacks of this fast system, both the fixed-point coupling method (with a moderate high under-relaxation factor equal to 0.8) and the stochastic approximation allows a fast convergence of the calculation, reaching a steady state after few iterations (Fig. 6.7). The value of Δ_n does not decrease increasing the number of iteration since it is affected by the statistical fluctuation of the Monte Carlo method. An increase the number of neutron histories simulated can lead to a reduction of the relative power variation at convergence.

From CFD calculations, we obtain the distribution of the temperature field. The mean temperature is 1284 °C for the fuel and 440 °C for the lead, calculated over the volumes. Fig. 6.8 shows the temperature contours, along the radial direction, obtained at the middle of the active region. The temperature of the coolant is higher near the border of the fuel pins, reaching differences until 70 °C with the regions near the wall. For external FA, this difference could be higher. The fuel temperature, as expected, is maximum at the center of the pins, with differences more than 1300 °C with the border, according to the study of the fuel pin design reported in [6.19]. The velocity profile along the axial direction are shown in Fig. 6.9.

6.3 Role of the activity, general goals and future development

The activity is the step forward of the development of a multi-physics code for lead-cooled fast reactor aimed at supporting both the design choice and the verification of other numerical tools. This tool is meant to represent an additional tool to be used in combination with the classic system codes in order to give a deeper insight about the complex physical phenomena occurring in the reactor (and their mutual interactions). In particular, the Monte Carlo – CFD coupling developed in this activity is aimed at obtaining a better accuracy in the neutronics/thermal-hydraulics modelling of the ALFRED reactor. Along with the design support, this activity is aimed at providing assistance to the code verification of the FRENETIC code, in collaboration with Politecnico di Torino. Two coupling approaches has been tested on a one-sixth of LFR, providing both good results and making possible the coupling between a Monte Carlo and a CFD code.

Near-term efforts will focus on efficient use of the available computational resources (i.e., parallelization, optimization) and easy modification of the modelling description with OpenFOAM to develop a multi-physics platform. In addition, extension to the entire fuel assembly and to the entire core can be considered prior development of a porous media approach in order to reduce the computational burden of the coupled calculation.

	SERPENT	ERANOS [14]	MCNPX [14]
Max power in FA (MW)	2.25	2.42	2.21
Total worth of 12 CRs (pcm)	-8511	-9100	-8500
Total worth of 4 SRs (pcm)	-2957	-3700	-3300
Effective delayed neutron fraction (pcm)	336	336	-

Tab. 6-1 – Comparison of some core parameters.

	SERPENT	ERANOS [14]
Doppler constant (pcm)	-580 ± 18	-555
Lead expansion coefficient (pcm/K)	-0.282 ± 0.113	-0.271
Axial fuel expansion (pcm/K)	-0.153 ± 0.019	-0.148
Axial cladding expansion (pcm/K)	$+0.044 \pm 0.006$	+0.037
Axial wrapper expansion (pcm/K)	$+0.036 \pm 0.006$	+0.022
Radial grid expansion (pcm/K)	-0.766 ± 0.007	-0.762

*Tab. 6-2 – Comparison of the reactivity coefficients, BoC.*

C_μ	C_1	C_2	$C_{3,RDT}$
0.09	1.44	1.92	0

Tab. 6-3 – Default parameters applied in the OpenFOAM solver for k-ε turbulence model.

Parameter	Correlation	Reference
Lead density	$\rho \ (kg \ m^{-3}) = 11367 - 1.1944 \cdot T \ (K)$	[16]
Lead thermal conductivity	$\lambda \ (W \ m^{-1} \ K^{-1}) = 9.2 - 0.011 \cdot T \ (K)$	[16]
Fuel density	$\rho \ (kg \ m^{-3}) = 10443$	[14]
Fuel thermal conductivity	$\lambda \ (W \ m^{-1} \ K^{-1}) = \left(\frac{1}{0.197 + 2.885 \cdot 10^{-4} \cdot T(K)} + 7.64 \cdot 10^{-11} T(K)^3 \right) \cdot 1.157$	[17]

Tab. 6-4 – Correlations for density and thermal conductivity of coolant and fuel.

(a)   *(b)*
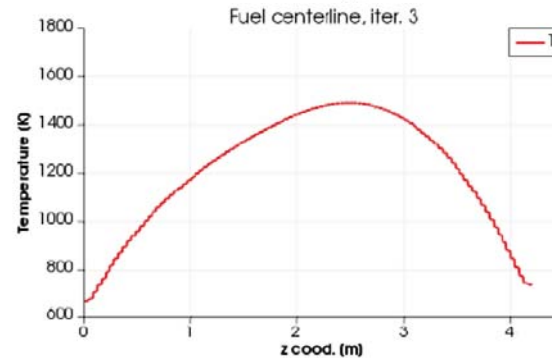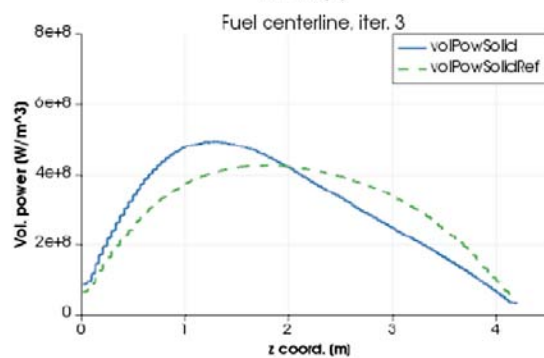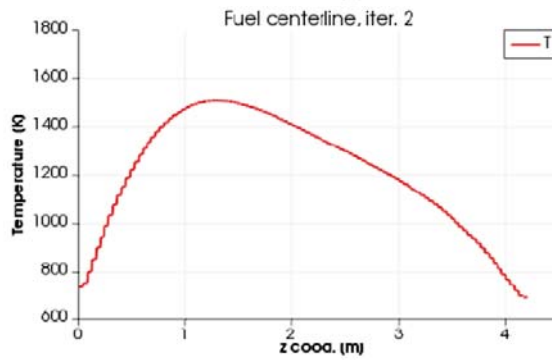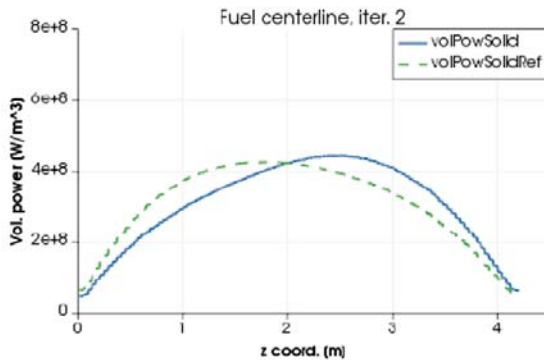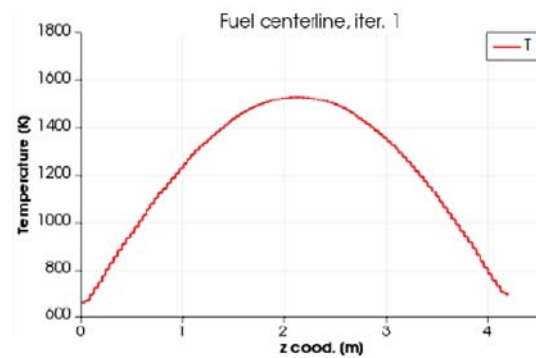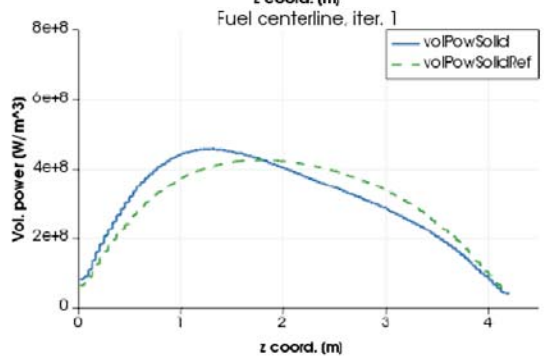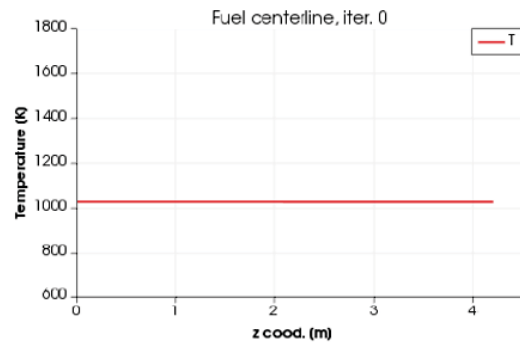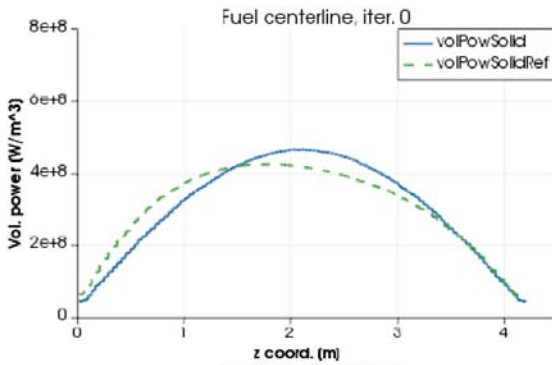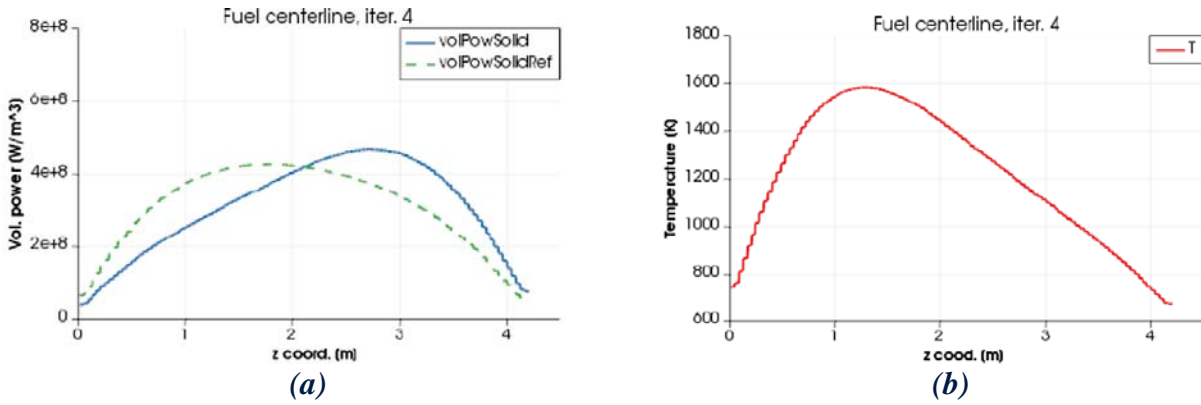
Fig. 6.1 – Unstable behavior of Monte Carlo – CFD coupling (EPR case). Evolution of a) volumetric power, b) fuel temperature in the first 4 iterations.
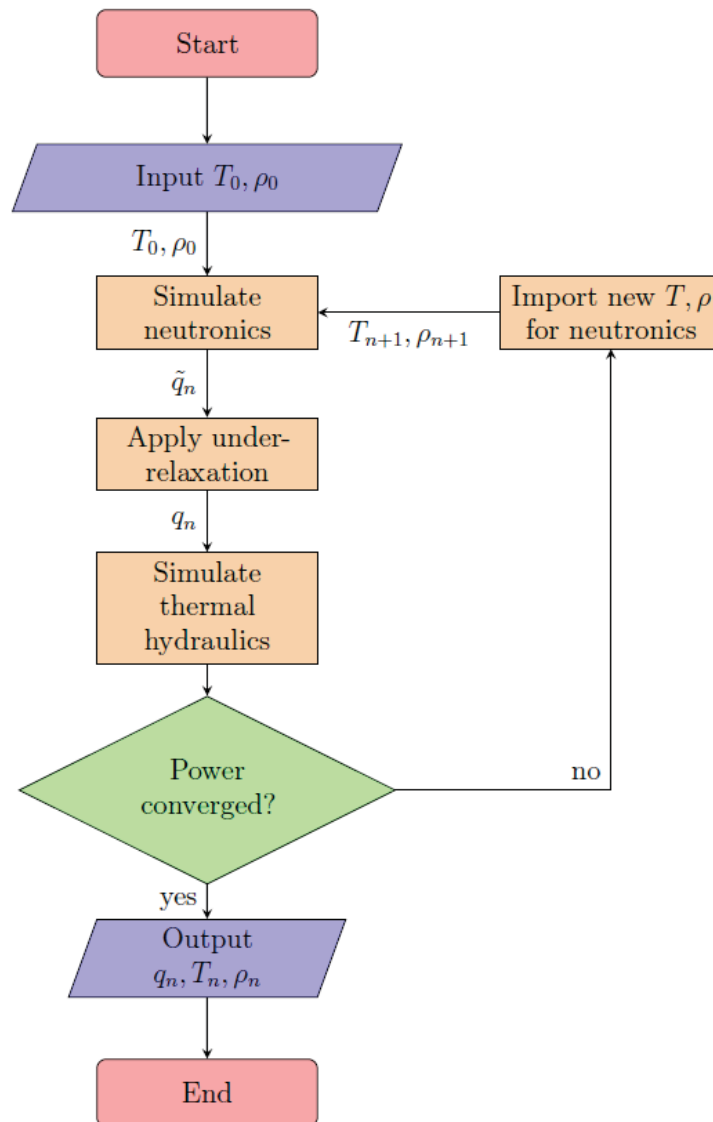
Fig. 6.2 – The fixed-point coupling algorithm.
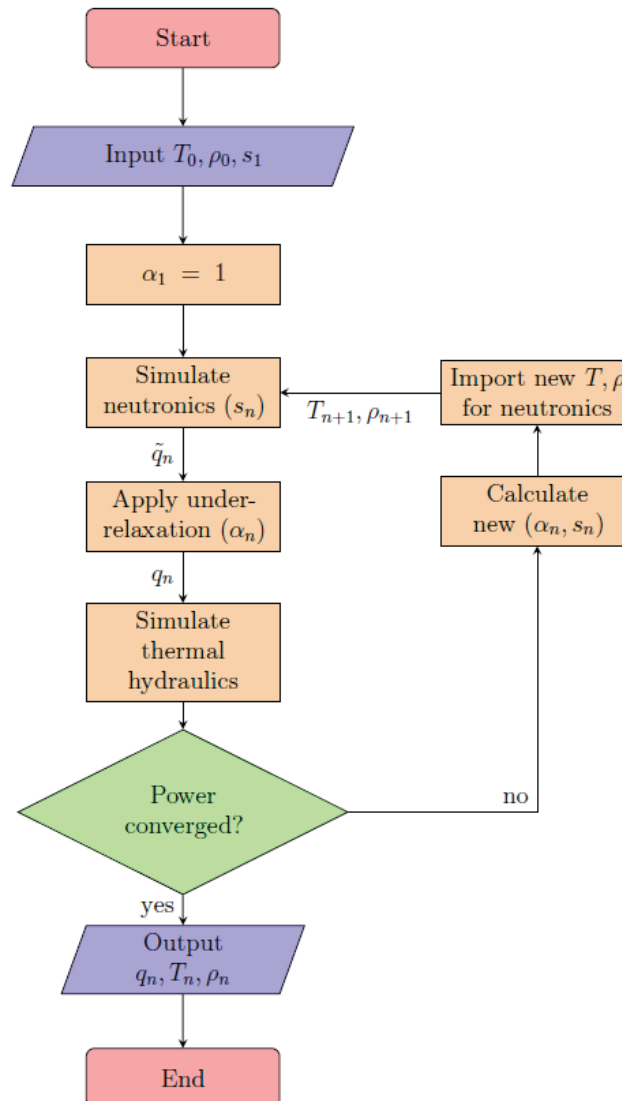
Fig. 6.3 – The stochastic approximation coupling algorithm

(a)   *(b)*
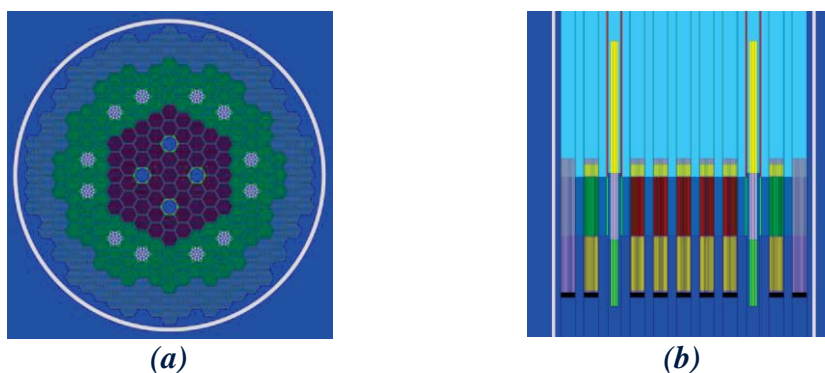
Fig. 6.4 – Radial view (a) and longitudinal view (b) of the SERPENT model of the ALFRED reactor.
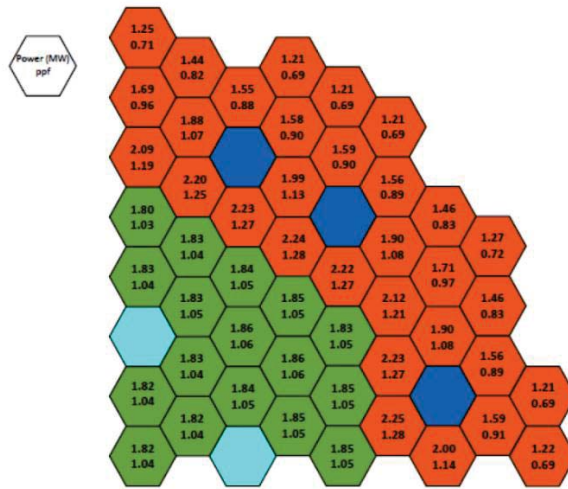
Fig. 6.5 – Power peaking factor of one-fourth of ALFRED reactor core for BOC.

(a)   *(b)*
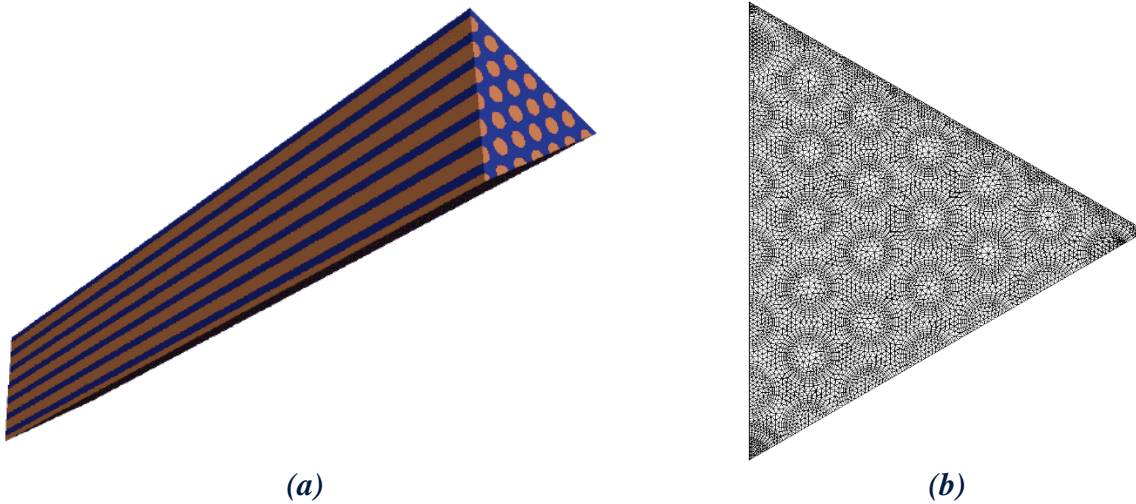
Fig. 6.6 – a) Geometry and b) mesh of ALFRED one-sixth of FA.
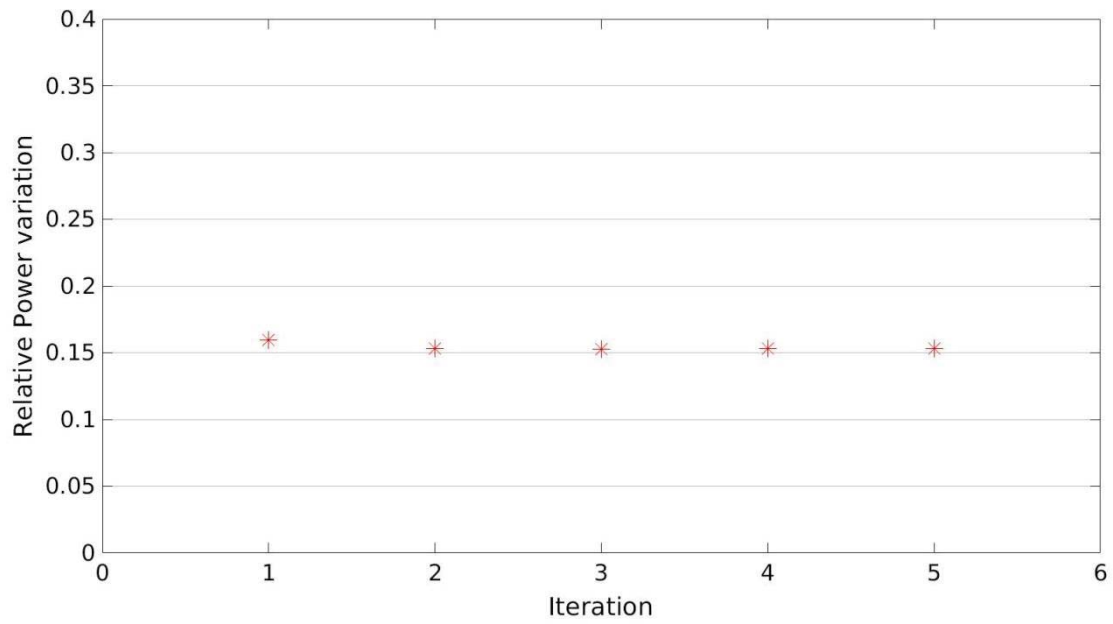
Fig. 6.7 – Relative power variation at each iteration for the fixed-point scheme.
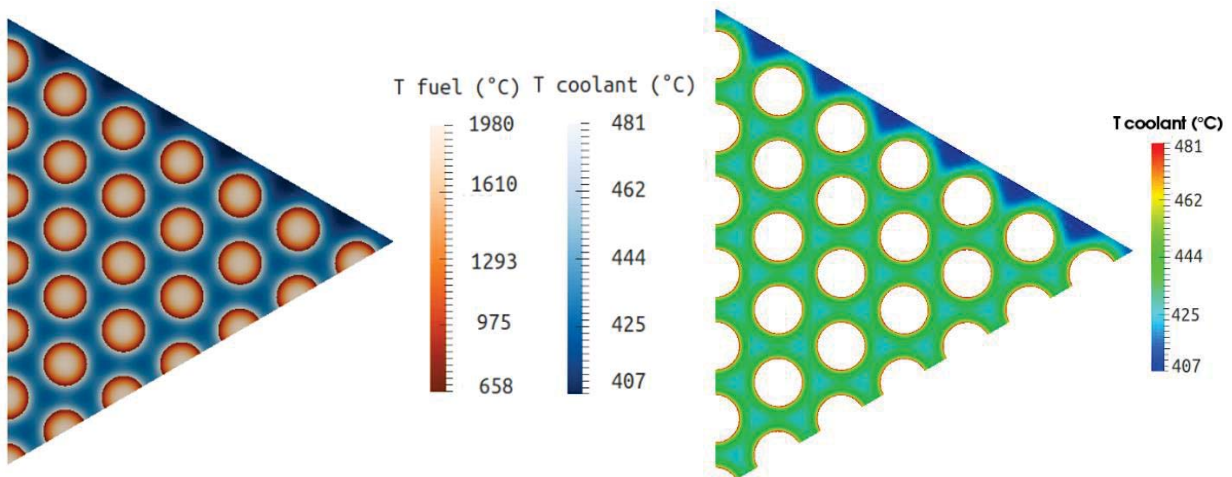
Fig. 6.8 – Temperature profile calculated with the Monte Carlo – CFD coupling scheme.

Fig. 6.9 – Velocity profile calculated with the Monte Carlo – CFD coupling scheme.

6.4   List of References

[6.1]   A. Cammi, V. Di Marcello, L. Luzzi, V. Memoli, M.E. Ricotti, A multi-physics modelling approach to the dynamics of Molten Salt Reactors, Ann. Nucl. Energy. 38 (2011) 1356–1372. doi:10.1016/j.anucene.2011.01.037.

[6.2]   M. Aufiero, A. Cammi, O. Geoffroy, M. Losa, L. Luzzi, M.E. Ricotti, H. Rouch, Development of an OpenFOAM model for the Molten Salt Fast Reactor transient analysis, Chem. Eng. Sci. 111 (2014) 390–401. doi:10.1016/j.ces.2014.03.003.

[6.3]   A. Cammi, V. Di Marcello, L. Luzzi, V. Memoli, The multi-physics modelling approach oriented to safety analysis of innovative nuclear reactors, Adv. Energy Res. 5 (2011) 171–214.

[6.4]   D. Kotlyar, Y. Shaposhnik, E. Fridman, E. Shwageraus, Coupled neutronic thermo-hydraulic analysis of full PWR core with Monte-Carlo based BGCore system, Nucl. Eng. Des. 241 (2011) 3777–3786. doi:10.1016/j.nucengdes.2011.07.028.

[6.5]   M. Vazquez, H. Tsige-Tamirat, L. Ammirabile, F. Martin-Fuertes, Coupled neutronics thermal-hydraulics analysis using Monte Carlo and sub-channel codes, Nucl. Eng. Des. 250 (2012) 403–411. doi:10.1016/j.nucengdes.2012.06.007.

[6.6]   N. Capellan, J. Wilson, S. David, O. Méplan, J. Brizi, A. Bidaud, A. Nuttin, P. Guillemin, 3D coupling of Monte Carlo neutronics and thermal-hydraulics calculations as a simulation tool for innovative reactor concepts, Proc. Glob. 2009. (2009) 1358–1367.

[6.7]   M. Aufiero, M. Fratoni, A new approach to the stabilization and convergence acceleration in coupled Monte Carlo–CFD calculations: The Newton method via Monte Carlo perturbation theory, Nucl. Eng. Technol. 49 (2017) 1181–1188. doi:10.1016/j.net.2017.08.005.

[6.8]   P. Bianchini, Computational features of neutronics and thermal hydraulics coupled simulations, Politecnico di Milano, 2017.

[6.9]   H.G. Weller, G. Tabor, H. Jasak, C. Fureby, A tensorial approach to computational continuum mechanics using object-oriented techniques, Comput. Phys. 12 (1998) 620–631.

[6.10] OpenFOAM, OpenFOAM, (2016). http://www.openfoam.org/.

[6.11] J. Leppänen, M. Pusa, T. Viitanen, V. Valtavirta, T. Kaltiaisenaho, The Serpent Monte Carlo code: Status, development and applications in 2013, (2015). doi:10.1016/j.anucene.2014.08.024.

[6.12] J. Dufek, W. Gudowski, Stochastic Approximation for Monte Carlo Calculation of Steady-State Conditions in Thermal Reactors, Nucl. Sci. Eng. 152 (2006) 274–283. doi:10.13182/NSE06-2.

[6.13] J.M. Pounders, Stability and near-optimal underrelaxation of coupled reactor physics calculations, in: Phys. React. 2016, PHYSOR 2016 Unifying Theory Exp. 21st Century, 2016.

[6.14] G. Grasso, C. Petrovich, D. Mattioli, C. Artioli, P. Sciora, D. Gugiu, G. Bandini, E. Bubelis, K. Mikityuk, The core design of ALFRED, a demonstrator for the European lead-cooled reactors, Nucl. Eng. Des. 278 (2014) 287–301. doi:10.1016/j.nucengdes.2014.07.032.

[6.15] B.E. Launder, D.B. Spalding, The numerical computation of turbulent flows, Comput. Methods Appl. Mech. Eng. (1974). doi:10.1016/0045-7825(74)90029-2.

[6.16] OECD, N.E. Agency, Handbook on Lead-bismuth Eutectic Alloy and Lead Properties , Materials Compatibility , Thermal- hydraulics and Technologies, 2015. doi:ISBN 978-92-64-99002-9.

[6.17] Y. Philipponneau, Thermal conductivity of (U, Pu)O2-x mixed oxide fuel, J. Nucl. Mater. 188 (1992) 194–197. doi:10.1016/0022-3115(92)90470-6.

[6.18] C. Castagna, S. Lorenzi, A. Cammi, A Multi-physics Modelling Approach for the analysis of Lead

Fast Reactors, in: Proc. 27th Int. Conf. Nucl. Energy New Eur. Portoroz, Slov. Sept. 10 - 13, 2018.
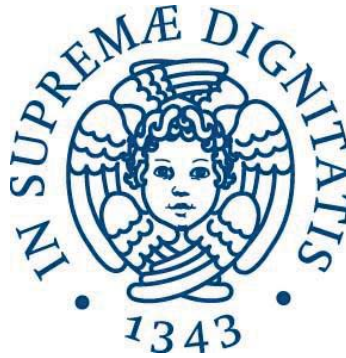
[6.19] L. Luzzi, A. Cammi, V. Di Marcello, S. Lorenzi, D. Pizzocri, P. Van Uffelen, Application of the TRANSURANUS code for the fuel pin design process of the ALFRED reactor, Nucl. Eng. Des. 277 (2014) 173–187. doi:10.1016/j.nucengdes.2014.06.032.

7 SIMMER III-RELAP5 COUPLING CODES DEVELOPMENT

N. Forgione, B. Gonfiotti, C. Ulissi

(Page intentionally left blank)

7.1 Background and references

Thermal-hydraulic and safety analyses are a central issue in the advance, design and licensing of nuclear power plants (NPPs). Particularly, the study of the plant behaviour in accidental situations has always been one of the chief concern of nuclear safety. These investigations are essential to assess the consequences of a postulated accident and to assist the design of the facilities in order to assure the structural integrity of the components, or, furthermore, to avoid putting at risk the whole system.

One of the major safety issues regarding the WCLL-BB for the fusion DEMO reactor is the interaction between the primary coolant (water) and the neutron multiplier (lead lithium), due to a rupture in the coolant circuit [7.1]-[7.2]. This accident scenario involves an exothermic chemical reaction between PbLi and water with the production of hydrogen, in addition to critical interactions in a complex multiphase system in non-thermal equilibrium which may lead to vapour explosion and pressurization of the vessel [7.3].

Recently, UNIPI successfully implemented a PbLi/water reaction model in the code SIMMER-III [7.4], permitting the estimation of the energy and the hydrogen generation. Validation activity was concluded on LIFUS5 experimental campaign available in literature and is ongoing on experimental tests in LIFUS5/Mod3 for the EUROfusion project.

However, simulation of the whole facility solely with the SIMMER code still remains unfeasible for the extremely high computational effort required and the consequent long calculation time. Therefore, SIMMER should be used only to analyse a smaller part of the domain, where significant accuracy might be required; on the other hand, the remaining part of the system - mainly characterised by 1D components such as pipes - should be simulated with STH codes to reduce the computational effort. In terms of this typology of codes, the University of Pisa retains a strong experience in the use and improvement of the STH code RELAP5 [7.5]-[7.8].

This report describes the development and assessment of a coupling methodology between the codes SIMMER and RELAP5/Mod3.3, with the final aim of simulating the whole LIFUS5/Mod3 experimental facility and providing a powerful and reliable tool for the prediction of the chemical and thermal-hydraulic behaviour of complex loop experimental facilities. First the results of simple test cases are presented and then it is shown the nodalization of the complete LIFUS5 facility together with preliminary results for the coupled codes simulation of a simplified version on one of the test proposed for the experimental campaign.

7.2 Body of the report concerning the ongoing activities

7.2.1 Principles of the coupling tool

The coupling tool between the SIMMER and RELAP5 codes, developed at the University of Pisa, can be classified as a "two-way", "non-overlapping" and "online" procedure, since computational domains of the two codes communicate by separated interfaces (text files) which are used to exchange data in both directions with synchronized progression in time.

The coupling development was based on four fundamental pillars:

- Reduce as much as possible the input required by the final user;
- Stand-alone capabilities to run without the support of any other application except MATLAB;
- Modular approach to ease the maintenance of the code and the introduction of new features;
- Lightweight on CPU, HDD and RAM to reduce as much as possible the computation time.

The interaction is managed by several Mathworks MATLAB scripts which also have the role to check the "consistency" of the physical properties exchanged at the interface. An explicit method was chosen as numerical scheme; the data exchange configuration is shown in Fig. 7.1 whilst the workflow is shown in Fig. 7.2.

The coupling procedure consists of four phases: the first one is manually performed by the user, while the remaining three phases are controlled by the coupling tool. These four phases are:

- Steady-state phase;
- Pre-check phase;
- Run phase;
- Save phase.

In the steady-state phase, an initial steady-state calculation is performed with both RELAP5 and SIMMER III. The input-decks of each code must contain the geometrical description of the zones analysed within the specific code, as well as all the other data required to reproduce the investigated transient. The aim of this first phase is to create *restart*/*SIMBF files* containing all the data required to simulate the transient. The duration of these steady-state calculations is user/transient dependent, and different times can be also employed for the two codes (for instance: 1 s in SIMMER III and 5 s in RELAP5). The Pre-check phase checks the coherence between the *restart*/*SIMBF files* created during the previous phase and the data given as input in the MATLAB coupling script. This phase is performed only once at the very beginning of the coupled calculation. The Run and Save phases are then recursively repeated until the end of the coupled calculation. As the names suggest, the Run phase controls the step-by-step advancement in time of the calculation, while the Save phase is devoted to the saving of the results obtained at the end of each step.

7.2.2 Assessment of the coupling capabilities – Simple test cases

To assess the capabilities of the coupling tool, several tests were performed and compared with simulations obtained from a *stand-alone* RELAP5 setup. These tests are a variation of the typical *manometer flow oscillation problem*, i.e. two tanks at different pressure connected together but initially isolated through a valve. Since no appreciable differences should exist between the *coupled* and the *stand-alone* calculations for these simple cases, this is considered to be a good starting test for the coupling tool validation.

The system considered consists of two tanks at different pressure (Fig. 7.3) joined by a horizontal pipe. A valve is placed in the middle of the pipe to control the flow between the two tanks. The tanks are filled with water and inert non condensable gas (nitrogen). In the test the valve is suddenly opened and the transient of the pressurisation/depressurisation of the two tanks is analysed.

Tab. 7-1 summarises the five different setup simulated. The five cases differ for the initial level of the water, the pressurisation of the high pressure tank and the temperature of the water (one case).

The *stand-alone* RELAP5 nodalization (Fig. 7.4(a)) consists of 6 pipes: 2 pipes divided into 20 volumes each to simulate the tanks, and the remaining 4 pipes divided into 10 volumes each to simulate the vertical parts (2) and the horizontal parts (2) of the connecting tube. A valve is also installed between the 2 horizontal pipes, and it is assumed to open after 2.1 s from the beginning of the calculation. In turn, the low-pressure tank and its vertical tube were simulated with SIMMER III in the *coupled* calculation (Fig. 7.4 (b)). The axial subdivision of the vertical pipe and the low-pressure tank is the same of the *stand-alone* calculation: 10 axial levels/volumes for the vertical pipe, and 20 axial levels/volumes for the low-pressure tank. In turn, the vertical pipe is divided in one *radial level* only making it identical to that used in the *stand-alone* calculation, while the low-pressure tank is subdivided into 12 *radial levels*.

The computed total pressure and velocity transients for the five different cases are shown in Fig. 7.5 to Fig. 7.9, and they are compared with the equivalent standalone calculation. The pressurisation of the low-pressure tank is well reproduced in all cases but one (case number 3). The results present some differences only when the system starts oscillating once equilibrium is reached this is probably due to the fact that SIMMER III does not consider the distributed pressure drops. In case 3 (Fig. 7.7) the discrepancies might depend instead on RELAP5 which – unlike SIMMER - neglects the heat exchange in axial direction (Fig. 7.10). The presented results show that the coupling tool is able to reproduce the general behaviour of the simulated system and the SIMMER III code is capable to catch complex 2D phenomena that cannot be reproduced with RELAP5 alone.

7.2.3   Assessment of the coupling capabilities – LIFUS5 facility

LIFUS5/Mod3.3 is an experimental facility under design and construction at the ENEA Brasimone laboratories (Italy). The aim of the facility is to investigate the ingress of water at high pressure in heavy metal liquid pools (PbLi, LBE, etc.). The facility consists of an injection line partially filled with water and Argon, and a reaction tank (S1-B) in which the heavy metal liquid is contained (Fig. 7.11). The injection line and the S1-B tank are initially isolated by means of a rupture disk installed at the exit of the injection line (in the S1-B tank). The S1-B tank is initially at atmospheric pressure, while the injection line is at a higher pressure.

- The first zone spanning from the closing rupture disk up to the valve VP-SBL-07 at a very low pressure (the aim is have this part of the injection line empty);
- The second zone spanning between the VP-SBL-07 and the VP-SBL-05 valves filled with water;
- The third zone spanning from the VP-SBL-05 valve up to the beginning of the injection line filled with Argon at high pressure.

Once the three zones are set up, the valve VP-SBL-05 opens pressuring the water in the second zone, and then also the VP-SBL-07 opens to start the water injection in the S1-B tank. When the water at high pressure reaches the exit of the injection line the rupture disk breaks up, and the ingress of water in the S1-B tank occurs. The tests are supposed to last no more than few seconds. Finally, the VP-SBL-07 valve closes again to avoid the ingress of Ar in the heavy metal liquid pool. The main geometrical dimensions of the experimental facility are reported in Fig. 7.11and in Tab. 7-2, while the main design data are reported in Tab. 7-3.

7.2.4   The RELAP5/Mod3.3 and the SIMMER III simplified nodalizations

As shown in Fig. 7.11, the S1-B tank and the ending part of the injection line are reproduced with SIMMER III, while the remaining part of the injection line with RELAP5. The dimensions were all set according to the data actually available. It is important to notice that, in this preliminary assessment, the geometry of the S1B tank has been simplified, neglecting the internal structures.

The RELAP5 nodalization consists in a series of *pipe* connected through single junctions. Each *pipe* is subdivided into a sufficient number of *volumes* each having a total length of 0.01 m to have L/D ≈ 1 (Fig. 7.11).

The implemented pressure drop coefficients and their position in the nodalization are summarized in Tab. 7-4. Note that the distributed pressure drops are considered assuming a surface roughness of $3x10^{-5}$ m along the entire injection line.

The SIMMER III nodalization reproduces the S1-B tank and the ending part of the injection line; however, in this phase of the assessment the internal parts were not included in the computational domain. A

cylindrical geometry is assumed consisting of 20 radial levels and 62 axial levels. Each axial level has a height of 0.01 m, except the last one which is 0.015 m high. Instead, the radial dimensions are mixed: the first level spans for 6.35 mm, the following twelve levels for 6.41063 mm, then 3 levels for 7.2141 mm, and finally 4 levels for 5.89505 mm. The cells reproducing the injection line are characterized by a pressure drop coefficient at the passage from a cell to another of 0.02 to account for the distributed pressure drops. Additional pressure drops are considered at the top of cells (1,7) (total value of 0.23) and cell (1,13) (total value of 0.495) to consider the complex geometry of the ending injection line part. The injection line and the S1-B tank are isolated through *virtual walls*. The *virtual wall* reproducing the rupture disk instantly disappears at a given time to simulate its opening. Three non-calculation zones are also used to reproduce the hemispherical bottom of the S1-B tank. The first non-calculation zone spans from cell (2,1) up to cell (20,7), the second zone from cell (14,8) to cell (20,10), and the third one from cell (17,11) to cell (20,13). The remaining cells are filled with water (injection line), heavy metal liquid up to the 50th axial level, a mixture of heavy metal liquid and incondensable gas in the 51st axial level, and with an incondensable gas from the 52nd axial level to the top. As requested by the *coupling tool*, a *continuous inflow/outflow* boundary condition in cell (1,1) is assumed. Fig. 7.12 shows the employed SIMMER III nodalization.

7.2.5   LIFUS5/Mod3 coupled codes preliminary simulation results

Due to a limitation of SIMMERIII it is not possible to impose the value of the injected liquid fraction as boundary condition: to obtain the injection of single phase water it is necessary to set the cell involved in the coupling filled with water as initial condition (i.e. water liquid fraction equal to 1 at t = 0); this forced to start the simulation with the injection circuit (simulated through RELAP5) also filled with water from the beginning and - to avoid the formation of vapour - to set the overall temperature of water to 303 Kelvin. This conditions of course differ from the experimental setup described above; however, even with this modification, the proposed setup can be considered valid for the preliminary assessment of the complete simulation. Furthermore, as mentioned above, the exact experimental setup is yet to be decided and, therefore, only qualitative results could be actually analysed. The presented setup is summarised in Tab. 7-5. The initial conditions in the SB1 Tank are shown in Fig. 7.13.

The system remains at rest for 1 second (Fig. 7.13) and then the valve in the injection circuit (controlled by RELAP5) is opened and the water starts to enter in the SIMMER domain through the injection line region (Fig. 7.14). After 1.04 seconds the virtual wall which separates the injection region and the PbLi region disappears and the water is injected into the tank (Fig. 7.15); there is a first increase in temperature - in a confined region at the outlet of the injection pipe - due to the pressurisation of the small amount of gas present at the beginning of the transient (Fig. 7.15) and then a higher increase because of the chemical reaction of the water with the PbLi.(Fig. 7.16 andFig. 7.17).

The activation of the chemical reaction looks clear also from Fig. 7.18 and Fig. 7.19 where the volume fraction of the products of the reaction (namely, LiOH and Li$_2$O) is shown: at the beginning the two products are not present inside the reactor (Fig. 7.18), but they start to appear as soon as the water jet reaches the PbLi region (Fig. 7.19).

7.3   Role of the activity, general goals and future development

The Department of Civil and Industrial Engineering (DICI) of the University of Pisa has a notable experience in the use and development of the codes SIMMER III (SEARCH project (FP7-EC) [7.9],[7.10], CIRCE-SGTR for MAXSIMA project [7.11], LIFUS5/Mod2 for LEADER [7.12] and THINS projects [7.13]) and the development of methodologies for the coupling of different codes with the code RELAP5 [7.5]-[7.8].

Recently, DICI developed an original coupling technique between the SIMMER III and RELAP5/Mod3.3 codes, using MATLAB as an interface among the two codes. Furthermore, in a previous work, the model for chemical interactions between water and PbLi were also implemented by DICI in SIMMER III. Therefore, on the one hand SIMMER III is apt to simulate 2D axis symmetric domains and it is particularly fitted for the analysis of water and PbLi interaction, whilst on the other hand RELAP5 code is suitable for the simulation of composite pipe systems as 1D geometry and hence it can reduce the computational effort of the complete simulation. As a result, this coupling tool can provide high accuracy in calculations involving complex geometries and physical phenomena, such as multiphase flow in experimental loop facilities involving chemical reaction, at a relatively low computational cost.

The coupling technique was initially applied to simple test cases (manometer flow oscillation problems) in order to obtain a first assessment of the tool, obtaining satisfactory results on the prediction of the pressurisation transient of the whole system, when compared to results obtained through simulations performed using RELAP5 as standalone code (i.e. using RELAP5 to simulate the whole system).

Furthermore, a more advanced validation process was started, with the final aim of simulating the whole experimental campaign to be conducted at ENEA Brasimone in the LIFUS5/Mod3 facility. Since the facility is still under development, a simplified nodalization was created and simulations with a preliminary setup were performed. In the nodalization the tank containing the liquid PbLi was simulated by SIMMER III, while the water injection line was simulated using RELAP5. The qualitative results were satisfactory: the injection of water from the RELAP5 domain into the SIMMER domain and the chemical interaction between water and the liquid metal were well captured.

As future work, the completion of the validation is foreseen with a full quantitative analysis of the computational results and a comprehensive comparison with the available experimental data from the LIFUS5/Mod3 facility.

Test case	Init. Cond. (RELAP5)	Init. Cond. (SIMMER III)
1. Tanks at different initial pressure	10 bar / 20°C	1 bar / 20°C
2. High pressure tank kept at 10 bar during the transient	10 bar / 20°C	1 bar / 20°C
3. High pressure tank kept at 10 bar with different water temperature in the two tanks	10 bar / 80°C / 0.5 m	1 bar / 20°C / 0.5 m
4. High pressure tank kept at 50 bar	50 bar / 20°C / 0.95 m	1 bar / 20°C / 0.25 m
5. High pressure tank kept at 100 bar	100 bar / 20°C / 0.95 m	1 bar / 20°C / 0.25 m

Tab. 7-1 – Manometer flow oscillation problem test cases

Volume	Parameter	Dimension
S1-B	H (m)	0.555
	D (m)	0.257
	V (m^3)	0.026590
Free gas	V (m^3)	To Be Decided, for the reference test: 0.001815
Inj-device	H (m)	0.06-0.106
	D (inch)	1/2''
	D$_{orifice}$ (m)	To Be Decided
Inj-line	L (m)	~ 9.72
	D (inch)	1/2''

Tab. 7-2 – Geometrical features of the LIFUS5/Mod3.3 facility

Parameter	Design Value
Abs. pressure in S1-B (bar)	1
PbLi temperature in S1-B (°C)	330
Injected water temperature (°C)	300
Abs. pressure in injection line (bar)	0.01
Gas cylinder pressure (bar)	155
Free gas volume (m^3)	TBD

Tab. 7-3 – Design data of the LIFUS5/Mod3.3 facility

From	To	Value
PIPE197	PIPE200	0.9
PIPE202	PIPE203	3.67
PIPE207	PIPE210	0.9
PIPE212	PIPE220	0.9
PIPE221	PIPE222	1.02
PIPE222	PIPE223	3.67
PIPE225	PIPE230	0.9
PIPE232	PIPE233	3.67
PIPE234	PIPE240	0.9

Tab. 7-4 – Summary of the pressure drop coefficients implemented in the RELAP5 nodalization (LIFUS5/Mod3.3 facility)

Parameter	Design Value
Abs. pressure in S1-B (bar)	1
PbLi temperature in S1-B (°C)	330
Injected water temperature (°C)	30
Abs. pressure in injection line (bar)	1
Gas cylinder pressure (bar)	155
Free gas volume fraction (m^3)	0.25

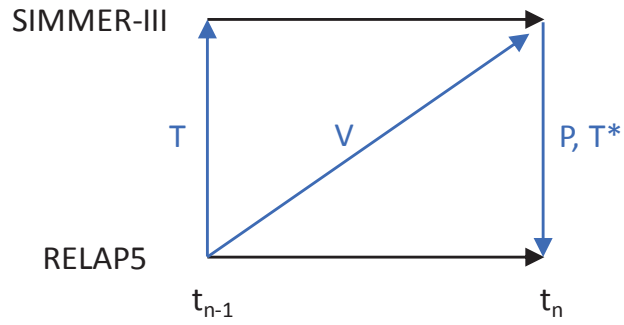*Tab. 7-5 – Initial and boundary conditions for the SIMMER/RELAP5 simulation of LIFUS5*

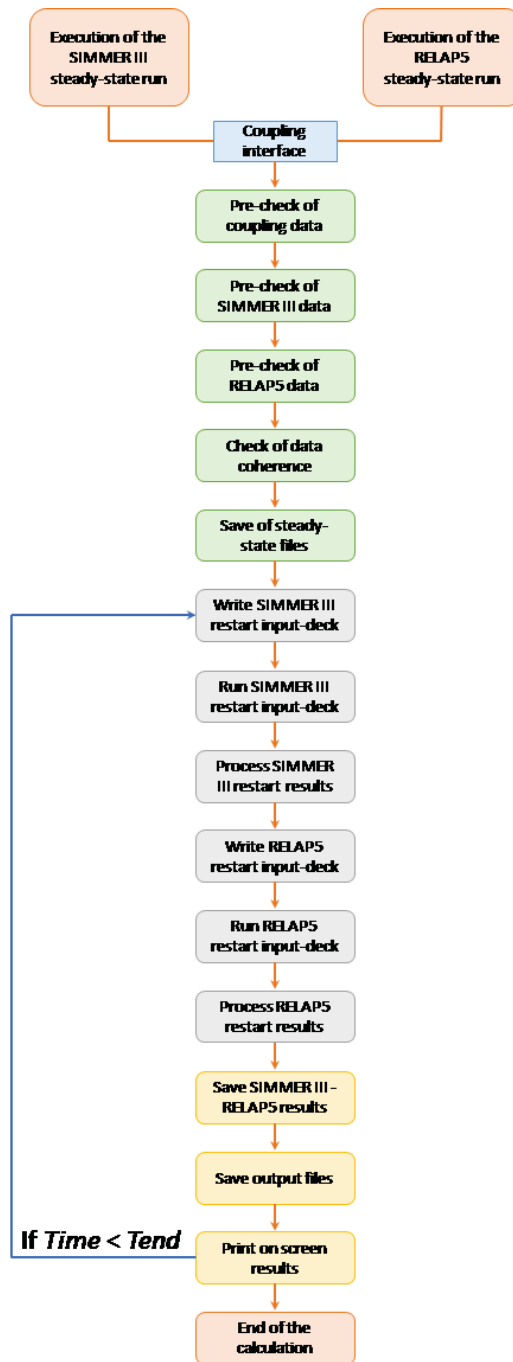*Fig. 7.1 – Data exchange configuration*
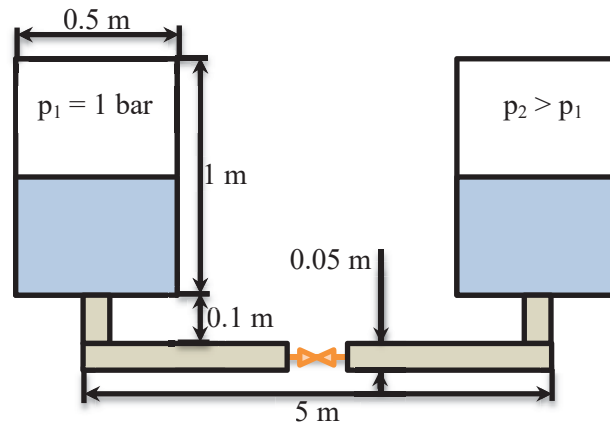
Fig. 7.2 – Coupling tool workflow
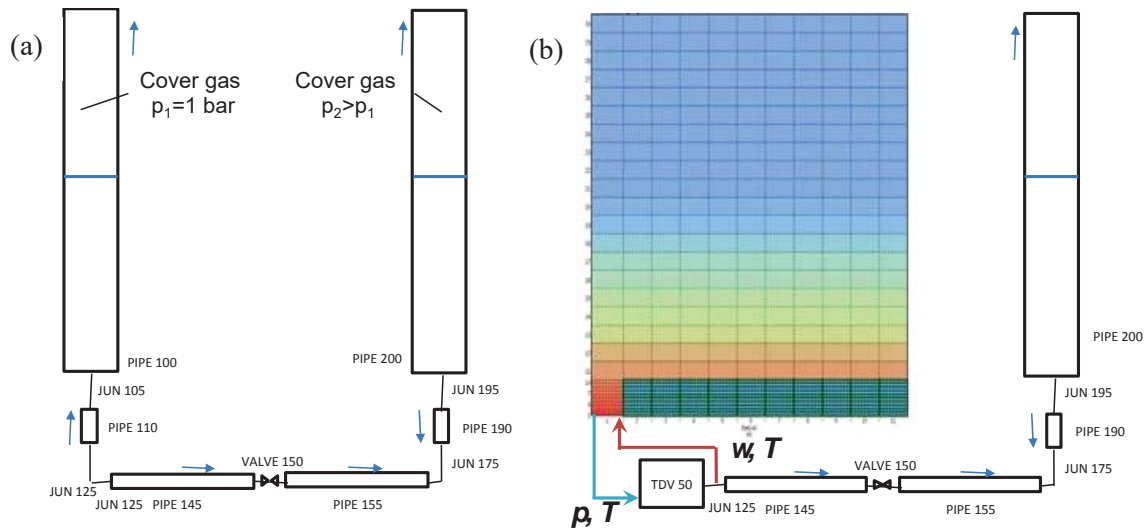
Fig. 7.3 – Geometry of the system

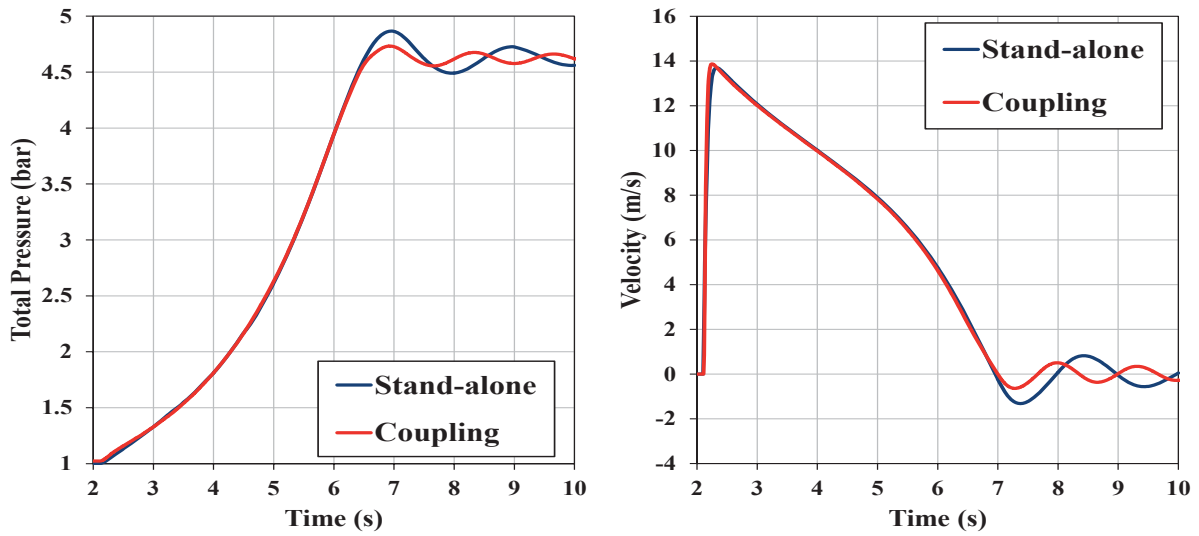

Fig. 7.4 – Stand-alone and coupled nodalizations
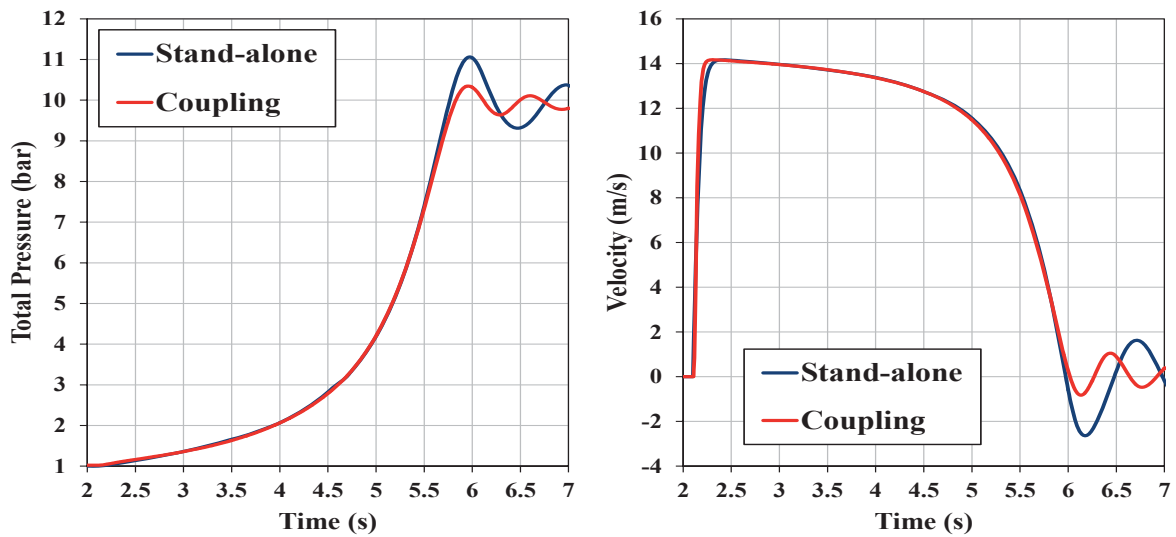
Fig. 7.5 – Case 1 results

Fig. 7.6 – Case 2 results
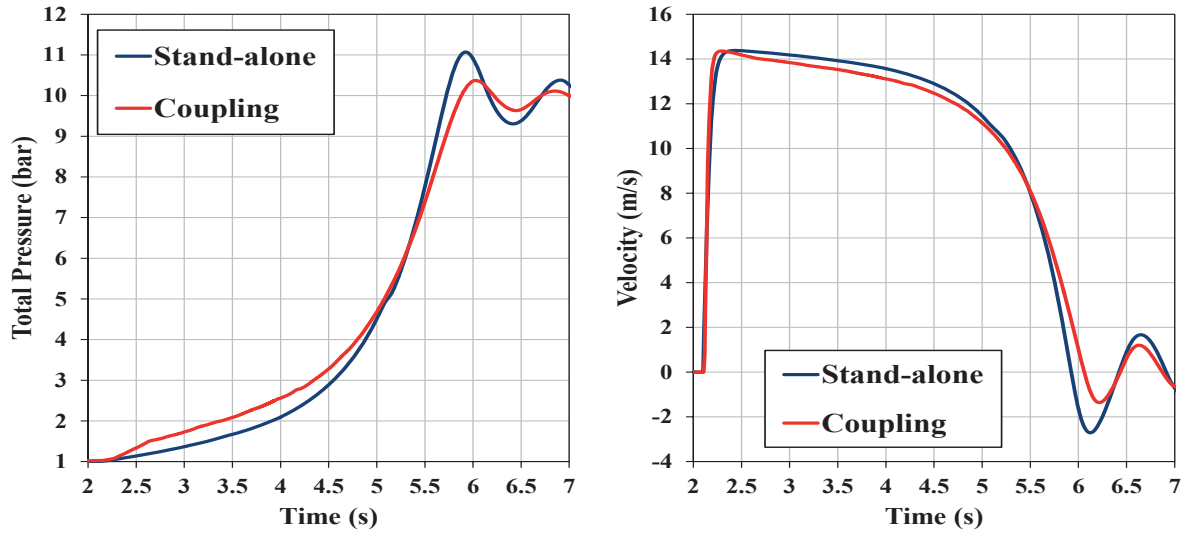
Fig. 7.7 – Case 3 results
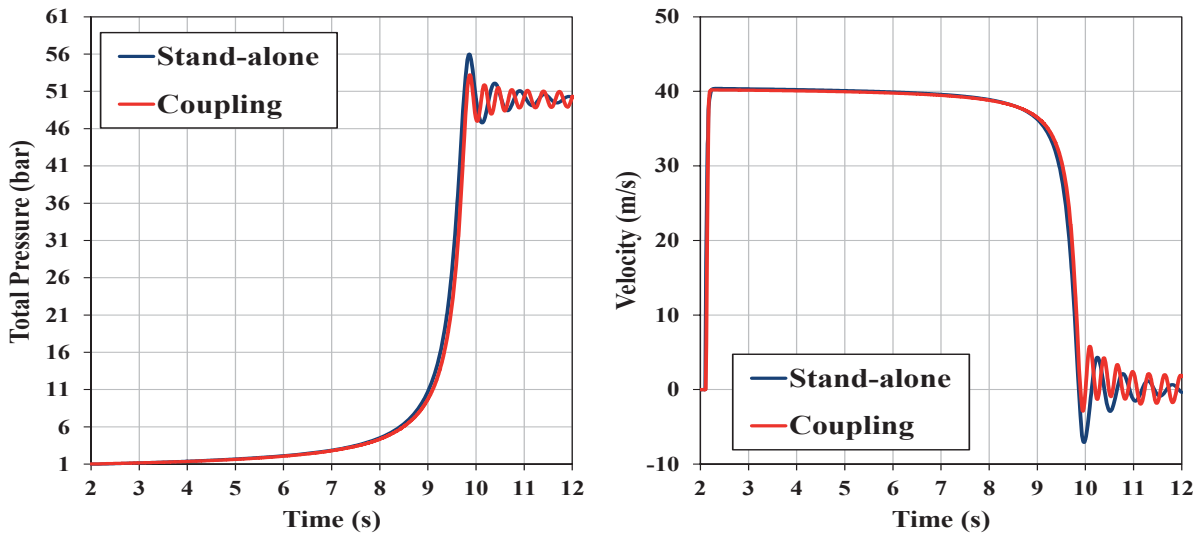
Fig. 7.8 – Case 4 results
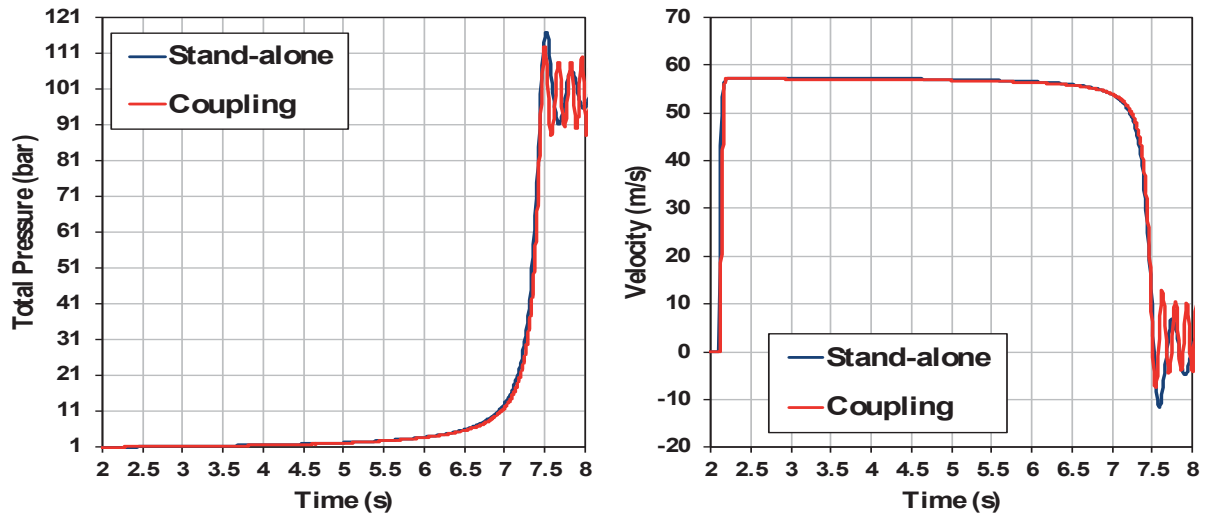
Fig. 7.9 – Case 5 results
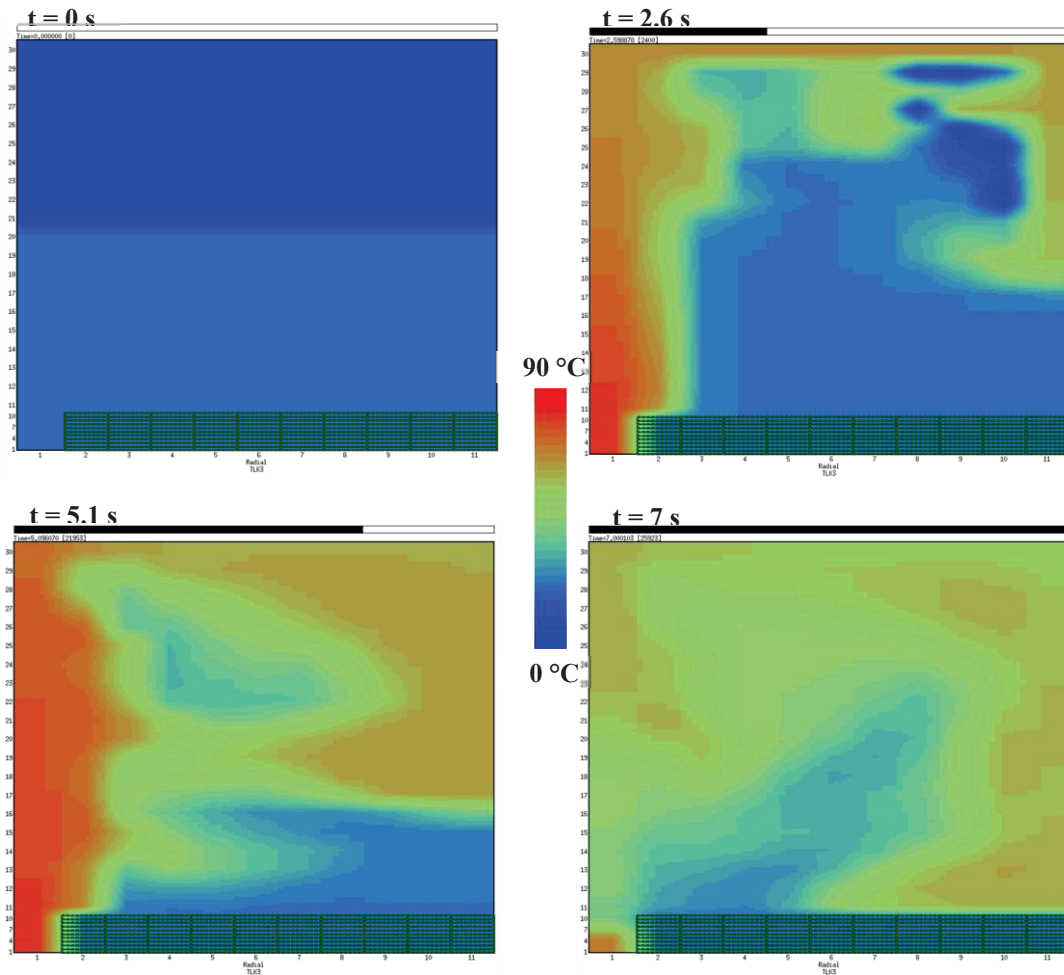
Fig. 7.10 – Temperature evolution in the low-pressure tank in case 3
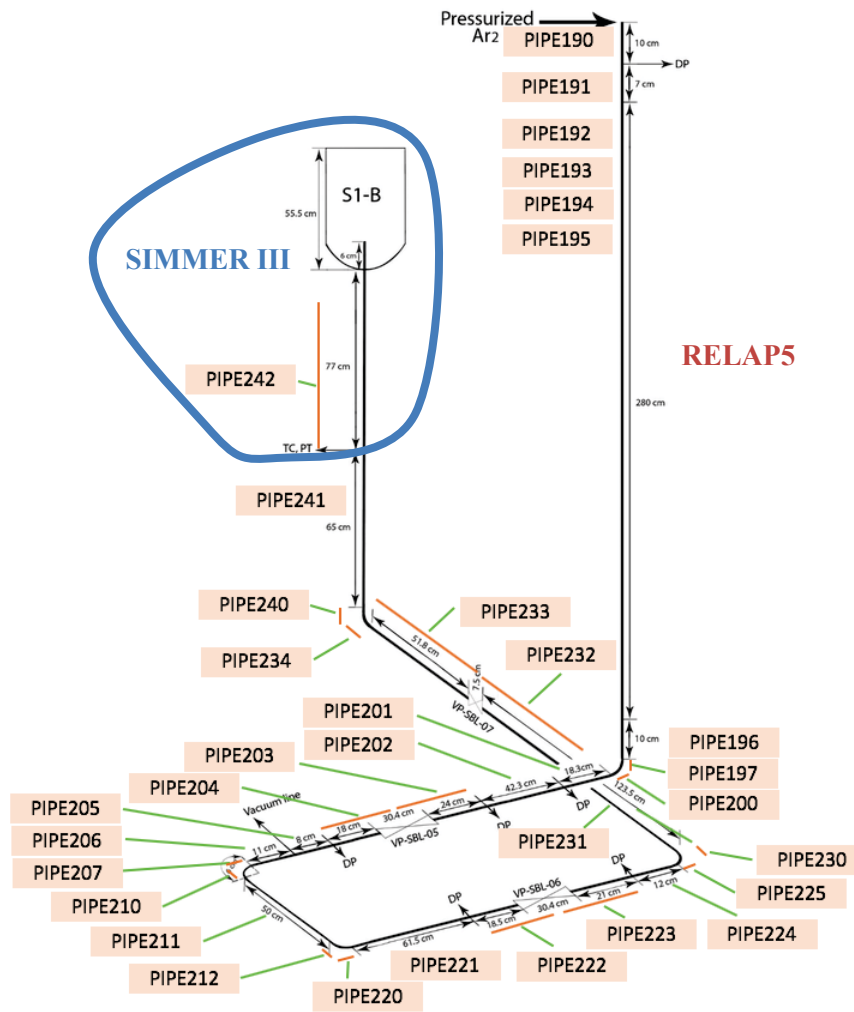
Fig. 7.11 – Geometrical features of the LIFUS5/Mod3.3 facility and nodalization scheme
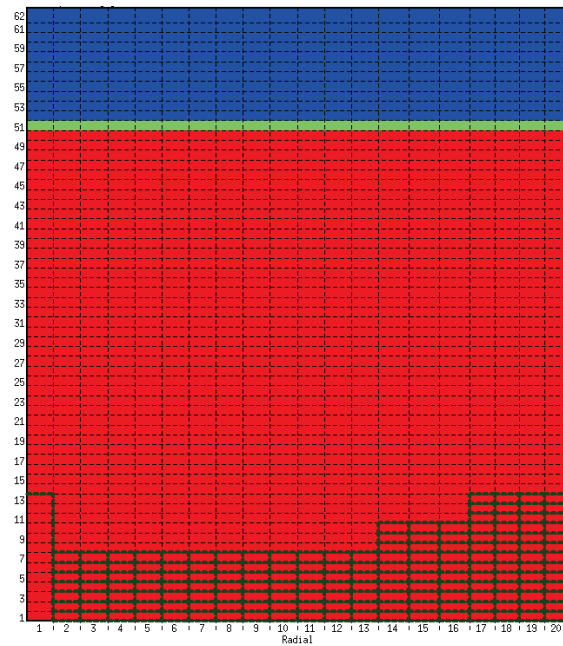
Fig. 7.12 – SIMMER III nodalization of the LIFUS5/Mod3.3 facility (S1-B tank and ending injection line part)
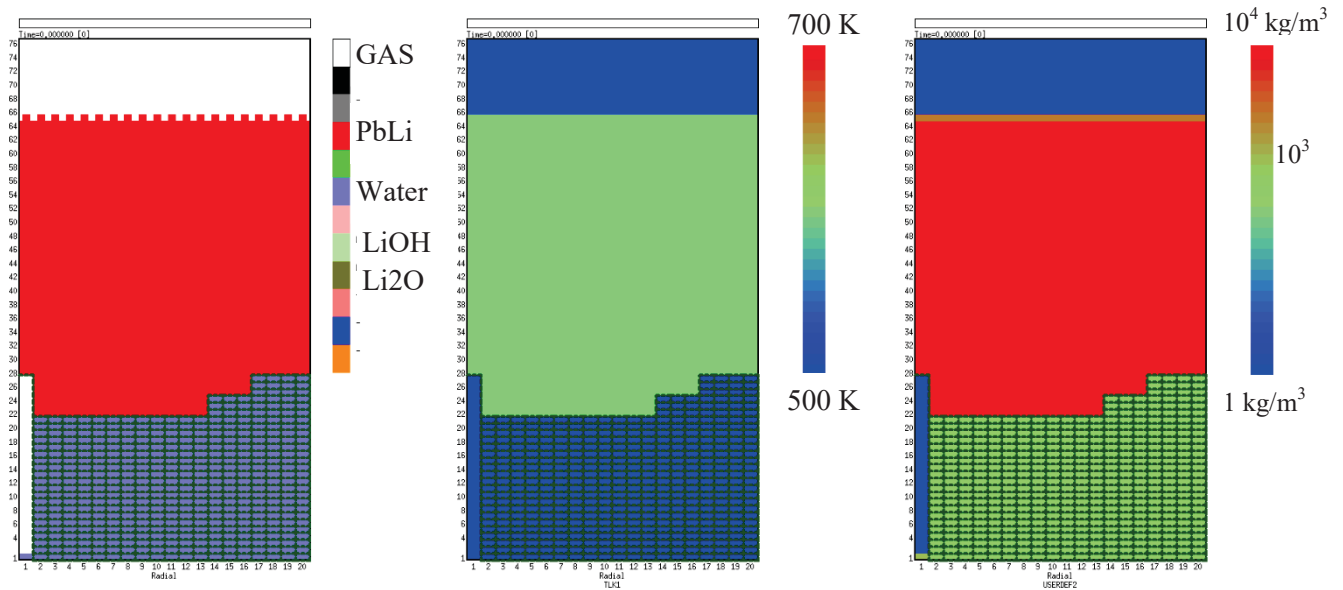
Fig. 7.13 – Initial conditions (from time = 0 to time =1) of the SB1 Tank – Fluids typology (LEFT), PbLi temperature (CENTER) and Fluids density (RIGHT)
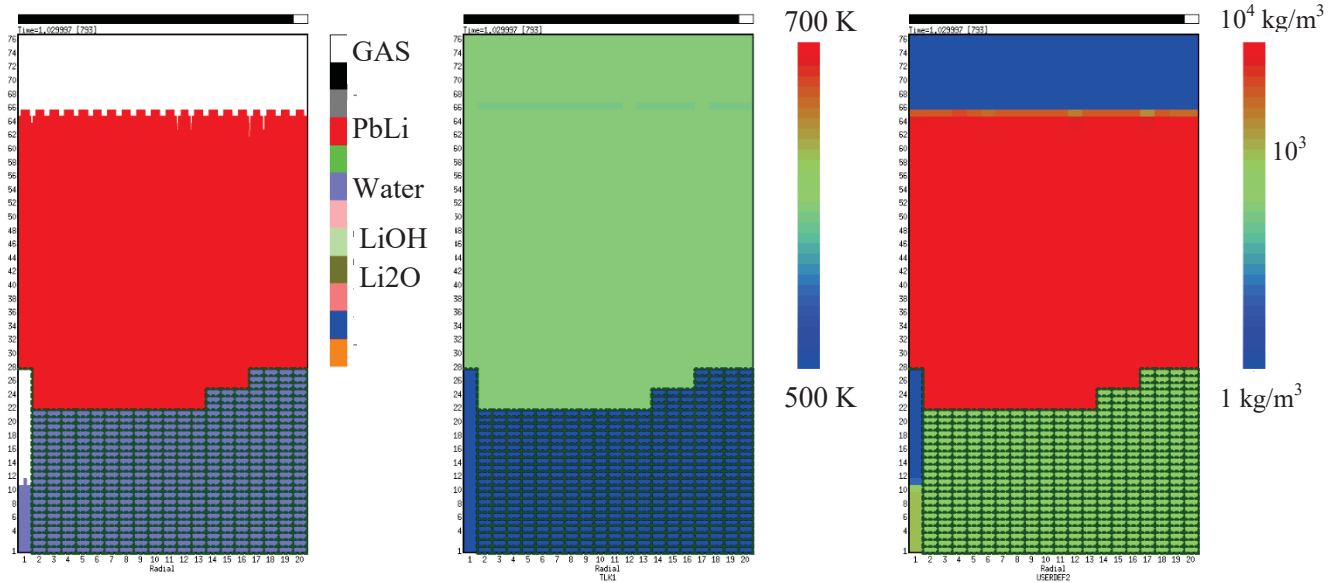
Fig. 7.14 – Time = 1.03 s (0.03 s after start of injection) - Fluids typology (LEFT), PbLi temperature (CENTER) and Fluids density (RIGHT)
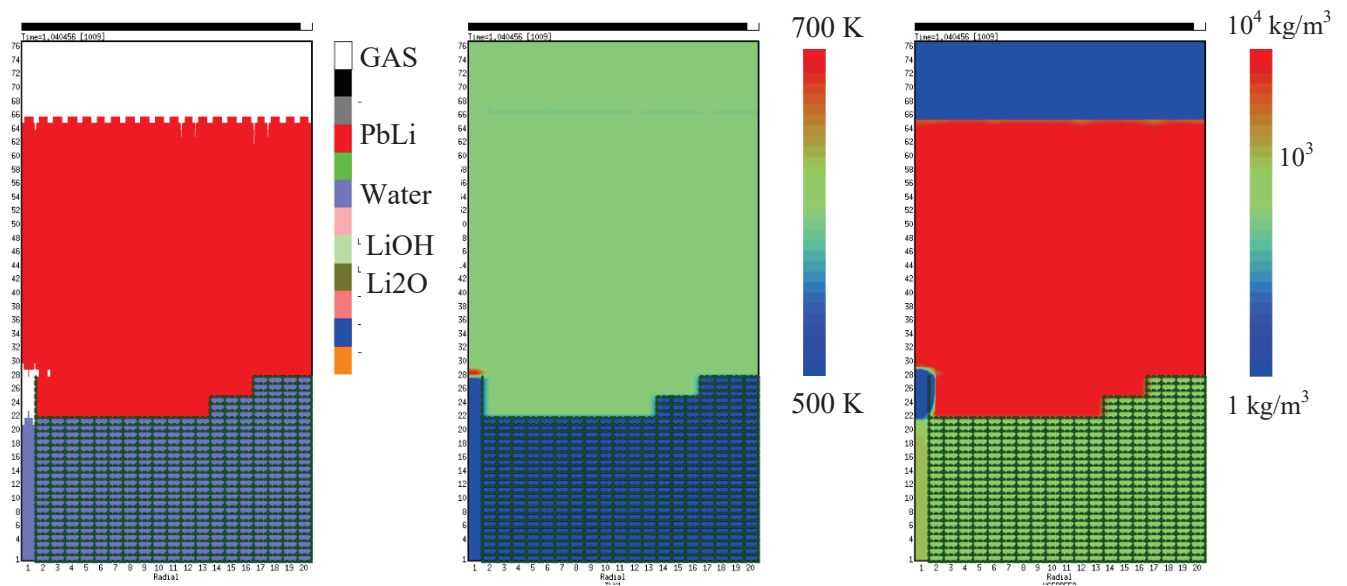
Fig. 7.15 – Time = 1.04 s - Fluids typology (LEFT), PbLi temperature (CENTER) and Fluids density (RIGHT)
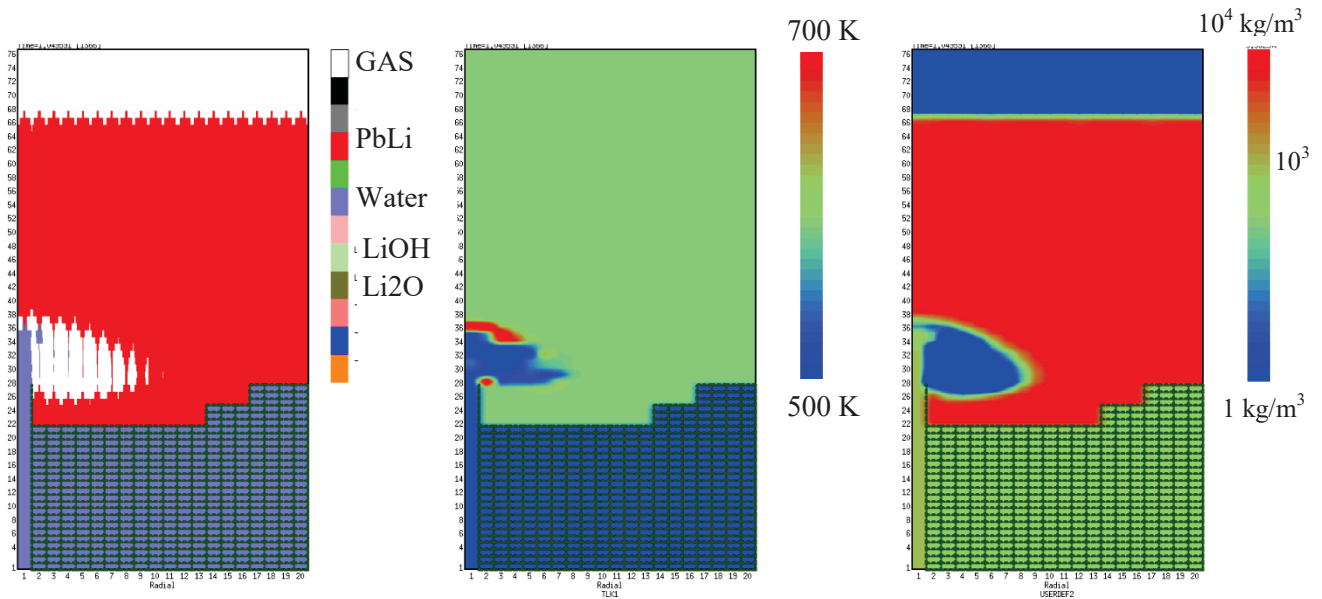
Fig. 7.16 – Time = 1.05 s - Fluids typology (LEFT), PbLi temperature (CENTER) and Fluids density (RIGHT)

Fig. 7.17 – Time = 1.06 s - Fluids typology (LEFT), PbLi temperature (CENTER) and Fluids density (RIGHT)

Fig. 7.18 – Time = 1.04 s - Fluids typology (LEFT), LiOH volume fraction (CENTER) and Li2O volume fraction (RIGHT)

Fig. 7.19 – Time = 1.06 s - Fluids typology (LEFT), LiOH volume fraction (CENTER) and Li2O volume fraction (RIGHT)

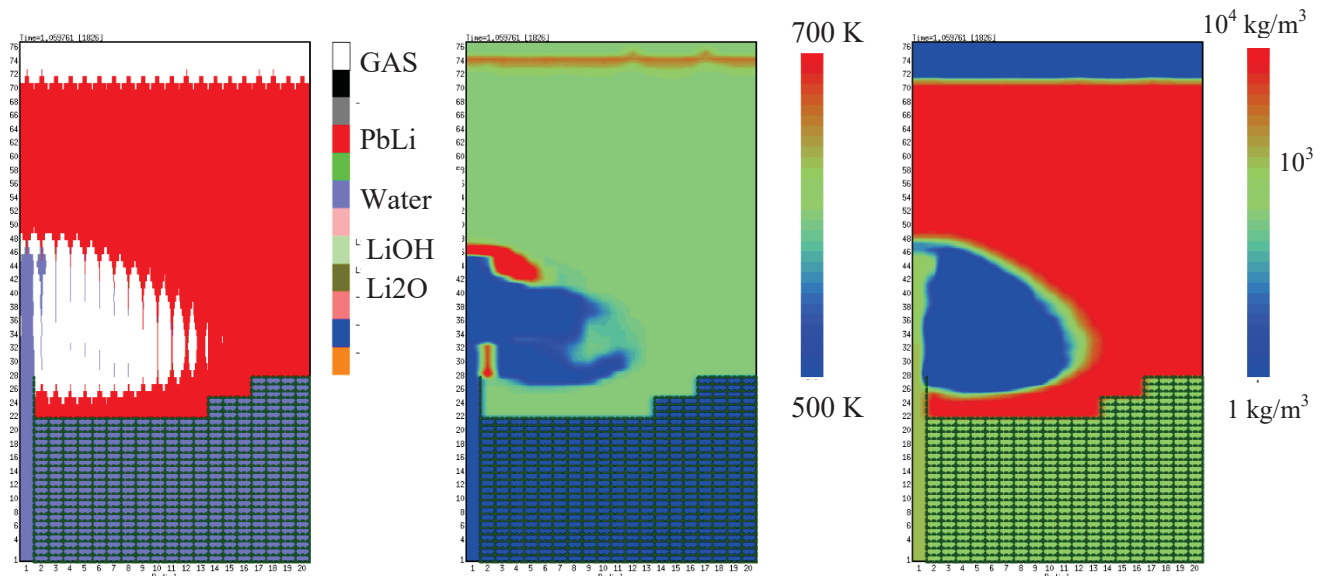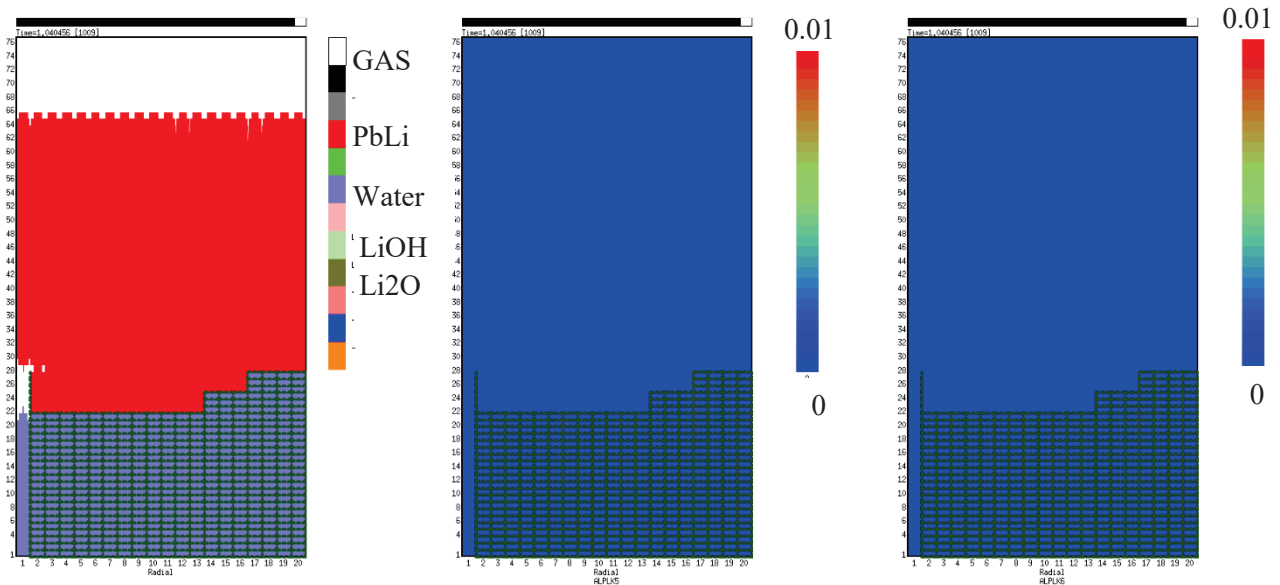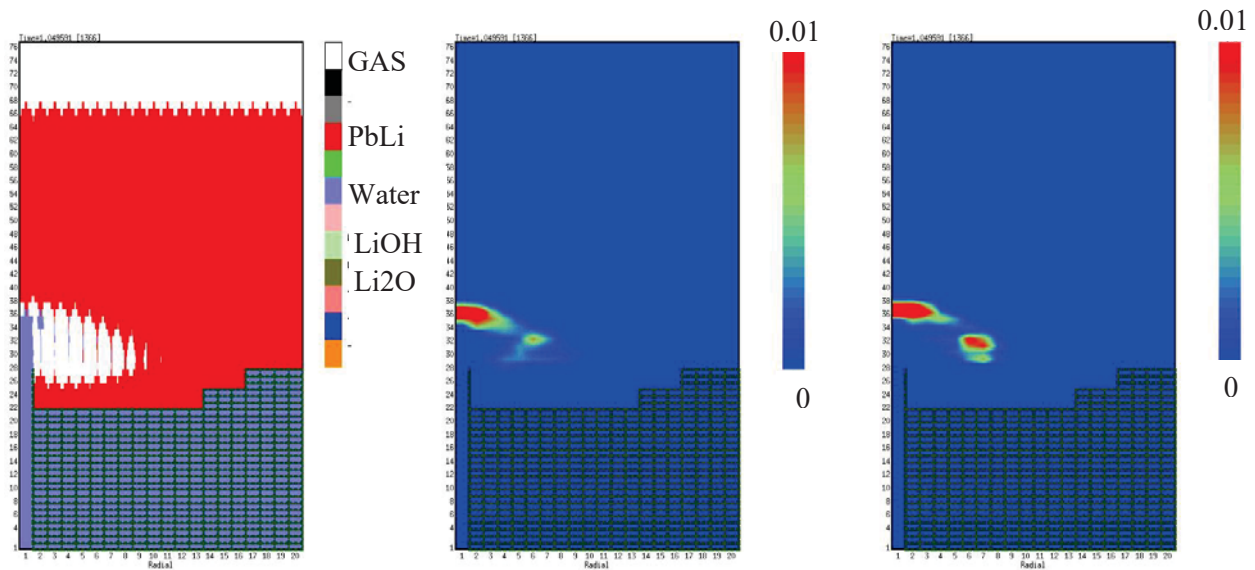|	Title: Development of BE numerical tools for LFR design and safety analysis Project: ADP ENEA-MSE PAR 2017	Distribution **PUBLIC**	Issue Date 27.11.2018	Pag.	
		Ref. ADPFISS-LP2-158	Rev. 0	199 di 213	

RICERCA SISTEMA ELETTRICO

7.4 List of References

[7.1] Del Nevo A, Martelli E, Agostini P, Arena P, Bongiovì G, Caruso G, et al. WCLL breeding blanket design and integration for DEMO 2015: status and perspectives. Fusion Engineering and Design 2017;124:682–6. doi:10.1016/j.fusengdes.2017.03.020.

[7.2] Martelli E, Del Nevo A, Arena P, Bongiovì G, Caruso G, Di Maio PA, et al. Advancements in DEMO WCLL breeding blanket design and integration. International Journal of Energy Research 2017;42:27–52. doi:10.1002/er.3750.

[7.3] Eboli M, Del Nevo A, Pesetti A, Forgione N, Sardain P. Simulation study of pressure trends in the case of loss of coolant accident in Water Cooled Lithium Lead blanket module. Fusion Engineering and Design 2015;98–99:1763–6. doi:10.1016/j.fusengdes.2015.05.034.

[7.4] Eboli M, Forgione N, Del Nevo A. Implementation of the chemical PbLi/water reaction in the SIMMER code. Fusion Engineering and Design 2016;109–111:468–73. doi:10.1016/j.fusengdes.2016.02.080.

[7.5] Oriolo F, De Varti A, Fruttuoso G, Leonardi M, Bocci S, Forasassi G. Modifiche del Codice RELAP5 versione MOD3.2/Beta per la Simulazione di Sistemi Refrigerati con leghe di Pb o Pb-Bi. Università di Pisa; 2000.

[7.6] Bianchini G, Bocci S, Carta M, Forasassi G, Fruttuoso G, Mattioda F, et al. Calcoli di Benchmark su Nocciolo ADS. Confronto tra i Risultati della Versione Integrata del codice RELAP5/PARCS Modificata per la Trattazione di Sistemi Sottocritici con Sorgente Refrigerati a Pb-Bi e i Risultati del codice NILO. Università di Pisa; 2001.

[7.7] Ambrosini W, Forgione N, Oriolo F. Limiti di applicabilità dell'accoppiamento tra il codice RELAP5 Mod. 3.3 e il codice PARCS multigruppo alla simulazione di sistemi sottocritici raffreddati a metalli liquidi pesanti. Università di Pisa; 2007.

[7.8] Martelli D, Forgione N, Barone G, di Piazza I. Coupled simulations of the NACIE facility using RELAP5 and ANSYS FLUENT codes. Annals of Nuclear Energy 2017;101:408–18. doi:10.1016/j.anucene.2016.11.041.

[7.9] Bandini G, Eboli M, Forgione N. Fuel Dispersion and Flow Blockage Analyses for MYRRHA-FASTEF Reactor by SIMMER Code. Volume 2B: Thermal Hydraulics, Prague, Czech Republic: ASME; 2014, p. V02BT09A005. doi:10.1115/ICONE22-30553.

[7.10] Angelucci M, Eboli M, Forgione N, Bandini G. Transient Analyses for the MYRRHA-FASTEF Reactor by SIMMER Code 2015:14.

[7.11] Pesetti A, Tarantino M, Forgione N. Test Section Design for SGTR Experimental Investigation in CIRCE Facility for HLMRS Supported by SIMMER-III Code 2016:V002T06A027. doi:10.1115/ICONE24-60716.

[7.12] Del Nevo A., Giannini N, Pesetti A, Forgione N. Experimental and numerical investigations of interaction between heavy liquid metal and water for supporting the safety of LFR gen. IV reactor design, Chicago: 2015, p. 14.

[7.13] Pesetti A, Del Nevo A, Forgione N. Experimental investigation and SIMMER-III code modelling of LBE–water interaction in LIFUS5/Mod2 facility. Nuclear Engineering and Design 2015;290:119–26. doi:10.1016/j.nucengdes.2014.11.016.

(Page intentionally left blank)

8 FUEL-COOLANT CHEMICAL INTERACTION

E. Macerata, M. Mariani, M. Giola, E. Mossini, M. Negrin

(Page intentionally left blank)

8.1   Introduction

The complete understanding of chemical compatibility among fuel, cladding and coolant within GEN IV Lead-cooled Fast Reactors is far from being achieved, although it is of paramount importance to foresee the consequences of a cladding failure event both in nominal and accidental conditions.

In this perspective POLIMI has continued the theoretical work already started in the previous PAR projects concerning the development, validation and application of a DFT-GGA approach to estimate missing thermochemical parameters for compounds of interests in the development of LFRs, as well as the thermodynamic analysis of the fuel-coolant system by means of the CALPHAD approach.

Within a more general vision, POLIMI has started a literature review in order to clarify how thermodynamic calculations could be integrated in multi-physics codes.

In parallel with these activities, great efforts have been dedicated to the experimental activities started in the previous PAR projects and aimed at studying chemical interactions among liquid lead and pellets of different oxides. The characterization of the pellets after the reactivity experiments have been completed by means of different techniques. Moreover, the work done enabled to derive significant indications to optimize the future interaction experiments.

8.2   Computational activities

8.2.1   Thermodynamic predictions by CALPHAD method

POLIMI has started the study of the U-O-Pb and La-O-Pb systems by CALPHAD method [8.1][8.2]. To this purpose, experimental binary phase diagrams as well as the required thermodynamic data have been collected. Thermodynamic parameters are both experimental values and data estimated by the DFT approach developed during the previous projects. All these information are input data for OpenCalphad, the free CALPHAD software we are using [8.3][8.4]. Attempts are still ongoing due to difficulties related to the database compatibility.

8.2.2   Integration of thermodynamic calculations in multi-physics codes

Several fuel performance codes are commercially available. The major drawbacks of such commercial codes are the fact that i) they are dedicated to a specific fuel form and composition, ii) they cannot run parallel on large computational networks, leading to longer computation time and to the impossibility to use complex models, and iii) they have often complementary features but they cannot be coupled and executed together.
Indeed, they should enable to simultaneously take into consideration a lot of phenomena, for example microstructure evolution, fission products release, thermo-chemistry of chemical reactions, phase stability, non-equilibrium phenomena and so on. To address all relevant natural phenomena in nuclear fuel, models and simulations have been developed for various time and space scales [8.5]. As described in Fig. 8.1 several methods and software packages have been developed to this purpose.

Thermodynamic computations are intended to provide source terms, material properties and boundary conditions for various transport phenomena in nuclear fuel codes, aimed at predicting the behaviour of fuel chemistry, fuel oxidation, fission gas release and many other matters pertaining to nuclear fuel behavior under normal and abnormal operating conditions [8.6].

A literature review has been started in order to highlight examples of coupling of multi-dimensional fuel performance codes with thermo-chemical codes and the main results achieved.

A few thermo-chemical codes for nuclear fuel behavior modeling have been developed. For example, the VICTORIA code, developed at Sandia National Laboratories in the US, is a model for radionuclide behavior

in the coolant system in severe accidents, and it incorporates a thermodynamic equilibrium calculation procedure based on a stoichiometric Gibbs energy minimization algorithm [8.7]. In the widely used severe accident code ASTEC, it does not use a general thermodynamic equilibrium calculation but rather calculates the release of each element individually using parameterized models [8.8].

Another important example is the SOLGASMIX program developed by Eriksson [8.9]. It has been used at the Royal Military College of Canada (RMC) with their thermochemical fuel model (RMC Fuel Thermochemical Treatment, RFTT) to calculate the chemical equilibrium composition of irradiated fuel by Gibbs energy minimization. Later, the thermochemistry library Thermochimica has been developed by Piro et al. [8.10] to be used with the RFTT database and thermochemical models, based on a new and more efficient algorithm called the Partitioning of Gibbs Energy (PGE). As shown in Fig. 8.2, Thermochimica has been introduced in the AMP (Advanced Multi-Physics) multi-physics nuclear fuel performance code developed at ORNL. By exploiting different tools, Piro and co-workers in 2013 simulated the irradiated nuclear fuel behavior by coupling thermochemistry, isotopic evolution and heat transfer [8.11]. The coupling of multiple physical phenomena using the AMP, ORIGEN-S and THERMOCHIMICA codes provides the capability of predicting the spatial distribution of chemical elements as a result of nuclear fission, the increased production of fissile plutonium near the rim and the resulting change in specific power, the formation of various phases and their composition, the oxygen-to-metal ratio, the chemical potential of every component in the system, and other related thermodynamic properties. The predicted elemental concentrations of many pertinent fission and activation products, oxygen partial pressure and oxygen-to-metal ratio agree well with measurements of highly irradiated fuel.

Further, Baurens and co-workers in 2014 presented the results obtained from the incorporation of the chemical solver ANGE in the thermo-mechanical fuel behavior code ALCYONE to study the Iodine-Stress Corrosion Cracking (I-SCC) at CEA in France [8.12]. The AdvaNced Gibbs energy (ANGE) code is the renamed SAGE Gibbs energy minimization code, which is in turn a successor to SOLGASMIX. The coupling of the codes along with coupling to the MARGARET fission product release module is shown in Fig. 8.3. The results are promising but further improvements are foreseen in the future: one could be that the thermo-chemical module with an oxygen redistribution model could feedback the oxygen-to-metal ratio to the fuel performance code for using in calculations of thermal and mechanical properties.

The coupling of thermochemical codes with fuel performance codes will be further explored with particular attention to the LFR features.

8.3 Experimental activities

During this project POLIMI has concluded the experimental campaign started in the previous project and aimed at studying the chemical interaction between liquid lead and several compounds representative of the main fission products, in the conditions experienced in the reactor during the nominal operation or under accidental maloperation. Different oxides were chosen for the experiments: lanthanum oxide (La_2O_3), cerium oxide (CeO_2), strontium oxide (SrO) and zirconium oxide (ZrO_2). Besides FPs oxides, also iron oxide (Fe_2O_3) and calcium oxide (CaO) were included to investigate their behaviour in contact with liquid lead, in this campaign separately and in the future mixed with FPs.

First, powders were characterized by X-Ray Diffraction (XRD) and Differential Scanning Calorimetry (DSC) to check purity and composition. Then, preliminary investigations by DSC has been performed on samples obtained by mixing Pb and oxide powders, to check a possible rapid reactivity in the temperature range considered. Fig. 8.4 shows the temperature profile applied to the DSC crucibles and the DSC curve of the system Pb-CeO_2: two peaks can be perfectly seen, corresponding to Pb melting and solidification. From DSC curves the values of the melting temperature and the enthalpy of fusion can be derived.

As summarized in Tab. 8.1, the melting temperatures and melting enthalpies obtained for the different systems are coherent and close to that of pure Pb, thus confirming the absence of reactivity between Pb and the four oxides in the experimental conditions used.

On the basis of the first illustrative results, several reactivity experiments were performed with oxide pellets in a furnace at temperatures ranging from 500 to 750°C for reaction times up to 7 hours, as summarized in Tab. 8.2.

For each compound, different pellets were prepared in air, but the oxygen trapped in caused problems during the thermal treatment. Therefore, new pellets were prepared under inert atmosphere inside a glove box filled with argon kept at constant oxygen level (no more than 0.1 ppm). For lanthanum, strontium and iron oxides the pellets were formed and maintained their shape, while in the case of cerium, zirconium and calcium some problems were observed. For these reasons, the pellet preparation will be reconsidered and optimized. Where possible, the pellet has been weighted and density has been calculated. For the experiments at lower temperatures glass test tubes are positioned in the graphite crucible, while at the higher temperatures pyrex test tubes were used. In each test tube, a FP oxide pellet is covered by about 4 g of Pb in pieces. Lead wire, provided by Alfa Aesar, was used with a purity of 99.9%.

After the thermal treatment, each system was analysed first by a visual analysis and subsequently by means of XRD and SEM-EDX techniques. In fact, while XRD analysis gives information on the composition of the whole material inserted in the sample holder in terms of phases, EDX gives the elemental composition of the surface of the selected zone of interest. With the first technique, it is possible to detect phases that are present in the sample over 3-5 weight%, while SEM-EDX detects the presence of elements above about 1 weight%. The samples studied exhibited a different behavior at a first visual analysis. In the case of the lanthanum oxide, the whole pellet was recovered and separated from solidified lead, while for cerium oxide only fragments of the pellet could be analyzed. At 550°C the pellet of SrO was found on the tube wall as it was blowed up during the thermal treatment. This behavior was not yet understood and further investigations are ongoing.

In order to be able to identify new phases coming from the chemical reaction between Pb and FP oxide, each pellet was analyzed by XRD. To this purpose, the contact surface of the pellet was scratched and the powder was placed in the sample holder with the dome in order to keep the inert atmosphere (see Fig. 8.5).

XRD patterns of each sample were compared with reference patterns available in the XRD library. Fig. 8.6 shows the XRD spectra of Ce_2O after contact with Pb at 550 and 750°C for about 5 hours: before the thermal treatment samples were identified as cerianite and no changes were found after the reactivity experiments with Pb.

Three phases could be recognized in the La_2O_3 pellet (Fig. 8.7): lanthanum oxide, plattnerite, which is a form of lead (IV) oxide PbO_2, and $Pb_2O(CO_3)$, that is reasonable taking into consideration the "history" of lanthanum oxide reagent. In the case of iron oxide pellet, the samples showed the same behaviour at 550°C and 750°C, turning from hematite to maghemite as a result of the thermal treatment.

Summarizing, from XRD characterization of the contact surface of the oxide pellets after reactivity experiments, it is possible to state that in the experimental conditions adopted (temperature and duration of the experiment) no new compounds are formed at the interface between Pb and oxides.

In addition, SEM-EDX analyses have been performed on the scratched powders coming from the reactivity experiments. The powders were placed on the sample holder and remain under inert atmosphere both during

preparation and the transfer to the instrument. The sample holder is then positioned inside the SEM chamber, where it is opened under high vacuum and the acquisition started.

In general, the SEM-EDX analyses of the scratched powders highlighted the presence of impurities due to the pressing procedure and thus, confirmed the results previously obtained with XRD and DSC. In particular, EDX analysis excluded lead diffusion into the oxide pellet in the very first layers of the pellet, at the interface with lead.

Finally, to estimate a metal release from the pellet to Pb during the interaction, a portion of Pb will be dissolved by microwave digestion and analysed by ICP-MS.

8.4 Conclusive remarks

During this year POLIMI has attempted to exploit the thermochemical data estimated by DFT-GGA approach in the previous projects to compile the database needed to the OpenCalphad software for studying U-O-Pb and La-O-Pb systems. Simulations by OpenCalphad are still ongoing.

Furthermore, a literature review has been started highlighting examples of coupling of multi-dimensional fuel performance codes with thermo-chemical codes in nuclear applications. Simulations seem to be in good agreement with experiments. This review will be further completed with particular attention to the case of LFRs.

Concerning the experimental studies on chemical reactivity between liquid lead and some oxides of fission products, the interaction experiments started in the last project have been continued by using higher temperatures (up to 750°C) and longer reaction time. After the contact with Pb at high temperature, the pellets have been recovered and the contact surface with Pb was characterized by XRD and SEM-EDX. Both the techniques confirmed that in the experimental conditions adopted (temperature and reaction time) no new compounds are formed at the interface between Pb and oxides and excluded Pb diffusion into the oxide pellet in the very first layers of the pellet, at the interface with lead. The characterization of the samples will be completed by analyzing with ICP-MS a portion of Pb in order to detect a possible metal release from the pellet.

Moreover, the work done have highlighted also the need to optimize the pellet preparation and to change the experimental set-up. In the future reactivity experiments a different sample container, like a Swagelok vessel, will be adopted and suitable gas purifiers will be introduced to guarantee very low oxygen content (< 1 ppb) during the thermal treatment.

The results achieved within this PAR project and the previous ones have been presented at the 14° Workshop on European Collaboration on Radiological and Nuclear Engineering and Radiation Protection, held in Macugnaga (VB), Italy on 29/5-01/06/2018, and a part of the experimental work has been published on the Journal of Nuclear Materials in the article M. Cerini, O. Benes, K.Popa, E. Macerata, J.-C. Griveau, E. Colineau, M. Mariani, R.J.M. Konings, *Thermodynamic properties of $Pb_3U_{11}O_{36}$*, Journal of Nuclear Materials (2018) 510, 38-42.

	Lead Melting Temperature [°C]	Lead Melting Enthalpy [J/g]
Reference Pb*	327.4 ± 0.1	23.0 ± 2.6
Pb	327.3 ± 0.1	21.6 ± 1.9
Pb - La$_2$O$_3$	327.9 ± 0.1	21.5 ± 2.1
Pb - Fe$_2$O$_3$	327.0 ± 0.1	21.5 ± 1.8
Pb - CeO$_2$	327.2 ± 0.1	21.5 ± 1.9
Pb - SrO	327.9 ± 0.1	21.7 ± 2.1

*From Literature

Tab. 8.1 - Results of the DSC preliminary investigations

	Pellet (1 g)	Pb [g]	T [°C]	t [min]	pellet setup
A1	-	2.5	500	310	-
A2	La$_2$O$_3$	2.3	500	310	air
A3	Fe$_2$O$_3$	2.5	500	310	air
B1	Fe$_2$O$_3$	4	500	210	air
B2	La$_2$O$_3$	4.3	500	210	air
B3	SrO	4.2	500	210	air
C1	Fe$_2$O$_3$	4.5	550	290	argon
C2	CeO$_2$	4.7	550	290	argon
C3	SrO	4.3	550	290	argon
D1	Fe$_2$O$_3$	4.6	550	345	argon
D2	La$_2$O$_3$	4.5	550	345	argon
D3	La$_2$O$_3$	4.2	550	345	argon
E1	Fe$_2$O$_3$	4.4	750	300	argon
E2	La$_2$O$_3$	4.3	750	300	argon
E3	CeO$_2$	4.5	750	300	argon
F1	La$_2$O$_3$	4.9	550	290	argon
F2	SrO	4.8	550	290	argon
G1	CeO$_2$	4.9	750	290	argon
G2	Fe$_2$O$_3$	4.8	750	290	argon

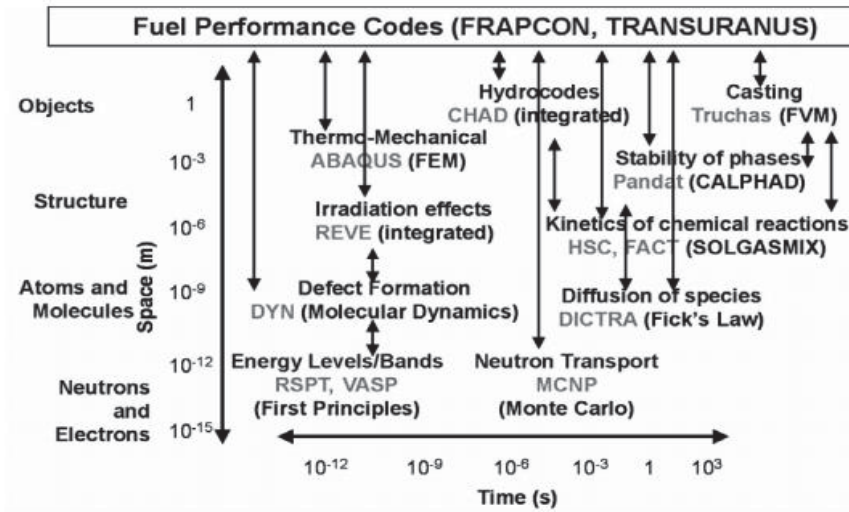*Tab. 8.2 - Summary of reactivity experiments*

Fig. 8.1 – Methods (in bracket) and software packages (in grey) for simulating relevant phenomena in nuclear fuel.
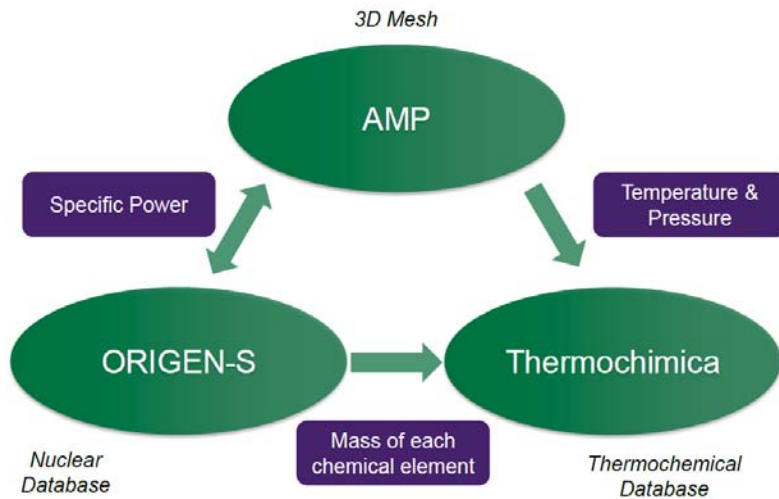

Fig. 8.2 – Integration of the Thermochimica thermochemistry library into the multiphysics nuclear fuel performance code AMP.
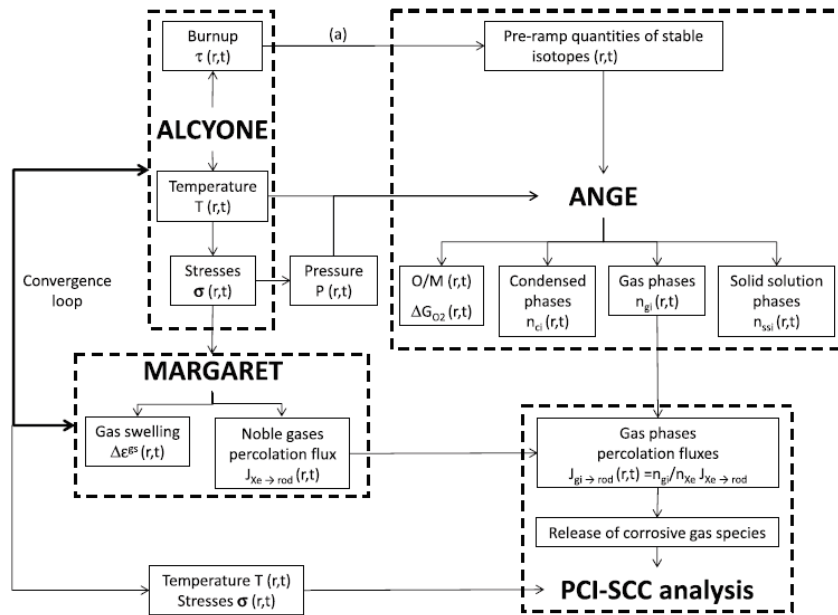
Fig. 8.3 – Coupling between the thermo-mechanical fuel code ALCYONE, the inert fission gas model MARGARET, and the thermo-chemical code ANGE.
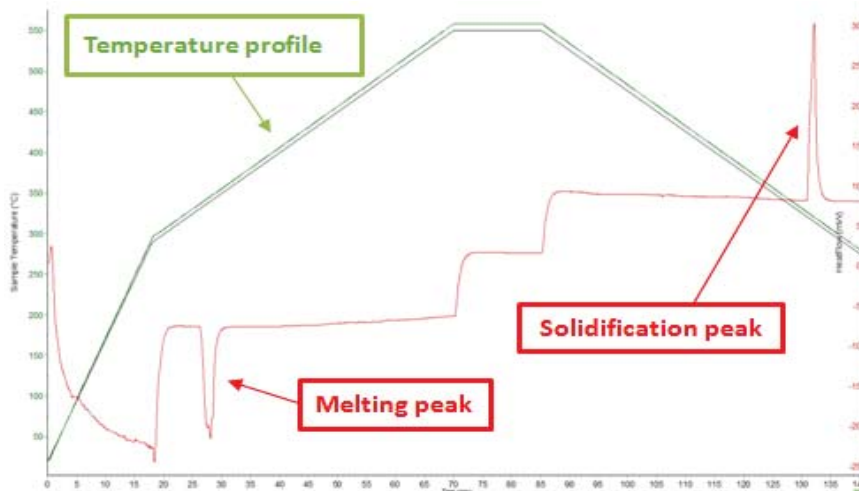

Fig. 8.4 – DSC curve of the system Pb – CeO$_2$: temperature profile and heat flow curve.
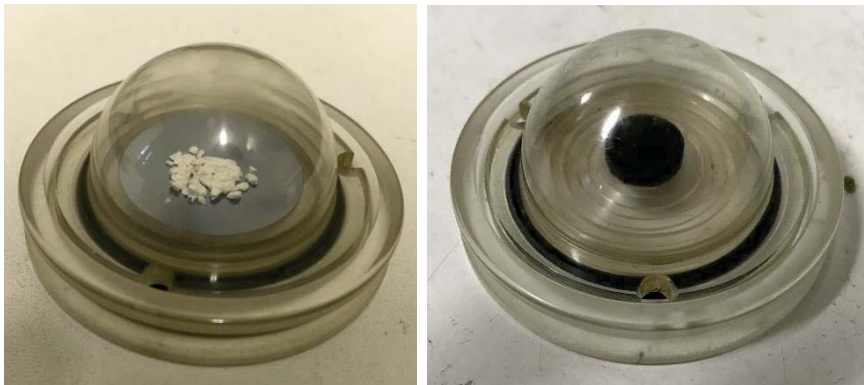
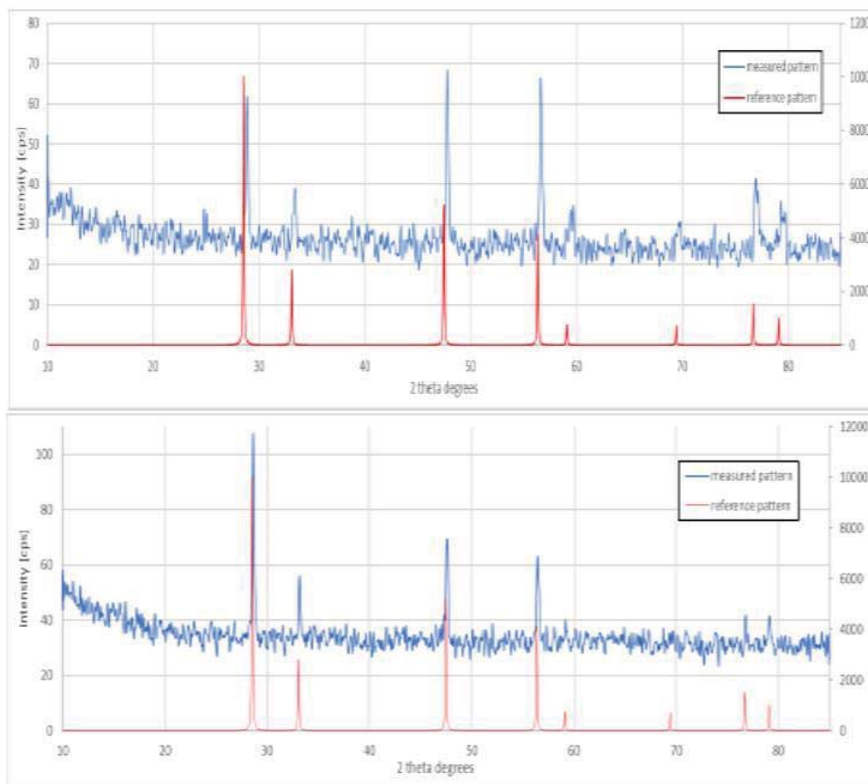*Fig. 8.5 – Sample holder for XRD analysis: CeO₂ (left) and Fe₂O₃ (right).*

Fig. 8.6 – XRD patterns of Ce₂O pellet after reactivity experiment with Pb at 550°C (top) and 750°C (bottom).

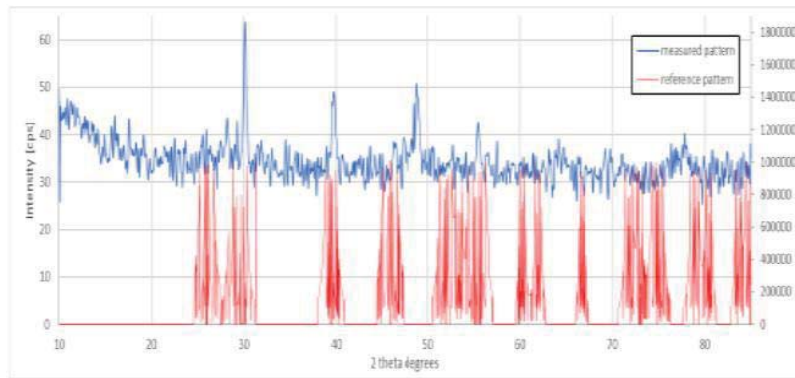*Fig. 8.7 – XRD patterns of La₂O₃ pellet after reactivity experiment with Pb at 550°C.*

8.5 List of References

[8.1] Hickel et al., Phys. Status Solidi B 251, 1, 9-13 (2014)

[8.2] Kattern et al., Tecnol. Metal. Mater. Miner., 13, 3-15 (2016)

[8.3] Kattern et al., Calphad, 24, 55-94 (2000)

[8.4] OpenCalphad web page at http://www.opencalphad.org, visited 1 August 2016.

[8.5] Report NEA/NSC/R/(2015)5

[8.6] Loukusa et al., JNM 481 (2016) 101-110

[8.7] N. E. Bixler. VICTORIA 2.0: a mechanistic model for radionuclide behavior in a nuclear reactor coolant system under severe accident conditions. Technical Report NUREG/CR-6131, US NRC, 1998

[8.8] G. Brillant, C. Marchetto, and W. Plumecocq. Fission product release from nuclear fuel I. Physical modelling in the ASTEC code. Ann. Nucl. Energy, 61:88–95, 2013.

[8.9] G. Eriksson. Thermodynamic studies of high temperature equilibria. XII. SOLGASMIX, a computer program for calculation of equilibrium compositions in multiphase systems. Chem. Scripta, 8:100–103, 1975.

[8.10] M. H. A. Piro, S. Simunovic, T. M. Besmann, B. J. Lewis, and W. T. Thompson. The thermochemistry library Thermochimica. Comp. Mater. Sci., 67:266–272, 2013.

[8.11] Piro et al., JNM 441 (2013) 240-251

[8.12] Baurens et al., JNM 452 (2014) 578-594

DISTRIBUTION LIST

#	NOME	ISTITUZIONE	E-MAIL
1			
2			
3			
4			
5			
6			
7			
8			
9			
10			
11			
12			
13			
14			
15			
16			